Navigation and Autonomy of Soaring Unmanned Aerial Vehicles

Jonathan H. A. Clarke
Department of Aeronautical and Automotive Engineering
Loughborough University

A thesis submitted for the degree of
Doctor of Philosophy
September 2012

I would like to dedicate this thesis to my loving parents, without their ever-present support and encouragement I would never have come this far...

Acknowledgements

Firstly, I would like to thank Mrs Parker at the Dyslexia Institute for the four years she spent with me helping me learn how to read, write and develop coping mechanisms. Without the time and energy she spent I would never have recovered from being so so far behind my classmates. The confidence she helped instil played a significant part in getting me to where I am now.

I would like to express my deepest gratitude and sincerest thanks to my tutor and supervisor, Prof. Wen-Hua Chen, for his constant guidance, help and advice over the past 8 years. He is a wise and inspirational leader, I only wish I will be able to emulate his light-hearted and kind manner of dealing with people. It has been an absolute privilege to be able to benefit from his vast knowledge while working under his guidance. I am eternally grateful for the opportunities he has afforded me.

I am grateful to all of the members of Loughborough Universities Autonomous System Laboratory who have made it such a wonderful place to research, work and play. The sometimes hectic environment never fails to inspire and motivate. I would like to thank Owen McAree, Simon Howroyd and Tom Bamber who assisted with many of the practical aspects of testing. I would especially like to thank Dr. Cunjia Liu, who I am proud to call friend.

My gratitude also goes to Prof. Wen-Hua Chen and the Department of Aeronautical and Automotive Engineering at Loughborough University who have both financially supported my studies and provided the excellent working environment.

I would also like to thank Dr. Jim Gautrey and Dr. Alastair Cooke from the National Flying Laboratory Centre at Cranfield University for their being so accommodating and allowing me to use their Jetsteam 31 aircraft for practical verification.

Last but most importantly, I would like to express my sincerest thanks and gratitude to my parents who lovingly provided me with opportunities to learn and grow in ability and confidence from a rocky start. Their never ending support through the good and bad times has got me to this point.

Abstract

The use of Unmanned Aerial Vehicles (UAV) has exploded over the last decade with the constant need to reduce costs while maintaining capability. Despite the relentless development of electronics and battery technology there is a sustained need to reduce the size and weight of the on-board systems to free-up payload capacity.

One method of reducing the energy storage requirement of UAVs is to utilise naturally occurring sources of energy found in the atmosphere. This thesis explores the use of static and semi-dynamic soaring to extract energy from naturally occurring shallow layer cumulus convection to improve range, endurance and average speed.

A simulation model of an X-Models XCalibur electric motor-glider is used in combination with a refined 4D parametric atmospheric model to simulate soaring flight. The parametric atmospheric model builds on previous successful models with refinements to more accurately describe the weather in northern Europe. The implementation of the variation of the MacCready setting is discussed. Methods for generating efficient trajectories are evaluated and recommendations are made regarding implementation.

For micro to small UAVs to be able to track the desired trajectories a highly accurate Attitude Heading Reference System (AHRS) is needed. Detailed analysis of the practical implementation of advanced attitude determination is used to enable optimal execution of the trajectories generated. The new attitude determination methods are compared to existing Kalman and complimentary type filters. Analysis shows the methods developed are capable of providing accurate attitude determination with extremely low computational requirements, even during extreme manoeuvring. The new AHRS techniques reduce the need for powerful on-board micro processors. This new AHRS technique is used as a foundation to develop a robust navigation filter capable of providing improved drift performance, over traditional filters, in the temporary absence of global navigation satellite information.

All these algorithms have been verified by flight tests using a mixture of manned and unmanned aerial vehicles and avionics developed specifically for this thesis.

Contents

List of Figures

Nomenclature

General Symbols

A	State Transition Matrix
α	Angle of Attack
AR	Aspect Ratio
$a_{x,y,z}$	Local Acceleration
B	Input Matrix
β	Angle of Side-slip
C_{D_0}	Form Drag Coefficient of Aircraft
C_D	Drag Coefficient of Wing
C_d	Drag Coefficient of Aerofoil Section
C_L	Lift Coefficient of Wing
C_l	Lift Coefficient of Aerofoil Section
$C_{1,2,etc}$	Constant 1, 2, etc
DCM	Direction Cosine Matrix
ε	Induced Drag Factor
g	Gravitational Acceleration Constant (9.81m/s/s)
H	Measurement Matrix
$K_{1,2,etc}$	Arbitrary Gain 1, 2, etc

M	Mass
n	Normal Load Factor
ρ	Air Density
ϕ, θ, ψ	Global (Euler) Roll, Pitch, Yaw Angles
$\dot{\phi}, \dot{\theta}, \dot{\psi}$	Global (Euler) Angular Rates
p, q, r	Local Angular Rates
R	MacCready Setting
r	Radius
$r_{x,y,z}$	Global Acceleration
S	Surface Area of Wing
TAS	True Air Speed
u	Forcing or Control Vector
V	Aircraft Velocity
v	Measurement Noise Vector
VSI	Vertical Speed Indicator
$V_{Tail\,Wind}$	Tail Wind Component of Wind
w	Vertical Velocity
w^*	Convective-layer Velocity Scale or Process Noise Vector
x	State Vector
X, Y, Z	Global Position
z	Measurement Vector
Z_i	Convective-layer Scale
$\frac{dC_L}{d\alpha}$	Lift Curve Slope of Wing

$\frac{dC_l}{d\alpha}$	Lift Curve Slope of Aerofoil Section

Subscripts

b	Bias
i	Inner
m	Measured
o	Outer
$peak$	Peak Value
t	True
w	Noise

Acronyms

ADAHRS	Air Data augmented Attitude Heading Reference System
ADC	Analogue to Digital Converter
ADGNS	Air Data augmented Global Navigation System
AHRS	Attitude Heading Reference System
AoA	Angle of Attack
BGA	British Gliding Association
BST	British Standard Thermal
CLEKF	Closed Loop Extended Kalman Filter
COTS	Components Off The Shelf
[DCM]	Direction Cosine Matrix
DOF	Degrees of Freedom
dsPIC	Digital Signal Programmable Integrated Circuit
EGNOS	European Geostationary Navigation Overlay Service

EKF	Extended Kalman Filter
[E]	Euler Transition Matrix
GNSS	Global Navigation Satellite System
I^2C	Inter Integrated Circuit
IAS	Indicated Airspeed
IMU	Inertial Measurement Unit
INS	Inertial Navigation System
LKF	Linear Kalman Filter
LQE	Linear Quadratic Equation
LSA	Lower Stall Angle
LSV	Lower Stall Value
LUCAS	Loughborough University Centre for Autonomous Systems
MEMS	Micro-Electro-Mechanical System
MSAS	Multi-functional Satellite Augmentation System
NED	North East Down
NMEA	National Marine Electronics Association
OPU	On-board Processor Unit
PIC	Programmable Integrated Circuit
PID	Proportional Integral Differential
PI	Proportional Integral
RAT	Ram Air Turbine
SBAS	Satellite-Based Augmentation Systems
UART	Universal Asynchronous Receiver Transmitter

UAS	Unmanned Aerial System
UAV	Unmanned Aerial Vehicles
UKF	Unscented Kalman Filter
USA	Upper Stall Angle
USV	Upper Stall Value
VSI	Vertical Speed Indicator
WAAS	Wide Area Augmentation System
WLAN	Wireless Local Area Network

Chapter 1

Introduction

1.1 Overview

Over the last two decades the use of Unmanned Aerial Vehicles (UAVs) and Unmanned Aerial Systems (UAS) has exploded. Fig. 1.1 shows the selection of the UAVs used for this project. As the use of UAVs has increased the demands placed upon the platforms have also increased. Simultaneously people desire greater access to flying assets lower down the chains of command; whether that is for military purposes or civilian work. This requirement necessitates the use of smaller aircraft without loss of performance. Typically the limiting factors for these small UAVs is short flight duration, limited range and payload. Many activities such as forest fire monitoring, border patrol, atmospheric research, communication relays and other surveillance tasks require greater persistence from the UAS used. Although advancements in engine and battery technology, along with miniaturisation of much of the on-board systems, have provided performance and capability improvements, there is an increasing demand for the introduction of novel methods to improve the range and persistence of the aircraft. One such novel solution is the extraction of energy from naturally occurring phenomena such as atmospheric convection.

In order to understand the challenges associated with high accuracy autonomous flight, and clarify the structure of this thesis, it is useful to build a picture of the physical and theoretical systems necessary for the successful execution of the algorithms. With the goal of increased range and, or persistence of the UAVs in question it is possible to see the building blocks necessary to reach the goal. A model of all the elements required is shown in Fig. 1.2

Figure 1.1: Range of Aircraft to Be Used in the Development

Many elements form the basic blocks that contribute to the successful completion of the high level task. Even completion of blocks that may be regarded as simple, require a combination of hardware and theory development. Fig. 1.2 shows the basic interactions between the elements.

For improvements to be made to the methods used to extract energy from atmospheric convection it is advantageous to start in a simulation environment before moving on to real-world flight tests. The use of a simulator allows the algorithms to be tested in a controlled environment where the conditions are both fully understood and repeatable. However for the results of the simulation to be both meaningful and useful the simulation environment must be realistic. Three key areas of the simulation environment need to accurately reflect reality; the atmospheric model, the aircraft flight dynamics and the aircraft flight control structure.

A detailed atmospheric model is needed in order to understand the interactions between the airframe and the atmosphere. The higher the fidelity of the atmospheric model the more trust can be placed in the predictions made. This thesis presents a 4 dimensional model that extracts the best elements from many other well established parametric atmospheric models.

Autonomous soaring can be simulated with rudimentary knowledge of the

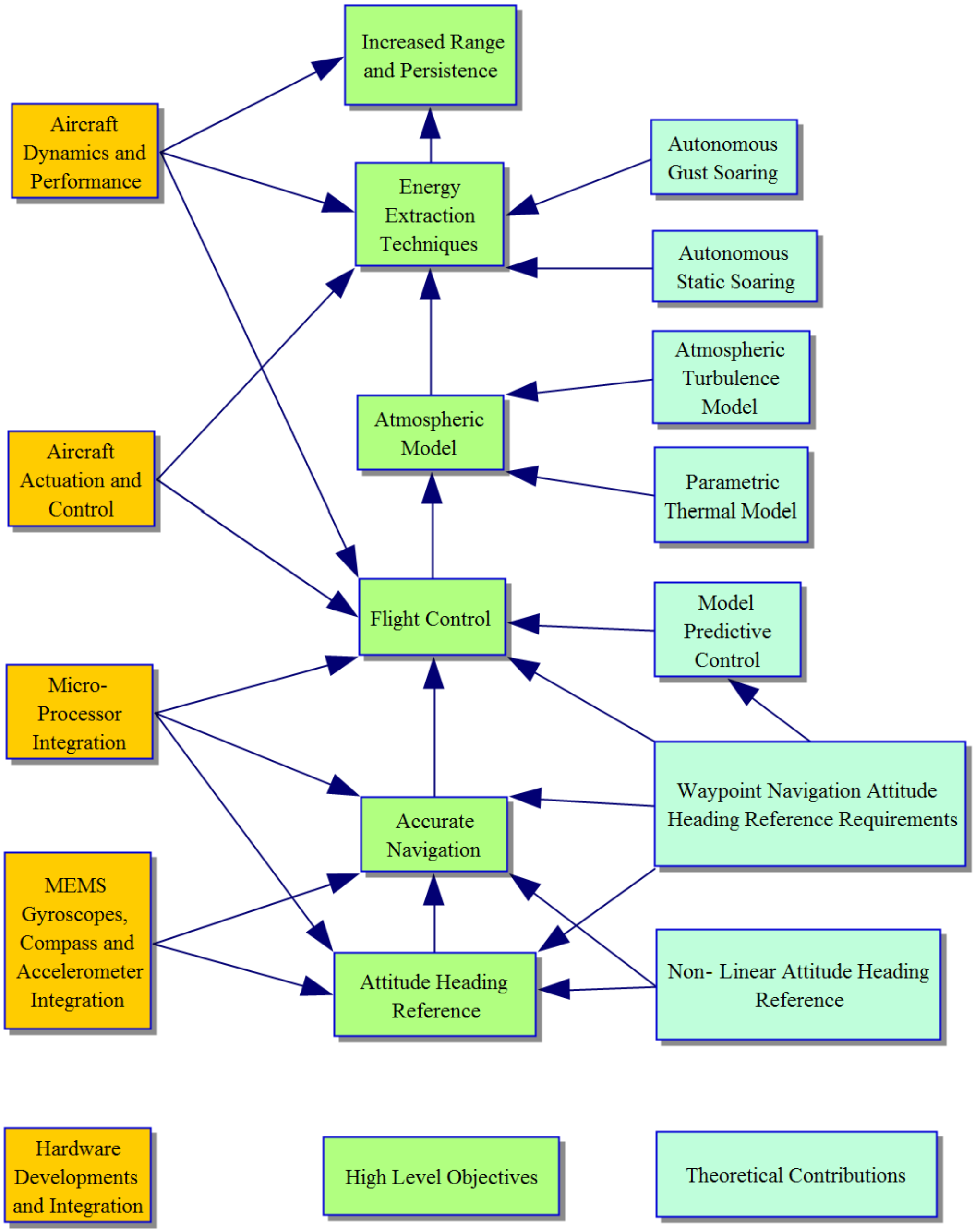

Figure 1.2: Thesis Structure

aircraft in question but in order to optimise the algorithms an accurate model of the aircraft in question is required. The exact performance of the airframe is unimportant but the fidelity of the model needs to be high. The aircraft dynamics need to be accurate because the combination of the flight control system and the soaring controller is likely to cause the aircraft to fly close to the stall. To that end a detailed non-linear aircraft model is explored to derive generic rules for the benefit correlations underlying the systems.

A survey of Components-Off-The-Shelf (COTS) autopilots showed that none had sufficient capacity for soaring flight. It was therefore decided to design a modular autopilot with an open architecture from scratch. This facilitated the implementation and testing of advanced navigation and flight control algorithms. Inexpensive Micro-Electro-Mechanical System (MEMS) sensors and miniature digital signal processors were used. This enabled the use of a new advanced closed loop implementation of an extended Kalman filter for the Attitude Heading Reference System (AHRS). Validation was by comparison with proven filtration techniques such as complementary, linear Kalman, extended Kalman and unscented Kalman filters.

1.2 Aim

The aim of this thesis is to produce and validate a set of algorithms that enable micro to small unmanned aerial vehicles to utilise atmospheric energy, more specifically atmospheric convection, in order to improve their range and/or endurance.

1.3 Thesis Structure

This thesis is arranged as follows:

- After this Introduction, Chapter 2 provides a literature review on the topics related to this thesis, supplying more detail about aspects of extracting energy from atmospheric phenomena. Then a justification of the soaring methods chosen is included with the associated discussion. Attitude heading reference was subject to considerable work; therefore this is also included in the discussion of the state of the art.

- Chapter 3 details the development of the soaring strategies with application to increased range and persistence. An extremely high fidelity 4 dimensional parametric atmospheric model is derived and used to validate the soaring strategies. The assumption of cloud streets is included instead of classical assumption of a random distribution normally used in 2D models. The assumption of a random 2D thermal distribution is shown to be valid, as the full 4D simulation resembles a random distribution if a 2D cross section is chosen. A new implementation of Reichmanns centring technique is presented with good results. The classical soaring approaches are modified and rules are given for their practical application to UAV. Statistical analysis of the typical benefit of including soaring is presented.

- Chapter 4 details the development of an Air Data augmented Attitude Heading Reference System (ADAHRS). The development of the AHRS was necessary because the accuracy of the existing AHRS was found to be insufficient for the task of soaring. The algorithms are extensively tested using the simulation environment introduced in Chapter 3.

- Chapter 5 presents a detailed comparison of a new low computational burden closed loop implementation of a Kalman type filter against a range of more classical Kalman type filters. The closed loop implementation provides a high performance low power attitude estimation solution capable of substantially improving the performance of micro to small size UAV with low power processing units onboard. Extensive simulations are used to evaluate the relative performance merits of the filters.

- Chapter 6 extends the application of the closed loop Kalman filter derived in Chapter 5 to an Air Data augmented Global Navigation System (ADGNS). Chapter 6 details the use of the filter to augment inertial and air data position information with global navigation satellite systems. Again extensive simulations are used to evaluate the relative performance merits of the filters.

- Chapter 7 introduces the custom hardware used for the real world testing of the algorithms developed in Chapters 4, 5 and 6. The avionics hardware designed, manufactured and programmed specifically to facilitate the tests presented in Chapter 8.

- Chapter 8 uses real world practical flight tests to validate the theoretical and simulation results from Chapters 4, 5 and 6. The ADAHRS reference data is validated with the use of custom hardware against data from Cranfield University's flight test laboratory Jet Stream 31. This validation process includes the implementation of the ADAHRS, AHRS, and ADGNS algorithms developed on a low powered micro processor.
- Chapter 9 concludes this thesis with a summary of pertinent results and discussions.

Chapter 2

Literature Review

2.1 Introduction

This chapter presents a literature review focusing on the three subject areas tackled by this thesis; autonomous soaring, augmented AHRS, and data fusion and filtering. Although AHRS and data fusion may appear distinct and quite separate to autonomous soaring, they are in fact integrally linked as autonomous soaring imposes extra challenges on the AHRS.

2.2 Atmospheric Energy

2.2.1 Soaring Flight

Over recent years the use of unmanned aerial vehicles has exploded. The demands placed on modern unmanned aerial vehicles have introduced new design challenges for all the disciplines involved. As the size of the aircraft involved decreases the load bearing capacity also decreases leaving less and less volume and payload available for the systems required to fulfil the desired objectives. To that end new technologies have been employed to increase the overall efficiency of the aircraft and decrease the size and weight of the systems necessary to operate them. The improvements in miniature sensor and battery technology have contributed largely to the successes achieved so far. Although the advancements in the existing technology provide constant improvements, there is an ongoing search for new approaches to the problem. To that end it is possible to look to the natural world for inspiration.

A lot can be learned by looking at birds that perform similar feats of range and endurance as are required of UAVs. There are several birds with similar performance requirements to UAVs. Birds that frequently perform long distance surveillance type mission profiles are falcons, eagles and vultures. Other birds like frigates, albatrosses and gulls perform massive feats of endurance. By looking at birds with similar mission profiles it is possible to gain an insight into possible improvements. The vulture is a large bird which travels long distances scavenging for food before returning to the nest. The vulture's hunting habits resemble a surveillance type mission profile. One of the most striking differences between the vulture's flight patterns and current UAVs is their use of thermal updrafts to stay aloft [45]. Vultures use bubbles of rising air, known as thermals, to keep them aloft while they quickly cover vast distances with minimal energy expenditure. As a result the inclusion of this ability, autonomous soaring, has been of increasing interest to UAV operators in search of better performance; be that usable payload, range, endurance or cross-country speed.

The combination of these soaring techniques with high performance aircraft (aircraft with a low minimum sink rate and a relatively flat drag polar) has not gone unnoticed; as early as the 1920s pilots have been using various soaring techniques for recreational flying in sailplanes. As a result there have been numerous papers published on the methodology of efficiently using energy from thermal updrafts. In the late 1950s MacCready [40] addressed the mathematical problem of the optimal speed-to-fly between thermals to most efficiently utilise them for cross-country speed. Almost two decades later Reichmann [48] proposed a modification of MacCready's theory [40] proving that there was a more efficient method than MacCready's 'Optimum' theory. Soaring techniques have historically been ignored by the surveillance community because the differences in aircraft wing loading, operating speeds and efficiency rendered them pointless. However with the latest generation of UAVs this is no longer the case. There is a wide area of applications where the performance of the UAV could benefit from utilising autonomous soaring techniques; these include atmospheric research, border control, communications, forest-fire monitoring, land management, remote sensing and surveillance. The result of the change in application of this theory means that the field of autonomous soaring is still an emerging field. Wharington [61] first suggested that soaring could be used to extend the performance of UAVs in 1998, since then work has been conducted on all the many variations of soaring. Opti-

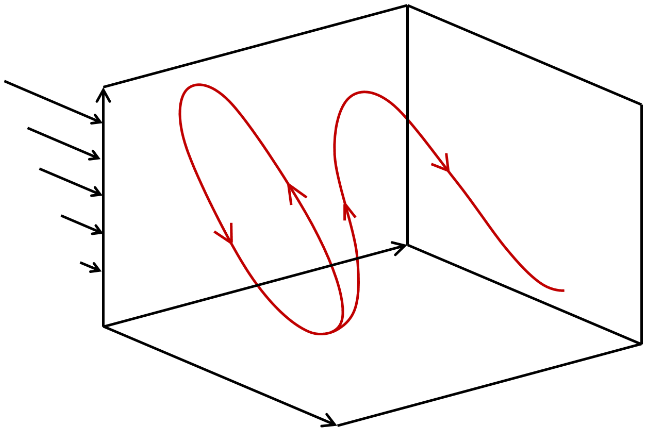

Figure 2.1: Dynamic Soaring

mal guidance algorithms using neural networks and reinforced learning [59] have been applied to the autonomous soaring problem although not practically tested, due to their high computational burden preventing real-time operation. Heuristic control algorithms have demonstrated promising results [6] [22] [8]. These theories will be discussed in greater detail in Chapter 3.

There are several different methods of soaring used by humans and birds; the basic types will now be briefly explained.

Dynamic soaring is the use of a wind gradient or a shear layer to increase the bird's or aircraft's total energy. Birds that extract a larger proportion of their energy by soaring dynamically include the frigate bird, albatross and gulls.

Dynamic soaring extracts energy from the air by the aircraft climbing through a wind gradient into wind and thus increasing its airspeed before turning down wind and diving through the wind gradient again, again increasing the aircraft's airspeed. This process can be repeated continuously to maintain flight indefinitely. Dynamic soaring presents several major challenges for practical implementation on aircraft. One major problem is the highly aerobatic nature of the flight manoeuvres needed to maintain flight. This in combination with the proximity to the large object needed to create the wind shear or gradient places extreme demands on the on-board sensors. This mode of soaring was discounted due to the high risk to the aircraft and inability of commercial autopilots to reliably execute the highly dynamic flight patterns accurately enough.

Static soaring is the act of circling or tacking in a rising air current. Although neither the aircraft nor the centre of the pattern that the aircraft flies is stationary,

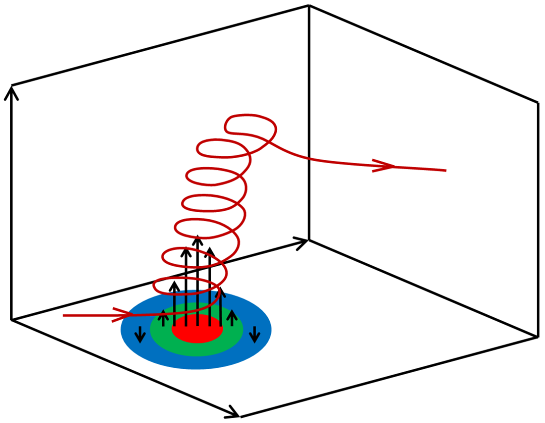

Figure 2.2: Static Soaring

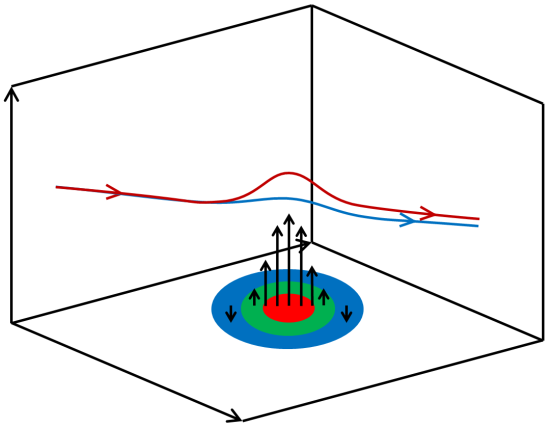

Figure 2.3: Dolphining

the aircraft's attitude is varied relatively slowly in none aggressive manoeuvres; thus the method is referred to as 'static'.

Static soaring can be used to exploit specific atmospheric phenomena like shallow layer cumulus convection or orthographic wave. The convective structure or shell is known as a 'thermal' when the updraft is strong enough to support continued flight of an aircraft.

There are many other variations of soaring between the two extremes of dynamic and static soaring. One such example is a form of semi-dynamic soaring known as 'dolphining'.

The act of 'dolphining' is a direct application of the classical speed-to-fly theory [40]. Classical speed-to-fly theory predicts the optimal speed-to-fly to maximise the potential range of the aircraft. Classical speed-to-fly theory and its application will be discussed in detail in chapter 3. The logical extension of this is to try to spend more time in air that is rising and less in air that is sinking, relative to the nominal cruise speed for still air.

There are many ways of potentially utilising atmospheric energy. Rather than using atmospheric energy to increase range and/or endurance these could be traded off in exchange for electrical energy generated by Ram Air Turbines (RAT) [16]. Alternatively the extra range and endurance provided could be traded off to gain cross-country speed, as competition sailplanes do.

In order to facilitate the development of soaring algorithms it is necessary to understand the atmospheric structures the aircraft is flying in. The following section will detail the existing atmospheric models applicable to soaring.

2.2.2 Atmospheric Models

In order to simulate and ultimately attempt to optimise the aircraft's trajectory, it is necessary to have a model of the atmospheric structures that the aircraft is flying through. Although ideally a model of high fidelity should be used to simulate and optimise the control algorithms, in reality a relatively crude model can be used effectively, provided that it can reflect the salient characteristics of the updraught structures.

Once the vertical motion of shallow layer convection is sufficiently strong to support the continued flight of an aircraft it is referred to as a 'thermal'. Thermal structures can be visualised as a bubble of rising air which is typically described as a vortex ring [6] [38] [56] [57]. All of the following models are vortex ring type parametric models. Nearly all of the existing models of thermals have been produced for hotter countries than the UK.

2.2.2.1 Thermal Profiles

Before moving on to complex thermals models, it is worth investigating existing 2D thermal models.

The 'British Standard Thermal' (BST) [29] that is used by the British Gliding Association (BGA) is given in Equation (2.1) and shown in Fig. 2.4 . The BST is normally given in feet and knots. Therefore the BST has a radius of 1000 feet and a core velocity of 4.2 knots. This translates to an outer radius,r_o , of 304.8m with a peak core velocity, w_{peak}, of 2.16 m/s. The radial distance from the centre of the thermal is denoted by r.

$$w = w_{peak}(1 - (\frac{r}{r_o})^2) \tag{2.1}$$

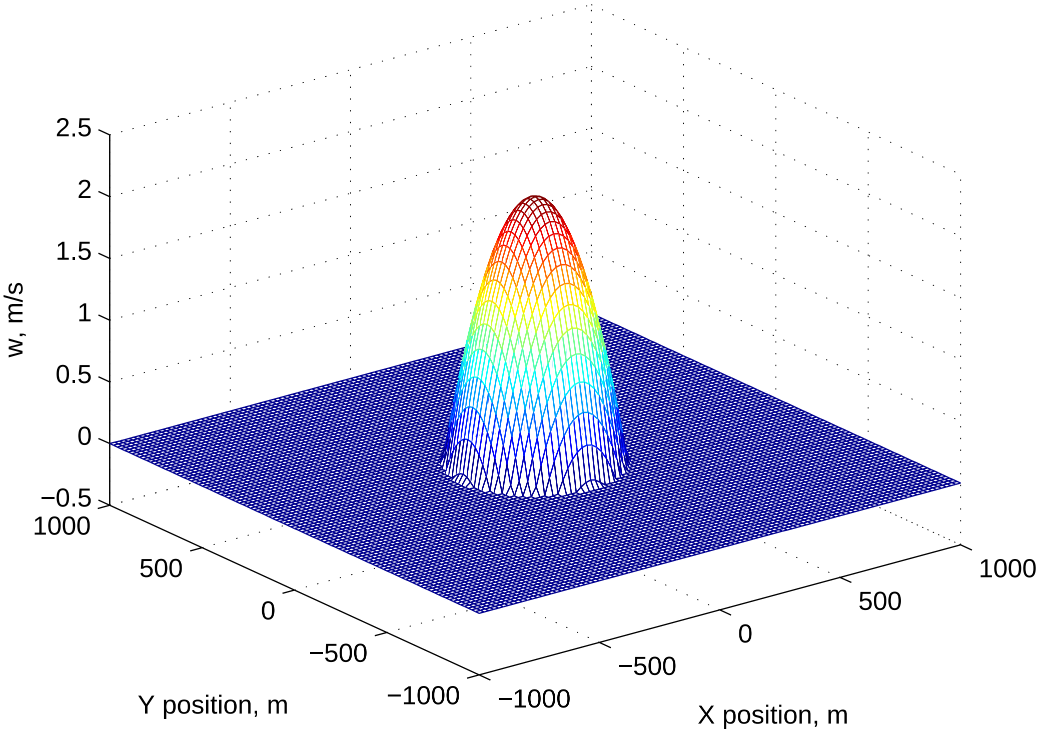

Figure 2.4: British Standard Thermal Profile [29]

The magnitudes used in the BST [29] will be used as a starting point to base the models on. It is worth stating that the BST is not a mean thermal for Britain but is an optimistic case that the BGA uses to assess full-size glider performance. The mean thermal strength that Allen [6] detected at Desert Rock in July of 2002 was 2.69m/s with a maximum strength of 6.3m/s. It is therefore suggested that the BST may represent a typical thermal on a hot summers day in Britain.

Another parametric profile that has been used is that of Wharington [59], given in Equation (2.2) and shown in Fig. 2.5. Although this model is less accurate than others [6], it lends itself well to mathematical analysis [22] [47].

$$w = w_{peak} e^{-(\frac{r}{r_0})^2} \tag{2.2}$$

Wharington used a range of thermal sizes and strengths from 40m to 80m in radius and with core velocities from 3m/s to 9m/s.

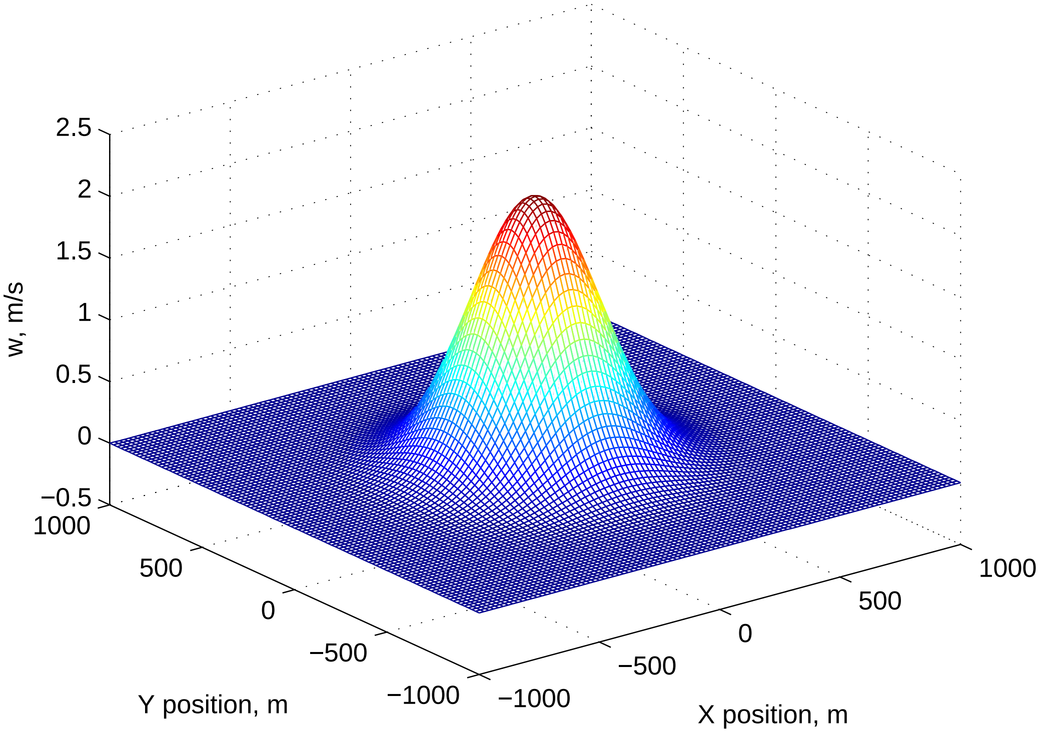

Figure 2.5: Wharington's Thermal Profile [59]

These profiles are useful but neither of these profiles models the possible presence of sink surrounding the thermal. There is an enormous body of anecdotal evidence suggesting that sink is almost always associated with thermals in the British climate [14] [20] [29] [40] [47] [56]. It is therefore useful to consider less widely used thermal profiles that include the presence of sink around the thermal. One such thermal profile was proposed by Gedeon [25]. The profile used by Gedeon is given in Equation (2.3) and shown in Fig. 2.6.

$$w = w_{peak}(1 - (\frac{r}{r_o})^2) e^{-(\frac{r}{r_o})^2} \tag{2.3}$$

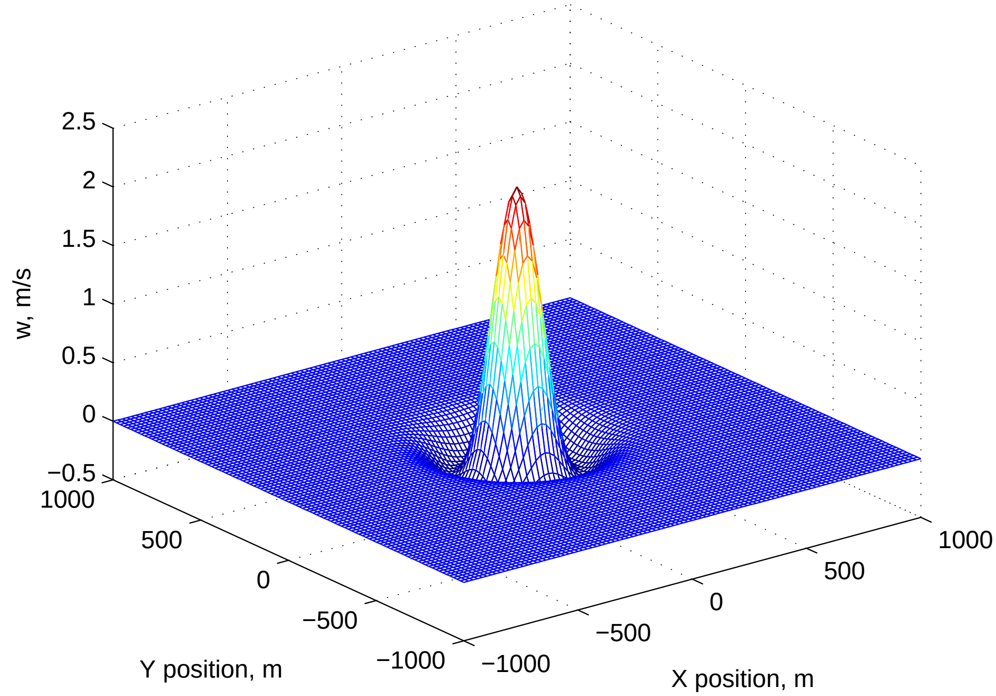

Figure 2.6: Gedeon's Thermal Profile [25]

This profile shares desirable aspects of the previous two models. Like the profile used by Wharington it is mathematically elegant while sharing a similar profile to the BST. The similarities are caused by the profile using an exponential decay with the same core shape, $(1-(\frac{r}{r_o})^2)$, as the BST.

Although the profiles presented represent a good starting point, they do not model atmospheric sink or provide any information on the variation of strength or the radius of the thermal with height. Nor do the profiles presented provide any information about the time dependent nature of the thermal. Once sufficiently centred in a thermal this detail has a negligible effect. However, when considering methods of centring, it is advantageous to consider the foregoing factors.

One notable piece of work that included variations in the thermal's profile with altitude was by Allen, although he chose to largely ignore the associated down drafts and arrived at a family of parametric profiles, as shown in Fig. 2.7 [6] and Fig. 2.8.

Allen [7] used atmospheric data to generate the core velocities but his prediction of sink does not match anecdotal evidence of the almost inevitable presence

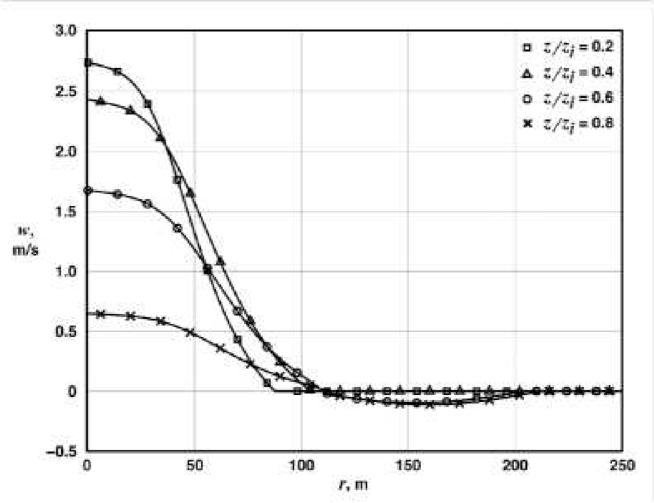

Figure 2.7: Allen's Thermal Cross-sections [6]

of localised sink around the thermal as described in [47], [56] and [57]; as Allen used conservation of mass to calculate a mean atmospheric sink rate, which he added to his entire map. Although there is no denying that conservation of mass does apply to the global atmosphere, it may be argued that local weather systems will also have an effect. It can be frequently observed that regions of high pressure effectively suppress thermal formation over large areas of the country [47] [57]. Additionally, wave conditions and anticyclones can both suppress thermal formation. It is also known that strong down drafts form separately to known thermals. Conservation of mass is a good starting point for the atmospheric maps but for large maps, overlying a large period sinusoidal distribution for atmospheric wave may yield improved realism [20] [47] [57].

2.2.2.2 Thermal Distribution with Height

Lenschow [38] published a set of equations that predicts the vertical velocity distribution with height of a thermal given the convective velocity scale, w^*, and the convective-layer scale, Z_i, as given in Equation 2.4. The convective layer scale depends on atmospheric conditions on a given day and is typically taken as the height of the first inversion layer, which is the same order of magnitude as cloud base. Typically the convective layer scale in the UK is around 1500m but can vary widely.

The graph shown in Fig. 2.9 illustrates the good and bad points of the thermal

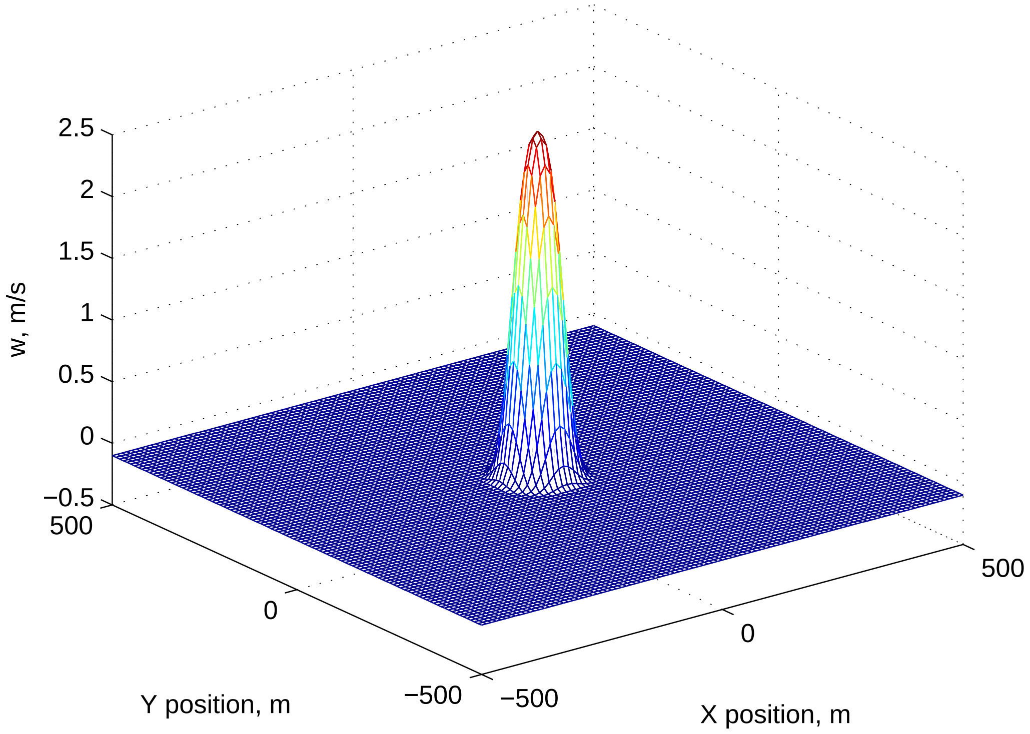

Figure 2.8: Allen's Thermal Profile [6]

velocity distribution with height. The distribution predicts the sink associated with the inversion layer but the maximum vertical velocity predicted is lower than that predicted by others including Bradbury [14].

$$w = w^{*}(\frac{Z}{Z_i})^{\frac{1}{3}}(1 - 1.1\frac{Z}{Z_i}) \tag{2.4}$$

Lenschow also developed an expression for the distribution of the outer thermal radius with height, as given in Equation (2.5) and shown in Fig. 2.10.

$$r_0 = 0.102(\frac{Z}{Z_i})^{\frac{1}{3}}(1 - 0.25\frac{Z}{Z_i})Z_i \tag{2.5}$$

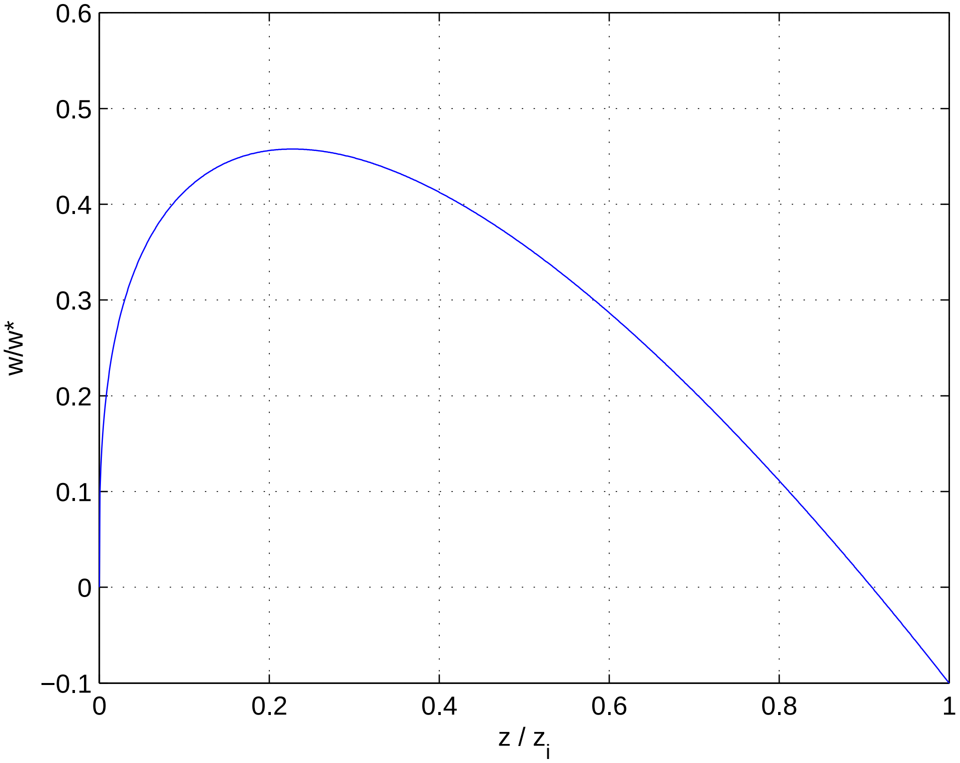

Figure 2.9: Lenschow Thermal Velocity with Height

2.2.2.3 Thermal Spacing

An equation capable of estimating the distances between thermals at a constant height ratio, Z/Z_i , of 0.4 was provided by Lenschow [38].

$$\frac{N_L Z_i}{L} = 1.2 \tag{2.6}$$

N_L is the number of up-drafts encountered over a length L. Equation (2.6) can be rearranged to give the number of up-drafts in a given area as shown in Equation (2.7).

$$N = \frac{0.6XY}{Z_i r_o} \tag{2.7}$$

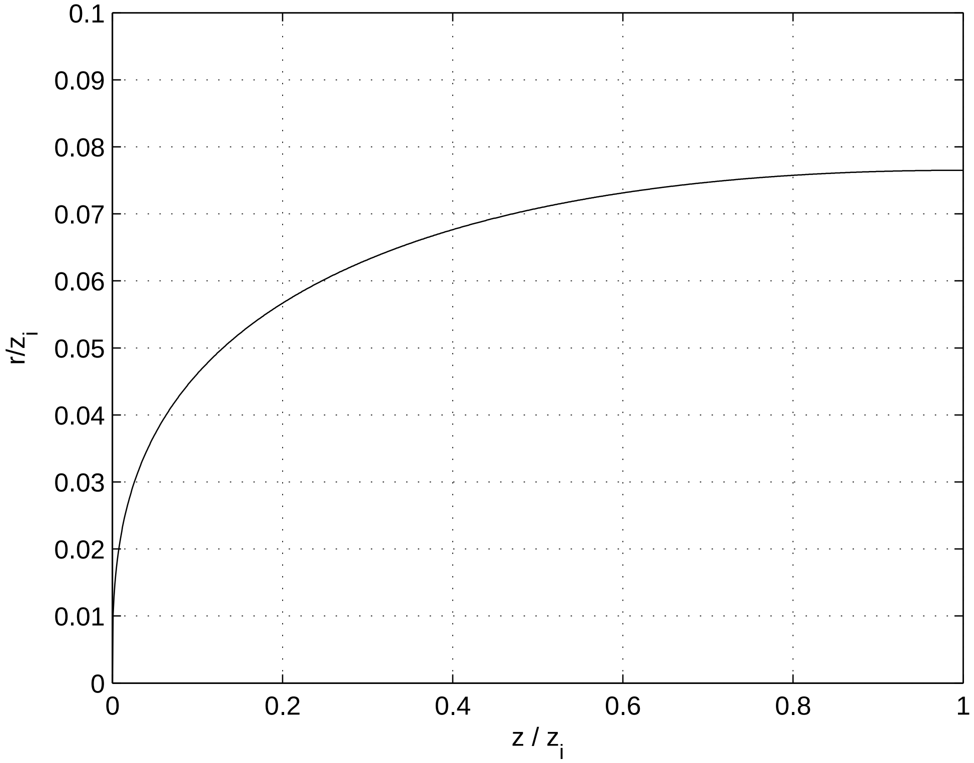

Figure 2.10: Lenschow Thermal Radius with Height [38]

2.2.2.4 Thermal Rotational Behaviour

Thermal structures have a rotational velocity in the horizontal plane ($\dot{\psi}$ as defined by Euler notation in Fig. 2.19); this phenomenon can be readily observed in hot climates where dust or sand is drawn up inside the thermal. By flying in the opposite direction to the natural rotation of the thermal the effective airspeed of the aircraft is increased allowing the aircraft to orbit in the thermal more efficiently [64]. It has been anecdotally suggested that the rotational direction is due to the Coriolis Effect (rotation of the Earth) but this does not fit with the author's gliding experience, which suggests that other factors like the prevailing weather system and the influence of orthographic factors have a larger influence.

While gliding on the 11/03/2012 it was noticed by the author that a pair of buzzards travelling alongside, on encountering rising air turned in opposite directions to each other. This may indicate cooperative behaviour in finding the core of a thermal in what was very weak conditions. This also may indicate no clear horizontal rotational behaviour of the thermal.

2.2.2.5 Thermal Turbulence

One issue that is not addressed by any of the aforementioned distributions is how to model the turbulence associated with thermals. The area of turbulence that is used by glider pilots to fly is the turbulence that exists at the edge of the thermal. Glider pilots [20] use the turbulence to work out where they are relative to the core of the thermal in both lateral and vertical directions. Although this is a more advanced task for a UAV it may prove beneficial. The cores of thermals tend to be relatively smooth.

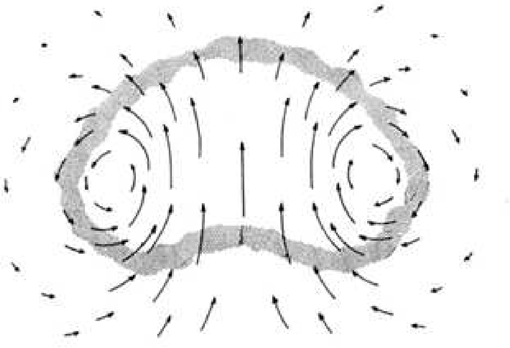

Figure 2.11: 2D Cross-Section of a 'Thermal' Produced by a Salt Water Simulation [56]

Fig. 2.11 shows an artists impression of the results of experiments carried out in salt-water. The experiments involved using a tank of water [56], which represented the adiabatic lapse rate, with a marked salt solution introduced. It was noted that the motions behind the bubble were "small and the trailing material was very tenuous". The grey dots on the edge of Fig. 2.11 represent the areas of turbulence and the arrows represent the flow vector. Note that sink was also noticed around the edge of the salt-water convection.

The modelling of the turbulence in a thermal is complicated and requires more consideration than that provided in this thesis. The turbulence has not been implemented in the 3D/4D simulations presented later.

2.2.2.6 Super-adiabatic Convection

So far the discussion on thermal structure has concentrated on developed thermals; thermals above the super-adiabatic layer. Although the thermals described are of the larger fully developed type, the smaller, possibly stronger, thermals found lower should not be discounted for use by a UAV. Fig. 2.12 shows an illustration of a typical thermal layer structure with the volatile super-adiabatic layer shown.

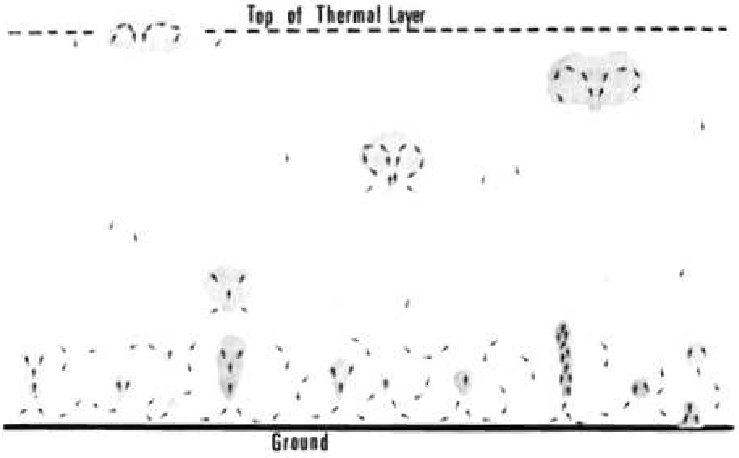

Figure 2.12: Super-adiabatic Layer [57]

The vast majority of the work conducted on thermals and their structure and strengths has concentrated its application on full size aircraft. UAVs are inherently much smaller than full size sailplanes and can utilise smaller thermals as a result. Care needs to be taken during the flight tests to measure and later represent the smaller volatile pockets of convection found in the simulations and optimisation. This has particular importance to UAVs as they will likely have missions that dictate flying lower or having restrictive height limits placed on them. All thermal atmospheric energy should be exploited.

2.2.3 Autonomous Soaring

Although soaring techniques have been investigated from before the 1930s there application to UAVs is a relatively new field. Wharington [61] was the first to propose that autonomous soaring could be a viable method for extending UAV performance (range, endurance and usable payload capacity) in 1998. Since then all aspects of soaring have been at least partially investigated. Although virtually all the possible soaring methods have been researched very few of the methods have been practically implemented or proved practically viable; a good example of this is dynamic soaring.

There have been a number of promising papers published detailing heuristic and optimal trajectories for dynamic soaring [60] [64] [13] [35]. Although dynamic soaring is clearly possible, birds and humans perform dynamic soaring already, the papers highlight the difficulty of the problem. The heuristic controllers developed [60] were rejected as they "were shown not to be particularly useful" . The optimal dynamic soaring solutions [64] were much more promising but again highlighted the problem of needing to judge the wind gradient precisely. The implication of the optimal solution is that the aircraft would need to operate a matter of metres from the ground, or other large objects. All the successful flight tests conducted have been with human piloted sensor aircraft in large lamina shear layers. As a result despite dynamic soaring being a very attractive source of energy in the UK, as there is generally a constant and predictable wind gradient, the difficulties mentioned above are so high that this is not suitable for practical soaring verification exercises.

A more readily applicable variant of dynamic soaring is using gusts. Patel [46] showed that a significant performance improvement could be had with the employment of simple pitching manoeuvres in turbulent air.

Since Wharington [59] first proposed that static soaring was a viable option optimal guidance algorithms have been developed using reinforcement learning and a neural-based thermal locator to detect and utilize thermals. The results presented showed that both heuristic controllers and reinforcement learning [59] could be effectively combined with a thermal locating algorithm to improve UAV performance. Algorithms utilising reinforcement learning have proved too computationally expensive for real-world application.

The first demonstration of eternal flight of a soaring UAV was by Cocconi [17], during the summer of 2005, when his 4.27m (14ft) span solar powered motor-glider flew continuously for 48 hours. Although this achievement is impressive the glider was not autonomous, instead the glider was flown in thermals by a group of experienced model glider pilots.

The first glider to demonstrate autonomous soaring was NASA's Cloud Swift (SBXC) glider [6] [7] under the guidance of Allen. Despite high endurance flights not being the stated aim of the project they successful demonstrated endurance increases of over 1hr when compared with the aircraft's still air endurance. Despite completely heuristic controllers being implemented to only a moderate level of success a lot can be learned from the thermal models and optimisation procedures used.

The current state of the art is the work presented by Edwards [22]. Building on the work conducted by Allen, Edwards refined the thermal locator and included a heuristic speed-to-fly solution. Having completed many gliding competitions in California ALOFT now holds most of the (unofficial) model gliding world records (2008). The records include the longest flight without human intervention and the longest goal-and-return flight.

Although the work presented is impressive, the bulk of the successful validation has been on heuristic controllers despite the presence of optimal controllers. It is also worth highlighting the fact that all the tests have been carried out in hot climates (California etc).

Converting algorithms developed for southern California into algorithms that are applicable to the UK climate requires considerable development and is one of the key contributions presented in this thesis.

2.2.3.1 Autonomous Centring in a Thermal

In colder climates where the rise rate of the thermal may be lower compared to the vorticity of the thermal the sink around the thermal may be considerable. Once the aircraft is sufficiently well-centred in the thermal the presence of sink around the edge of the thermal may be ignored but in order to evaluate the ability of a given algorithm to efficiently centre on a thermal the sink has a profound effect on the success rate.

There are many methods for centring in a thermal but two of the most widely used are the Piggot and the Reichman techniques.

The Piggot technique can be summarised as follows;

"If you are in a more gentle turn and feel a surge of lift, steepen your turn

immediately as this will move your circle over towards the place where you felt the lift” [47]

Whereas the Reichman technique is often summarised as;

“As climb improves, flatten the circle to $\approx 15 \rightarrow 20\,\text{deg}$*. As climb deteriorates, steepen the bank to* $\approx 50\,\text{deg}$*. If climb remains constant, keep constant bank of* $\approx 25 \rightarrow 30\,\text{deg}$*.”* [48]

Cowling observed “The point mass model simulation earlier demonstrates that Piggot’s technique works well for negligible lag times and with perfect knowledge of the air mass velocity around the vehicle. For the full simulation model however, it appears that despite using accelerometers the response time is sufficiently long for Reichmann’s technique to be more applicable than that of Piggot.” [19]

Experienced human pilots are good at both interpreting the data provided and critically projecting and extrapolating it. This form of model predictive control reduces the lag of the pilot/aircraft. The model predictive nature of some techniques means that the success achieved depends on the accuracy of the pilot’s internal model or put another way their experience and skill. When considering thermal structure it is logical to base further work on Reichmann’s technique.

Other notable British work on the utilisation of up-drafts has been presented by Lee [37] [36] but he concentrated on the exploitation of orthographic lift. Although orthographic lift is a viable source of energy it is localised and dependent on a specific topography and wind conditions [28]. This means that the problem can be reduced into two parts; the prediction of the flow field around a given topography with assumed wind conditions, and trajectory optimisation in that flow field [34] [36]. Although the 3 dimensional flow field can be viewed as uncertain it varies with wind conditions and not time. As such the approaches optimised for orthographic lift are not suitable for exploiting purely convective lift. On the other hand the opportunistic nature of the algorithms produced for fleeting convective lift with its time dependent nature, although not optimal, are transferable to the exploitation of orthographic lift. This thesis considers time dependent lift structures meaning that grid searches and other approaches as used for orthographic lift are not applicable.

2.3 Attitude Heading Reference and Navigation Systems

2.3.1 Introduction

When this project was started, attitude determination was assumed to be commercially available. However, when the first practical tests were carried out it became apparent that none of the commercially available autopilots were capable of executing the soaring algorithms to the desired accuracy. Soaring flight poses specific challenges for MEMS sensor based AHRS because of the dynamic nature of the manoeuvres executed. This demonstrated a clear need for development in that subject area, and thus necessitated a deviation from the initially planned direction of the project.

This section of the literature review seeks to explain the state of the art and the need for development.

Two different types of sensors are typically relied on to obtain attitude information, gyroscopes and accelerometers. Both have inherent problems. In theory if prefect gyroscopes were used then the attitude of the vehicle could be calculated from integration of the local angular rates of the vehicle. However in reality gyroscopes have biases and noise present that introduces drift in the sensor data. If this flawed gyroscope data is integrated to get attitude then the error on the estimation will grow indefinitely eventually rendering the estimation useless.

For highly accurate gyroscopes as found on larger aircraft this is not a pressing issue as the gyroscopes provide useful data for many hours without the need for correction to be applied. This is not the case with MEMS gyroscopes as used on many UAVs. MEMS gyroscopes vary in quality and accuracy but typically the estimation supplied by a MEMS gyroscope is only useful for seconds, if the drift is not addressed.

The following section introduces various methods used to combine and augment the sensor readings to provide a estimation of the aircraft's attitude and heading.

2.3.2 Data Fusion Techniques

There are several techniques used to augment gyroscopes but the majority of AHRS use filtering based on a form of tilt sensing [62] [55]. Using accelerometers to find the gravity vector is a good solution for constraining gyroscope drift as the estimation of attitude provided by the gyroscopes is smooth but drifts, whereas the accelerometer estimation is noisy but does not drift. To constrain the drift of the gyroscope's estimate of attitude, accelerometers are used to provide an estimate of roll and pitch from the gravity vector, and magnetometers are used to provide an estimate of heading. However accelerometers measure centripetal and other accelerations of the aircraft as well as gravitational acceleration, this makes extracting attitude information form accelerometers troublesome.

A commonly used solution is to assume that there is no centripetal acceleration [42]. This may certainly be valid with aircraft that are not expected to perform dynamic manoeuvres for extended periods of time, like rotary aircraft. Adopting this assumption for fixed wing aircraft means that if the aircraft is required to perform circling flight for extended periods of time the AHRS is susceptible to spiral mode failure. Spiral mode failure is the accumulation of errors in one direction associated with biased turning flight, resulting in the aircraft spiralling into the ground. The causes of spiral mode failure will be discussed in detail in Chapter 4.6.2. Spiral mode failure or a 'death spiral' is a known phenomenon and is one of the key parts of the Human Factors exam for pilots [2].

An alternative method to correct for the non-gravity component of the accelerations measured by the on-board accelerometers is to alter the filtering when accelerated conditions are experienced [62]. This is usually done when the AHRS detects high angular rates or accelerated flight conditions. If the filtering process is switched off this limits the duration of aggressive manoeuvres that the system is capable of enduring. This constraint is not a problem for systems using accurate gyroscopes as they can still function for hours [26] but for MEMS systems as used in micro to small UAV this can be a critical constraint [9], as switching the filtering off means the aircraft is vulnerable to spiral mode failure.

It is possible to go a long way to mitigating the risk of spiral mode failure by seeking to account for centripetal acceleration, which makes up a large part of the unwanted accelerometer reading. A estimation of centripetal acceleration can be made by using the gyroscope angular rate measurements in conjunction with a measure of aircraft speed [63] [27]. This approach is widely used and largely alleviates the need for switching filtering techniques [62]. This basic approach although effective relies on local angular rate (gyroscope) measurements that in turn rely on the acceleration predictions to correct for the noise and biases that are present in their measurements. This loop creates instability in the AHRS estimation. It also relies on an accurate measure of speed. This is the basic approach built upon in Chapter 4.

Another alternative is to fuse more sensor data together to provide a more accurate estimate of attitude from on-board sensors. It is possible to use Global Navigation Satellite Systems (GNSS) data to provide a better estimate of aircraft attitude but these methods still rely on the availability of satellite information [11]. These GNSS based solutions are capable of providing adequate performance but remain unattractive for many users as they are extremely vulnerable to GNSS denial. This vulnerability to GNSS denial means that these GNSS based solutions can not be used in safety critical and military applications. A GNSS devoid alternative is to use on-board air data systems to correct the attitude estimates used. A method of using air data to augment the AHRS is presented in Chapter 4.

The inclusion of magnetometers to aid the attitude estimation is implicit/ essential. However the use of other sensors such as horizon detection and laser altimeters can be used to aid AHRS and INS accuracy. These sensors will not be considered further as they are not typically available to micro to small UAV.

Section 2.3.2.1 details a basic overview of sensor behaviour of the Inertial Measurement Units (IMU) together with the historic developments, that form the basis of AHRS. Then Section 2.4 will introduce the basics of sensor filtering.

2.3.2.1 Inertial Measurement Units

An IMU is a sensor usually consisting of a three-axis gyroscope and a three-axis accelerometer. Although some IMU's have a three-axis magnetometer not all do. These sensors combine to provide a measurement of acceleration relative to free-fall and angular rate in all three axes. With the subtraction of gravitational acceleration a measurement of the actual acceleration in the coordinate frame is provided. In recent years the term IMU has come to encompass a wide assortment of inertial systems including AHRS and Inertial Navigation Systems (INS). In reality an IMU is just a building block in more complex systems such as AHRS and INS. These more complex systems require on-board processing, memory, and temperature compensation to provide digital interfaces with many other systems. An example of this is the INS which uses the IMU to provide a measurement of position, velocity and orientation relative to a known origin.

This thesis concentrates on the application of IMU to micro to small UAV so it can be assumed that MEMS sensors are being discussed, IMU pre-date the relatively recent advent of MEMS sensors. The first INS can be attributable to rocket designers such as Robert Goddard and Wernher von Braun in the early 1930s. The Second World War saw widespread use of IMU based bomb-sights to provide precision bombing. Indeed without the high accuracy attitude and position determination provided by IMU the Apollo space program would have been impossible.

Despite IMU having been around for 70 years or more the gyroscopes and accelerometers used were mechanical. This meant that the units were large, heavy, and had to be carefully calibrated to attain the high precisions required, thus keeping unit costs high and out of the practical reach of most applications. Developments over the years including laser ring Gyroscope technology improved the robustness and accuracy of the sensors but did little to reduce size, weight, and costs. It was not until the introduction of MEMS based inertial sensors in the mid-1990s that use of the IMU started to proliferate in many of the modern applications where they are found today. Despite their initially profoundly poor performance relative to classical accelerometers and gyroscopes MEMS sensors provided a cheap, low power, small, lightweight alternative. These attractive attributes have contributed to the explosion in the use of MEMS sensors in everyday appliances from games consoles all the way through to mobile phones.

2.3.3 Sensor Quality

There is a plethora of different sensors available with the associated disparate range in performance. In order to help clarify and describe the approximate sensor quality a four-tier-grading system is commonly applied. Fig. 2.13 and Fig. 2.14 show the two opposite ends of the range of sensors available, high and low sensor quality respectively.

Table 2.1 shows some of the salient parameters and relative performance of different qualities of accelerometers. Table 2.2 shows some of the salient parameters and relative performance of different qualities of gyroscopes. These parameters are not an exhaustive list but are intended to highlight the gulf in performance between high-performance sensors and the sensors used in this thesis project which fall under the lower end of the automotive category.

Table 2.1: Accelerometer Performance

Grade	Bias [mg]	Horizontal Error due to Bias in 60s [m]	Alignment Error [deg]	Horizontal Error due to Misalignment in 60s [m]	Pitch/ Role Error [deg]
Navigation	0.025	0.44	0.05	15	0.0014
Tactical	0.3	5.3	0.1	31	0.017
Industrial	3	53	0.5	150	0.17
Automotive	125	2200	1	310	7.2

Table 2.2: Gyroscope Performance

Grade	Gyroscope Drift $[deg/\sqrt{hr}]$	Horizontal Error in 60s [m]	Scale Error [ppm]	Angle Error in 360 degrees [deg]	Gyroscope Alignment Error [deg]
Navigation	0.002	0.0013	5	0.0018	0.0018
Tactical	0.07	0.46	100	0.036	0.036
Industrial	3	3.3	500	0.18	0.36
Automotive	5	6.6	60,000	22	3.6

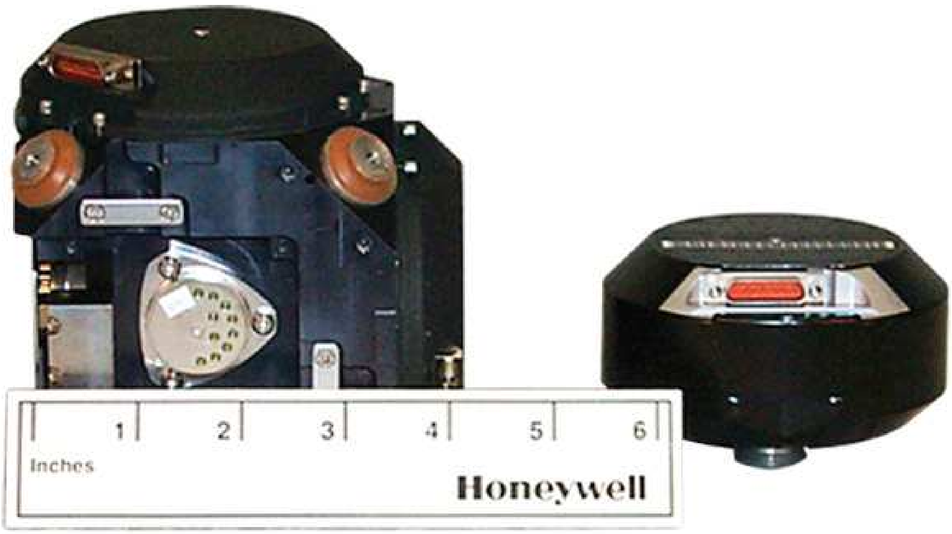

Figure 2.13: Honeywell NAV100 IMU, Navigation Grade Inertial Measurement Unit

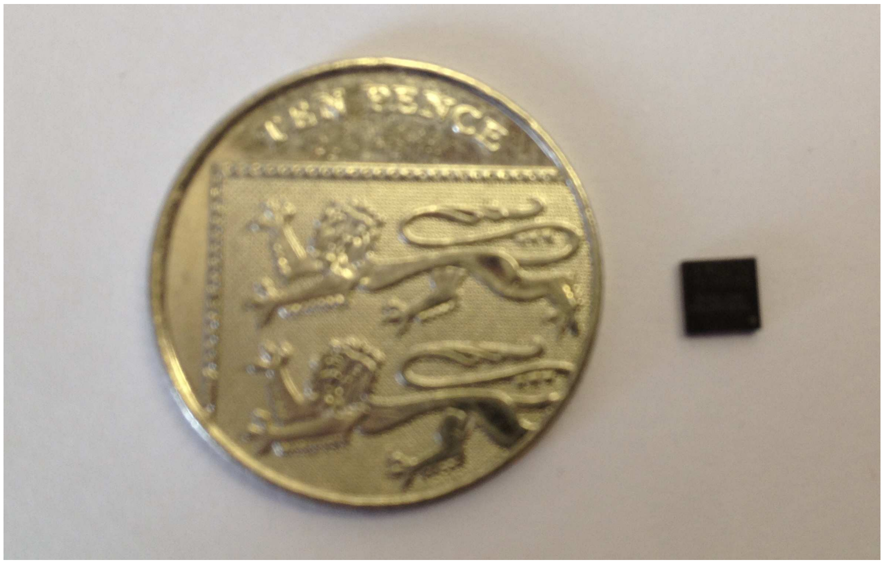

Figure 2.14: Automotive Grade MEMS Sensors Used in this Thesis

2.4 Filtering Techniques

Having discussed some of the many disparate sources of information available in Section 2.3.1 these datasets then need to be combined to provide a single reference source. Data provided by gyroscopes, accelerometers, magnetometers, pressure sensors, and GNSS can be combined to provide a estimation of attitude and position. This section seeks to introduce key filtering techniques that are widely used in industry including Kalman filtering and complimentary filtering.

The most widely used filtering technique in avionic applications is a Kalman-type filter. The Kalman filter [32] needs no introduction as it is widely regarded as the industry-standard means of integrating data.

Although extensive work was conducted with Unscented Kalman Filter (UKF), the performance of the UKF and Extended Kalman Filter (EKF) was found to be to almost identical. This demonstrates that despite experimenting with aerobatics including tail-slides and Half-Cuban manoeuvres there was insufficient difference to warrant inclusion in the discussions presented.

Over recent years the Kalman filter has been the subject of extensive work and numerous papers [58] [62] [24] [27] [30] [11]. There are now three common types of Kalman filter, the original Linear Kalman Filter (LKF) [32], the non-linear or EKF [53] and a generalised non-linear UKF [30]. These three filters and their relationship to each other are dealt with in Appendix A.

For a basic introduction to Kalman Filters refer to [58] and for further information refer to [41].

2.4.1 Complimentary Filtering

A complimentary filter is one of the simplest filtering techniques available. As such it is computationally elegant, and as a result efficient to implement on microprocessors. In its simplest form a complimentary filter merely finds the average between two sensor readings. However a complimentary filter becomes much more powerful when combining datasets with disparate time responses. An apt example of this is the combination of gyroscope and accelerometer estimates of attitude. Gyroscope measurements can be extremely accurate over short time periods but drift. Accelerometer estimates on the other hand can be extremely noisy over a short time period but tend not to drift and have predictable behaviours. If the problem of centripetal acceleration discussed in Section 2.3.2

is momentarily ignored a simple example can be generated. The test shown is of a tilting platform oscillating in one axis with an amplitude of 1 radian. Although this test was completed with the sensors shown in Chapter 7, on top of a real platform, the data shown here is of a simulation. Fig. 2.15 shows the basic structures of a complimentary filter used to provide the filtering performance shown in Fig. 2.16. The two complimentary filter structures are mathematically identical although the structure on the right is the one used, because it is more computational efficient to implement.

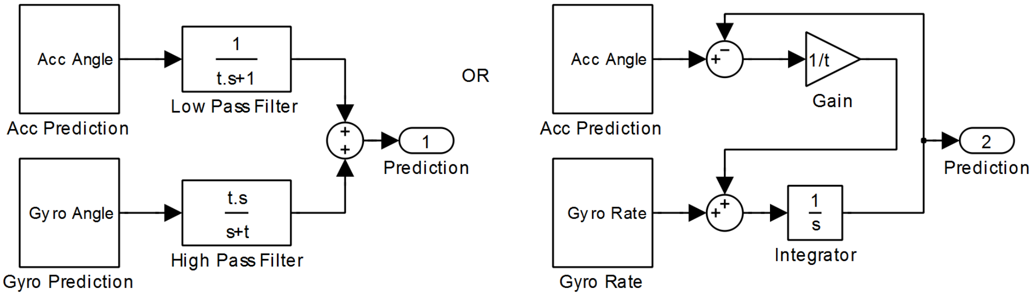

Figure 2.15: Complimentary Filter Structures

Fig. 2.17 shows the pair of complimentary frequency distributions used, in a bode plot showing that the pair of complimentary low and high pass filters provides a unity response across the entire frequency range. This basic structure allows for the best attributes of two disparate datasets to be combined to provide a single attitude solution. This technique can provide adequate performance for many systems, when processing power is at a premium.

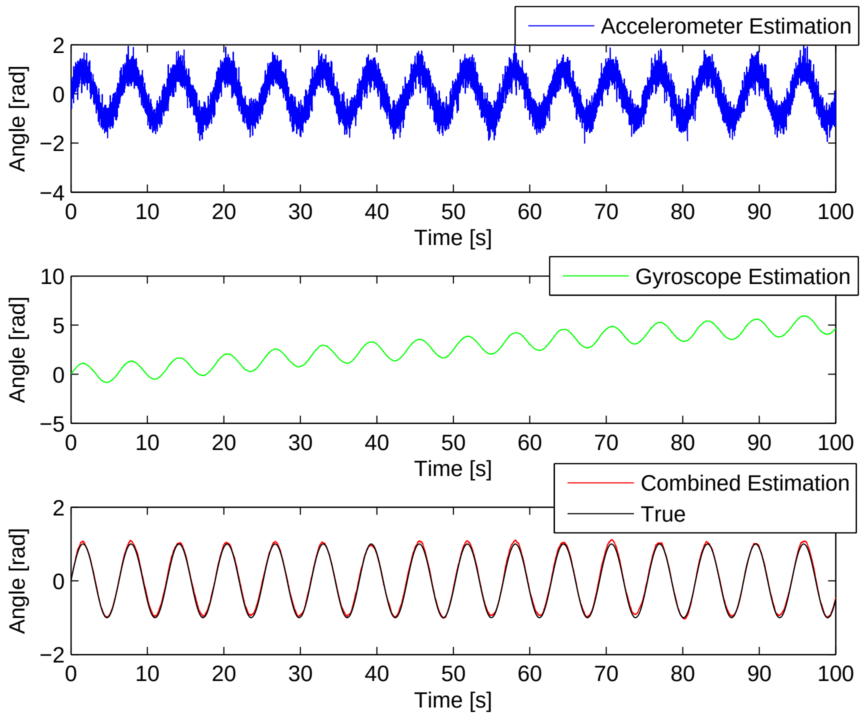

Figure 2.16: Example Complimentary Filter Results

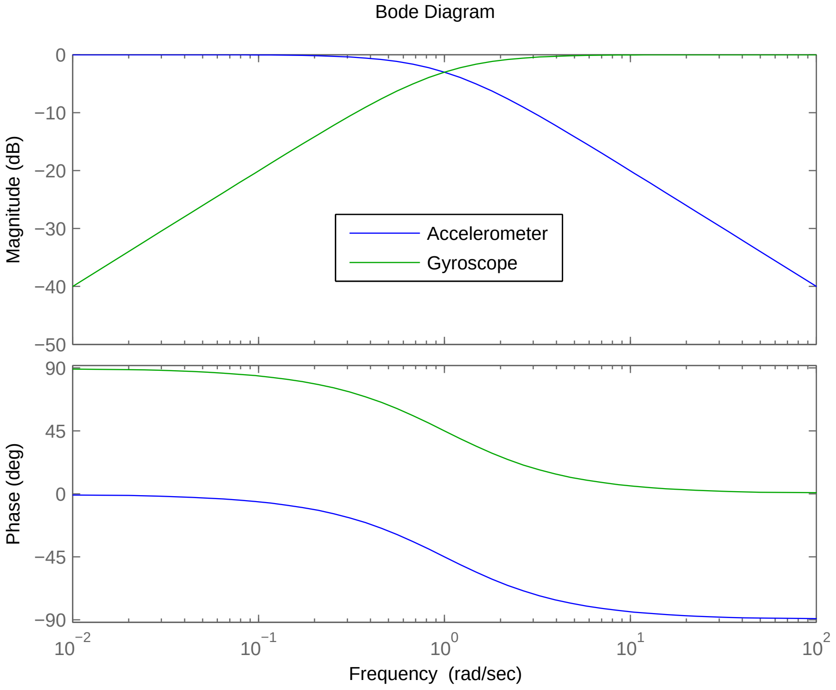

Figure 2.17: Complimentary Filter Bode Plot

Although complimentary filters are widely used they lack the overall performance of Kalman type filters as they struggle to compensate for the presence of biases. This means that applications that require highly accurate attitude estimation may have to rob processing power from other tasks for the AHRS to allow it to run a more powerful Kalman filter. Ideally what is desired is a filter with the performance of a Kalman filter while maintaining the computational elegance of a complimentary filter. A solution to this problem is proposed and discussed in more detail in Chapter 5.

2.5 Reference Frames

The determination of attitude is based on the interrelationship between relative frames of reference. The three frames of reference of interest are the fixed frame (Denoted with $_e$ in Fig. 2.18 , the inertial frame (Denoted with $_i$ in Fig. 2.18) and the North-East-Down (NED) frame (Denoted with N,E,D, in Fig. 2.18 and Fig. 2.19). Unless stated otherwise this is the notation used throughout this thesis. This notation is common to most texts but American notation and some COTS differ. Exceptions of note are altimeters and Vertical Speed Indications (VSI) which both use up as positive.

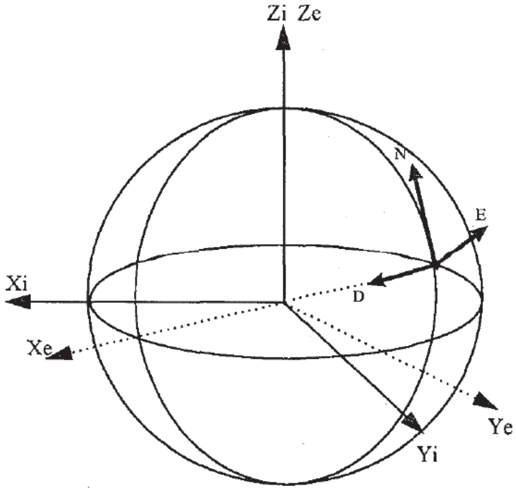

Figure 2.18: Inertial Frames [52]

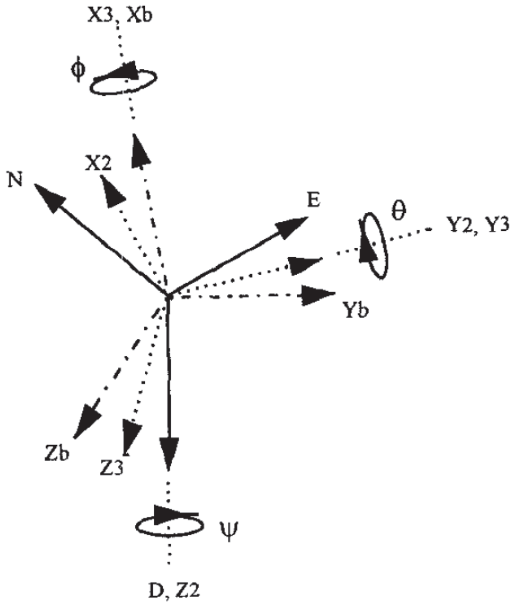

Figure 2.19: Euler Angles [52]

2.6 Summary

This chapter provides a literature review on the three aspects that will be covered in this thesis, namely autonomous soaring, augmented AHRS and sensor fusion and filtering.

Firstly, the basic principles of soaring flight and its historic application have been explained. With the principles of soaring flight established modern developments in autonomous soaring flight have been critiqued. The inclusion of soaring in flight control systems has been justified.

The extra strains placed on the AHRS by autonomous soaring flight have been explained. An aggravating factor adding to the difficulty of autonomous soaring flight is sensor behaviour, so sensor behaviour has been discussed. With the inclusion of autonomous soaring flight placing extra demands upon the on-board AHRS, methodologies for improving overall accuracy of sensor estimation of attitude by utilising extra sensors, such as air data sensors, have been discussed.

Finally methods for fusing diverse datasets to provide accurate AHRS have been introduced, including linear Kalman, extended Kalman, unscented Kalman and complimentary filters.

Chapter 3

Autonomous Soaring

3.1 Introduction

Typically, the limiting factors for small UAVs are short flight duration, limited range and payload. Many activities such as forest fire monitoring, border patrol, atmospheric research, communication relays, and other surveillance tasks, require great persistence from the airframes used. Although advances in engine and battery technology, along with miniaturisation of much of the on-board systems, continue to provide performance and capability improvements, there is still a need for the introduction of novel methods to improve the range and persistence of the aircraft. One such novel solution is the extraction of energy from naturally occurring phenomena, such as atmospheric turbulence and convection.

Techniques to extract energy from shallow layer cumulus convection have been employed by full-size glider pilots to increase their range and duration for nearly 100 years. These soaring techniques have historically been ignored by the surveillance community because the differences in aircraft wing loading, operating speeds and efficiency rendered them pointless. However, with the latest generation of UAVs, this is no longer the case.

For progress to be made in the improvement of the methods used to extract energy from atmospheric convection, it is advantageous to start in a simulation environment before moving on to real-world flight tests. The use of a simulator allows the algorithms to be tested in a controlled environment where the conditions are both fully understood and repeatable. However, for the results of the simulation to be both meaningful and useful the simulation environment must be realistic. Three key areas of the simulation environment need to accurately reflect reality; the aircraft flight dynamics, the atmospheric model, and the aircraft flight control structure.

This chapter presents a method of using shallow layer cumulus convection to extend the range and duration of a small UAVs. A simulation model of an X-Models XCalibur electric motor-glider is used in combination with a refined parametric thermal model to simulate soaring flight. The parametric thermal model builds on previous successful models with refinements to more accurately describe the weather in northern Europe. The implementation of the variation of the MacCready [40] setting is discussed. Methods for generating efficient trajectories are evaluated and recommendations are made regarding real-world implementation.

Sections 3.2, 3.3, 3.4 deal with the aircraft dynamics, flight control structure, and the atmospheric model respectively. Having established the simulation environment, section 3.5 shows how suitable atmospheric convection can be identified and exploited. Section 3.6 gives some pertinent results. Section 3.7 highlights the key conclusions and recommendations for real-world implementation.

3.2 Aircraft Flight Dynamics Model

Autonomous soaring can be simulated with rudimentary knowledge of the aircraft in question but in order to optimise the algorithms an accurate model of the aircraft in question is required. The type of aircraft is unimportant for the purpose of optimisation as long as the actual aircraft dynamics are well represented. The X-Models XCalibur was chosen as the test aircraft, as it has the best performance of all the aircraft available at Loughborough University. The X-Models XCalibur is a self launch electric glider with a 3.2m span and a typical take-off weight of 3.5 kg, giving a wing loading of approximately 120 Pa. The XCalibur was developed from X-Models F3J competition aircraft and as such has a performance comparable with larger gliders used by other researchers [8] [22]. An accurate model of the aircraft in use also facilitates the stabilisation and control algorithms to be validated in conjunction with the high-level trajectory generation algorithms.

A non-linear model that includes the stall behaviour of the aircraft is necessary for this study. This is important because the combination of the speed-to-fly and path planning algorithms may cause the aircraft to fly close to the stall condition. If the aircraft was to stall, it is important to know how the control structure would behave.

The chosen environment for constructing the dynamics model was MATLAB / Simulink. The dynamics model is made up of four distinct parts: left and right wings, elevator and rudder. The fuselage is neglected in the calculations because of its small influence in relation to the aircraft's responses and the difficulty involved in modelling it accurately. The glider dynamics model also includes a model of the motor, providing data for the simulation of the initial launch procedure and any subsequent powered flight that may be required.

The coefficients used in the model presented are based on the performance parameters of the XCalibur used at Loughborough University, as confirmed by flight tests.

3.2.1 Aerodynamic Assumptions

The aerodynamic characteristics of the aerofoil can be built up from first principles knowing the basic characteristics of the aerofoils in question. The basic aerodynamic characteristics follow the trends laid out by Stengel [54]. To arrive at a workable aerodynamic model the aerofoil's characteristics are discretised into different regions. The lift and drag coefficients of the wing panels are represented by C_L and C_D. The aerodynamic Angle of Attack (AoA) on the given wing panel is given by α. The three regions depicted in Fig. 3.1 are: the central linear region dominated by the lift curve slope $\frac{dC_L}{d\alpha}$, a static region at $C_{L_{max}}$ that softens the stall, and a sinusoidal region that mimics the stalled wing behaviour. The regions are depicted in Fig. 3.1.

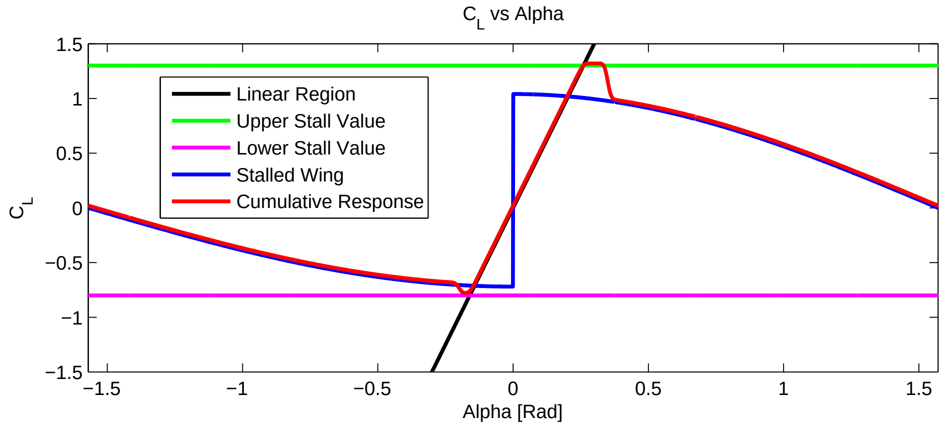

Figure 3.1: Lift Coefficient

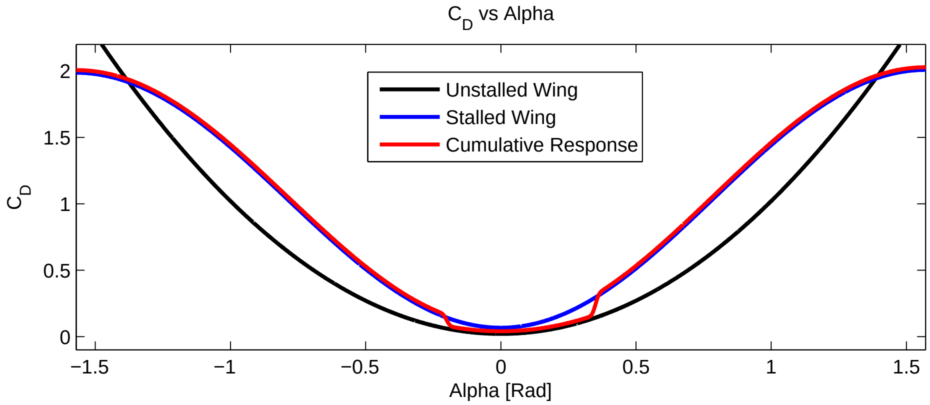

Figure 3.2: Drag Coefficient

Like the C_L vs AoA characteristics the C_D vs AoA characteristics are built up by discretising the characteristics into two regions; the un-stalled region and the stalled region. The clear increase in drag when the aerofoil stalls can be seen in Fig. 3.2. The equations used to predict the lift and drag coefficients of each panel are presented in Equation 3.1 and Equation 3.2. The upper and lower stall angle of the wing sections are represented by α USA and α LSA respectively. Zero incident lift coefficient of the wing is denoted by C_{l_0}. The rigging angle of the wing section is represented by α_r.

$$C_L(\alpha) = \begin{cases} LSV\sin(\alpha) & \text{if } \alpha_{LSA} \geq \alpha \\ (\alpha+\alpha_r)(\frac{dC_l}{d\alpha}) + C_{L_0} & \text{if } \alpha_{USA} \geq \alpha \geq \alpha_{LSA} \\ USV\sin(\alpha) & \text{if } \alpha \geq \alpha_{USA} \end{cases} \tag{3.1}$$

$$C_D(\alpha) = \begin{cases} C_{D_0} + \varepsilon C_L^2 + (1-\cos(2\alpha)) & \text{if } \alpha_{LSA} \geq \alpha \\ C_{D_0} + \varepsilon C_L^2 & \text{if } \alpha_{USA} \geq \alpha \geq \alpha_{LSA} \\ C_{D_0} + \varepsilon C_L^2 + (1-\cos(2\alpha)) & \text{if } \alpha \geq \alpha_{USA} \end{cases} \tag{3.2}$$

Where ε is the induced drag factor $\varepsilon = 1/\pi e(AR)$, where e is the Oswald efficiency factor [54] and AR is aspect ratio.

This approach is designed to reflect the aerodynamic performance of the real aircraft. Fig. 3.3 and Fig. 3.4 show wind tunnel tests carried out on a NACA 0015 aerofoil section by Sandia National Laboratories [50]. It was deemed essential to have an aerodynamic model that could accurately model post stall behaviour of the aircraft because of the likelihood of the soaring controller causing the aircraft to stall. Although the aircraft is not intended to fly backwards it is possible for poorly tuned gains to cause oscillatory behaviour resulting in a tail slide.

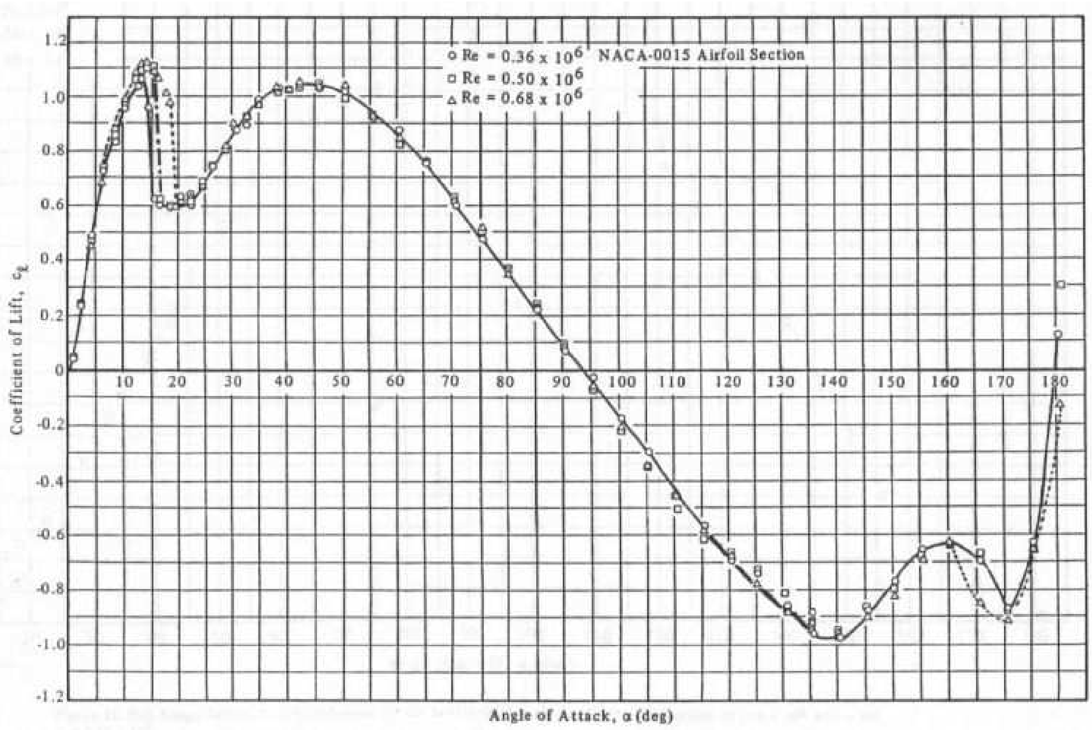

Figure 3.3: Lift Coefficient Plot of NACA-0015 [50]

The aerofoil parameters are then tuned to reflect the performance of the aircraft in question. The coefficients in the simulation are pseudo-coefficients that enable the performance of the simulation model and the actual aircraft to be matched and are not necessarily exactly the coefficients of the aerofoil sections etc. A detailed discussion of the methodologies used to tune these parameters is given in Chapter 8. An accurate prediction of the aerodynamic moments is problematic and has not been attempted. The simulation model does not include the effects of the slip stream from the motor on the empennage. As mentioned earlier the fuselage is not taken into consideration so the effects of side slip are not modelled. The XCalibur is fitted with butterfly air-brakes; these are modelled as a pure drag change on the main wings. Although in reality butterfly air-brakes alter the lift distribution over the entire wing, softening the spin characteristics of the aircraft, landing performance is not of interest so these aspects have been neglected.

These aerodynamic properties are then added to a standard 6 Degrees Of Free-

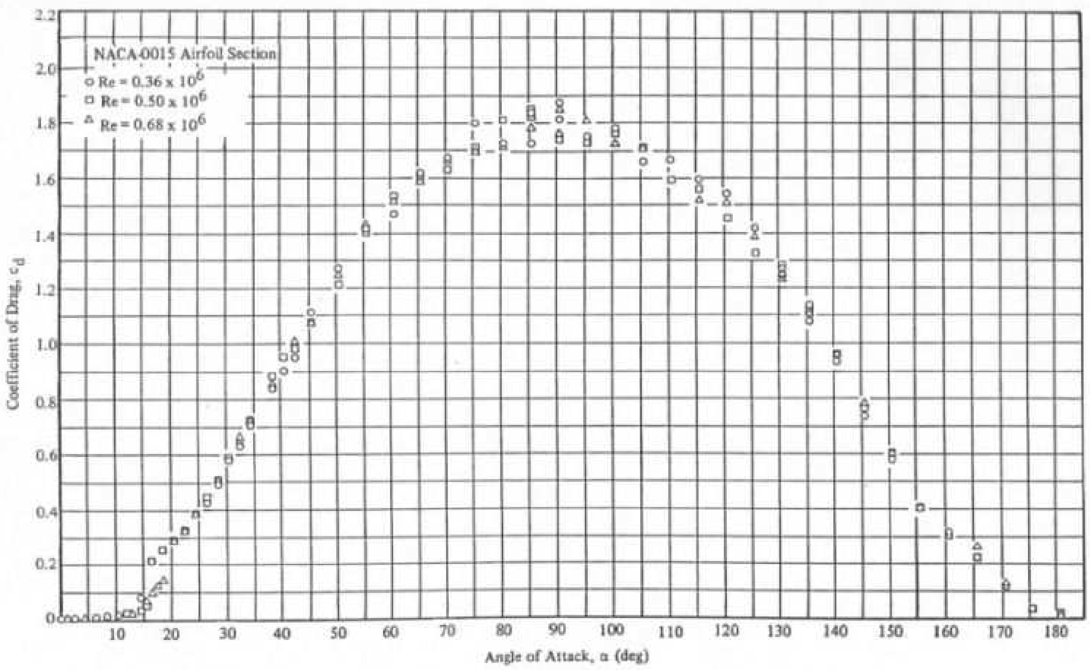

Figure 3.4: Drag Coefficient Plot of NACA-0015 [50]

dom (DOF) fixed wing kinematic model. The inputs to this model are the same inputs available to the real aircraft. The inputs include: throttle position, aileron deflection, elevator deflection, rudder deflection and butterfly brake deflection.

Ultimately the coefficients used in the model presented above will be derived using experimental flight test data. However in preliminary tests this flight test data was not available, instead an experienced pilot with knowledge of the airframe involved provided an initial estimate of the parameters. The testing revealed that despite the assumptions made the aircraft spins and, more importantly, recovers as the real aircraft does, as show in Fig. 3.5.

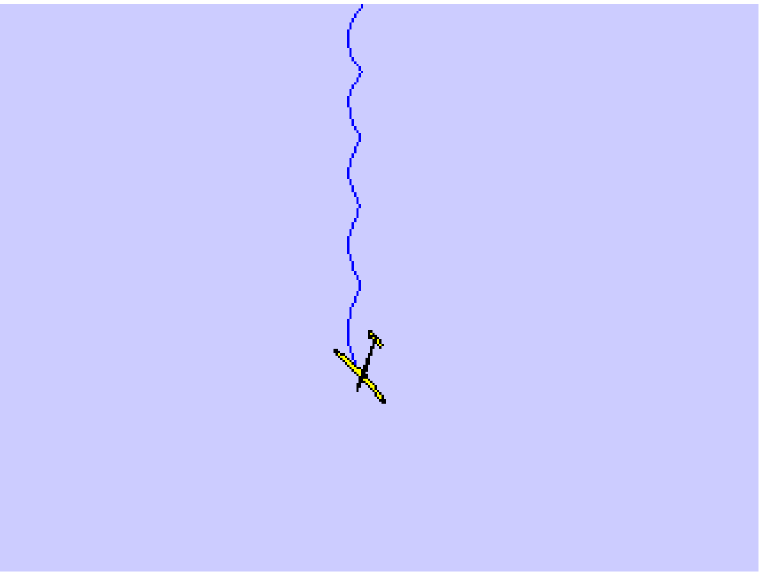

Figure 3.5: Glider Simulation Model Demonstrating Realistic Spin Behaviour

3.3 Aircraft Control Structure

The flight control system is critical to the successful execution of any generated trajectory. While the limitations of the flight control system will always impose constraints on the trajectory generation algorithms, it is advantageous to maximise the flight control performance to keep these practical limitations to a minimum.

For the trajectories generated to be useful it is imperative that the flight control system be representative and has comparable performance to the real platform. The flight control system is based on a nested Proportional Integral Differential (PID) architecture; the simulation was set-up to reflect this.

The controller features the use of feed forward control based on roll angle and roll rate as part of the pitch and yaw controllers respectively. This is to pre-emptively suppress fluctuations in pitch and yaw due to what would otherwise be uncoordinated control actions. As these parts of the controller are a simple form of model predictive control they are more platform dependent than the other parameters. Aircraft with higher aspect ratios will tend to have a larger adverse yaw reaction to roll necessitating different gains in the controller. The general control structure is shown in Fig. 3.6. The MATLAB/Simulink implementation is shown in Fig. 3.7.

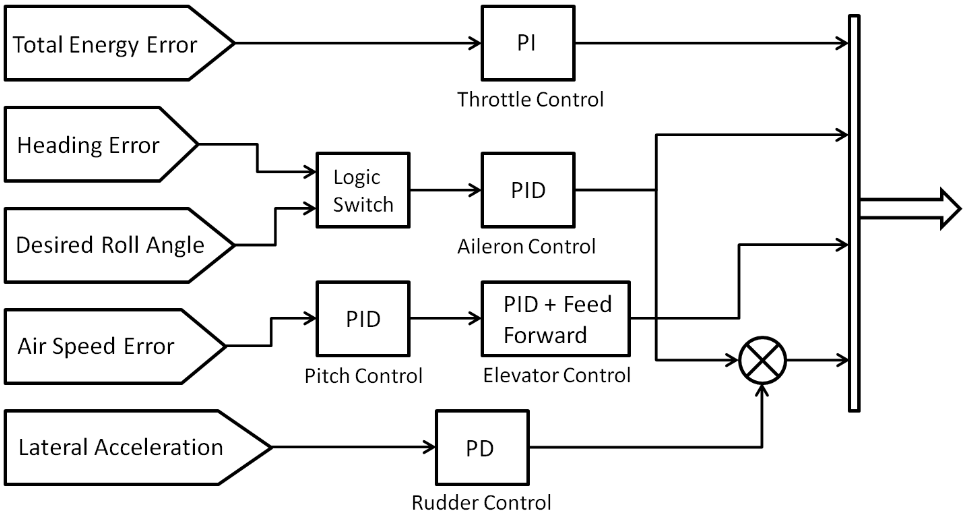

Figure 3.6: Control Structure Block Diagram

There are more advanced control systems that can be simulated but these pose implementation problems on the real aircraft. Therefore this control structure is not designed to reflect an optimal solution but instead provide adequate performance with ease of implementation. This allows the actual aircraft to use an identical control structure, allowing the simulation to more accurately reflect the performance capabilities of the aircraft in question.

3.4 Shallow Layer Cumulus Convection

In order to simulate and ultimately attempt to optimise the aircraft's trajectory, it is necessary to have an accurate model of the atmospheric structures that the aircraft is flying through. Once the vertical motion of shallow layer convection is sufficiently strong to support the continued flight of an aircraft it is referred to as a 'thermal'. Some of the pertinent thermal models have been introduced in Chapter 2. Almost all of the existing models of thermals have been produced for hotter countries than the UK, the following section modifies the existing profiles to fit the British climate.

As discussed in Chapter 2 the only existing parametric thermal profile intended for the British climate is the BST. This thermal profile is intended to be

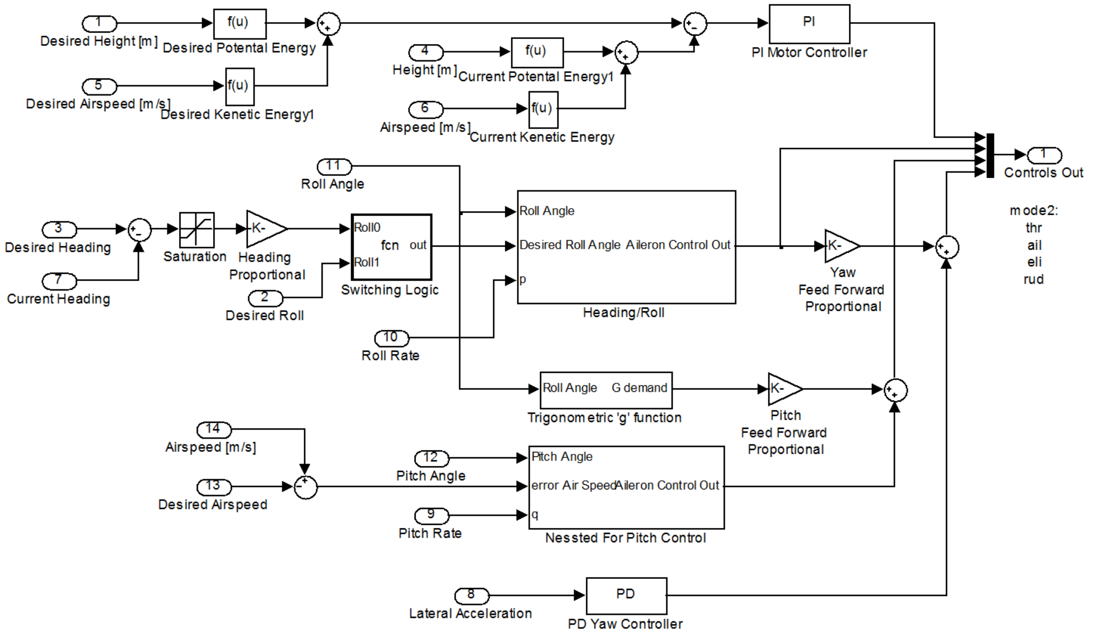

Figure 3.7: Control Structure MATLAB / Simulink Implementation

used for the handicapping of full size gilders and as a result is simple, with no sink associated with the thermal. The BST does however provide a good starting point for the typical size and strength of the thermal structures. As such the size and strength of the thermals used in the simulation environment will be normally distributed about the size and strength of the BST at an outer radius of 304.8m and a peak core velocity of 2.16 m/s.

Another parametric profile that has been used is that of Wharington [59]. Although his model is less accurate than others [7] [47], it lends itself well to mathematical analysis [22].

These profiles are useful but neither of these profiles models the possible presence of sink surrounding the thermal. There is an enormous body of anecdotal evidence suggesting that sink is almost always associated with thermals in the British climate [14] [20] [29] [40] [47] [56]. It is therefore useful to consider less widely used thermal profiles that include the presence of sink around the thermal. One such thermal profile was proposed by Gedeon [25]. This profile shares desirable aspects of the previous two models. Like the profile used by Wharington it is mathematically elegant while sharing a similar profile to the BST.

Building from the profile proposed by Gedeon [25] it is possible to generalise that profile by including extra parameters that allow the size and magnitude of the associated sink to be controlled.

$$w = w_{peak}(1 - (\frac{r}{\sqrt{C_1} r_o})^2)e^{-(\frac{r}{\sqrt{C_1} r_o})^2} \tag{3.3}$$

C_1 and C_2 control the radius and magnitude of the sink associated with the thermal structure.

These added parameters make the profile more flexible. It is possible to force the profile to more closely match the profiles of measured thermals [7]. Although the increasing complexity causes extra challenges when completing analytical analysis the extra realism is deemed advantageous. The new generalised profile is shown in Fig. 3.8.

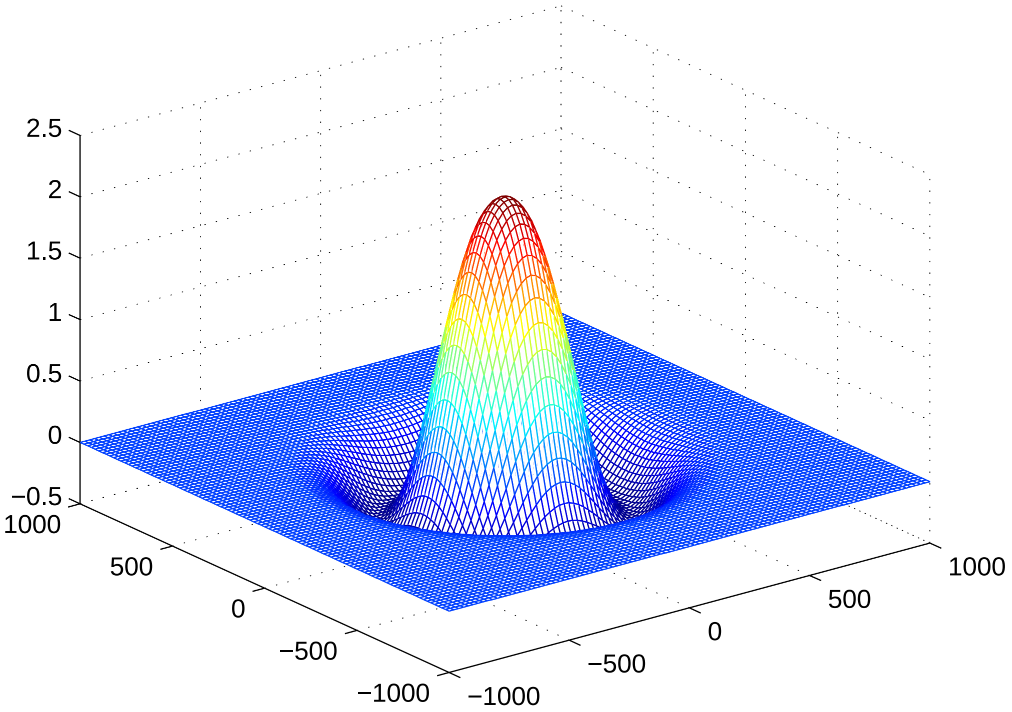

Figure 3.8: Proposed Thermal Profile

Despite the new thermal profile having localised sink associated with it, this is still not sufficient to satisfy conservation of mass. To comply with conservation of mass, a zero net vertical movement is enforced over the maps generated.

Although the profiles presented represent a good starting point, they do not model the variation of strength or the radius of the thermal with height. Nor do the profiles presented provide any information about the time dependent nature of the thermal. Once sufficiently centred in a thermal this detail has a negligible effect. However, when considering methods of centring, it is advantageous to consider the foregoing factors.

One notable piece of work that included variations in the thermal's profile with altitude was by Allen [7], although he chose to largely ignore the associated down drafts when he arrived at his family of parametric profiles.

Lenschow [38] published a set of equations that predicts the vertical velocity distribution with height of a thermal given the convective velocity scale, w^*, and the convective-layer scale, Z_i. The convective layer scale depends on atmospheric conditions on a given day and is typically taken as the height of the first inversion layer, which is the same order of magnitude as cloud base. Typically the convective layer scale in the UK is around 1500m but can vary widely.

Lenschow's distribution predicts the sink associated with the inversion layer but the maximum vertical velocity predicted is lower than that predicted by others including Bradbury [14]. It is therefore proposed that the maximum vertical velocity is likely to occur at a higher height ratio but at an equivalent height when compared with warmer climates. This hypothesis is based on the assumption that the thermal will take a similar height to develop but will be disrupted earlier in its ascent due to lower inversion layers in colder climates.

Lenschow developed an expression for the distribution of the outer thermal radius with height, as described in Chapter 2, this will be used in its entirety. Fig. 3.9 shows a cross section through the resultant thermal structure. The dry adiabatic lapse rate is used to calculate the rise rate of the thermal.

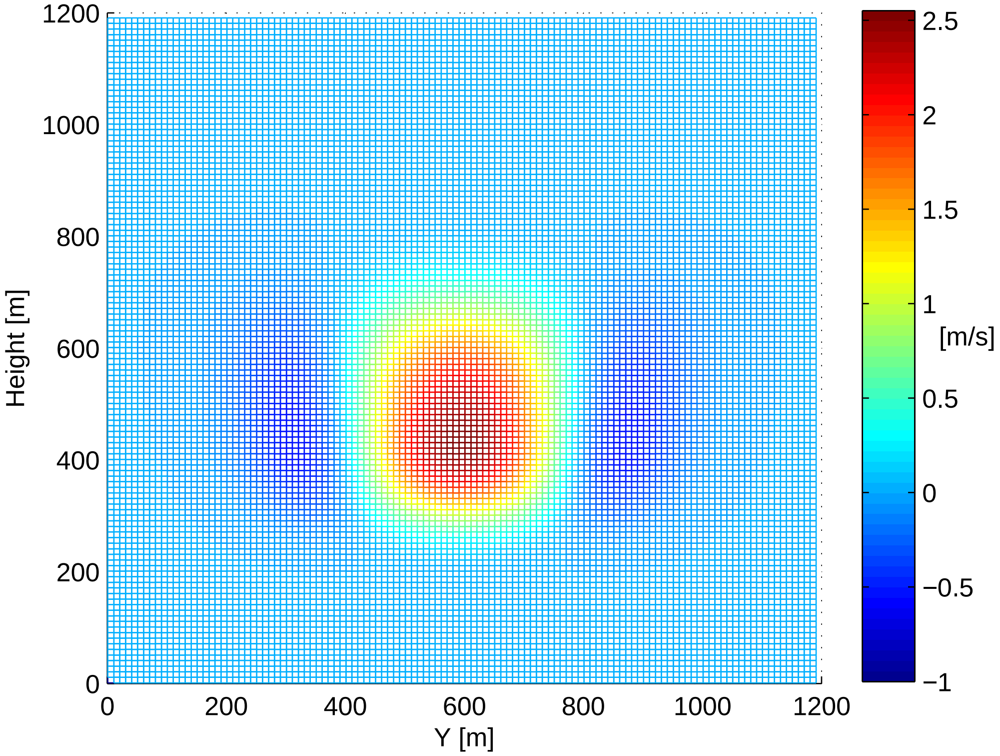

Figure 3.9: Resultant Thermal Cross Section

In order to optimise the utilisation of thermals it is critical to have a model of their spacing on a 3D map. Lenschow provided an equation capable of estimating the distances between thermals at a constant height ratio,Z/Z_i , of 0.4. A guide to the distances between the thermals was given as 1.5 to 2.5 times the convective scale by Wallington [56]. Delafield suggested that the distances were between 2 and 3 times the convective scale [20]. This would tend to suggest that the thermal spacing to height ratio is not consistent between different climates. An explanation of this phenomenon may be that there is a minimum spacing for the formation of thermals for them not to merge. In warmer climates the characteristic convective length scale will be much larger than that of a temperate climate. A reduction in spacing of thermals in a temperate climate, although less than in warmer climates, is not sufficient to maintain an equivalent thermal spacing to convective length scale ratio. Following the anecdotal evidence from Wallington [56] and Delafeild [20], Lenschow's equations can be reworked using the numbers proposed above to take the following forms for a British climate.

$$\frac{N_L Z_i}{L} = 0.5 \tag{3.4}$$

$$N = \frac{0.25XY}{Z_i r_o} \tag{3.5}$$

Although there is no way of verifying Equation (3.4) and Equation (3.5) without more accurate flight data, they are more consistent with anecdotal evidence of the British climate.

Although Lenschow provided a prediction of mean distance between thermals their positioning on a given map is often given as random. On occasions when the thermals have no obvious trigger this is a fair assumption. However, in the British Isles the thermals often do have trigger points; a dark field, a power station, a factory, a motorway etc. The effect of these trigger points is to set up a line or 'street' of thermals downwind from the trigger point [20] [57]. Fig. 3.10 show the formation of cloud-streets above Husbands Bosworth airfield in Leicestershire on a summers day.

Figure 3.10: Cloud-Street Formation Above The Gliding Centre at Husbands Bosworth, 2011

Knowledge of this phenomenon can be used to improve the likelihood of the aircraft encountering another thermal. When seeking to contact another thermal it is advisable to fly up or down wind from the previously encountered thermal, assuming this track deviation is within acceptable bounds. As the assumption of thermal streets is valid even if clouds do not form, this atmospheric phenomenon can be exploited by the soaring controller.

Fig. 3.11 shows the resultant map if Lenchow's equations are combined with the assumption of the presence of cloud-streets.

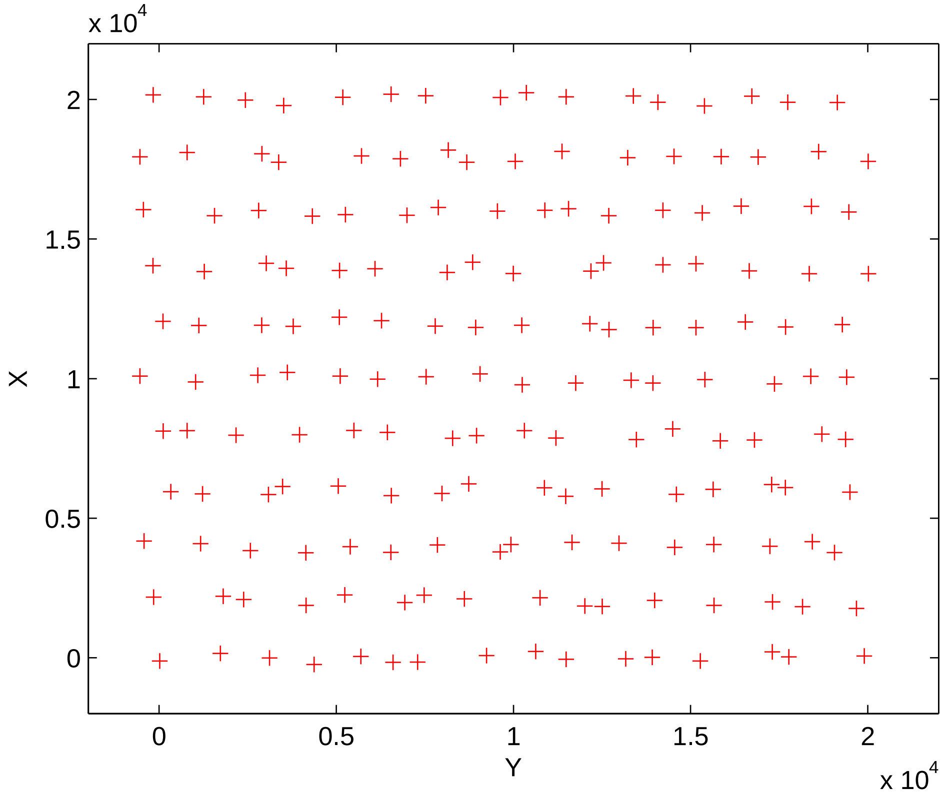

Figure 3.11: 2D Trigger Map

At first glance Fig. 3.11 is a very dense and regular map, but after the trigger times are distributed a 2D section of the map is as shown in Fig. 3.12. It can be seen that Fig. 3.12 has an almost random quality despite the map in Fig. 3.11 being well structured. This provides insight into why the assumption of randomised thermal positions on a 2D map provides a good likeness. The map used in the simulations presented here uses a 4D map, with the position and strength of the thermals varying with time. The thermal structures are modelled as drifting with the wind making the environment highly dynamic.

The 3 dimensional, time dependent simulation environment presented will be used to assess the performance of the soaring algorithms throughout this chapter.

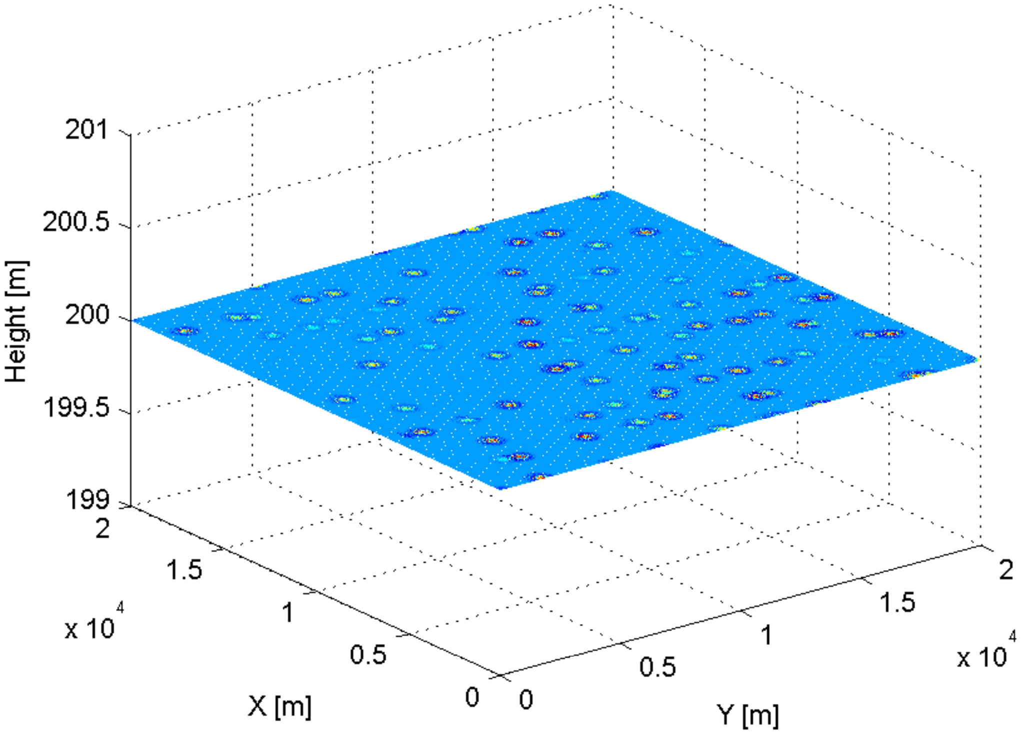

Figure 3.12: 2D Cross Section of 4D Thermal Map

3.5 Trajectory Optimisation

The problem of trajectory optimisation for a pure glider is a classical problem that has been explored by many. However, the problem of trajectory optimisation for a UAV, which is almost inevitably not a pure glider, is subtly different. There are many seemingly conflicting mission profiles; making a general case almost impossible. Two opposite ends of the spectrum are; maximising cross-country speed where if a sufficiently strong thermal is not encountered the UAV will continue under its own power to the objective, and persistence over target where even areas of reduced sink should be utilised. The ability to continue on task without the use of thermals changes the approach taken. Before discussing flight strategies it is pertinent to develop two capabilities; optimal flight between and efficient exploitation of thermals. The following theory was based on the assumption of the availability of powered flight, albeit with an associated penalty.

The following two subsections will deal with the optimal speed-to-fly theory and an efficient heuristic method for optimising energy extraction from thermals.

3.5.1 Speed-to-Fly Theory

The classical speed-to-fly problem is one of the optimum speed-to-fly in order to maximise the range of an aircraft given a certain height. Although this problem normally is aimed at aiding gliders and as such includes a MacCready setting, a prediction of the strength of the next thermal, it does not have to.

The speed-to-fly optimisation presents a number of practical problems. To attempt to clarify some of the issues associated with the calculation of the optimum speed-to-fly a number of derivations will be presented.

3.5.1.1 Derivation of Drag Polar

The first derivation is of the drag polar showing the assumptions made. This follows the commonly accepted derivation [54]. An attempt has been made to use standard notation where ρ, V, S are the atmospheric density, velocity and wing area respectively.

$$Drag = \frac{1}{2}\rho V^2 S C_D \tag{3.6}$$

where the coefficient of drag of the aircraft, C_D, has already been introduced as a function of form drag, C_{D0}, and the coefficient of lift, C_L. The induced drag factor, ε, is used to express the wing efficiencies under a wing load factor, n. Mass and gravitational acceleration take their normal notations, M and g. All the notation used can be found in the nomenclature.

$$C_D = C_{D0} + \varepsilon C_L^2 \tag{3.7}$$

$$C_L = \frac{nMg}{\frac{1}{2}\rho V^2 S} \tag{3.8}$$

$$Sink\ Rate = \frac{Drag\ \times\ Velocity}{Mg} \tag{3.9}$$

The motor is ignored for the purpose of the calculation of the drag polar. In reality, this data can be recorded by a series of measured glides at known velocities. The non-linear function $p(V)$ is introduced to express the drag polar as a function of aircraft velocity.

$$Sink\ Rate = \frac{\frac{1}{2}\rho V^3 S C_D}{Mg} \tag{3.10}$$

$$p(V) = \frac{\frac{1}{2}\rho V^3 S[C_{D0} + \varepsilon(\frac{nMg}{\frac{1}{2}\rho V^2 S})^2]}{Mg} \tag{3.11}$$

$$p(V) = \frac{\rho V^3 S C_{D0}}{2Mg} + \frac{2\varepsilon n^2 Mg}{\rho V S} \tag{3.12}$$

$$\frac{dp(V)}{dV} = \frac{3\rho V^2 S C_{D0}}{2Mg} - \frac{2\varepsilon n^2 Mg}{\rho V^2 S} \tag{3.13}$$

3.5.1.2 Derivation of the Speed-to-Fly Equation

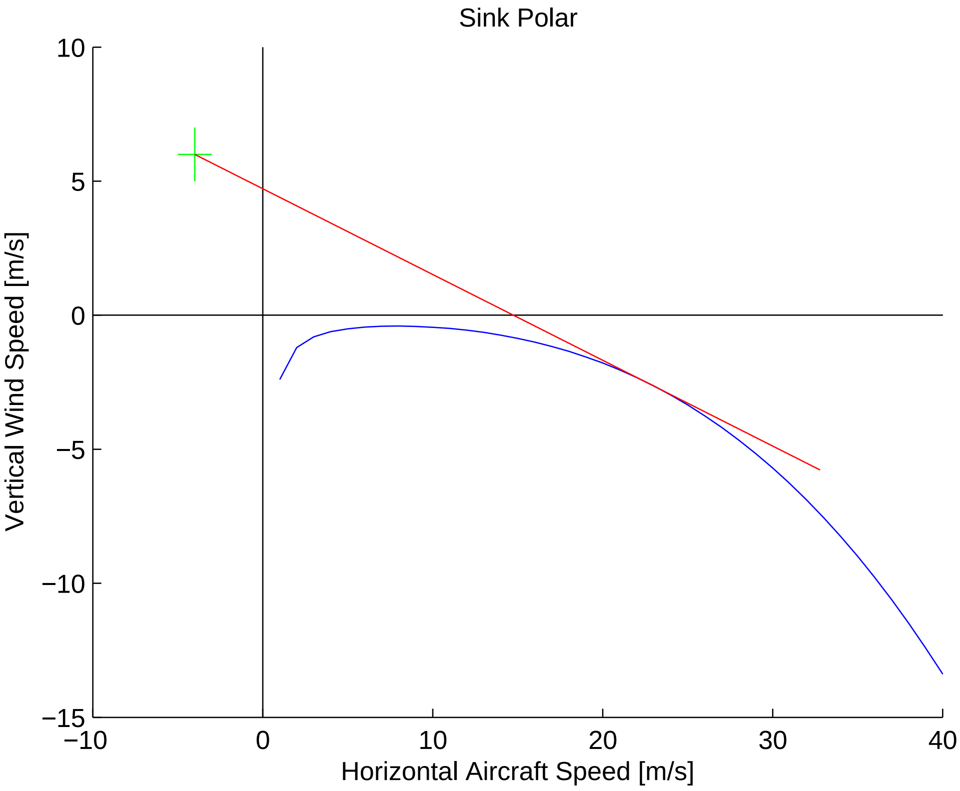

Figure 3.13: Speed-to-Fly Polar

Fig. 3.13 denotes the sink polar for the current aircraft simulation with the optimal speed-to-fly marked using a tail wind of 4m/s and in air sinking at 6m/s.

Alternatively the graph could be read as an aircraft with a 4m/s tail wind and still air with a MacCready, R, setting of 6m/s. The graph is unambiguous with regard to tail wind.

$$\frac{p(V) - V_{climb} + R}{V - V_{Tail\,Wind}} = \frac{dp(V)}{dV} \tag{3.14}$$

$$0 = p(V) - V\frac{dp(V)}{dV} + V_{Tail\,Wind}\frac{dp(V)}{dV} - V_{climb} + R \tag{3.15}$$

Substituting in the drag polar of the aircraft, we arrive at Equation (3.16), which can be rearranged into the form shown in Equation (3.17).

$$\begin{aligned} 0 = {} & \frac{\rho V^3 S C_{D0}}{2Mg} + \frac{2\varepsilon n^2 Mg}{\rho V S} - \frac{3\rho V^3 S C_{D0}}{2Mg} - \frac{2\varepsilon n^2 Mg}{\rho V S} \\ & + V_{Tail\,Wind}\frac{3\rho V^3 S C_{D0}}{2Mg} - V_{Tail\,Wind}\frac{2\varepsilon n^2 Mg}{\rho V S} - V_{climb} + R \end{aligned} \tag{3.16}$$

$$0 = -\frac{\rho V^3 S C_{D0}}{Mg} + V_{Tail\,Wind}\frac{3\rho V^2 S C_{D0}}{2Mg} - V_{climb} + R - V_{Tail\,Wind}\frac{2\varepsilon n^2 Mg}{\rho V^2 S} \tag{3.17}$$

The equation above is solved for V once the tailwind and instantaneous climb rate are known. Leaving aside the issues that surround an appropriate value for the MacCready setting, the equation is of 5th order. 5th order equations are more computationally intensive than lower order equations as they are not analytically solvable. It has been noticed in [64] that the authors deduct and then neglect the effect of wind on the desired speed-to-fly. Neglecting the wind speed reduces the problem to the 4th order making it immediately solvable. If persistence of the aircraft is the only goal of the flight control system then this may be a suitable solution but the objective of this analysis is to maximise the aircraft's cross-country speed so wind cannot be ignored.

At this time there is no known elegant optimal solution to the speed-to-fly equation that can be implemented in this situation without a high computational burden. This holds true even including the solution presented by Edwards [22] as his solution is non-optimal and does not include the effect of wind or normal loading.

3.5.1.3 Choice of and Evaluation of Thermals

The identification of suitable thermals has been investigated in detail over the years [33] [56]. Equations predicting the optimum speed-to-fly to optimise overall cross country speed are well known [29] [40] but are incomplete without an estimate of the strength of the next thermal and therefore the climb rate that will be accepted; which is of course unknown until it is encountered. This prediction is generally referred to as the 'MacCready setting' [40] after the first person to pose this problem. The choice of the MacCready setting is a frequent topic of conversation at gliding clubs, but the problem boils down to how much risk can be tolerated. As the setting is a function of risk it follows that the setting is related to height, as a higher aircraft has a greater probability of encountering another thermal with the associated reduction in the risk of a forced landing or the use of a powered climb. Edwards [22] viewed landing out as unacceptable and his MacCready function reflects this. Others have a higher tolerance to risk and as such select a more aggressive MacCready function. The XCalibur is fitted with a powerful electric motor so if the mission demanded maximum cross country speed at all cost, the MacCready function could be set aggressively resulting in a profile that would ignore all but the strongest thermals, necessitating the use of the motor periodically. This powered climb and glide profile would be extremely power hungry, reducing range and crippling endurance. The choice of the function ultimately depends on the aircraft in question and the mission profile with its associated constraints. A good example of a constraint would be a maximum allowable height during the flight. The effect of this constraint would be to cause the MacCready function to tend to infinity at that height. In reality there are tolerances and safety margins. This type of constraint is shown in Fig. 3.14 as where the XCalibur is operated the operational limit is set at a height of 2000 feet.

Once the MacCready setting has been established the aircraft can fly at the appropriate speed for the conditions and assess any thermals encountered for suitability. To facilitate the correct identification of thermals two variometer readings are used; an instantaneous reading and an averaged reading. The averaged reading suppresses the influence of turbulence and helps to prevent the erroneous thermal detection. Once a thermal stronger than the MacCready setting is detected the soaring algorithms are triggered. At that stage the average reading must drop below a lower critical value before the search for lift is abandoned.

This is necessary because the aircraft will take a few turns to find the core of the thermal, with the sink that exists around the edge the average reading may fall considerably before recovering and stabilising. The instantaneous reading is used to position the aircraft in the thermal. Once the average reading has stabilised a decision can be made on whether the thermal is stronger than the MacCready setting, if not the thermal is left in the hope of finding a stronger thermal along track.

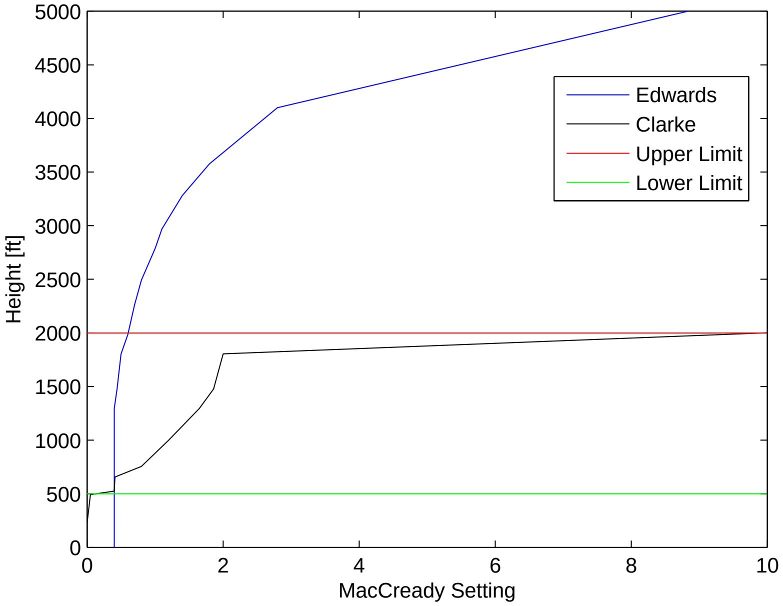

Figure 3.14: MacCready Risk Function

Similarly final glide calculations can also affect the MacCready setting as shown in Fig. 3.15 [18].

3.5.1.4 The Use of the Speed-to-Fly Equations and MacCready Errors

The speed-to-fly equation must be used wisely in the air as the sensor data is affected by gusts. Blindly following the speed-to-fly given will result in aggressive, and possibly unnecessary, pull-ups and dives that load the wing up causing extra drag and wasted energy. The direct application of the equations also requires a degree of feed-forward, which is difficult to quantify and optimise. It is advantageous to pull-up in strong lift conditions in order to slow down but it is disadvantageous to be diving and speeding up in sink. The ideal scenario is to

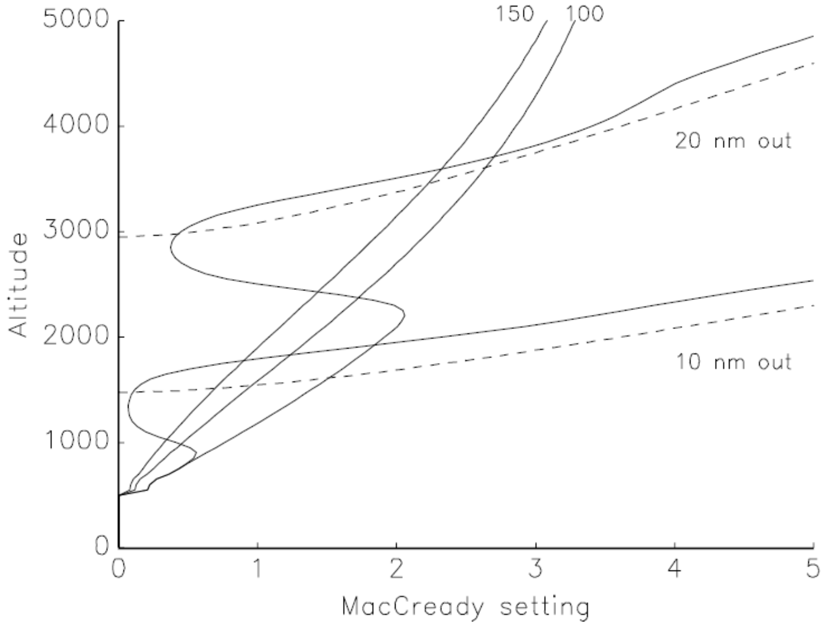

Figure 3.15: Optimal MacCready Risk Functions [18]

both slow down in the lift and then as the lift deteriorates to speed back up, so to be at or above cruise speed before encountering the inevitably stronger sink ahead. This scenario leads to an adoption of a complicated pitch controller.

The alternative to chasing the variometer reading is to select a cruise setting, and then deviate by a small amount until a thermal worth circling in is discovered. The adoption of this approach raises interesting questions over the interpretation of the speed-to-fly equations.

Reichmann [48] presented an interesting case study that emphasised the benefits of sampling as many thermals as possible. Reichmann effectively illustrated a practical example of the effect of MacCready errors as shown in Fig. 3.16. Although Reichmann [48] considered a classical implementation of MacCready using a prediction of the strength of the next thermal to be encountered, which is not directly applicable to UAV that have no ability to forecast strength of future thermals, the principles expressed can be adopted.

Although in Reichmann's example [48] the optimal speed-to-fly methodology did not produce the highest average cross-country speed it did result in the smallest maximum height loss, thus representing the least risky option for pure gliders.

However, very few UAVs are pure gliders.

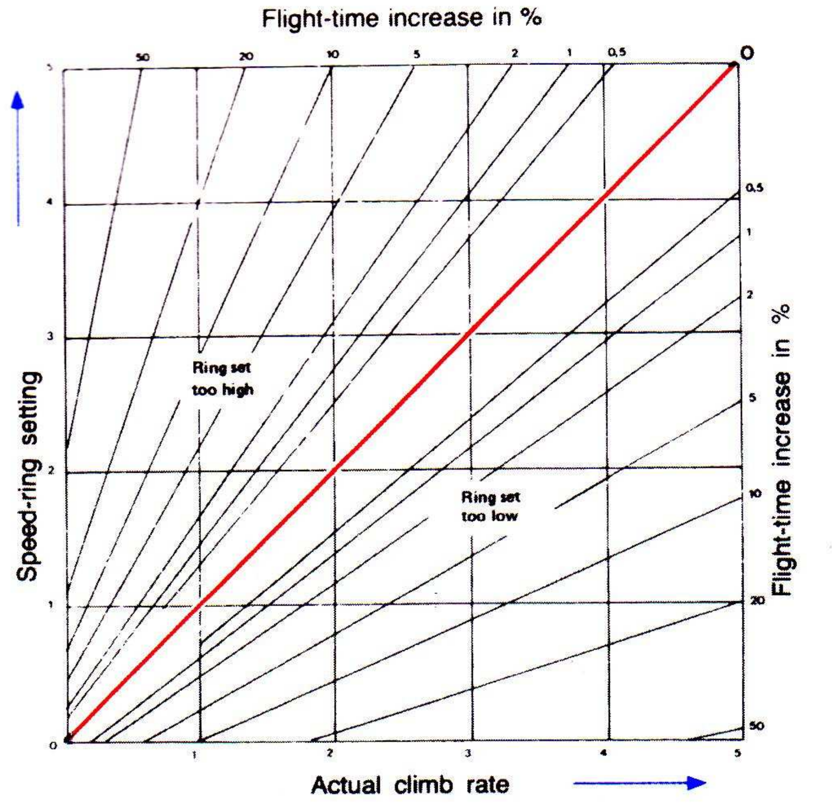

Figure 3.16: MacCready Errors [48]

To further illustrate the effect of flying slower than the optimal speed-to-fly prediction versus climbing in weak thermals two scenarios are depicted in Fig. 3.17 and Fig. 3.18. The first scenario is the UAV choosing to fly at maximum range speed (R=0), 12m/s, thus enabling it to fly further without being forced to accept a weak thermal, as a result the aircraft contacts a stronger thermal, 3m/s, and this gives the UAV an average speed of 9m/s.

The second scenario is the UAV has consistently encountered thermals of approximately 3m/s, as a result a MacCready setting of 3 (R=3) is applied and flies at the speed predicted by the optimal speed-to-fly equation, 16m/s. The aircraft in the second scenario flies faster but fails to reach a thermal of 3m/s again and is forced to accept a weaker climb of 1m/s. This gives the second aircraft an average speed of only 5m/s.

Fig. 3.17 and Fig. 3.18 illustrates the fact that the climb rate accepted has a much bigger influence on cross-country speed than the cruise speed used. In

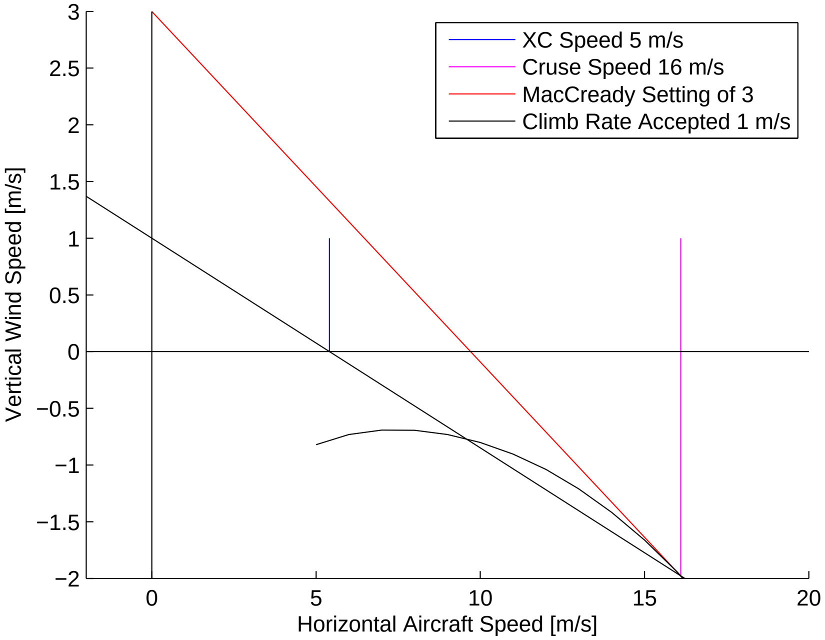

Figure 3.17: MacCready Drag Polar Example

reality the UAV might not have accepted the weaker climb, instead choosing to use its motor to continue on task, maintaining the higher cross-country speed at a penalty. This introduces the question of how to calculate the cruise speed.

Although a UAV may ultimately use soaring to improve cross-country speed, UAVs are used to complete tasks that may have time constraints. The time allocated to complete the tasks set ultimately dictates the minimum acceptable cross-country speed and as a result the minimum acceptable cruise speed. This minimum acceptable cruise speed should be used only in cases where this depicted cruise speed is not less than the equivalent optimal speed-to-fly speed with the MacCready setting of zero. If this most conservative MacCready setting is faster then this should be adopted in preference, as flying slower than this value is decreasing the aircraft's range and wasting energy unnecessarily.

3.5.1.5 The Use of Thermals to Improve Persistence Over a Target

The use of thermals to improve persistence requires a slightly different approach. As the UAV is only concerned with remaining on station weaker thermals may be utilised to good effect. With the aircraft only concerned with staying airborne the

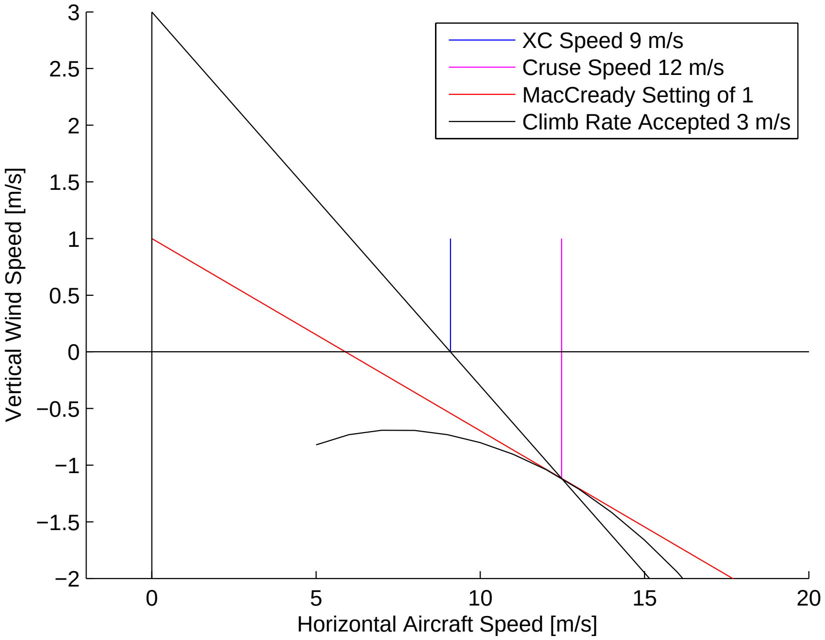

Figure 3.18: MacCready Drag Polar Example

aircraft should travel at the minimum sink speed (also known as minimum power speed). Any thermal should be used if the rate of energy gain is greater than the rate of energy expenditure plus the energy subsequently required to return the UAV to station.

$$\frac{dE_{thermal}}{dt} > \left(\frac{dE_{Aircraft}}{dt} + \frac{dE_{task}}{dt}\right) \tag{3.18}$$

3.5.2 Centring Within a Thermal

As time and height invariant thermal models aid visualisation, these have been used to design the soaring techniques. However, accurate atmospheric models are still required in order to validate the proposed techniques.

A thermal can be viewed as a vortex ring travelling upwards through the atmosphere with the aircraft's objective to be carried aloft in said vortex. In order to maximise the potential height gain of a given thermal the aircraft has to centre in the thermal as quickly as possible. If the aircraft does not find equilibrium inside the core of the thermal it will drop out of the bottom of the thermal. The factors that affect the aircraft's ability to find equilibrium include;

the up draught strength, size, or difficulty in locating the strongest lift.

The inclusion of the associated 'sink' around the edge of a thermal is often neglected [59] [6] [22] because the sink found around the edge of very strong thermals is relatively small. However, the sink found around thermals in the UK is not insignificant and impacts strongly on the ability of the aircraft to find the centre of the thermal.

As discussed earlier, the time taken to centre in the core of a thermal is critical to the successful exploitation of the thermal encountered. As a result there is a desire to both better understand and to further optimise the positioning algorithms.

Ensuring the aircraft always turns in one direction while soaring allows the operator on the ground to quickly assess the flight mode the autopilot is currently in. It was shown by Piggott [47] that reversing the direction of the turn in a thermal is un-advisable, hence a turn direction monitor was added to the soaring controller so that once a turn direction was chosen, it was not reversed.

Although there are algorithms to detect the relative location of the thermal with respect to the aircraft they are not infallible [59]. This leads to a worst-case scenario of the aircraft turning in the wrong direction once encountering the edge of a thermal. This is the scenario that will be investigated when considering the stability of thermal location algorithms.

The control implemented in the simulation presented is a relatively simple implementation of the Reichman method. Loughborough University operates a range of advanced autopilots. The autopilot that is fitted in the XCalibur is capable of accepting both heading and bank angle commands. This facilitates a more straightforward implementation of the Reichmann method.

Although the Reichman method provides good results, Allen [8] showed improvements by adding a thermal position estimator. The soaring controller therefore takes the following form given in Equation 3.19.

$$\begin{bmatrix} X_{est} \\ Y_{est} \end{bmatrix} = \begin{bmatrix} \frac{\widehat{\dot{E}x}}{\hat{\dot{E}}} \end{bmatrix} \tag{3.19}$$

X_{est} and Y_{est} are the estimated location of the thermal, $\widehat{\dot{E}x}$ is the time averaged energy position as given by Equation 3.20, where X and Y are current grid positions, $\dot{E}$ is the rate of change of aircraft energy i.e. Variometer reading. $\hat{\dot{E}}$ is the time averaged rate of change of aircraft energy, as given by Equation 3.21.

$$\left[\ \widehat{\dot{E}x}\ \right] = \left[\begin{array}{c} \frac{1}{Ks+1}(\dot{E}X) \\ \frac{1}{Ks+1}(\dot{E}Y) \end{array} \right] \tag{3.20}$$

$$\hat{\dot{E}} = \frac{1}{Ks+1}\dot{E} \tag{3.21}$$

Although Equation (3.19) is in continuous time form it can be readily discretised for implementation with the real autopilot. This form of estimation has the advantage of having a variable sample length, for the estimation of the location of the thermal. The filter gain, K, was chosen as the time to complete one soaring turn, but this does not have to be the case. A system level block diagram of the structure is shown in Fig. 3.19 and the complete soaring control structure used is shown in Fig. 3.20.

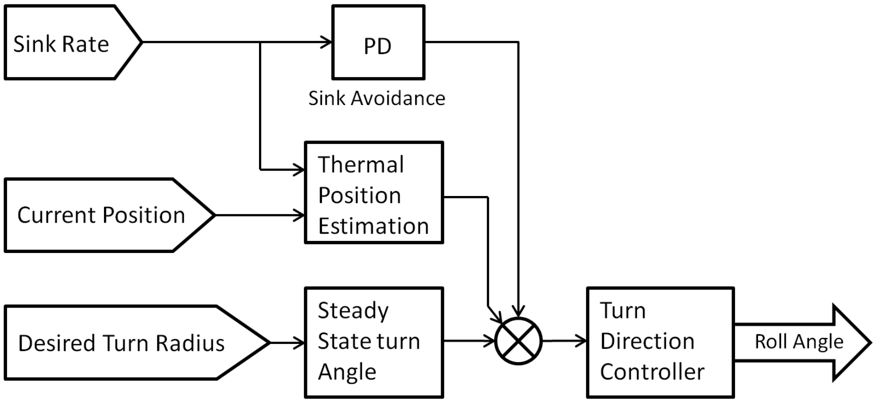

Figure 3.19: System Overview of Soaring Controller

Although Fig. 3.21 shows the new soaring controller performs better than Allen's method in the example quoted this is not always the case. This controller is of the same basic form as that used by Allen [8], with the exception that the autopilot he used could not accept bank angle commands, as a result his controller demands a turn rate. All that can be conclusively ascertained from the results is that the two methods are approximately equal. The advantage of this continuous soaring controller is that all of the terms in the controller have physical significance and are readily tunable in real-time. Although the use of low pass filters is more computationally intensive than other methods [59] [8] [22] it allows for dynamic adjustment of the number of data points used to estimate the centre of the thermal.

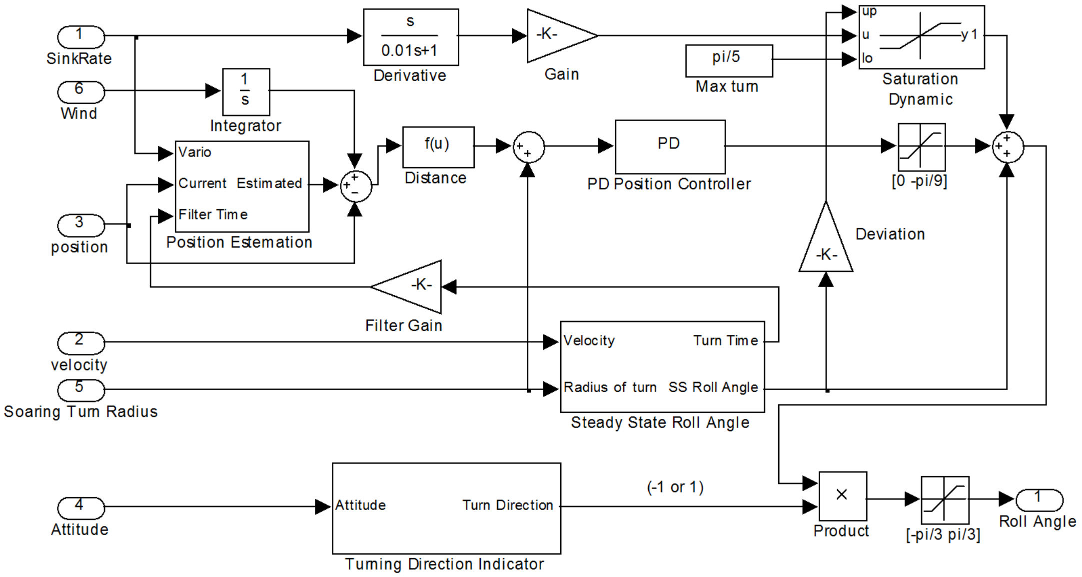

Figure 3.20: Soaring Controller Used

To maximise the aircraft's chances of finding thermals and thus maximising its cross-country speed potential, the flight control algorithms utilise cloud-street phenomena. To do this once a thermal has been found and utilised the trajectory is modified to fly directly into or downwind as long as this does not take the aircraft more than a critical angle off-track. The soaring controller also includes a prediction of the likely next thermal location along the current cloud-street. If the location of this thermal would take it more than the critical angle off-track the cloud-street is also rejected. This projection is based on the convective scale assumptions presented in Section 3.4.

There are more complex thermal position estimation algorithms but they tend not to offer substantial performance improvements and are not implementable in real-time so are not presented here [59].

3.6 Simulation of a Surveillance Type Mission

With the simulation environment in place it is possible to start investigating the feasibility of different mission profiles. Combinations of two mission profiles are of key interest, improved range and persistence over target with the use

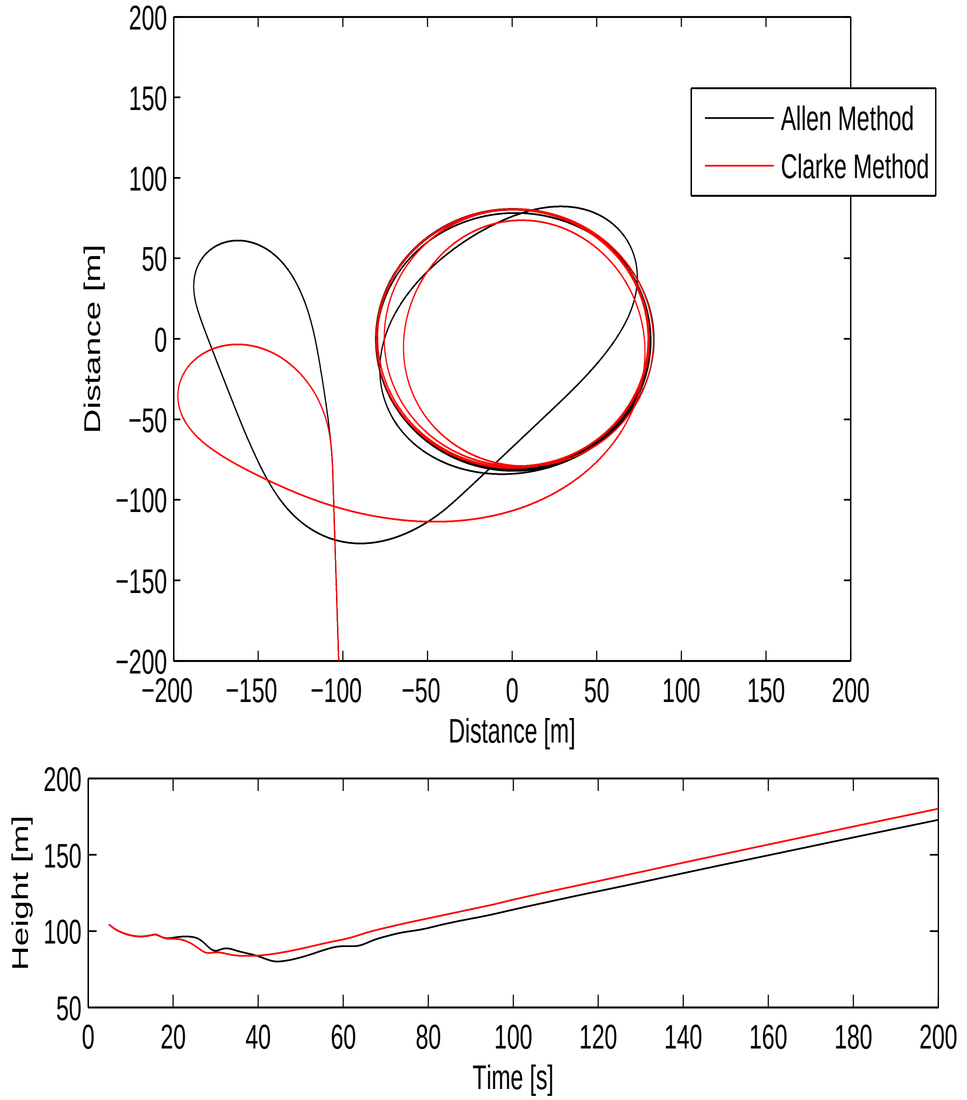

Figure 3.21: Performance Comparison of Centring Algorithms

of thermals. The first task involves using the aircraft's stored energy (kinetic, potential, and electrical) as efficiently as possible, while the second is purely a matter of minimising energy expenditure.

The XCalibur has the ability to release the brake on its folding propeller turning it into, an inefficient, RAT. This set-up is capable of providing a small but meaningful amount of power. Realistically the XCalibur is not capable of eternal flight because the RAT would only just provide enough power for on-board avionics systems. The use of this RAT is therefore ignored for the purposes of the simulations shown.

3.6.1 Improved Range

The simulation scenario chosen for this exercise was a 20km flight with a 10kts wind added 45 deg to the desired track. A 45 deg wind component is added because this is the worst case for the use of cloud-streets. The atmospheric map used is time dependent, as detailed in Section 3.4. To put the results into context 4 approaches will now be compared; powered flight, soaring flight, soaring flight utilising cloud-street phenomena and time constrained soaring flight.

The minimum safe altitude was chosen as 500ft. The cruise height was chosen as 1000ft. This was also used as the power-on altitude for the soaring simulations as thermals below this height are more broken and harder to centre in, thus reflecting best practice for improving cross country performance. The MacCready function shown in Fig. 3.14 was used as this was felt to represent a typical UAV risk function. The MacCready function used is not ultimately risk averse as UAVs generally do have motors and as such most applications have a speed-risk trade off. The impact of this function is to result in all the thermals encounter on some flights to be rejected in favour of cross country speed.

In order to get a reliable indication of the energy savings under these flight conditions and constraints, well over 400 flights were conducted with a spread of initial positions, although all were 20km from the end location. Fig. 3.22 shows 3 typical soaring flights.

The relative performance of the 4 approaches (opportunistic soaring, street soaring, time constrained soaring and powered flight) can be summarised by discussing the following 3 plots; the energy consumption, distance travelled, and time taken on task.

From Fig. 3.23 it is clear that there is a significant energy saving to be had

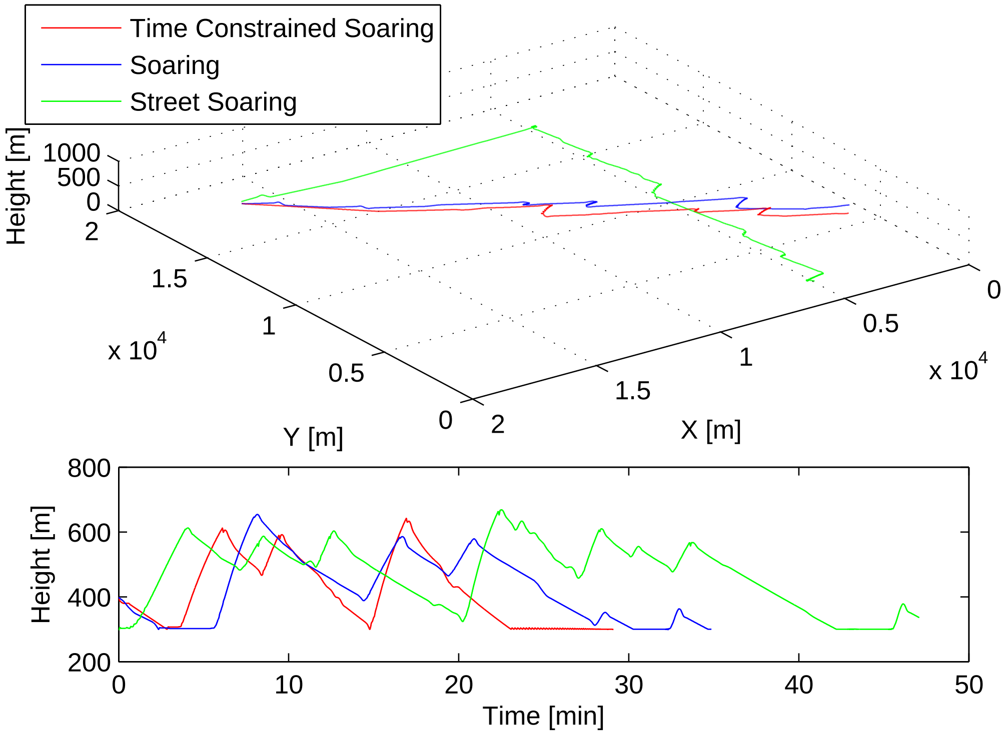

Figure 3.22: Typical Soaring Behaviours in a Simulated 20km Flight With a 10kts Wind

by the use of atmospheric convection in the form of thermals. However there is a large variance in the amount of energy saved on each flight. The use of cloud-streets provides the most reliable method for contacting thermals. It is worthy of note that the mean energy consumption of the street and non-street soaring methods are within 1% of each other. This is surprising as the wind vector is at the least favourable angle for street-following, resulting in a large increase in the distance travelled by the aircraft as can be seen from Fig. 3.24. This increase in distance flown causes the flight times to be substantially increased, as can be seen from Fig. 3.25. Despite the increase in distance flown by the street following soaring controller it still represents the least risky method of travel, providing the solution with the highest aircraft average height.

The asymmetry in the power consumption in the powered flight is due to the fact that the aircraft was still allowed to extract energy from the thermals by slowing down in rising air, also known as ‘Dolphining’. For the solely powered flights the aircraft was not allowed to turn in the rising air.

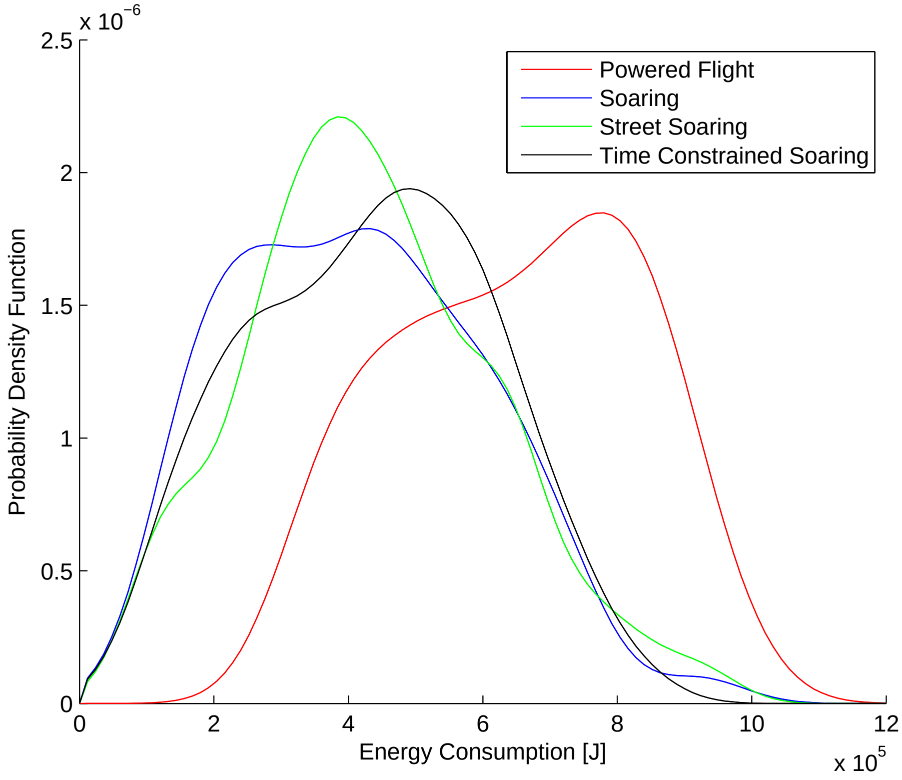

Figure 3.23: PDF of Energy Consumption

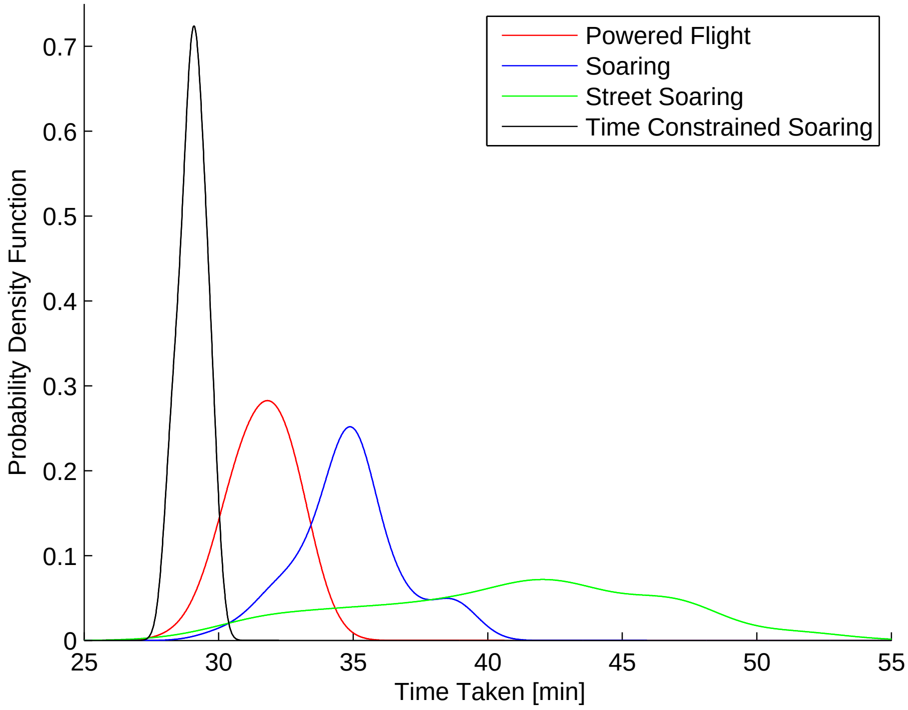

Figure 3.25: PDF of Time Taken

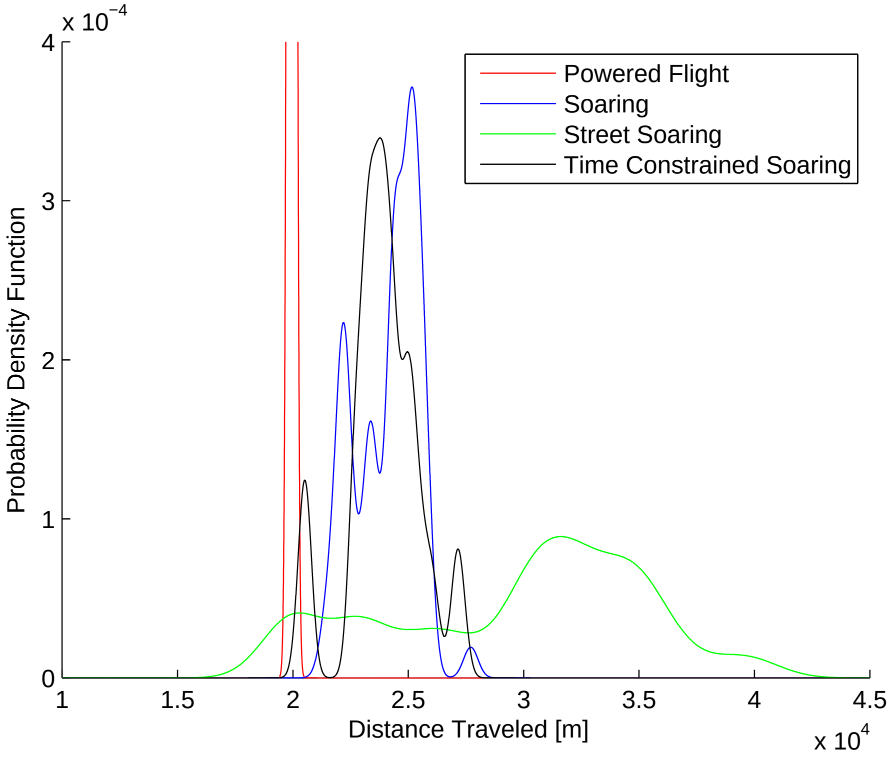

Figure 3.24: PDF of Distance Traveled

If flight time is critical the MacCready function and therefore climb rate and cruise speed can be dynamically adjusted to constrain the maximum time on task. On the task presented the time constrained soaring approach guaranteed that the task would be completed in 30 minutes. Thus this time constrained approach not only completed the task on average 8% faster than the powered flight but used on average 33%less battery energy in the process.

3.6.2 Improved Duration

Starting from a similar weather scenario as in Section 3.6.1, 10kts wind, the aircraft was tasked to keep itself within line of sight of a point on the ground. In order to maximise the chances the aircraft conducts a searching pattern until a suitable thermal is encountered. On finding a thermal the aircraft climbs until the maximum allowable height is achieved or the viewing cone is no longer sustainable. The viewing cone is the allowable intersect angle that is needed to keep the target in view as shown in Fig. 3.26. The minimum safe altitude was chosen as 500ft with a viewing cone angle of 45 deg.

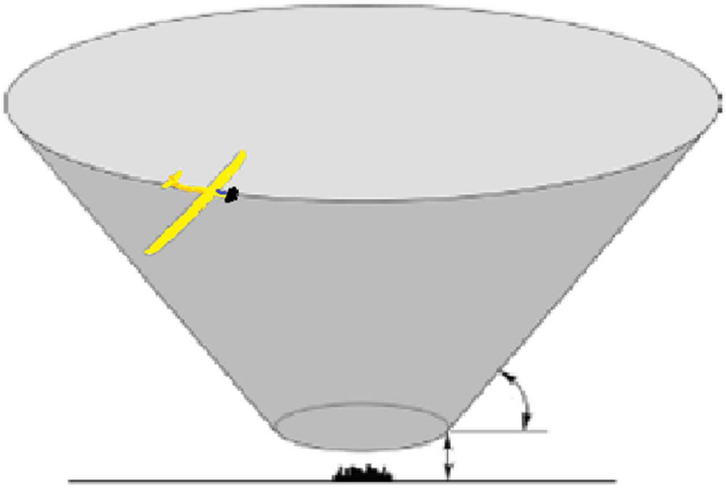

Figure 3.26: View Cone

An example of the climb and glide cycle is shown in Fig. 3.27.

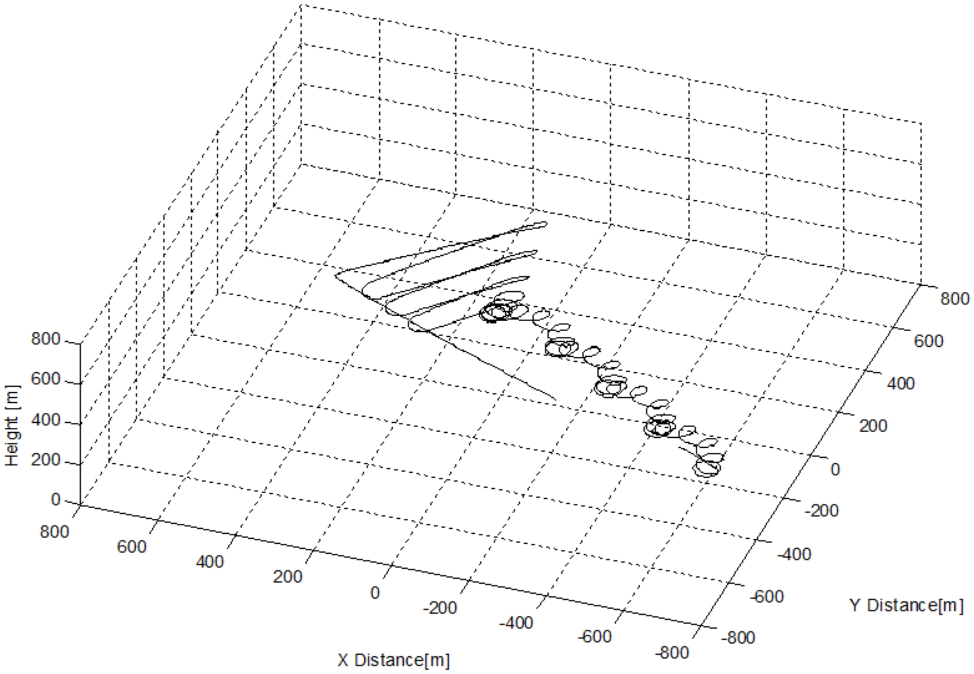

Figure 3.27: Thermal Loiter

The scenario was stopped after two hours without the motor having been used. This represents an average energy saving of over 95%. A 100% energy saving is not possible with the aircraft modelled as the servos that actuate the control surfaces and the power draw of the avionics are modelled. The aircraft modelled does not have a RAT to generate power.

3.7 Conclusion

A highly detailed simulation model has been developed consisting of a non-linear aircraft dynamics model, a 4D parametric thermal model and a realistic control structure. The parametric thermal model was updated from those previously used to more accurately reflect the British climate. The presence of non-trivial amounts of sink associated with the thermal structure along with the prevalence of cloud-streets has been reflected in the atmospheric model. The practical implementation of the MacCready function with restrictive height constraints has been discussed and implemented. A new flexible implementation of the Reichman centring technique was proposed and evaluated, providing promising results. These disparate elements were finally brought together in a simulated task. The simulated task was a 20km outbound journey in challenging conditions. The MacCready risk function was set up to reflect the availability of the motor on the UAV. The use of cloud-streets to help the probability of finding thermals was compared with purely opportunistic soaring. The use of thermal streets improved the chance of contacting a thermal and therefore resulted in a typical energy saving of 54%, over purely powered flight but increased the time taken to complete the task by up to 65%, with a typical increase of 30%. This variance in the time taken to complete the task is often undesirable. A purely opportunistic soaring approach resulted in a typical energy saving of 50% over purely powered flight but increased the time taken to complete the task by up to 25%, with a typical increase of 10%. This variance in the time taken to complete the task is significantly smaller than that of a street-following approach. If the time taken to complete the task is critical then streets can be used selectively in combination with the dynamic adjustment of the MacCready function to precisely set the cross-country, or average, speed over large distances. This adjustment of cross-country speed affords accurate control of the arrival time of the vehicle while maintaining large energy savings. The use of thermals to aid the persistence of UAVs over a target point was also considered, with the X-Models XCalibur aircraft able to remain in the locality of the target indefinitely without the need for its motor, by the use of thermals. This persistence over target utilising thermals gave an energy saving of above 95%.

Having demonstrated the benefits of autonomous soaring by extensive simulations it is now possible to move on to practical testing. A key foundation for achieving the efficiency gains demonstrated in this chapter is the ability to execute the desired piloting strategies precisely. In order to do this a highly accurate AHRS is needed. The following chapters detail the developments needed in attitude heading reference and navigation systems to provide the accuracy required for autonomous soaring.

Chapter 4

An Air Data Attitude Heading Reference System

4.1 Introduction

In this chapter the developments in the attitude heading reference algorithms and the utilisation of sensor hardware are dealt. A justification of the work is provided with the key problems explained. A pressure augmented solution is given to provide an ADAHRS. A practical iterative solution to solving the Direction Cosine Matrix (DCM) with accelerations is given in Section 4.4.

Attention is given to the AHRS because its performance has a profound impact on the aircraft's performance as a whole. The AHRS developed here has been developed for application in flight control systems on micro to small sized UAVs utilising MEMS sensors, as such automotive class sensors are assumed, making the need for effective sensor augmentation critical for overall system accuracy. Many UAVs rely on GNSS to augment their attitude estimation along with being solely relied upon for their navigation. These GNSS based solutions are capable of providing adequate performance but remain unattractive for many users as they are extremely vulnerable to GNSS denial. This vulnerability to GNSS denial means that these GNSS based solutions can not be used in safety critical and military applications. An air data augmented solution to the attitude heading reference problem provides a GNSS devoid solution that is attractive for many applications.

Chapter 6 describes an ADGNS that builds on the work presented in this chapter to reduce vulnerability to GNSS denial.

As discussed in Chapter 2 there are MEMS based autopilots commercially available but they tend to be primarily designed for military use [44] [3]. Whilst these offer a significant capability, they consist of closed architectures that make them troublesome and unsuitable for research environments. In a research environment, it is important to have the ability to implement new and novel techniques using all the sensor data available. For this reason many research establishments continue to develop their own hardware [6] [22] [11] [62]. Existing commercial autopilots tend to use way-point navigation as it allows the flight control system to compensate for poor sensor performance but restricts their application as they are unsuitable for sustained dynamic tasks like soaring. The specific challenges imposed by autonomous soaring on the AHRS will be discussed. New techniques are required to further improve the performance and reliability of the MEMS sensor based autopilots. This chapter details the development of an ADAHRS along with rigorous simulation testing of the algorithms presented. Extensive practical testing of the algorithms presented in this chapter will be presented in Chapter 8.

4.2 The Attitude Heading Reference Problem

The problems with obtaining accurate attitude and heading information originate with the types of sensors used. Three different types of sensors are typically used to obtain attitude information; gyroscopes, accelerometers and magnetometers. In theory if prefect gyroscopes were used then the attitude of the vehicle could be calculated from integration of the local angular rates of the vehicle. However in reality gyroscopes have biases and noise present that introduces drift in the sensor data. If this flawed gyroscope data is integrated to get attitude then the error on the estimation will grow indefinitely, eventually rendering the estimation meaningless. Fig. 4.1 is a plot of the sensor data recorded from the actual gyroscopes used within this thesis. Fig. 4.1 shows the rate and attitude errors for a single channel of a 3-axis gyroscope after correction for the earth's rotation. Fig. 4.1 shows that even after precise biasing of the gyroscopes that if the gyroscopes are not augmented by another reference source the attitude estimation will drift by more than 60° in one hour.

For highly accurate gyroscopes, as found on larger aircraft, augmentation is not a pressing issue as the gyroscopes provide useful data for many hours without

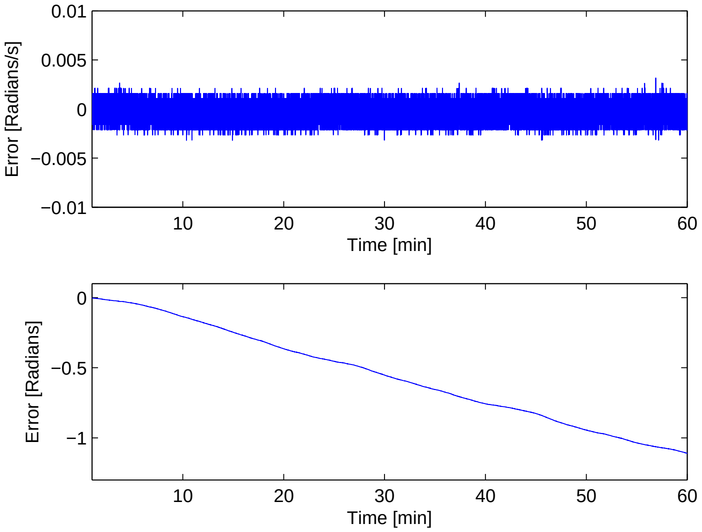

Figure 4.1: Gyroscope Drift

the need for correction to be applied. This is not the case with MEMS gyroscopes as used on many UAVs. MEMS gyroscopes vary in quality and accuracy but typically the estimation supplied by a MEMS gyroscope is only useful for seconds, if the drift is not addressed. There are a few different techniques used to augment the gyroscopes [62] [55] but all are based on a form of tilt sensing. Using accelerometers to find the gravity vector is a good solution for constraining gyroscope drift as the estimation of attitude provided by the gyroscopes is smooth but drifts, whereas the accelerometer estimation is noisy but does not drift. This tilt sensing approach can be analogised by equating this approach to the use of a pendulum to find vertical. The problem with this approach is that while the vehicle is undergoing any accelerations the pendulum will be perturbed and will not be aligned with the vertical axis. Usually when the AHRS detects high angular rates or accelerated flight conditions the filtering is stopped or altered to reflect the fact that the tilt sensor is no longer reading the gravity vector correctly [62]. The need to switch off the filtering process is problematic. The need to switch the filtering constrains the duration of aggressive manoeuvres that the system is capable of enduring. This constraint is not a problem for systems using accurate gyroscopes as they can still function for hours without augmentation but for MEMS based autopilots this can be a critical constraint. One such situation where this constraint is critical is when the aircraft is required to perform aggressive circling flight for a prolonged period of time; such as soaring. If the aircraft is required to circle in the same direction for an extensive period of time then the AHRS can suffer from spiral mode failure resulting in loss of control of the aircraft. Spiral mode failure will be discussed and illustrated later in this chapter, in Section 4.6.2. The solution presented in this chapter removes the need for a switching filter improving the robustness of the AHRS system as a whole.

The technique presented here assumes that the heading of the aircraft is known or can otherwise be estimated separately using magnetometer and gyroscope combinations. This is valid as heading is irrelevant when calculating roll and pitch.

It is frequently useful to work out the attitude of a vehicle from measured accelerations. This is done by finding a solution to the following equation.

$$[a] = [DCM][r] \tag{4.1}$$

where a and r represents local and global accelerations.

If both the local and global accelerations are known then it is possible to find roll and pitch as a function of the DCM. There are existing solutions for this problem given accelerated conditions [11] but these rely on an estimation of the global accelerations. The solution to the DCM problem is given in Section 4.4.

There are a few approaches to estimating the global accelerations of the vehicle in question. Along with a pressure augmented solution there are two other notable solutions; the assumption of unaccelerated flight or a tilt sensing approach [62] [55], and double differentiation of GNSS data [11]. As the objective is to produce a GNSS devoid solution to improve attitude estimation GNSS solutions will not be presented but will be briefly discussed.

4.2.1 Tilt Sensing Attitude Estimation

If the vehicle is assumed to be in an unaccelerated state then the only accelerations measured will be due to gravity. If this assumption is used then the solution is as follows:-

$$\theta = atan2(a_x, \sqrt{a_y^2 + a_z^2}) \tag{4.2}$$

$$\phi = atan2(a_y, a_z) \tag{4.3}$$

A further simplification that allows for the removal of the vertical axis accelerometer is as follows in Equation (4.4) and Equation (4.5). Evidently Equation (4.4) and Equation (4.5) are restricted to ±90° due to their inability to determine whether the vehicle is inverted, although this is a common problem and is simple to resolve using a switch case, purely using the sign of the vertical axis accelerometer.

$$\theta = asin(\frac{a_x}{g}) \tag{4.4}$$

$$\phi = asin(\frac{a_y}{g\cos(\theta)}) \tag{4.5}$$

However there are many situations where the vehicle may be in an accelerated state. If these situations are persistent and prolonged these equations above are not suitable. Clearly if the global acceleration of the vehicle in question is non-trivial and cannot be ignored a fuller solution is needed that takes this acceleration into account. One such solution which can be employed is the use of GNSS to measure and account for global accelerations.

4.2.2 GNSS Augmented Attitude Estimation

A way of approximating the global accelerations of the aircraft is to differentiate GNSS data. Although theoretically elegant the differentiation of GNSS data is fraught with difficulty as the data needs to be differentiated twice introducing large amounts of noise into the results [11]. The noise can be removed by using filters but this introduces large delays in the data. These delays need to be dealt with by synchronising the data sets again, this process introduces instability into the results [11].

Clearly a different means of approximating the global accelerations of the aircraft is desirable. The following derivation deals with the approximations for the global accelerations of a fixed wing UAV.

4.3 An Air Data Augmented Solution To Attitude Estimation

The approach presented here enables continuous correction of the gyroscope estimation of attitude. The technique presented allows an estimation of the global accelerations of the aircraft; allowing the gravity angle to be corrected. There are existing algorithms that seek to do this with various problems. A similar technique using GNSS to estimate the global accelerations exists [11], however the solution to Equation (4.1) requires local, a, and global, r, accelerations. This means that the GNSS data has to be differentiated twice; which in reality results in extremely slow and noisy estimations with ensuing stability problems. The air data augmented technique presented reduces the number of times the data has to be differentiated, and as a result reduces the problems of noise and latency. The air data augmented solution does not use GNSS and as a result is more applicable to systems where vulnerability to the withdrawal of GNSS is unacceptable.

The longitudinal global acceleration can be calculated from differentiating the horizontal component of the measured True Air Speed (TAS) of the aircraft. This velocity measurement however is performed in the local axis so VSI and Coriolis needs to be corrected for, to shift axes, as in Equation (4.6).

$$r_x = \frac{d}{dt}(\sqrt{TAS^2 - VSI^2}) - TAS(q \sin\alpha \cos\beta - r \sin\beta) \tag{4.6}$$

Where α and β are AoA and side-slip of the aircraft respectively. For most flight conditions β can be assumed to be negligible, because of the way this estimation will be minimised by the flight control system. As long as the data has no long term biases present, noise does not introduce problems, therefore short-term perturbations can be tolerated. If deliberate side-slip is likely to be demanded then it is beneficial to take this into account. Unlike side-slip the AoA of the pitot probe is variable and non-zero so needs approximating. A suitable equation for the AoA of the pitot probe is given by Equation (4.7) [54].

$$\alpha = \frac{nmg}{\frac{1}{2}\rho TAS^2 S \frac{dC_L}{d\alpha}} - \alpha_{set} \tag{4.7}$$

Using normal acceleration to calculate G-loading Equation (4.7) reduces to

Equation (4.8) [54].

$$\alpha = \frac{a_z m}{\frac{1}{2}\rho TAS^2 S \frac{dC_L}{d\alpha}} - \alpha_{set} \tag{4.8}$$

The inclusion of an estimate of AoA or α is beneficial, even key, as the AoA can commonly be anything from -10 to +10 degrees before the onset of the stall [5]. The assumed aerodynamic properties of the aircraft in question were discussed in Chapter 3.2.1. The measurement and calculation of the aerodynamic and dynamic model parameters are dealt with in Chapter 8. Some conventional high power and some delta aircraft are capable of even higher AoA. This means that AoA cannot be ignored as is customary in other similar approaches [15] [12] [21] [51]. The inclusion of AoA means that the local air vector can be calculated rendering both Coriolis and centripetal accelerations more accurate.

The lateral acceleration of the aircraft can be calculated from centripetal acceleration of the aircraft in a turn. The rate of change of heading of the aircraft and the aircraft's velocity is known so the centripetal acceleration can be calculated using Equation (4.9). The rate of change of heading information can be noisy due to Dutch Roll [10] of the aircraft and other disturbances but again the calculations that will be made using these estimations of acceleration will typically be part of a filter with a long time base, thus oscillations with a short time base will not be passed through on to the AHRS data.

$$r_y = TAS(q \sin\phi \sec\theta + r \cos\phi \sec\theta) \tag{4.9}$$

If the error in attitude is likely to be so large as to make a small angle approximation invalid then magnetometer heading of the aircraft can be differentiated to give the necessary rate of change of heading. Magnetometer heading is normally relatively noisy, again introducing latency problems after filtering.

The calculation of the vertical acceleration can be done by double differentiating the pressure altitude of the aircraft. Some autopilots also provide a Vertical Speed Indicator (VSI).

$$r_z = \frac{-d}{dt}(VSI) \tag{4.10}$$

This has similar problems to double differentiating GNSS altitude but the pressure altitude is generally smoother and at a much higher sample rate. The autopilot described in Chapter 7 and used in Chapter 8 samples the pressure sensors at approximately 4KHz. This means that the data can be differentiated without introducing as much noise and can be filtered without adding noticeable delays into the system. Two other approximations for vertical acceleration are given below.

$$r_z = \begin{bmatrix} 0 \\ 0 \\ 1 \end{bmatrix} \begin{bmatrix} DCM^{-1} \end{bmatrix} \begin{bmatrix} a \end{bmatrix} \tag{4.11}$$

Equation (4.11) is based on the assumption that the aircraft's attitude is known. At first glance this is contradictory as the aim is to find the attitude from the accelerations estimated. However, in reality, the nature of the DCM means that large errors in the attitude result in small changes in the estimated vertical acceleration. The use of the full DCM means that the only assumption made is that there are small errors in the estimated attitude; small error assumption.

$$r_z = TAS \cos\alpha(q\cos\phi - r\sin\phi) + \sin\theta\frac{d}{dt}(TAS\cos\alpha) + g \tag{4.12}$$

Equation (4.12) is less sensitive to errors in the attitude estimation but contains part of the Euler matrix which relies on an estimation of attitude. Although the estimation of acceleration is less sensitive to errors in attitude it assumes that the aircraft is not performing aggressive manoeuvres.

$$r_z = TAS(q\cos\phi - r\sin\phi) + g \tag{4.13}$$

Equation (4.13) is less sensitive to errors in the attitude estimation but still contains part of the Euler matrix which relies on an estimation of attitude. Both Equation (4.12) and Equation (4.13) contain an implied assumption that the aircraft is operating about the straight and level condition but with Equation (4.12) tolerating higher climb angles.

4.3.1 Verification of Methodologies

To verify these approximations a DOF model of a fixed wing aircraft was created in the MATLAB/Simulink simulation environment as detailed in Chapter 3. A 3D Bow Tie manoeuvre was used as a test, Fig. 4.2. To add complexity to the problem in order to show the relative strengths and weaknesses of the approaches a climb and descent was used in the flight plan. A 3D Bow Tie manoeuver is ideal to use as a control manoeuver as it incorporates all phases of flight; straight and level, climbing, descending, accelerating, decelerating, and turning in both directions. To further add realism representative biases and noise is added to all the sensors. The magnitudes of the biases and noise are chosen to mimic the sensors actual flight test performance. A table of sensor performance is given in Chapter 7. The following simulations are conducted in still air to enable clearer comparison of the results but this is not the case for subsequent chapters.

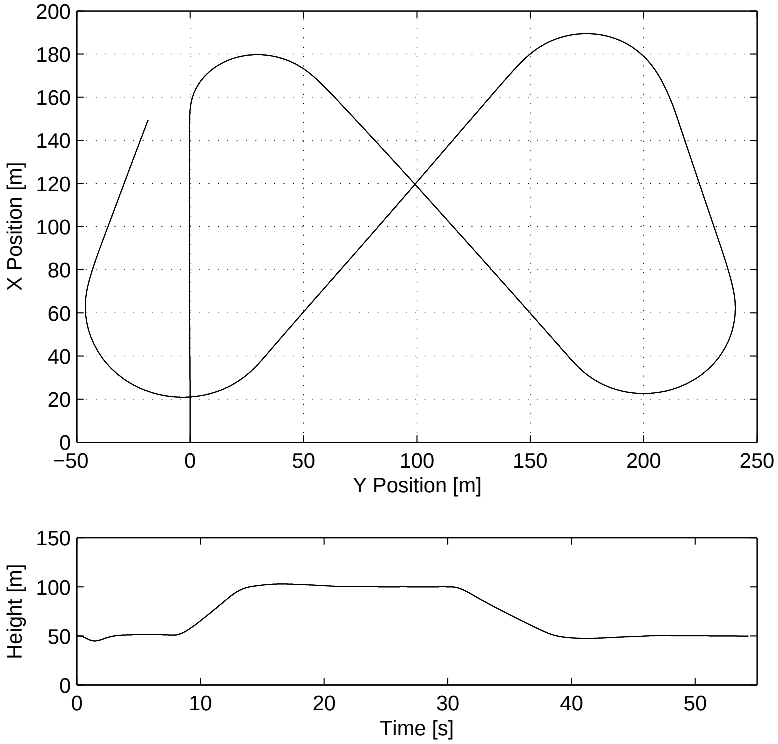

Figure 4.2: Simulated Test Flight

The true global accelerations of the aircraft as estimated in the simulation are compared to the simplified estimated global accelerations of the aircraft below in Fig. 4.3, Fig. 4.4 and Fig. 4.5.

Although the estimation is not perfect, there is a very high degree of correlation between the true and estimated values. There is a slight bias on the r_x as the estimated steady state AoA had a bias introduced for realism. This is reasonable as a small error in this estimation is likely to occur in reality due to approximations in weight and installation angles.

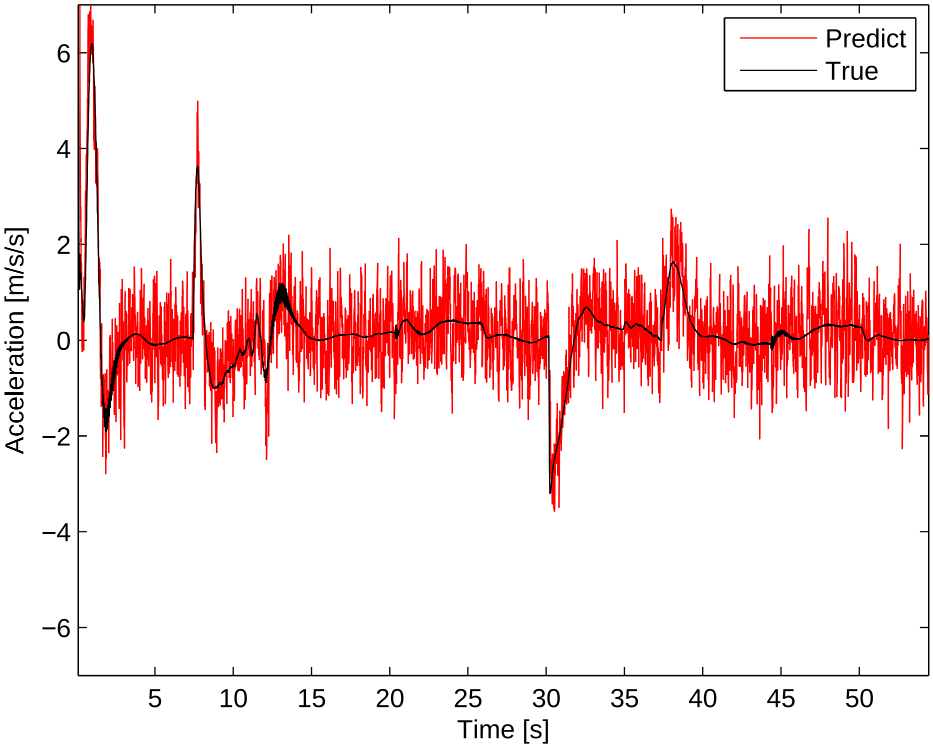

Figure 4.3: Estimation of X Acceleration

Fig. 4.4 shows that the estimated global acceleration tracks the true global acceleration perfectly. Fig. 4.4 displays the same noise power on the estimated readings as Fig. 4.3, although the true acceleration readings are higher, resulting in the noise having a small influence on the results. These properties are of key importance as the global lateral acceleration is the only global acceleration estimation needed when a fully pressure augmented reference attitude is generated. This will be discussed in detail later in this chapter.

Fig. 4.5 shows that the iterative DCM solution displays improved accuracy over the simplified TAS derived global vertical acceleration when the aircraft is climbing. This can be noticed between 12 and 15 seconds in Fig. 4.5. This is to be expected as the TAS derived solution has an implied straight and level assumption. The pressure altitude derived solution is the noisiest but tracks the true value accurately. The pressure altitude estimation will be used to provide a solution to the DCM problem stated but the global vertical acceleration only has a small influence on the air data based attitude estimation, therefore effort

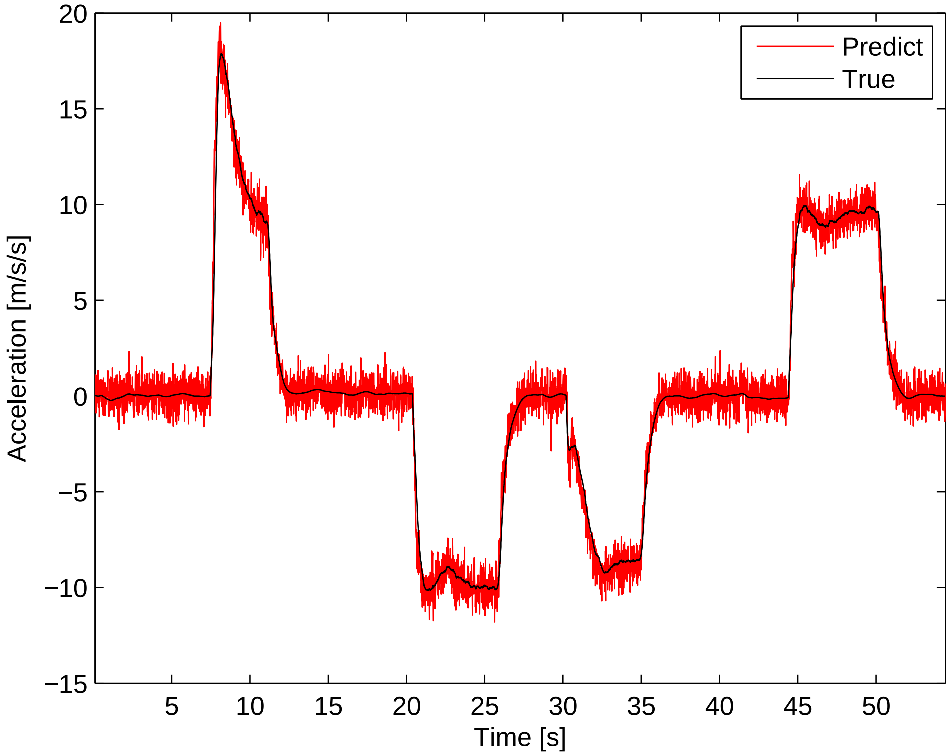

Figure 4.4: Estimation of Y Acceleration

has not been expended providing a better solution for global vertical acceleration estimation. The advantage of using pressure altitude is that it is independent of attitude estimation, therefore providing an extremely robust estimate. The disadvantage of this method is that with the type of sensor used on most UAVs this estimate can be extremely noisy as shown in Fig. 4.5. Filtering of the pressure data will be discussed later in this chapter in Section 4.5.1.

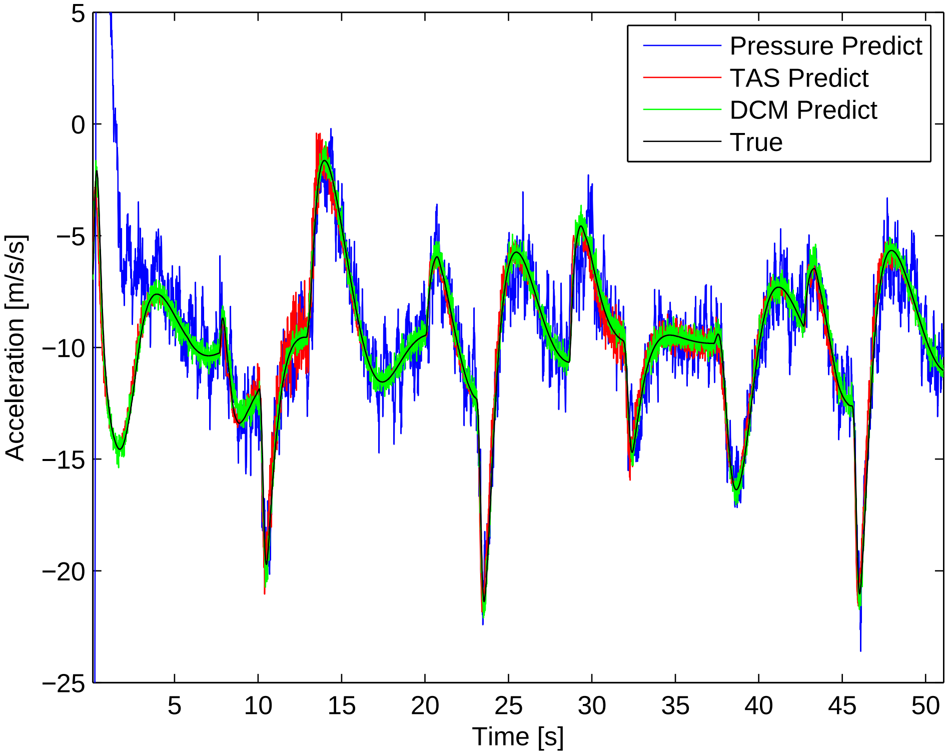

Figure 4.5: Estimation of Z Acceleration

4.4 Solution to the Estimation of Attitude from Accelerations

With an estimation of global acceleration it is possible to solve Equation (4.14) to give attitude, as both the local and global accelerations can either be measured or approximated.

$$[a] = [DCM][r] \tag{4.14}$$

where, local acceleration in $[a] = \begin{bmatrix} a_x & a_y & a_z \end{bmatrix}^T$ and global acceleration is $[r] = \begin{bmatrix} r_x & r_y & r_z \end{bmatrix}^T$. The $[DCM]$ is built up from successive angular transforms.

$$\begin{bmatrix} ox_3 \\ oy_3 \\ oz_3 \end{bmatrix} = \begin{bmatrix} 1 & 0 & 0 \\ 0 & \cos\phi & \sin\phi \\ 0 & -\sin\phi & \cos\phi \end{bmatrix} \begin{bmatrix} ox_2 \\ oy_2 \\ oz_2 \end{bmatrix} \tag{4.15}$$

$$\begin{bmatrix} ox_2 \\ oy_2 \\ oz_2 \end{bmatrix} = \begin{bmatrix} \cos\theta & 0 & -\sin\theta \\ 0 & 1 & 0 \\ \sin\theta & 0 & \cos\theta \end{bmatrix} \begin{bmatrix} ox_1 \\ oy_1 \\ oz_1 \end{bmatrix} \tag{4.16}$$

$$\begin{bmatrix} ox_1 \\ oy_1 \\ oz_1 \end{bmatrix} = \begin{bmatrix} \cos\psi & \sin\psi & 0 \\ -\sin\psi & \cos\psi & 0 \\ 0 & 0 & 1 \end{bmatrix} \begin{bmatrix} ox_0 \\ oy_0 \\ oz_0 \end{bmatrix} \tag{4.17}$$

The gravity component of acceleration readings is assumed to be vertical so the heading of the vehicle cannot be calculated. The heading of the vehicle is assumed to be irrelevant reducing the DCM to the following form.

$$\begin{bmatrix} DCM \end{bmatrix} = \begin{bmatrix} \cos\theta & 0 & -\sin\theta \\ \sin\phi\sin\theta & \cos\phi & \cos\theta\sin\phi \\ \cos\phi\sin\theta & -\sin\phi & \cos\phi\cos\theta \end{bmatrix} \tag{4.18}$$

$$\begin{bmatrix} a_x \\ a_y \\ a_z \end{bmatrix} = \begin{bmatrix} \cos\theta & 0 & -\sin\theta \\ \sin\phi\sin\theta & \cos\phi & \cos\theta\sin\phi \\ \cos\phi\sin\theta & -\sin\phi & \cos\phi\cos\theta \end{bmatrix} \begin{bmatrix} r_x \\ r_y \\ r_z \end{bmatrix} \tag{4.19}$$

With knowledge of both the local and global accelerations Equation (4.19) can be solved for ϕ and θ as follows .

$$\theta = atan\left(\frac{\cos\theta r_x - a_x}{\cos\theta r_z}\right) \tag{4.20}$$

$$r_\theta = r_x \sin\theta + r_z cos\theta \tag{4.21}$$

$$\phi = atan\left(\frac{-\cos\phi r_y - a_y}{\cos\phi r_\theta}\right) \tag{4.22}$$

This solution to the DCM problem is an iterative solution to finding the global Euler angles. As the solution is iterative there may be concerns about stability of the solution when the initial accuracy of the estimations is questionable. To that end it is possible to find an expression for $\cos\theta$ and $\cos\phi$ which is purely based on the perceived accelerations and does not rely on the previous approximation. Suitable approximation for $\cos\theta$ is given below, with a similar solution evident for $\cos\phi$ [11].

$$\cos\theta = \left(\frac{r_x a_x + r_z\sqrt{r_x^2 + r_z^2 - a_x^2}}{r_x^2 + r_z^2} \right) \tag{4.23}$$

$$\cos\phi = \left(\frac{r_y a_y + r_\theta\sqrt{r_x^2 + r_\theta^2 - a_y^2}}{r_y^2 + r_\theta^2} \right) \tag{4.24}$$

$$\theta = atan \left(\frac{\left(\frac{r_x a_x + r_z\sqrt{r_x^2+r_z^2-a_x^2}}{r_x^2+r_z^2}\right) r_x - a_x}{\left(\frac{r_x a_x + r_z\sqrt{r_x^2+r_z^2-a_x^2}}{r_x^2+r_z^2}\right) r_z} \right) \tag{4.25}$$

$$r_\theta = r_x \sin\theta + r_z cos\theta \tag{4.26}$$

$$\phi = atan \left(-\frac{\left(\frac{r_y a_y + r_\theta\sqrt{r_x^2+r_\theta^2-a_y^2}}{r_y^2+r_\theta^2}\right) r_y - a_y}{\left(\frac{r_y a_y + r_\theta\sqrt{r_x^2+r_z^2-a_y^2}}{r_y^2+r_\theta^2}\right) r_\theta} \right) \tag{4.27}$$

There are benefits to both iterative and non-iterative approaches. Iterative approaches typically behave more stably during highly aggressive manoeuvring while non-iterative approaches remove dependencies that in certain circumstances, where the AHRS performance is exceptionally poor, can provide a more reliable reference. These characteristics will be demonstrated later in this chapter.

4.5 Air Data Based Pitch Estimation

An alternative solution to the use of perceived accelerations is to use pressure data to provide a direct estimation of pitch. This can be done by combining the VSI with the TAS and an approximation of the aircraft's AoA.

$$\theta = asin\left(\frac{VSI}{TAS}\right) + \frac{a_z m}{\frac{1}{2}\rho TAS^2 S \frac{dC_L}{d\alpha}} - \alpha_{set} \tag{4.28}$$

This method of using pressure data is not susceptible to singularities in a solution. However there are inaccuracies introduced by the approximations of AoA. The exact performance differences will be discussed with the aid of plots later in this chapter.

4.5.1 Filtering of Air Data

Air data offers many advantages over GNSS Data when used for attitude estimation. Air data can usually be measured at an extremely high sample rate, with 2 kHz plus sample rates used for this project. However in certain circumstances customised or specialist hardware is not available or affordable. In these circumstances where high-quality Analogue to Digital Converters (ADC) are either not affordable or impractical, the air data may be extremely noisy. This was the circumstance discovered in this project. The exact details of the hardware will be given in Chapter 7. To mitigate the sensor noise problem closer integration of the sensors available was utilised. The approach chosen was to use the accelerometers and gyroscopes to augment the pressure sensors as follows in Equation (4.29) and Equation (4.30).

$$TAS = \int \left(k_p(TAS_{ref} - TAS) + \int (k_i(TAS_{ref} - TAS))dt + a_x - g\sin(\theta) \right) dt \tag{4.29}$$

$$\begin{aligned} VSI = \int \Bigg(& k_p(VSI_{ref} - VSI) + \int (k_i(VSI_{ref} - VSI))dt \\ & -a_x \sin(\theta) + a_y \cos(\theta)\sin(\phi) + a_z \cos(\phi)\cos(\theta) + g \Bigg) dt \end{aligned} \tag{4.30}$$

(The VSI has the opposite sign to the Euler velocity notation ,w, or V_z. This is intended to match all existing COTS hardware which usually share American notation which defines up as positive, unlike Euler.)

The effect of Equation (4.29) and Equation (4.30) is to tighten the integration between all of the sensors. At first glance this may appear undesirable as any error in attitude would be compounded in a propagation of error onto the pressure sensors, rendering the entire system unstable, in reality however, because of the nature of the DCM, large attitude errors are necessary to induce meaningful errors onto the air data estimations. To further mitigate the propagation of errors onto the AHRS the filter gains are chosen to force the pressure measurement to dominate the output ensuring stability of the entire system.

4.6 ADAHRS/AHRS Simulation Performance Comparison

This section provides a set of simulation results comparing the classical filter switching techniques purely based on accelerometer and gyroscope data with the air data augmented approach advocated. To do this the simulation model based on the X-Models XCalibur motor glider presented in Chapter 3 will be once again used to investigate the relative performances. To further add realism representative biases and noise is added to all the sensors. The magnitudes of the biases and noise are chosen to mimic the sensors actual flight test performance. A table of sensor performance is given in Chapter 7.

Again a 3D Bow Tie manoeuvre was used as a test as show in Fig. 4.2 because it highlights all the flight phases of interest. For the simulation comparison a simple linear complimentary filter is employed. A linear complimentary filter is used because it is the most likely to be employed on a micro to small UAV that the air data augmented approach presented is designed for. To provide a realistic and meaningful comparison between the approach advocated and existing approaches two approaches will be compared. A relatively modern switch mode filtering technique not using air data augmentation will be compared with a standard complimentary filter and a complimentary filter using air data augmentation.

Before discussing the overall AHRS performance it is useful to review the relative performance of the reference algorithms discussed previously in this chapter. Once these attitude references have effectively been compared their impact on the AHRS accuracy as a whole can then be assessed.

4.6.1 Reference Attitudes

Pitch angle is needed before roll angle can be calculated, it is therefore logical to consider the pitch estimation first. Three methodologies for the estimation of pitch angle will be considered; purely tilt sensing, pressure augmented tilt sensing and the air data based pitch estimation. In order to fully demonstrate the differences between the approaches the approaches will be compared with and without sensor noise present. Fig. 4.6 shows a comparison of the five approaches.

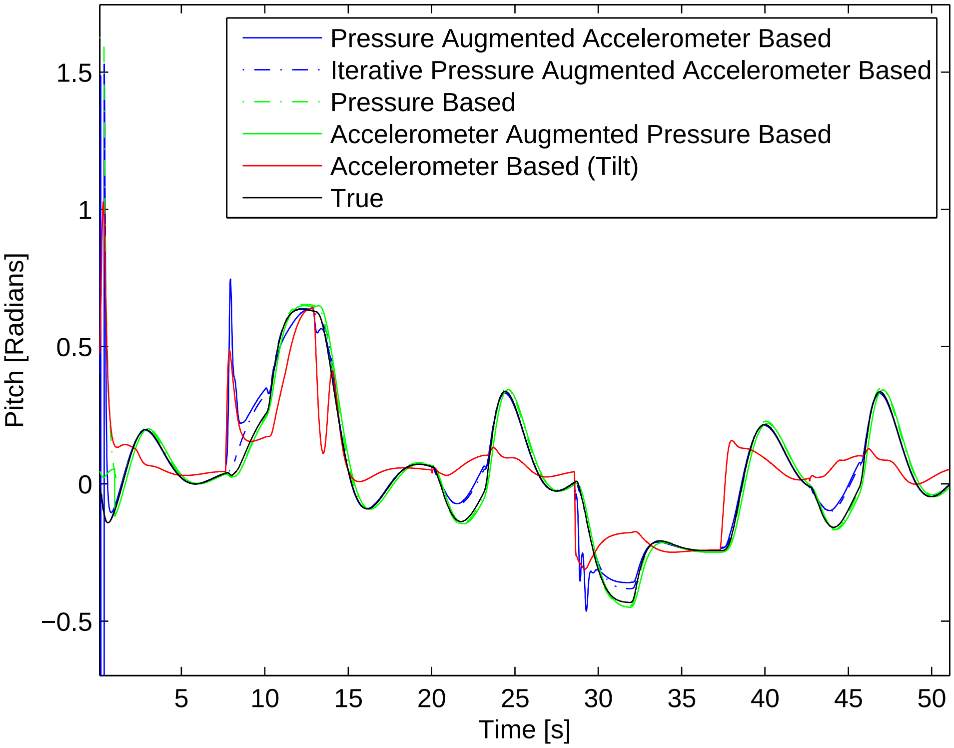

Figure 4.6: Pitch Angle Estimations

It can be clearly seen from Fig. 4.6 that the purely tilt sensing approach is badly affected by aircraft accelerations. The two pressure augmented solutions provide a more accurate reference. The tilt sensing approach gave the worst results with the variance of 58.7 (standard deviation of 7.7 degrees). The accelerometer augmented pressure-based solution gave the best results the variance of 0.7 (standard deviation of 0.8 degrees) over the flight test. The results are summarised in Table 4.1.

Table 4.1: Comparison of Pitch Angle Estimations

Methodology	Variance	Standard Deviation
Accelerometer Based (Tilt)	1.02	0.13 [rad]
Pressure Augmented Accelerometer Based	0.26	0.07 [rad]
Iterative Pressure Aug..Accelerometer Based	0.05	0.028[rad]
Pressure Based	0.6	0.031 [rad]
Accelerometer Augmented Pressure Based	0.012	0.014 [rad]

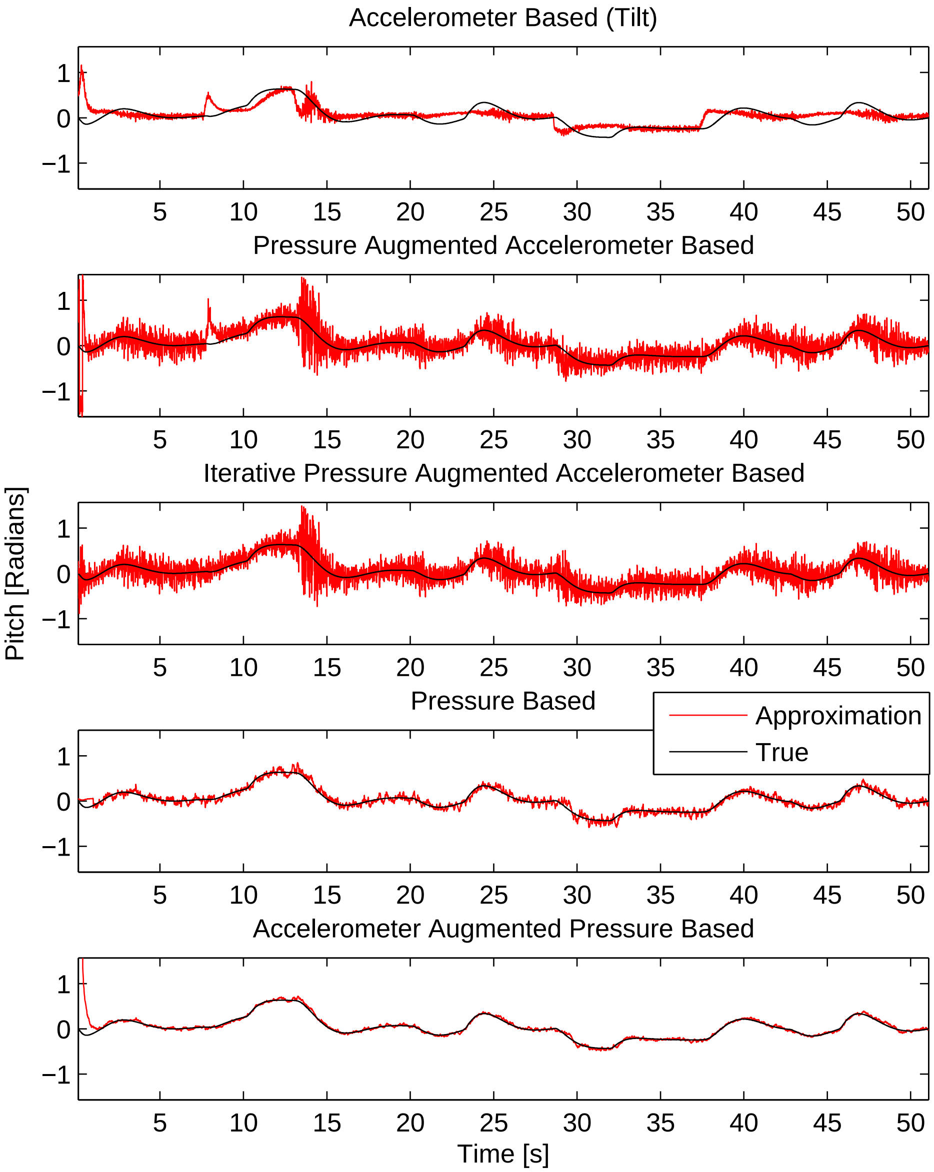

Figure 4.7: Pitch Angle Estimations with Noise Present

Fig. 4.7 shows the effect of the inclusion of noise in the simulation. From Fig. 4.7 it can be seen that the two pressure-based approaches have a much higher noise tolerance.

The reference roll angles are based upon the reference pitch angles and are now discussed. Unfortunately there is no such equivalent method for calculating roll angle purely on pressure measurements so only the purely tilt sensing, pressure augmented accelerometer based approaches will be discussed.

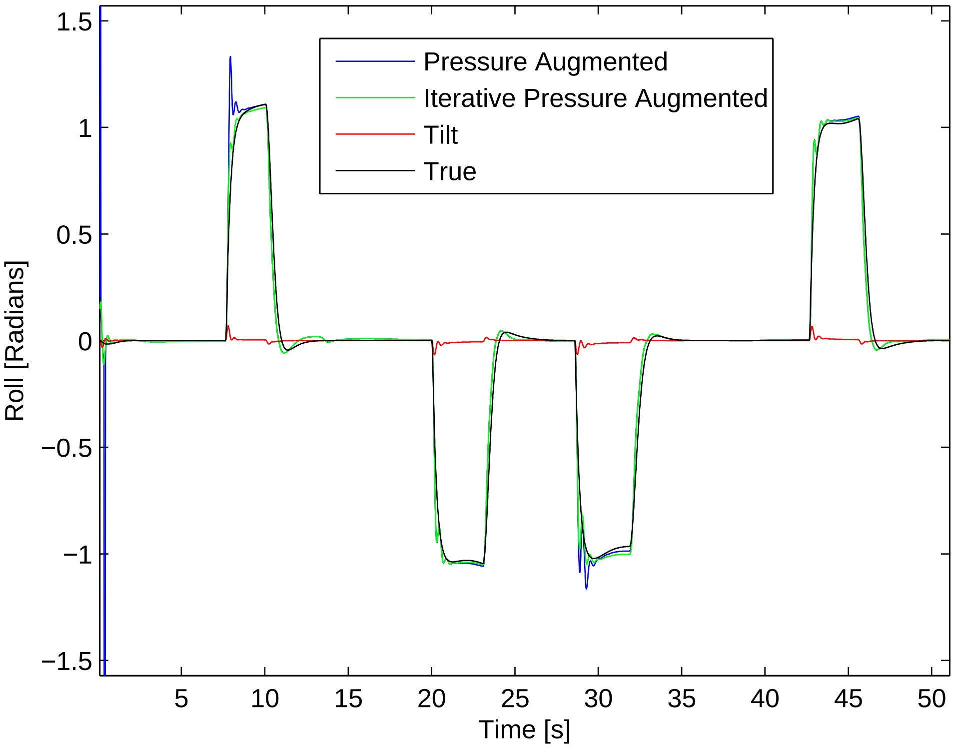

Figure 4.8: Roll Angle Estimations without Noise Present

Fig. 4.8 highlights two important factors that have a strong bearing on the accuracy of the AHRS overall. The first is that the tilt sensing approach is incapable of estimating roll angles correctly. This is due to the fact that the aircraft is reasonably successfully executing balanced turns. This means that there is little lateral acceleration measured, resulting in the tilt sensing approach estimating nominally zero roll regardless of the roll angle. If this data is incorporated into the AHRS system it will cause spiral mode failure, as will be shown later in this chapter. The second important result to be shown by Fig. 4.8 is that the pressure augmented solutions accurately estimate the steady-state roll angles with the iterative approach providing better dynamic stability during climbing and descending turns, as shown at approximately 10 seconds and 30 seconds in Fig. 4.8. The relative accuracy of the three methodologies is shown in Table 4.2.

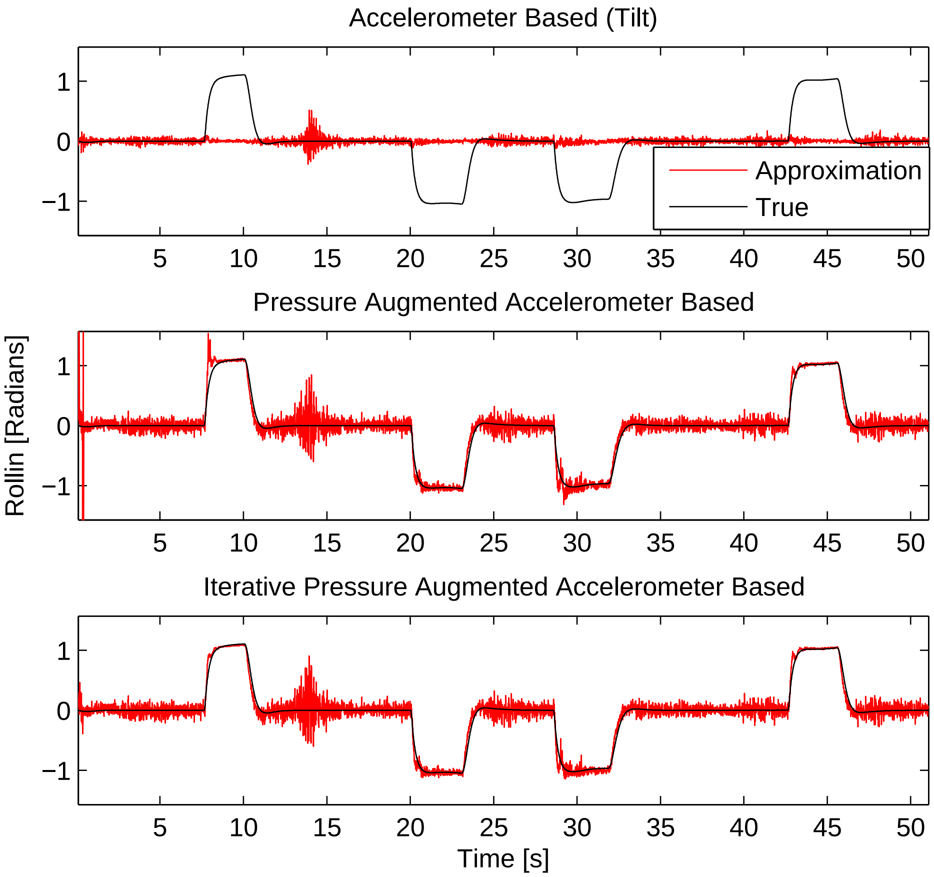

Figure 4.9: Roll Angle estimating with Noise Present

Table 4.2: Comparison of Roll Angle Estimations

Methodology	Variance	Standard Deviation
Accelerometer Based (Tilt)	13.5	0.49 [rad]
Pressure Augmented Accelerometer Based	1.1	0.14[rad]
Iterative Pressure Aug..Accelerometer Based	0.12	0.05 [rad]

Fig. 4.9 shows the effect of sensor noise on the three methodologies. Fig. 4.9 shows reference noise reducing at a higher roll angles. This is not due to a decrease

in actual sensor noise but due to pressure data dominating at the higher turn rates generated by higher roll (or bank) angles. The pressure augmented solutions are more susceptible to the introduction of noise than the purely accelerometer based approach, however the complete lack of useful roll data provided by the purely accelerometer based approach renders this point moot.

4.6.2 Spiral Mode Failure

To emphasise the failure mode it is useful to look at a more strenuous fly pattern; circling flight at high bank angle. To simplify the explanation the switch mode filtering is turned off [62]. With the switch mode filtering turned on the gravity angle would not be used in this scenario meaning the AHRS would solely rely on the gyroscopes. This reliance on the gyroscopes means that the accuracy of the AHRS would steadily degenerate as in the example provided in Section 4.2. With sole reliance on the gyroscopes most flight control architecture are capable of keeping the aircraft airborne for more than 20 minutes, even with very poor AHRS data, however eventual failure of the flight control systems is inevitable. This failure of the flight control systems is unacceptable. The only alternative is to continue with some form of filtering with respect to a reference. The following example seeks to illustrate what would happen if an un-augmented tilt angle was used as the reference angle.

Fig. 4.10 shows a 3-D representation of the spiral mode failure, while Fig. 4.11 shows the reference roll angle provided by the accelerometers along with the gyroscope stabilised output from the AHRS, this allows us to investigate the cause of the failure.

In the simulation presented here the aircraft successfully circled for 30 Seconds before the flight control system was no longer able to compensate for the accumulating errors in the attitude data. The loss of control resulting in a spiral dive is shown in Fig. 4.10.

Fig. 4.11 clearly illustrates what caused the failure. As the aircraft's flight control system initiates a co-ordinated turn lateral acceleration experienced by the on-board accelerometers is negligible. The result of this is that the reference roll angle is consistently lower than the actual roll angle of the aircraft. In this case where the flight control system initiates an accurate coordinated turn the roll reference is negligible. If this diminishing estimation of roll angle is coupled with a controller that is tasked with maintaining a fixed bank angle a spiral

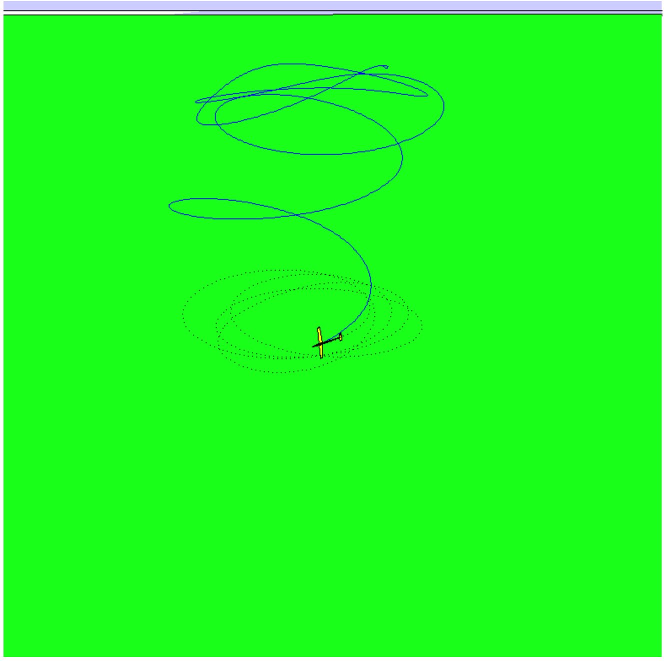

Figure 4.10: Spiral Mode Failure

mode failure will follow. This is a widely understood phenomena and there are approaches to minimising its influence [62] [23]. One promising approach is the use of sliding gain or switch gain filters [62], these detect the accelerated flight condition and dynamically alter the filter coefficients, prolonging stability.

This approach of using tilt derived references with dynamically altering filter coefficients will be now compared with a classical fixed gain complimentary filter type structure that is using air data augmented reference attitudes, as introduced above.

4.6.3 ADAHRS/AHRS Attitudes

The 3D Bow Tie manoeuvre will be used as the test trajectory as show in Fig. 4.2. As in the previous section, pitch angle estimations will be considered first as they are needed as the basis for the roll angle estimations.

Fig. 4.12 shows the relative performance of the two approaches chosen with respect to the actual pitch angles. Fig. 4.12 shows that the classical tilt derived estimation performed remarkably well when compared with augmented solutions. This is because the aircraft does not undergo prolonged longitudinal acceleration for large proportions of the flight.

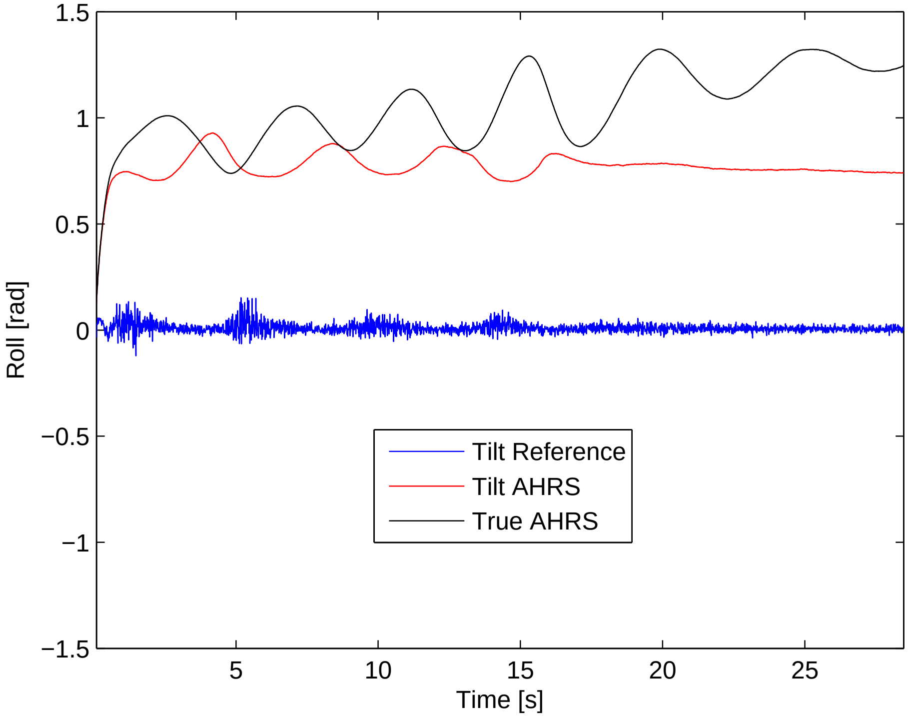

Figure 4.11: Roll Angle Estimations For The Spiral Mode Failure Example

With the use of realistic sensor noise as measured from the autopilot systems employed in this thesis the air data augmented tilt sensing approach provides a pitch accuracy of better than 1.76 degrees standard deviation. The purely tilt sensing approach using sliding gain filtration provides a standard deviation of 4.64° under the test conditions summarised above. If switch mode filtering is not used the standard deviation is greater than 10°.

Fig. 4.13 shows the relative performance of the two approaches chosen with respect to the actual roll angle.

As alluded to in Section 4.2 the purely tilt sensing approach fails to measure any roll angle, this is because the flight control system successfully executes good quality co-ordinated turns; meaning the aircraft does not experience any lateral acceleration.

With the use of realistic sensor noise as measured from the autopilot systems employed in this thesis the air data augmented tilt sensing approach provides a roll accuracy of better than 1.6° standard deviation. The purely tilt sensing approach using sliding gain filtration provides a typical standard deviation of 1.7°

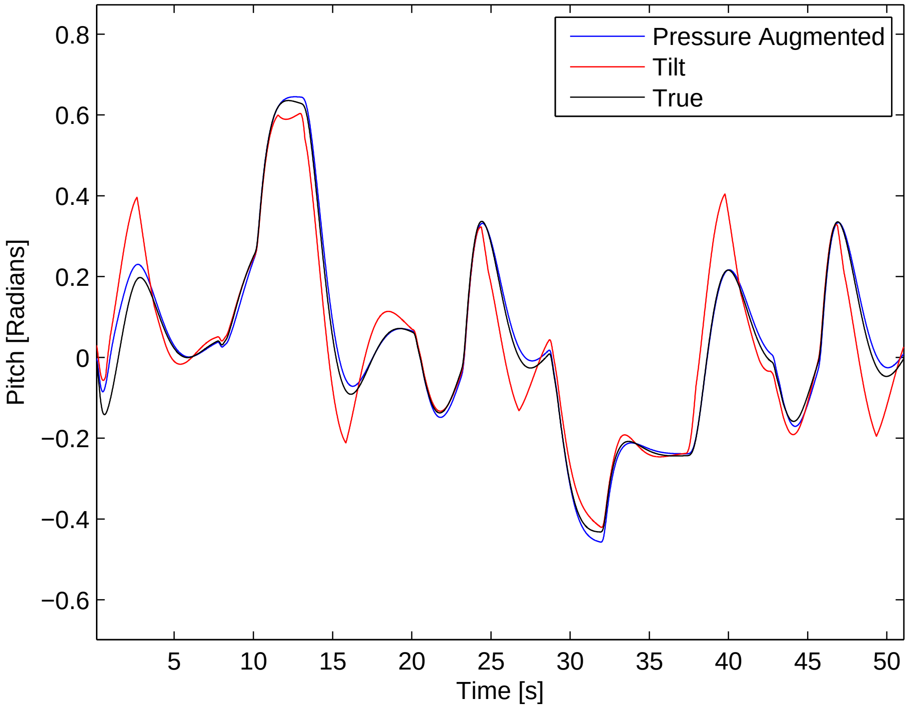

Figure 4.12: AHRS Pitch Angle Estimations

under the test conditions summarised above. If switch mode filtering is not used then the error is greater than 20°.

The performance improvements represent a 60% improvement in pitch and a 5% improvement in roll accuracy over a standard tilt sensing architecture using switch mode filtering.

4.7 Conclusion

This chapter documented the development of an ADAHRS. The continued development of AHRS was justified with specific application on micro to small unmanned aerial vehicles that are required to perform sustained dynamic flight patterns. It was shown that by increasing the coupling between other popular avionic sensors such as airspeed and pressure altitude further improvement in the accuracy of the reference attitude provided to the sensor fusion algorithms can be gained. The increased coupling between on-board sensors was shown to provide a more robust estimate of attitude during continual aggressive manoeu-

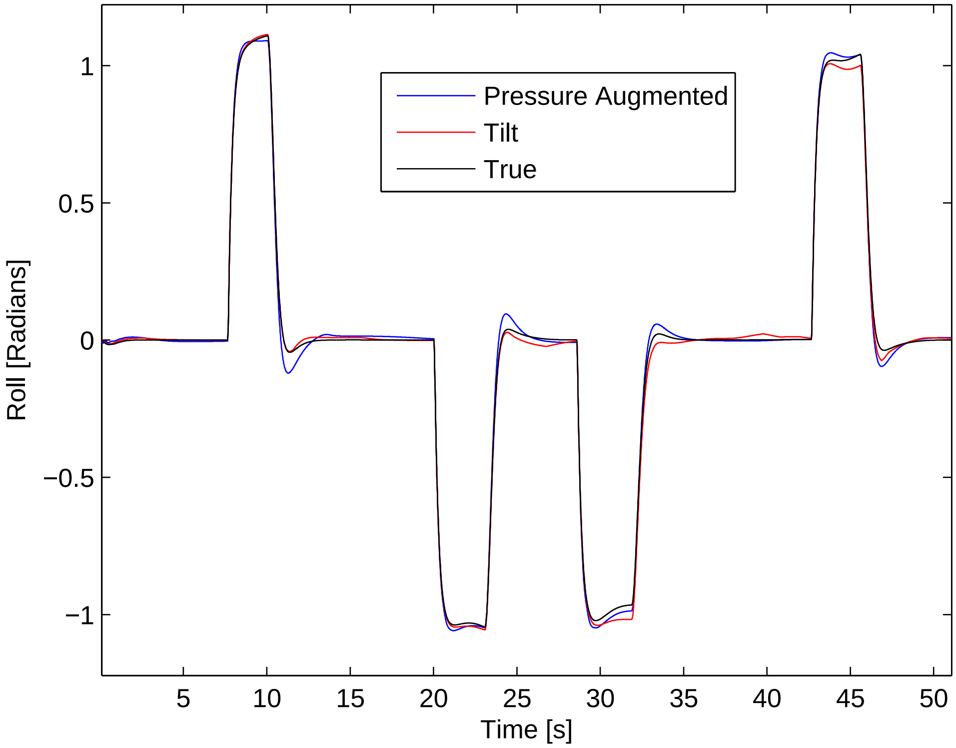

Figure 4.13: AHRS Roll Angle Estimations

vring. A practical iterative solution to the DCM problem was given and analysed in comparison to a non-iterative approach. This showed that the iterative DCM solution was more stable during dynamic flight phases such as rapid changes in climb rate with the associated longitudinal accelerations and pitch angles. The proposed ADAHRS estimation solution was compared with a rival solution that uses switch mode filtering. The continuous constant gain complimentary filter approach using an air data augmented reference angle provided a 60% improvement in pitch and a 5% improvement in roll accuracy over a standard tilt sensing architecture using switch mode filtering when compared using a typical control flight pattern; a Bow Tie flight pattern as shown in Fig. 4.2. This represents a relatively small advantage, however the air data augmented solution provided a stable and accurate AHRS solution in continual dynamic flight where the purely tilt sensing solution would completely fail regardless of filtering type.

The iterative DCM solution along with the air data augmented reference attitudes proposed in this chapter will be the basis of the AHRS attitude estimations provided in Chapter 5. This novel ADAHRS will then be subject to extensive practical testing in Chapter 8.

Chapter 5

A New Closed Loop Kalman-Type Filter

5.1 Introduction

In this chapter the developments in the sensor fusion algorithms are documented in detail. This chapter presents a new closed loop solution to the AHRS sensor fusion problem, as introduced in Chapter 2, that provides good results for a fraction of the computational requirements of a Kalman filter. Exhaustive simulation results are presented comparing the performance of the proposed filter with existing complimentary and Kalman filter type architectures.

Extensive flight testing will be used to evaluate the real world performance of the same range of filters in Chapter 8.

Attention is given to the filters used in the AHRS because the AHRS not only strongly impacts on the flight performance of the aircraft but the computational requirements are unavoidable, impacting on the performance of other systems and in turn the capabilities of the aircraft as a whole. The accuracy of the AHRS also has a strong bearing on the accuracy of the INS thus affecting the navigation systems. Therefore the relative performance and computational burden of the AHRS system is of key importance to all UAVs, and particularly to micro UAVs where computational resources are scarce.

The development of the AHRS will be dealt with in the following sections:

- A local implementation of the complimentary filter is introduced
- Exhaustive simulated flight test validation of the combined AHRS is discussed with the aid of a:

  - Static scenario with large initial angle error and gyroscope bias

  - Dynamic scenario with realistic initial angle error, gyroscope bias and only a short non-dynamic period before a series of manoeuvres

- Key conclusions are drawn and recommendations made before the filters are combined with navigation in Chapter 6 and real world tests are conducted Chapter 8

5.1.1 Critique of the Open Loop Kalman Filtering Approach

The Kalman filter is the standard filter for attitude problems. The Kalman filter is a powerful tool for solving discrete time problems but it has several important drawbacks for practical implementation, particularly on low power microprocessors as found on many micro to small unmanned aerial vehicles. The main problem with the implementation of the Kalman filter is that it involves a matrix inversion. This inversion imposes a considerable computational burden on the small processors used. In addition to the computational burden the matrices are not always immediately solvable, meaning iterative solvers have to be employed introducing indeterminism and numerical instability. None of the above mentioned problems are trivial although modern micro processors are improving all the time. A common solution to these problems is to use simple complimentary filters to fuse data sets. This is an elegant solution with low computational demand but complimentary filters generally represent a significant performance penalty over Kalman filters. Clearly a filter that offers the performance of a Kalman filter while retaining the stability and low computational demand of a complimentary filter is what is desired. The closed loop implementation of a Kalman filter to be discussed provides such a solution. Before introducing the new closed loop derivation of the extended Kalman filter it is useful to derive and discuss the equivalent classical Kalman filters in more detail.

5.2 The Origins of the Filters

All of the filters are derived from the same basic sensor error model of the gyroscopes. As shown below in Equation (5.1).

$$\begin{bmatrix} p_m \\ q_m \\ r_m \end{bmatrix} = \begin{bmatrix} p_t \\ q_t \\ r_t \end{bmatrix} + \begin{bmatrix} p_b \\ q_b \\ r_b \end{bmatrix} + \begin{bmatrix} p_w \\ q_w \\ r_w \end{bmatrix} \tag{5.1}$$

This is a cumbersome expression so notation is introduced such that the gyroscope measurement $\boldsymbol{m} = [\begin{array}{ccc} p_m & q_m & r_m \end{array}]^T$ is made up of the actual local angular rate $\boldsymbol{u} = [\begin{array}{ccc} p_t & q_t & r_t \end{array}]^T$, a bias $\boldsymbol{b} = [\begin{array}{ccc} p_b & q_b & r_b \end{array}]^T$ and a noise term $\boldsymbol{w} = [\begin{array}{ccc} p_w & q_w & r_w \end{array}]^T$. It is also convenient to introduce the global attitude $\boldsymbol{x} = [\begin{array}{ccc} \phi & \theta & \psi \end{array}]^T$ at this stage.

This can then be built on to find an appropriate model for the Euler angle approximations. As shown below in Equation (5.2)

$$\boldsymbol{x} = E(\boldsymbol{x})\,(\boldsymbol{m} - \boldsymbol{b}) \tag{5.2}$$

where $E(\boldsymbol{x})$ is the Euler translation matrix given in Equation (5.3).

$$E(\boldsymbol{x}) = \begin{bmatrix} 1 & \cos(\phi)\tan(\theta) & \sin(\phi)\tan(\theta) \\ 0 & \cos(\phi) & -\sin(\phi) \\ 0 & \sin(\phi)\sec(\theta) & \cos(\phi)\sec(\theta) \end{bmatrix} \tag{5.3}$$

The measurement model used is based upon inferred gravitational accelerations to ascertain where vertical is with respect to the aircraft. Gravitational acceleration cannot be used to calculate the heading of the aircraft so magnetometer readings are combined to provide a measurement of heading.

$$\begin{bmatrix} a_x \\ a_y \\ a_z \\ \psi \end{bmatrix} = HX + v_w \tag{5.4}$$

The H is used to relate the measurement to the attitude estimation. This H matrix is derived from the DCM as in Equation (5.5). X is the state vector and

w and v are the process and measurement noise vector respectively.

$$\left[DCM\right] = \begin{bmatrix} \cos\theta & 0 & -\sin\theta \\ \sin\phi\sin\theta & \cos\phi & \cos\theta\sin\phi \\ \cos\phi\sin\theta & -\sin\phi & \cos\phi\cos\theta \end{bmatrix} \tag{5.5}$$

This results in the measurement equation taking the form shown in Equation (5.6).

$$z = \begin{bmatrix} -g\sin\theta \\ g\cos\theta\sin\phi \\ g\cos\phi\cos\theta \\ \psi \end{bmatrix} + v_w \tag{5.6}$$

The exact formulation of the X, A, H matrices will be dealt with in detail for the specific filter types in the following sections.

5.2.1 Linear Kalman Filter

As can be seen from Equation (5.2) and Equation (5.3), in the previous section, the dynamics of the system dealt with here can be strongly non-linear. However if the assumption that the aircraft is at low roll and pitch angles is used it is possible to partially linearise the problem. Key parts of the problem cannot be linearised without losing a significant amount of accuracy. It is therefore necessary to reformulate the filter as an error model filter before linearisation. A typical structural layout of an error model Kalman filter is shown next in Fig. 5.1.

This filter is based upon a small angle approximation meaning that local and global angular rates are assumed to be equal, as shown below in Equation (5.7).

$$\begin{bmatrix} \dot\phi \\ \dot\theta \\ \dot\psi \end{bmatrix} \approx \begin{bmatrix} p_m \\ q_m \\ r_m \end{bmatrix} \tag{5.7}$$

This assumption is evidently of questionable validity for aggressive manoeuvres but is a common assumption made in many filter techniques.

The linear Kalman process model and sensor model are as follows in Equation

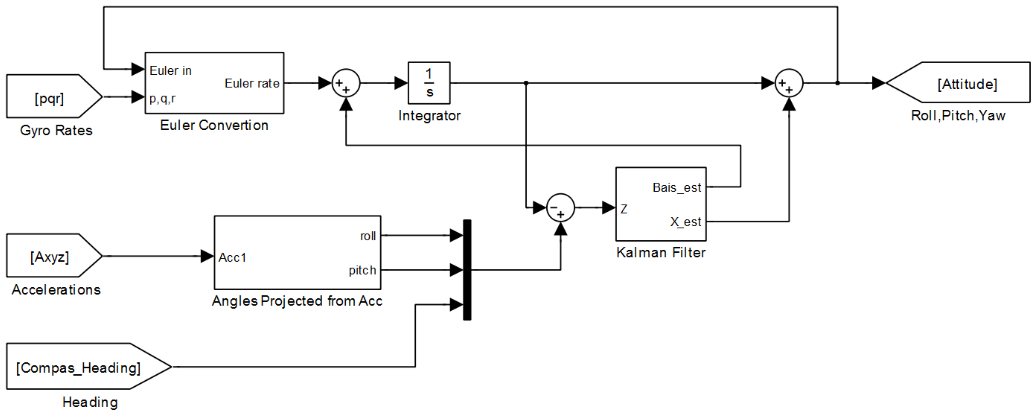

Figure 5.1: Linear Kalman Filter Structure

(5.8), and Equation (5.9).

$$\begin{bmatrix} \dot{\Delta\phi} \\ \dot{\Delta\theta} \\ \dot{\Delta\psi} \\ \dot{p}_b \\ \dot{q}_b \\ \dot{r}_b \end{bmatrix} = \begin{bmatrix} 0 & 0 & 0 & 1 & 0 & 0 \\ 0 & 0 & 0 & 0 & 1 & 0 \\ 0 & 0 & 0 & 0 & 0 & 1 \\ 0 & 0 & 0 & 0 & 0 & 0 \\ 0 & 0 & 0 & 0 & 0 & 0 \\ 0 & 0 & 0 & 0 & 0 & 0 \end{bmatrix} \begin{bmatrix} \Delta\phi \\ \Delta\theta \\ \Delta\psi \\ p_b \\ q_b \\ r_b \end{bmatrix} + \begin{bmatrix} 1 & 0 & 0 & 0 & 0 & 0 \\ 0 & 1 & 0 & 0 & 0 & 0 \\ 0 & 0 & 1 & 0 & 0 & 0 \\ 0 & 0 & 0 & 1 & 0 & 0 \\ 0 & 0 & 0 & 0 & 1 & 0 \\ 0 & 0 & 0 & 0 & 0 & 1 \end{bmatrix} w(t) \tag{5.8}$$

$$z(t) = \begin{bmatrix} 1 & 0 & 0 & 0 & 0 & 0 \\ 0 & 1 & 0 & 0 & 0 & 0 \\ 0 & 0 & 1 & 0 & 0 & 0 \end{bmatrix} \begin{bmatrix} \Delta\phi \\ \Delta\theta \\ \Delta\psi \\ p_b \\ q_b \\ r_b \end{bmatrix} + \begin{bmatrix} 1 & 0 & 0 \\ 0 & 1 & 0 \\ 0 & 0 & 1 \end{bmatrix} v(t) \tag{5.9}$$

5.2.2 Extended Kalman Filter

The EKF does not need to be an error model filter as the linear Kalman filter has to be. The EKF structure is a simple open loop implementation as shown in Fig. 5.2 this is because of the recursive nature of the filter itself combined with the fact that the filter is capable of handling all the non-linearities.

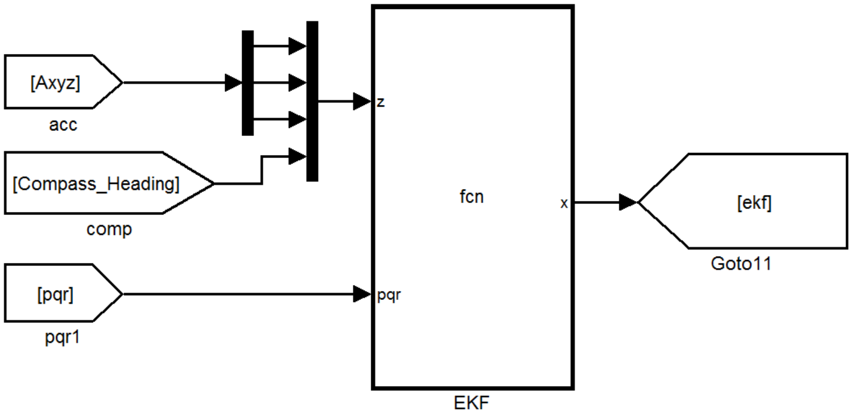

Figure 5.2: Extended Kalman Filter Structure

Expanding Equation (5.1) it is possible to obtain a more useful expression of the gyroscope model that can be used to build a process model.

$$\dot{\boldsymbol{x}} = E(\boldsymbol{x})\left(\boldsymbol{m} - \boldsymbol{b}\right) - E(\boldsymbol{x})\boldsymbol{w} \tag{5.10}$$

The state vector is chosen as follows in Equation (5.11).

$$X = \begin{bmatrix} \phi \\ \theta \\ \psi \\ p_b \\ q_b \\ r_b \end{bmatrix} = \begin{bmatrix} \boldsymbol{x} \\ \boldsymbol{b} \end{bmatrix} \tag{5.11}$$

The EKF process model and sensor model are as follows in Equation (5.12) and Equation (5.13).

$$\dot{X} = \begin{bmatrix} 0_{3x3} & E(\boldsymbol{x}) \\ 0_{3x3} & 0_{3x3} \end{bmatrix} X + \begin{bmatrix} E(\boldsymbol{x})\boldsymbol{m} \\ 0_{1x3} \end{bmatrix} - \begin{bmatrix} E(\boldsymbol{x})\boldsymbol{w} \\ \boldsymbol{b} \end{bmatrix} \tag{5.12}$$

$$z = \begin{bmatrix} -g\sin\theta \\ g\cos\theta\sin\phi \\ g\cos\phi\cos\theta \\ \psi \end{bmatrix} + \begin{bmatrix} v_{a_x} \\ v_{a_y} \\ v_{a_z} \\ v_\psi \end{bmatrix} \tag{5.13}$$

The UKF uses the same process and measurement models as an EKF.

5.2.3 The Derivation of a Closed Loop Extended Kalman Filter

Given the attitude $\boldsymbol{x} = [\ \phi \quad \theta \quad \psi\ ]^T$ as the state, gyroscope reading $\boldsymbol{m} = [\ p \quad q \quad r\ ]^T$ as the input, and accelerometer reading plus the compass reading $\boldsymbol{y} = [\ a_x \quad a_y \quad a_z \quad \psi_m\ ]^T$ as the output, the system can be written as

$$\dot{\boldsymbol{x}} = E(\boldsymbol{x})(\boldsymbol{m} - \boldsymbol{b}) \tag{5.14}$$

$$\dot{\boldsymbol{b}} = 0 \tag{5.15}$$

$$\boldsymbol{y} = h(\boldsymbol{x}) \tag{5.16}$$

where $\boldsymbol{b}$ is the bias for the gyroscopes and gyroscope measurement contains true angular rates $\boldsymbol{u}$ and bias $\boldsymbol{b}$, such that $\boldsymbol{m} = \boldsymbol{u} + \boldsymbol{b}$. The matrix $E(\boldsymbol{x})$ is

$$E(\boldsymbol{x}) = \begin{bmatrix} 1 & \sin\phi\tan\theta & \cos\phi\tan\theta \\ 0 & \cos\phi & -\sin\phi \\ 0 & \sin\phi\sec\theta & \cos\phi\sec\theta \end{bmatrix} \tag{5.17}$$

and the matrix $h(\boldsymbol{x})$ is

$$h(\boldsymbol{x}) = \begin{bmatrix} -g\sin\theta \\ g\cos\theta\sin\phi \\ g\cos\theta\cos\phi \\ \psi \end{bmatrix} \tag{5.18}$$

For the above system, an observer can be given as

$$\dot{\hat{\boldsymbol{x}}} = E(\hat{\boldsymbol{x}})(\boldsymbol{m} - \hat{\boldsymbol{b}}) + K_1(\hat{\boldsymbol{x}})(\boldsymbol{y} - h(\hat{\boldsymbol{x}})) \tag{5.19}$$

$$\dot{\hat{\boldsymbol{b}}} = K_2(\hat{\boldsymbol{x}})(\boldsymbol{y} - h(\hat{\boldsymbol{x}})) \tag{5.20}$$

where

$$\hat{\boldsymbol{b}} = \int K_2(\hat{\boldsymbol{x}})(\boldsymbol{y} - h(\hat{\boldsymbol{x}}))\,\mathrm{d}t \tag{5.21}$$

The observer dynamics can be further expressed as

$$\dot{\hat{\boldsymbol{x}}} = E(\hat{\boldsymbol{x}})\boldsymbol{m} - E(\hat{\boldsymbol{x}}) \int K_2(\hat{\boldsymbol{x}})(\boldsymbol{y} - h(\hat{\boldsymbol{x}}))\,\mathrm{d}t + K_1(\hat{\boldsymbol{x}})(\boldsymbol{y} - h(\hat{\boldsymbol{x}})) \tag{5.22}$$

By defining the estimation error

$$\boldsymbol{e} = \boldsymbol{x} - \hat{\boldsymbol{x}} \tag{5.23}$$

$$\boldsymbol{e}_b = \boldsymbol{b} - \hat{\boldsymbol{b}} \tag{5.24}$$

the error dynamics can be obtained, such that

$$\dot{\boldsymbol{e}} = [E(\hat{\boldsymbol{x}}) - E(\boldsymbol{x})]\boldsymbol{u} - E(\hat{\boldsymbol{x}})\boldsymbol{e}_b - K_1(\hat{\boldsymbol{x}})[h(\boldsymbol{x}) - h(\hat{\boldsymbol{x}})] \tag{5.25}$$

$$\dot{\boldsymbol{e}}_b = -K_2(\hat{\boldsymbol{x}})[h(\boldsymbol{x}) - h(\hat{\boldsymbol{x}})] \tag{5.26}$$

Linearising $h(\boldsymbol{x})$ around $\hat{\boldsymbol{x}}$ yields

$$h(\boldsymbol{x}) \approx h(\hat{\boldsymbol{x}}) + \left.\frac{\partial h}{\partial \boldsymbol{x}}\right|_{\hat{\boldsymbol{x}}} (\boldsymbol{x} - \hat{\boldsymbol{x}}) = h(\hat{\boldsymbol{x}}) + H(\hat{\boldsymbol{x}})\boldsymbol{e} \tag{5.27}$$

where

$$H(\hat{\boldsymbol{x}}) = \begin{bmatrix} 0 & -g\cos\hat{\theta} & 0 \\ g\cos\hat{\phi}\cos\hat{\theta} & -g\sin\hat{\theta}\sin\hat{\phi} & 0 \\ -g\sin\hat{\phi}\cos\hat{\theta} & -g\sin\hat{\theta}\cos\hat{\phi} & 0 \\ 0 & 0 & 1 \end{bmatrix} \tag{5.28}$$

By substituting Equation (5.27) into Equation (5.25) and assuming angular rate $\boldsymbol{u} \approx 0$, it follows that

$$\begin{bmatrix} \dot{\boldsymbol{e}} \\ \dot{\boldsymbol{e}}_b \end{bmatrix} = \begin{bmatrix} -K_1(\hat{\boldsymbol{x}})H(\hat{\boldsymbol{x}}) & -E(\hat{\boldsymbol{x}}) \\ -K_2(\hat{\boldsymbol{x}})H(\hat{\boldsymbol{x}}) & 0 \end{bmatrix} \begin{bmatrix} \boldsymbol{e} \\ \boldsymbol{e}_b \end{bmatrix} \tag{5.29}$$

Since the state matrix is not a triangular matrix, a Lyapunov candidate function is used instead of using traditional eigenvalue techniques, as follows.

$$V = \frac{1}{2}(\boldsymbol{e}^T\boldsymbol{e} + \boldsymbol{e}_b^T\boldsymbol{e}_b) \tag{5.30}$$

Assuming $K_1(\hat{\boldsymbol{x}})H(\hat{\boldsymbol{x}})$ is symmetric, the Lyapunov candidate functions derivative can be written as follows.

$$\begin{aligned}\dot{V} &= \boldsymbol{e}^T\left[-K_1(\hat{\boldsymbol{x}})H(\hat{\boldsymbol{x}})\boldsymbol{e} - \frac{E^T(\hat{\boldsymbol{x}})+E(\hat{\boldsymbol{x}})}{2}\boldsymbol{e}_b\right] + \boldsymbol{e}_b^T\left[-\frac{K_2(\hat{\boldsymbol{x}})H(\hat{\boldsymbol{x}})+H^T(\hat{\boldsymbol{x}})K_2^T(\hat{\boldsymbol{x}})}{2}\boldsymbol{e}\right] \\ &= -\boldsymbol{e}^T K_1(\hat{\boldsymbol{x}})H(\hat{\boldsymbol{x}})\boldsymbol{e} - \boldsymbol{e}_b^T\frac{[E(\hat{\boldsymbol{x}})+K_2(\hat{\boldsymbol{x}})H(\hat{\boldsymbol{x}})]+[E(\hat{\boldsymbol{x}})+K_2(\hat{\boldsymbol{x}})H(\hat{\boldsymbol{x}})]^T}{2}\boldsymbol{e}\end{aligned} \tag{5.31}$$

From Equation (5.28), it can be found that the "left inverse" of $H(\boldsymbol{x})$ is

$$H^+(\boldsymbol{x}) = \begin{bmatrix} 0 & \cos\phi\cos\theta & -\sin\phi\cos\theta & 0 \\ -\cos\theta & 0 & 0 & 0 \\ 0 & 0 & 0 & g\cos^2\theta \end{bmatrix}\frac{1}{g\cos^2\theta} \tag{5.32}$$

such that $H^+H = \text{diag}\{1, 1, 1\}$. Therefore, it is possible to design

$$K_1(\hat{\boldsymbol{x}}) = \begin{bmatrix} k_{11} & 0 & 0 \\ 0 & k_{12} & 0 \\ 0 & 0 & k_{13} \end{bmatrix} H^+(\boldsymbol{x}) \tag{5.33}$$

so that the first term in Equation (5.31) is negative when $\|\boldsymbol{e}\| > 0$. It is also possible to design

$$K_2(\hat{\boldsymbol{x}}) = -E(\hat{\boldsymbol{x}})H^+(\hat{\boldsymbol{x}}) \tag{5.34}$$

such that the second term is equal to zero and $\dot{V} \leq 0$. This suggests state $\dot{V}$ tends to zero with time according to Barbalat's lemma, so that $\boldsymbol{e}$ tending to zero. Again, by using Barbalat's lemma, as $\boldsymbol{e} \to 0$ and $\dot{e}$ is continuous, it can be shown from Equation (5.29) that $\boldsymbol{e}_b \to 0$.

This filter can be linearised about the straight and level point to give a linear version of the filter.

$$H^+(\boldsymbol{x}) = \begin{bmatrix} 0 & 1 & 0 & 0 \\ -1 & 0 & 0 & 0 \\ 0 & 0 & 0 & 1 \end{bmatrix} \tag{5.35}$$

$$K_1(\hat{\boldsymbol{x}}) = \begin{bmatrix} k_{11} & 0 & 0 \\ 0 & k_{12} & 0 \\ 0 & 0 & k_{13} \end{bmatrix} H^{+}(\boldsymbol{x}) \tag{5.36}$$

$$E(\boldsymbol{x}) = \begin{bmatrix} 1 & 0 & 0 \\ 0 & 1 & 0 \\ 0 & 0 & 1 \end{bmatrix} \tag{5.37}$$

$$K_2(\hat{\boldsymbol{x}}) = -E(\hat{\boldsymbol{x}})H^{+}(\hat{\boldsymbol{x}}) \tag{5.38}$$

This filter structure can be visualised as follows in Fig. 5.3.

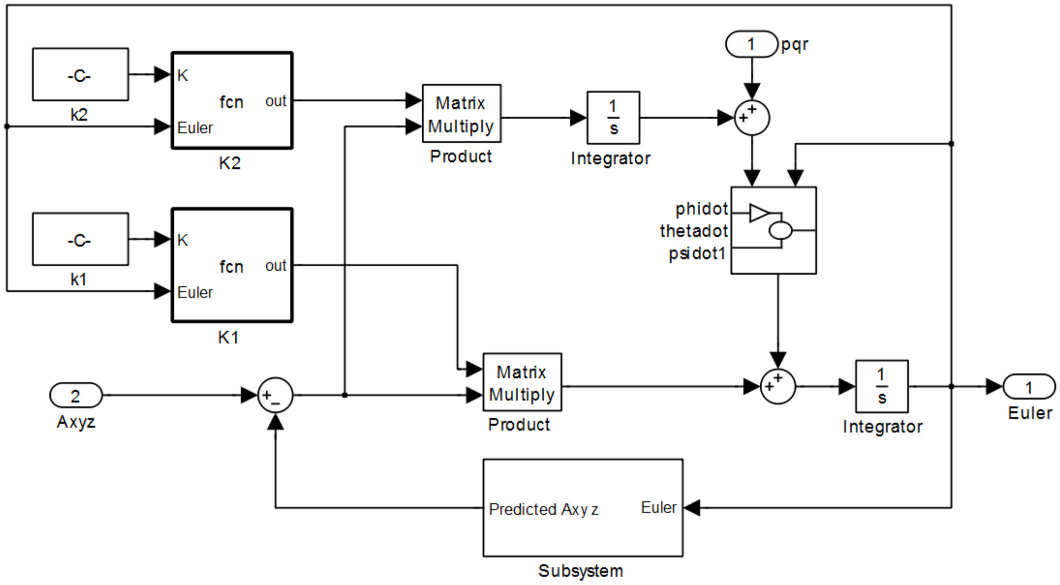

Figure 5.3: Constant Gain Closed Loop Kalman Structure

5.2.4 Local Implementation of the Complimentary Filter

The standard complimentary filter does not take into account attitude when forming its estimations.

The first and most profound consequence of the filter not taking into account the attitude is that the gyroscope biases are computed globally. This problem originates from the assumption that the aircraft is approximately level for the majority of the flight. However for circling (soaring) aircraft this assumption is not valid as the aircraft may be in a continuous high bank turn for many minutes. This can introduced instabilities in the filter as will be shown.

The second effect of not considering attitude and computing in the global axes is the introduction of filter inertia. This second issue is more pronounced when the aircraft is undergoing dynamic manoeuvres. The effect of this inertia on the filter will be explained after the effect of the axes conversion is illustrated.

The first problem of the biases being computed without taking into account the orientation of the aircraft can be straightforwardly addressed with the inclusion of a DCM before the bias approximation. As the filter structure is essentially of a Proportional Integral (PI) form this raises further questions as to whether the proportional approximation of error should also be computed in the local axes. Although it is possible to calculate the proportional error in the local axes this introduces a profound dependency on the filters approximation of the attitude of the aircraft, this is undesirable as it introduces instability into the filter. It may be noted at this point that the DCM used to calculate the error in the local axes and therefore approximate the biases on the gyroscopes also introduces an instability but this is effectively damped by the proportionality of the filter and therefore is tolerable. The two different filter structures are illustrated in Fig. 5.4 and Fig. 5.5.

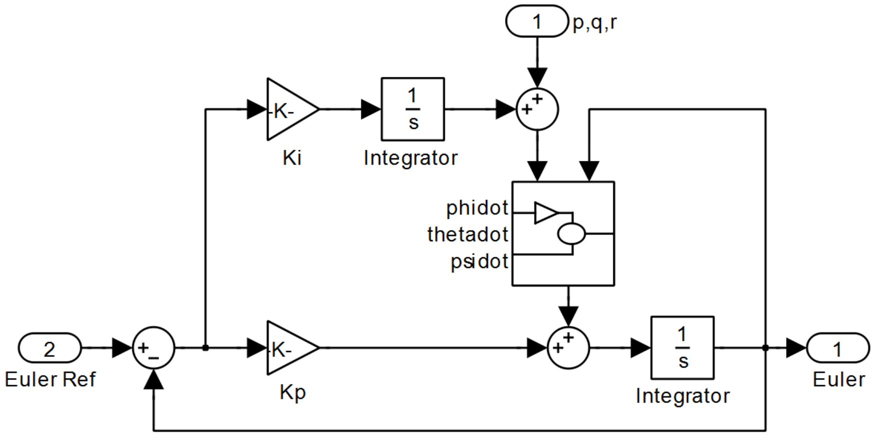

Figure 5.4: Normal Complimentary Filter Structure

To compare the two different filter structures shown above in Fig. 5.4 and Fig. 5.5 two different test conditions are chosen. The first is steady-state flight and the second is a steady-state turn with a bank angle of 1 radian (∼57 degrees). To provide challenging conditions for the filters a bias of 0.1 rad/s is added to all

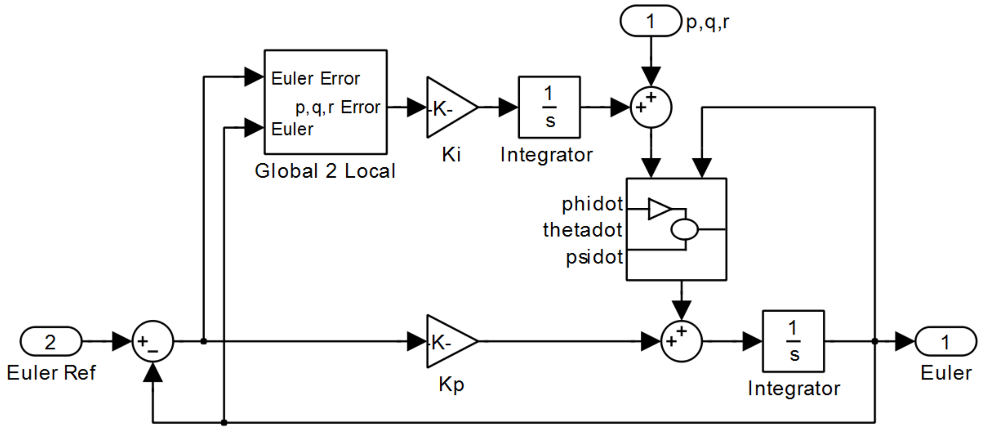

Figure 5.5: Local Complimentary Filter Structure

three gyroscope measurements.

Considering the circling (soaring) condition first, Fig. 5.6 shows that the classical complimentary filter fails to stabilise. This instability only starts to manifest itself at about 0.8 radians (∼45 degrees)

Further investigation reveals that this failure to stabilise is due to the fact that the bias approximations have diverged, as shown below in Fig. 5.7. The local and global biases are mirrored to add clarity to the plot. The true biases were 0.1 rad/s as shown by the dotted reference lines.

This can be contrasted with the performance of the two filters when the aircraft is in straight and level flight, as shown in Fig. 5.8 and Fig. 5.9.

It is also worthy of note that the pitch bias convergence is improved by the use of the localised structure even when in level flight.

The second issue is that the filter has virtual inertia. This inertia can be illustrated as follows:-

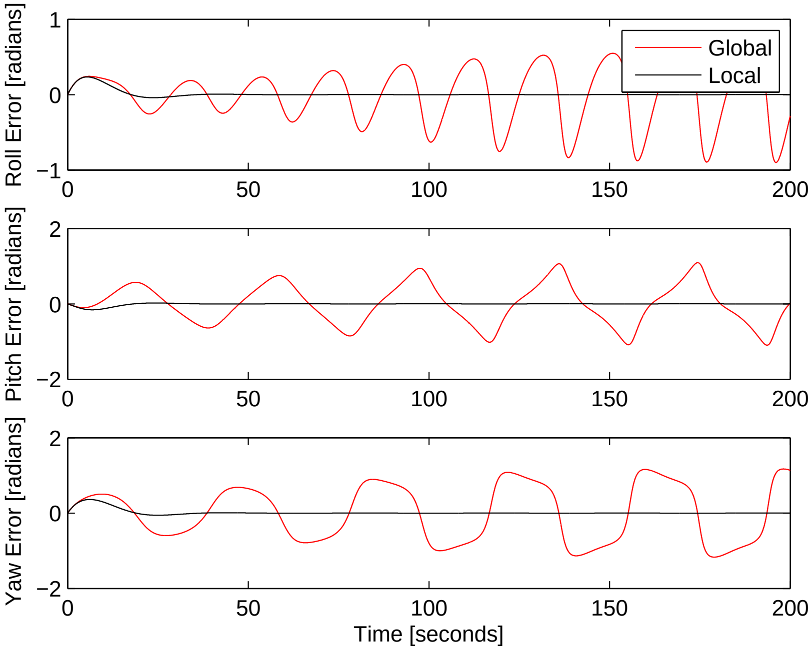

Figure 5.6: Comparison of Global and Local Complimentary Filters in Turning Flight

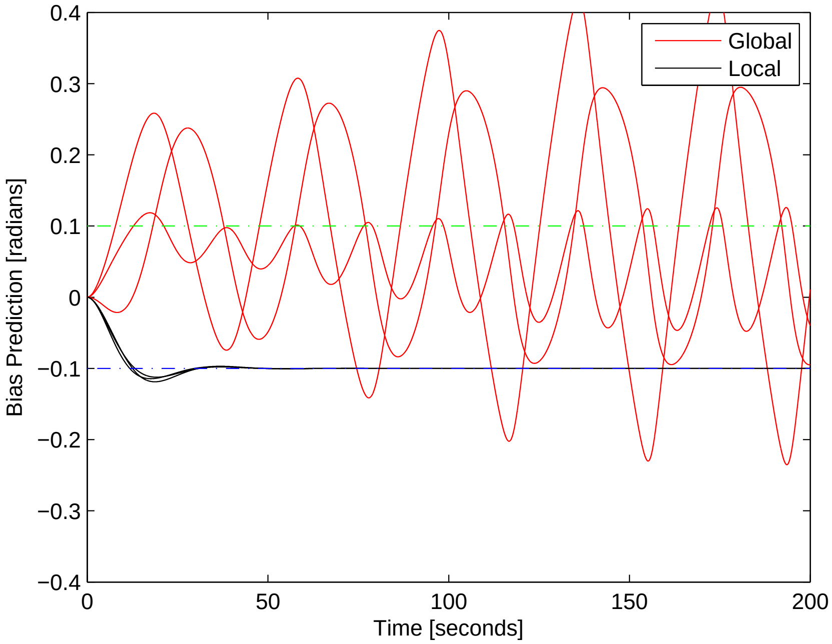

Figure 5.7: Comparison of Global and Local Complimentary Filters biases in Turning Flight

If it is assumed that there is initially no roll, pitch or yaw error with no yaw or pitch bias error but the roll bias is incorrect, this would lead to the roll estimation drifting. Eventually this drift would be constrained by the effect of the proportionality and the roll (p) bias would eventually tend to the correct value, thus eliminating any steady-state error. But if the aircraft yaws through 90 degrees before the effect of the integral can properly estimate the roll bias then there would be a roll error which in the yawing manoeuvre would be translated into a pitch error. As there is no true pitch rate error the proportionality would eliminate this but not before a small amount of wind-up on the pitch (q) bias measurement is produced. In this scenario there was no initial pitch error once the aircraft is yawed through 90 degrees so the roll error will be greatly reduced if not eliminated, this in turn has the effect of extending the amount of time needed for the bias estimate to converge.

Although the scenario above is highly contrived it serves to illustrate how the stability of the bias estimate and attitude estimate are affected by angular rotations. This effect is small and is usually ignored but stop the global implementation of the complementary filter stabilising in high bank angle turns.

For the many reasons provided above the local form of the complimentary filter as shown in Fig. 5.5 will be employed in the comparison of the filters that will follow.

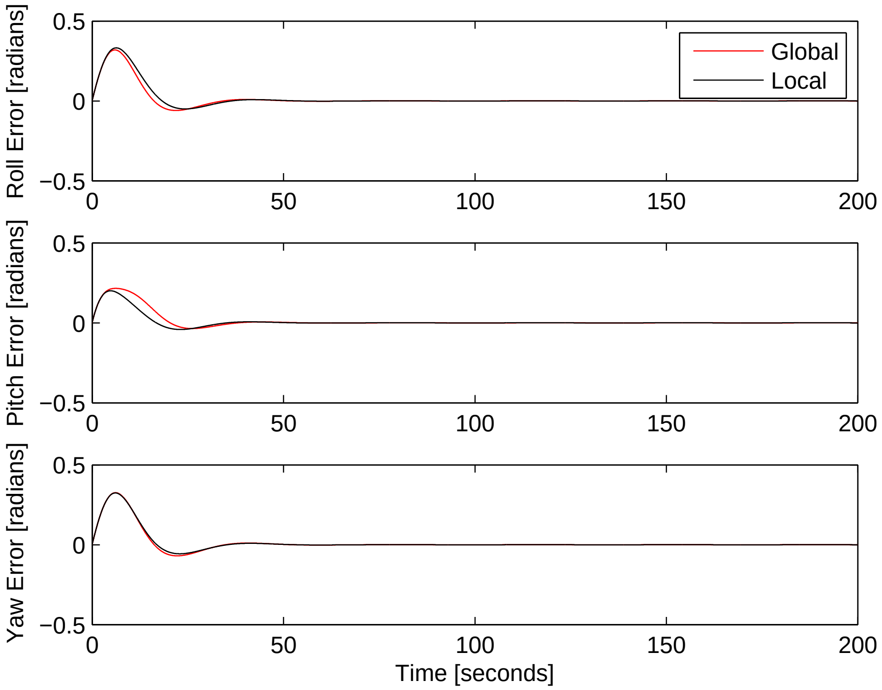

Figure 5.8: Stationary Comparison of Global and Local Complimentary Filters

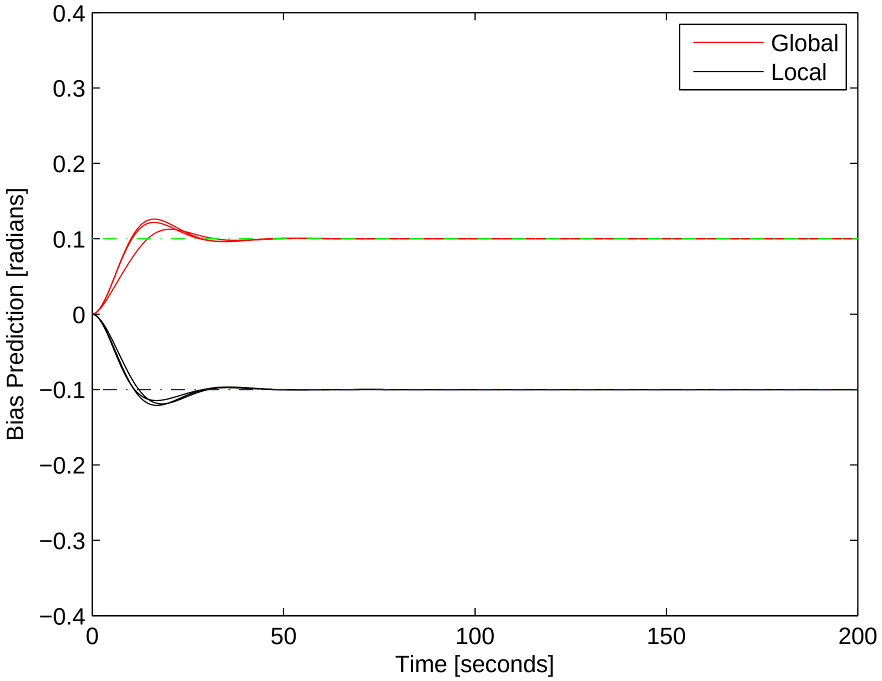

Figure 5.9: Stationary Comparison of Global and Local Complimentary Filters biases

5.3 Simulation Set-up

In order to evaluate the proposed filters, a common simulation and practical test is proposed. In order to rigorously test the stability of the algorithms a stationary bench test with large initial error (∼30 degrees) and bias (∼9 degrees/second)is employed. In order to facilitate the practical validation of the simulation results presented in this chapter a flight test is chosen that is easily repeatable in reality to allow a comparative set of results to be produced in Chapter 8. The flight test hardware facility is introduced in more detail in Chapter 7. It was therefore decided to use a pattern that can encapsulate a mixture of operational requirements and practical testing constrains. Due to UK air law UAVs are required to stay relativity low and close to the operator. This means that there is limited opportunity to let the AHRS settle before starting accelerated manoeuvres like circling. The test chosen is that of a short straight take-off followed by a clockwise circling assent, followed by an anticlockwise loiter. Both the climb and loiter will be done at high bank angles (∼60 degrees). Fig. 5.10 show the proposed flight pattern. This scenario although being extremely demanding is quite representative of a hurried flight, most typical of the launch of a backpack style aircraft, like the Raven or the Squall, as shown in Fig. 5.11. It also has bearing on all other aircraft as all are required to perform tight turns.

5.4 Simulation Results

This subsection deals with the detailed comparison of the filters highlighted so far in this chapter.

5.4.1 Attitude Reference Problem

As dealt with in Chapter 4 the problem of attaining accurate reference attitudes from accelerometer data is non-trivial. The following simulations assume that the filters have access to good, but not perfect, reference data as derived in Chapter 4.

This reference data takes a different form for the different filters. The reference either provides globally corrected accelerometer data or reference angles. It is noted that these accelerations and angles are not just based on the accelerometer readings.

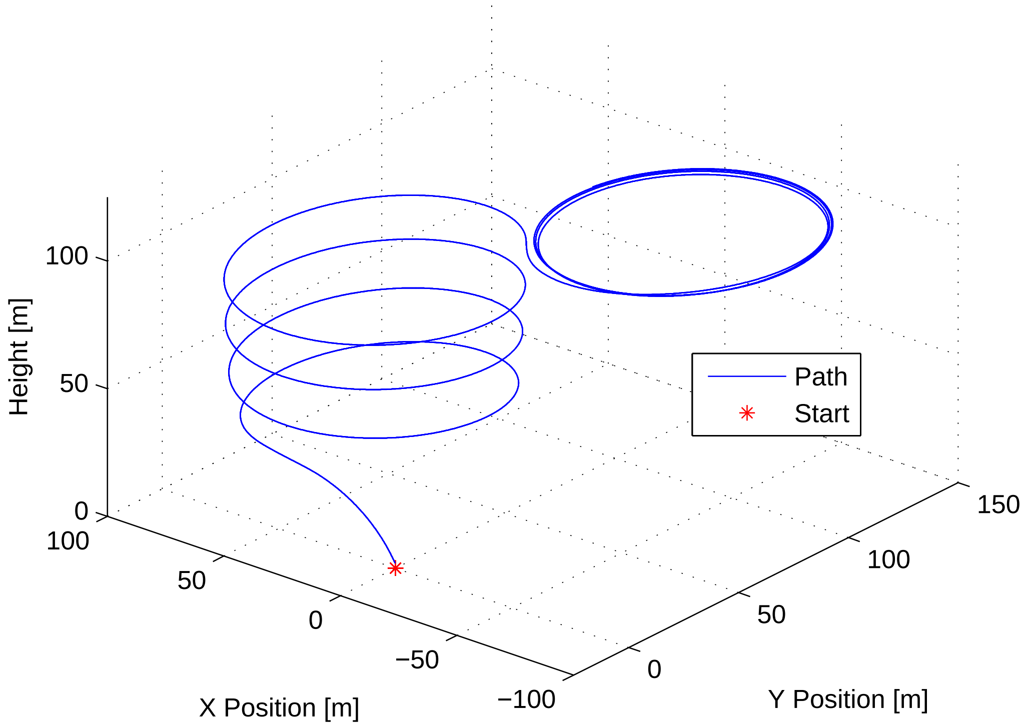

Figure 5.10: Circling Flight Path

5.4.2 Stationary Attitude Prediction

If the stationary test is considered first it can be seen from Fig. 5.12 that the performance of the proposed filter is extremely similar to the basic performance of a complimentary filter. This is to be expected as the filter follows the same basic PI form. It is seen from Fig. 5.12 that the global, and local implementation of the complimentary filter and the proposed filter all have nearly identical performance. Fig. 5.12 is not intended to differentiate between the individual filters as this is dealt with in later sections. This is due to the fact that the aircraft is stationary and therefore there are no genuine non-linear effects, indeed the inclusion of the non-linear terms is actually unhelpful as they introduce extra inaccuracies. It is therefore unhelpful to discuss the stationary test in detail as the results are not representative. The only helpful contribution that the stationary test provides is proof that the filter is stable with large initial attitude errors (∼30 degrees) and biases (∼9 degrees/second).

Figure 5.11: Phase3 Squall HP

5.4.3 Dynamic Attitude Prediction

The dynamic simulation results will now be discussed in greater detail. Fig. 5.13 and Fig. 5.14 show in greater detail the manoeuvres executed by the aircraft. Although Fig. 5.13 and Fig. 5.14 does show the relative performance of the filters the reader is not expected to deduce more than the approximate attitudes. Fig. 5.13 shows that the aircraft was initially launched at a high attitude, approximately 1 radian ($\sim$60 degrees) nose up. This high initial pitch attitude proved unsustainable for the autopilot as the autopilot was simultaneously commanded to execute a high banked climbing turn, approximately 1 radian ($\sim$60 degrees) right roll. The EP-Pioneer aircraft modelled lacked a sufficiently high thrust to weight ratio to maintain both the high roll angle and high climb rate (or climb angle). The autopilot therefore reduced the climb angle to prevent the aircraft from stalling. This relatively low climb angle unfortunately degrades the difficulty of the flight test as the low climb angle eliminates most of the non-linearities in the pitch term. Once at altitude the turn direction is reversed.

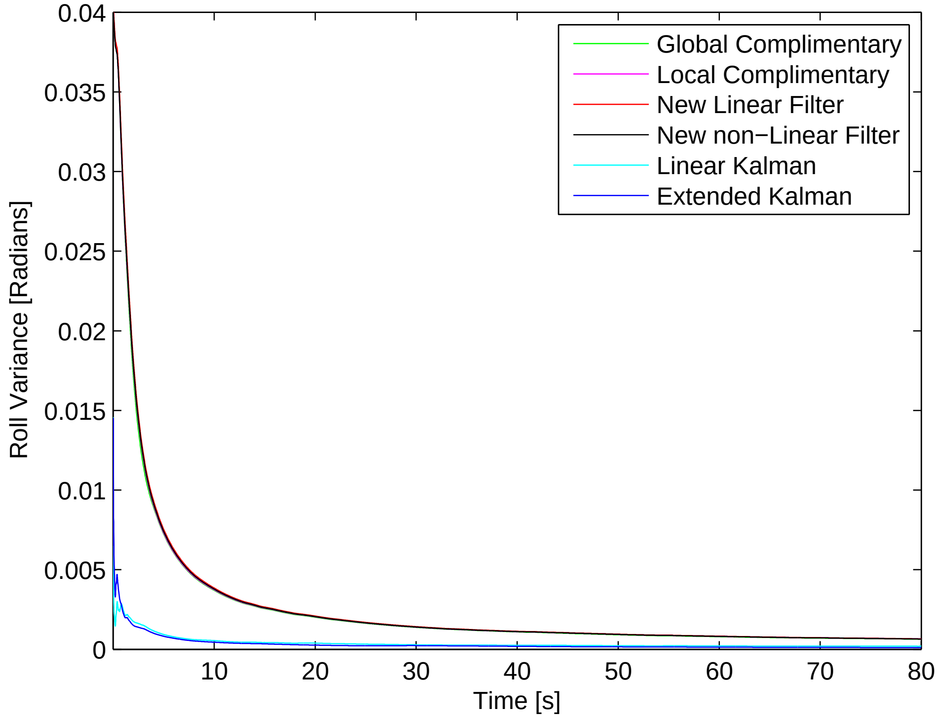

Figure 5.12: Roll Variance in stationary test

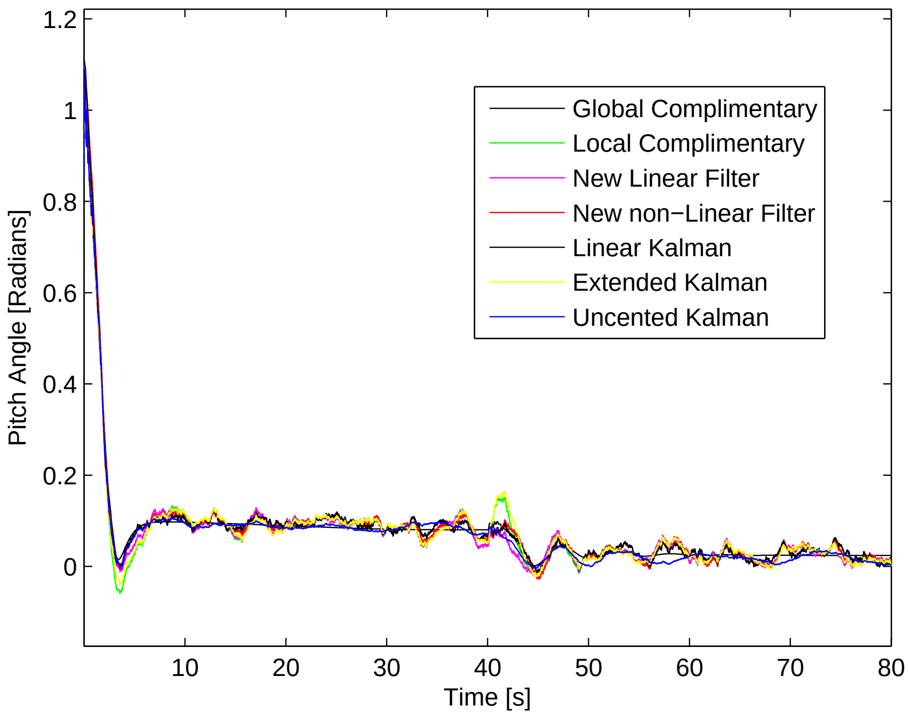

Figure 5.13: Pitch Angles

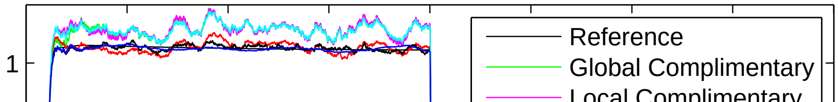

A review of Fig. 5.15 and Fig. 5.16, shows that all of the filter methods are able to provide a reasonably accurate estimate of pitch. This is because the low pitch angles render the pitch response nearly linear.

Unlike the pitch response the high roll angles render the roll response non-linear. Fig. 5.14 shows that the linear filters consistently over-estimate the roll angle. This over-estimation is demonstrated by the asymmetric errors shown in Fig. 5.16.

Fig. 5.17 shows the variation of pitch error variance with time for the filters. Fig. 5.17 clearly illustrates that the EKF performs significantly better than the other filters. The global complimentary filter performs the worst, again this is as expected. The LKF, local complimentary and the new linear filter all have similar performance, although the new linear filter is better than the other two. One interesting observation is that the local complimentary filter is more stable than the LKF and therefore outperforms it. The new non-linear filter falls halfway between the LKF and the EKF.

Fig. 5.18 shows the variation of roll error variance with time for all the filters under consideration. Unlike the pitch response the roll response is non-linear in its behaviour. This demonstrates itself in the clear step difference in the variance results between the linear and non-linear filters. The global complimentary, local complimentary and LKF all perform badly. The new non-linear filters perform as expected, closely tracking the performance of the EKF. Also noteworthy is the fact that despite the new linear filter being linearised it still retains most of the performance benefit, tracking the basic form of an EKF.

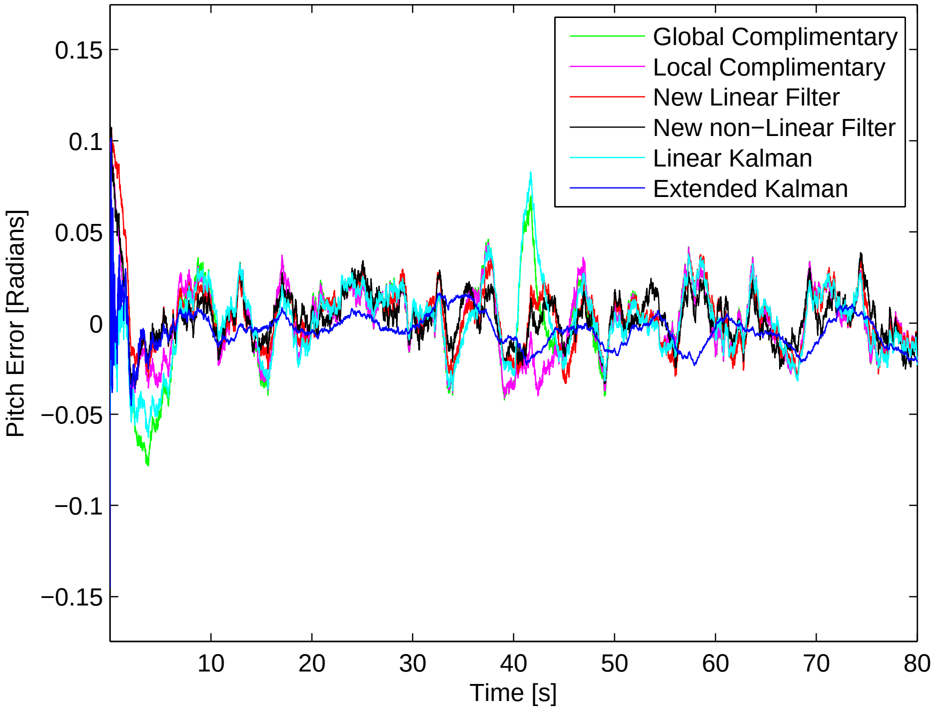

Figure 5.15: Pitch Error

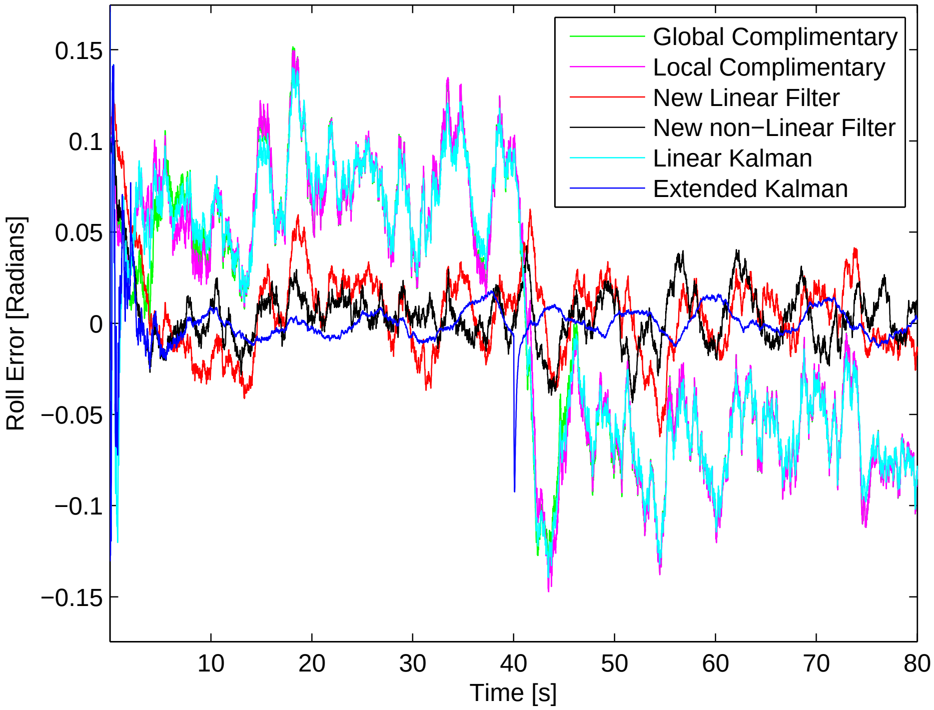

Figure 5.16: Roll Error

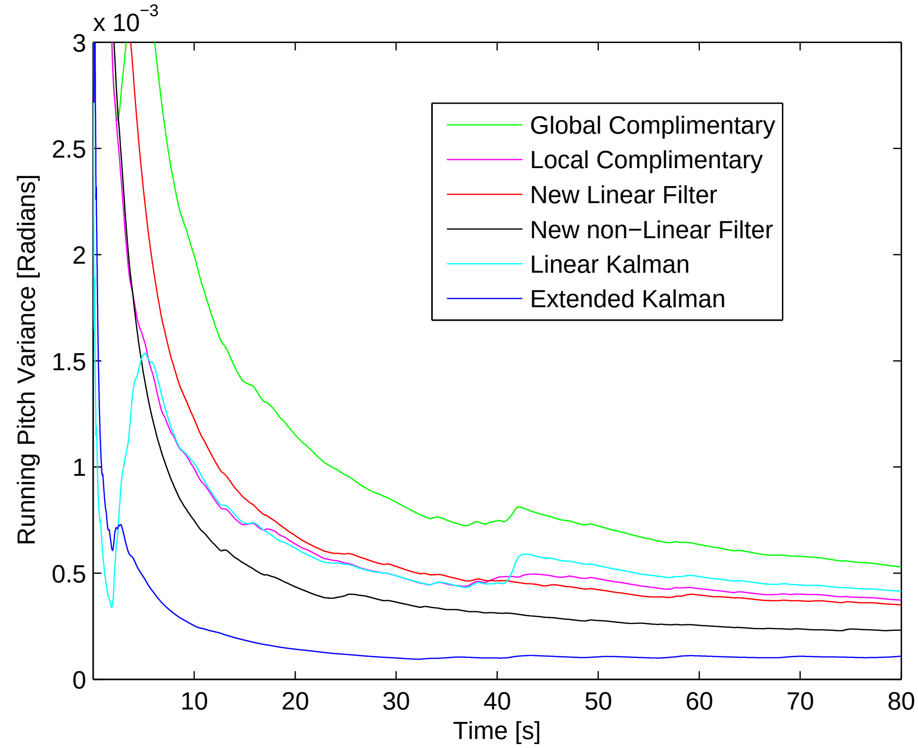

Figure 5.17: Pitch Variance

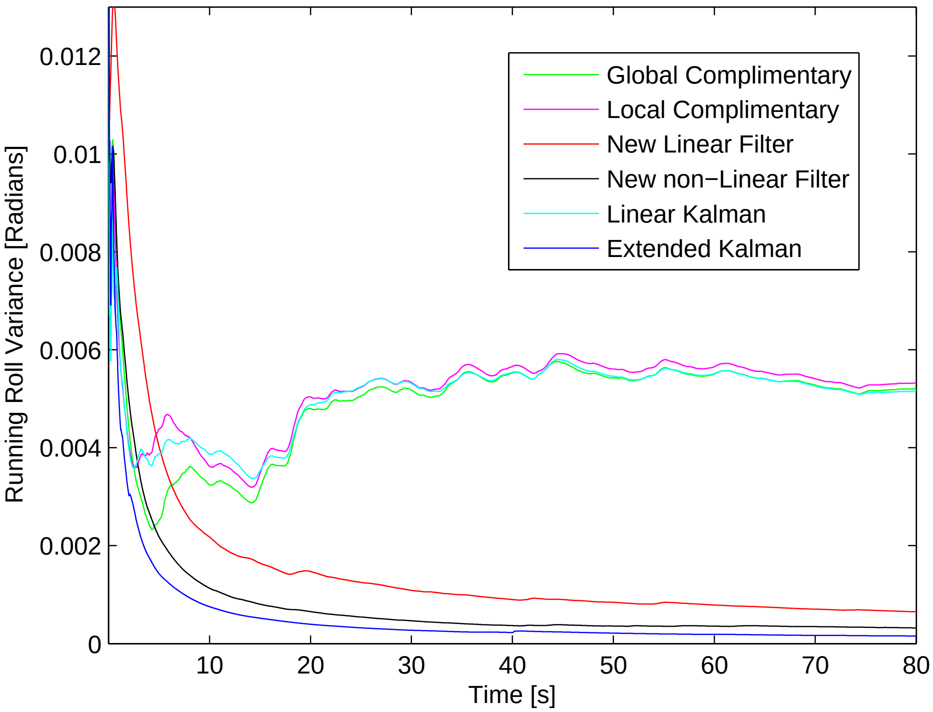

Figure 5.18: Roll Variance

5.4.4 Summary of Results

Table 5.1: Comparison of Pitch Angle Estimations

Methodology	Variance	Standard Deviation [rad]
Global PI complimentary	0.0005298	0.0230
Local PI complimentary	0.0003732	0.0193
New Linear Filter	0.0003508	0.0187
New Non-linear Filter	0.0002312	0.0152
Linear Kalman	0.0004151	0.0204
Extended Kalman	0.0001089	0.0104

Table 5.2: Comparison of Roll Angle Estimations

Methodology	Variance	Standard Deviation [rad]
Global PI complimentary	0.005213	0.0722
Local PI complimentary	0.005328	0.0730
New Linear Filter	0.0006494	0.0255
New Non-linear Filter	0.0003193	0.0179
Linear Kalman	0.005167	0.0719
Extended Kalman	0.0001541	0.0124

The relative filter performance discussed in the previous section is summarised in Tables 5.1 and 5.2. These results show that during prolonged aggressive flight manoeuvres, like circling, the complimentary filter is 5.8 times less accurate than an EKF, whereas the new CLEKF on average only shows 1.4 times the error of an EKF. Under less strenuous filtering conditions the pitch error of the complimentary filter is 2.2 times that of an EKF. The pitch error of the CLEKF is again around 1.4 times that of the EKF. This shows that the CLEKF is consistently tracking the performance of the EKF. This would lead to the conclusion that the CLEKF would also track the performance of the EKF under extremely non-linear flight conditions, albeit at a factor of around 1.4 times less accurate. The new CLEKF has been demonstrated to have an error standard deviation 4 times better than that of a complimentary filter under strenuous conditions. This significant performance improvement is provided with approximately the same computational burden as the complimentary filter.

5.5 Conclusion

This chapter documented the development of a CLEKF.

The implementation was shown to have adequate performance while not suffering from the ‘wind-up’ effects associated with open loop filters. This ‘wind-up’ or steady accumulation of the errors, although not a problem for desktop computers, can be a problem to low-power digital signal Programmable Integrated Circuits (dsPIC) as they have an inherent fixed precision in floating-point calculations. The new CLEKF removes the need to explicitly formulate Jacobian matrices, like the classical EKF, which are computationally expensive. The CLEKF presented offers almost the performance of an EKF, providing a solution that is more than 4 times more accurate than a complimentary filter, yet with the same computational requirements as a complimentary filter. Although the structure advocated does not offer the performance of a classical open loop EKF, the filter structure can be tuned off-line and then classical stability analysis can be applied to prove the stability of the system prior to deployment. This ability to prove the stability of the AHRS prior to embedding and deployment offers substantial benefits to many manufacturers seeking to make safety critical systems.

Chapter 8 will continue the work presented here into practical testing. Chapter 8 will graphically illustrate the performance difference between classical open loop Kalman filters and the new CLEKF advocated in this chapter.

Chapter 6

An Air Data Navigation System

6.1 Introduction

As the UAV technologies mature, UAVs are expected to do more and more advanced tasks. The continuing desire to expand the roles of UAVs brings with it a desire to use smaller and smaller aircraft. The use of micro UAVs brings with it its own challenges, in particular payload capacity and power reserves are at a premium. As a result micro UAVs do not tend to carry high power processors or precision navigation sensors as these are heavy and usually consume large amounts of power. The lack of processing power on board these aircraft has the potential to degrade the performance of the avionics systems on board. A key example of this performance trade-off is in the use of INS on board micro UAVs. Although effective data fusion algorithms for GNSS/INS combined systems have existed for many years [23] [52] these tend to be computationally burdensome, as a result many manufacturers rely purely on GNSS for navigation. Although pure satellite navigation is widely used to good effect [44] [3] the aircraft are vulnerable, as even temporary losses of signal render the aircraft unable to navigate. This is an unfortunate situation as large numbers of micro UAVs have the necessary sensors on board to provide a rudimentary estimate of the aircraft's position without using satellites. The question that remains is how to fuse the low quality datasets together in a practical and worthwhile manner.

The development of micro UAV-specific navigation algorithms will be dealt with in the following sections.

- A discussion of the data fusion techniques that are common

- A low computational burden INS GNSS filter
- GNSS augmented air data navigation solution

A summary of the pertinent results is presented at the end of the chapter.

6.2 Existing INS-GNSS Fusion Filters

Kalman filters have long been used to good effect to combine GNSS and INS data. However the Kalman type architecture has problems associated with it. In systems with high rates of drift, open loop Kalman filters suffer from wind up, making them undesirable for 8 and 16 bit microprocessors. A Kalman filter seeks to predict the error in the system so it can be eliminated. It follows that if the system error grows then so does the Kalman solution. Low quality INS can exhibit highly divergent behaviour with the position estimate tending off to infinity. This leads to computational accuracy problems on low power processors that have trouble managing and manipulating large floating point numbers [43]. The Kalman filter also involves finding the inverse of the following matrices, as given in Equation (6.1), to find the Kalman gain.

$$K_k = P_k^- H^T (H P_k^- H^T + R)^{-1} \tag{6.1}$$

Inverting the matrix given in Equation (6.1) can be computationally burdensome and is highly computationally burdensome for low-power processors, such as microchip PIC and dsPIC architectures [43] used for this project.

Although microprocessor technology is improving all the time there is still a desire to implement highly efficient filters on low-cost, low-power processors.

The following derivation seeks to re-express the Kalman type structure in a form more applicable to low-power processors.

6.3 The Derivation of a Closed Loop INS-GNSS Filter Following the Kalman Form

The derivations that follow are intended to be a complete derivation of the formulation of a closed loop filter based on the Kalman model. To aid with simplicity and understanding the initial filter design will be based on a linear error model Kalman filter. The basic structure of the Kalman filter is shown in Fig. 6.1

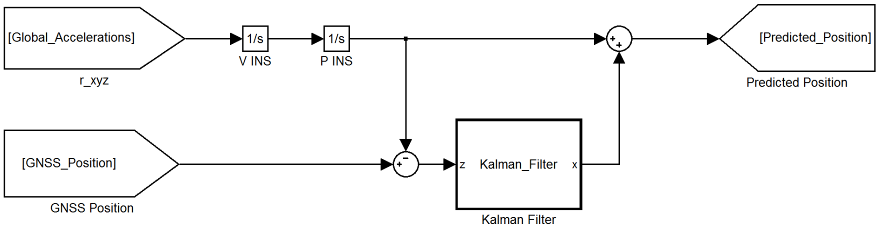

Figure 6.1: Basic Kalman Structure

The Kalman filter shown above is based on the standard linear state space equations as given in Equation (6.2) and Equation (6.3) below. For a discussion on the origins and formulation of Kalman filters can be found in Chapter 2.

$$\dot{X} = AX + Bw \tag{6.2}$$

$$Z = HX + v \tag{6.3}$$

The Kalman filter is formulated around an error model of the INS system based on the principal of interation of error over time. This is follows below.

$$\dot{\Delta P} = \Delta V \tag{6.4}$$

$$\dot{\Delta V} = \Delta a \tag{6.5}$$

$$\dot{\Delta a} = 0 + w_a \tag{6.6}$$

Here, Δ denotes error and P,V and a denote position, velocity and acceleration respectively. w_a is noise on the acceleration measurement.

The measurement model is based on the assumption that the position is the only directly comparator parameter for both INS and GNSS. As such the measurement model is based on the expected behaviour of both the INS and the

GNSS.

$$Z = P_{GNSS} - P_{INS} \tag{6.7}$$

The GNSS position is assumed to be the sum of the actual position plus the GNSS uncertainty. Likewise the INS position is assumed to be the sum of the actual position plus the cumulative error on the INS prediction. These assumptions allow us to rearrange Equation (6.7) purely as the sum of the error terms, as given in Equation (6.8).

$$Z = v_{GNSS} + \Delta P_{INS} \tag{6.8}$$

Equation (6.4) to Equation (6.6) and Equation (6.8) can be expressed in the state space form given in Equation (6.2) and Equation (6.3). This is done below in Equation (6.9) and Equation (6.10).

$$\begin{bmatrix} \dot{\Delta P} \\ \dot{\Delta V} \\ \dot{\Delta a_b} \end{bmatrix} = \begin{bmatrix} 0 & 1 & 0 \\ 0 & 0 & 1 \\ 0 & 0 & 0 \end{bmatrix} \begin{bmatrix} \Delta P \\ \Delta V \\ \Delta a_b \end{bmatrix} + \begin{bmatrix} 0 \\ 0 \\ 1 \end{bmatrix} w_a \tag{6.9}$$

$$Z = \begin{bmatrix} 1 & 0 & 0 \end{bmatrix} \begin{bmatrix} \Delta P \\ \Delta V \\ \Delta a_b \end{bmatrix} + v_{GNSS} \tag{6.10}$$

Looking at the Kalman equations in more detail the estimated error is given by Equation (6.11).

$$\dot{\hat{X}} = A\hat{X} + K(Z - H\hat{X}) \tag{6.11}$$

K is the vector of Kalman gains $K = [\ k_1 \quad k_2 \quad k_3\ ]^T$

Equation (6.11) can be rearranged as follows to express it as a transfer function, and thus facilitating analysis.

$$\dot{\hat{X}} = A\hat{X} + KZ - KH\hat{X} \tag{6.12}$$

$$\dot{\hat{X}} = (A - KH)\hat{X} + KZ \tag{6.13}$$

$$\dot{\hat{X}} - (A - KH)\hat{X} = KZ \tag{6.14}$$

The Laplace transform is then taken of Equation (6.14) to give Equation (6.15).

$$[sI - (A - KH)]\hat{X}(s) = KZ(s) \tag{6.15}$$

Equation (6.15) is then rearranged to give the transfer function desired, shown in Equation (6.16).

$$\hat{X}(s) = [sI - (A - KH)]^{-1}KZ(s) \tag{6.16}$$

Substituting the vectors and matrices back into Equation (6.16) we arrive at Equation (6.17).

$$\begin{bmatrix} \Delta P(s) \\ \Delta V(s) \\ \Delta a_b(s) \end{bmatrix} = \begin{bmatrix} s + k_1 & -1 & 0 \\ k_2 & s & -1 \\ k_3 & 0 & s \end{bmatrix} \begin{bmatrix} k_1 \\ k_2 \\ k_3 \end{bmatrix} Z(s) \tag{6.17}$$

Equation (6.17) can be rearranged to the following form, given in Equation (6.18).

$$\begin{bmatrix} \Delta P(s) \\ \Delta V(s) \\ \Delta a_b(s) \end{bmatrix} = \begin{bmatrix} \frac{k_1 s^2 + k_2 s + k_3}{s^3 + k_1 s^2 + k_2 s + k_3} \\ \frac{k_2 s^2 + k_3 s}{s^3 + k_1 s^2 + k_2 s + k_3} \\ \frac{k_3 s^2}{s^3 + k_1 s^2 + k_2 s + k_3} \end{bmatrix} \mathrm{Z}\,(\mathrm{s}) \tag{6.18}$$

If X(s) is given by Equation (6.18), the element of interest is the prediction of position error in the first row. It is desirable to eliminate the other terms and investigate the properties of this first-term more thoroughly.

$$\Delta\hat{P}\,(\mathrm{s}) = \frac{k_1 s^2 + k_2 s + k_3}{s^3 + k_1 s^2 + k_2 s + k_3}\,\mathrm{Z}\,(\mathrm{s}) \tag{6.19}$$

Although the expression given in Equation (6.19) is a useful rearrangement of the Kalman filter, it does not provide a complete solution to the inertial navigation problem. To provide a complete solution to the actual position of the vehicle, and not just position error, needs to be considered.

Equation (6.20) shows an appropriate expression for the structure shown in

Fig. 6.1.

$$\hat{P} = P_I + G(s)\,(P_{GNSS} - P_I) \tag{6.20}$$

As alluded to in Chapters 2 and 5, open loop structures are very often not computationally stable on low bit count microprocessors. As a result of this it is useful to rearrange Equation (6.20) into a feedback loop structure, as shown in Equation (6.21).

$$\hat{P} = G\,(s)\,P_{GNSS} + (1 - G(s))\,P_I \tag{6.21}$$

Expanding Equation (6.21) results in the form shown in Equation (6.22).

$$\hat{P} = \frac{k_1 s^2 + k_2 s + k_3}{s^3 + k_1 s^2 + k_2 s + k_3} P_{GNSS} + \frac{s^3}{s^3 + k_1 s^2 + k_2 s + k_3} P_I \tag{6.22}$$

Equation (6.22) fits into a feedback structure as shown in Fig. 6.2, below.

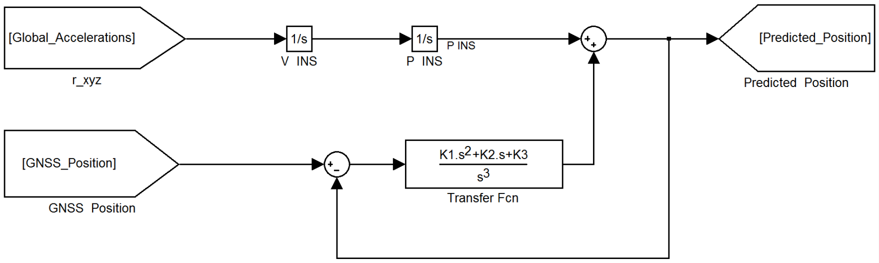

Figure 6.2: Constant Gain Kalman Feedback Structure

This is not a preferred structure because integrating lots of different parameters can be computationally costly on low power processors. By introducing the influence of the inertial navigation sensors before the integrations as global accelerations it is possible to remove 6 integration steps from the software. The resultant structure is shown below in Fig. 6.3.

It is observed that this is in a PID form, a commonly used and well understood control structure. This structure is useful but it is desirable to remove the derivative term from the function as the time derivative of GNSS is noisy and thus introduces unnecessary noise into the system. The moving of the derivative is done by changing the structure slightly, thus reducing the noise introduced. This is shown in Fig. 6.4.

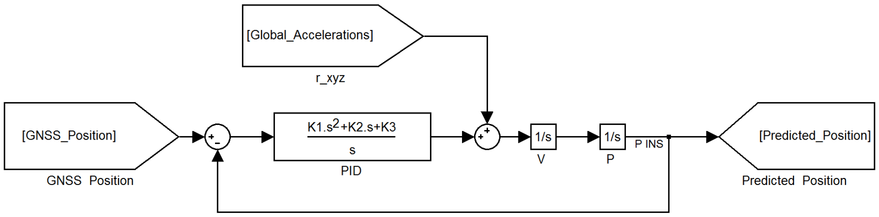

Figure 6.3: Initial Constant Gain Kalman Structure

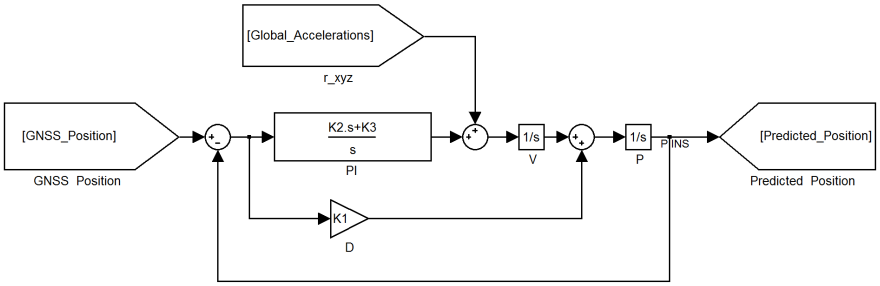

Figure 6.4: Constant Gain Closed Loop Kalman Structure

There is a striking similarity to the complimentary filter structure used by Jung and Tsiotras [31], although they arrived at the filter using a different derivation.

This is a linear filter and assumes that the contribution from the integral term is low. If there is a large accelerometer bias then there is an implicit assumption that the rate of change of heading is slower than the time scale of the filter. With considerable rate of change of heading and biases the solution is not stable. To overcome these problems the integral term can be removed or the filter can be modified to a non-linear form as show below in Fig. 6.5.

With this structure the integration is in the same reference frame as the bias is being introduced in. This enables the integral contribution to be non-minimal while removing the zero rate of change of heading assumption. This introduces more complexity to the implementation but the DCM required is already available because the DCM^T is needed for the basic INS calculation; meaning that there is minimal further computational burden.

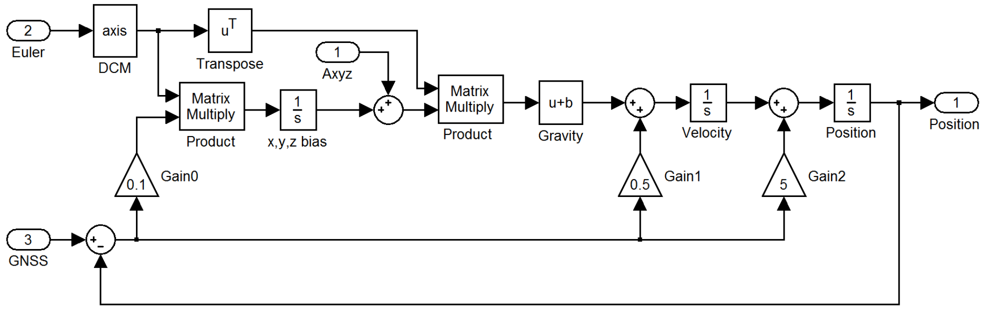

Figure 6.5: Non-linear Constant Gain Closed Loop Kalman Structure

6.4 A Constrained Closed Loop INS-GNSS Filter

The filter shown in Fig. 6.6 is a modified implementation of classical inertial navigation technique using accelerometer and gyroscope data as in the previous filter, shown in Fig. 6.5. This implementation however uses an assumption of zero net vertical and lateral local velocities. This assumption allows the elimination of erroneous wind-up errors in the vertical and lateral directions. Although there maybe vertical or lateral velocity present, introducing an error, these errors are smaller than the errors that would result from allowing the unconstrained build up of velocity. To help reduce the errors associated with the zero net vertical and lateral local velocities assumption a wash-out filter is used instead of rigidly setting the velocities to zero.

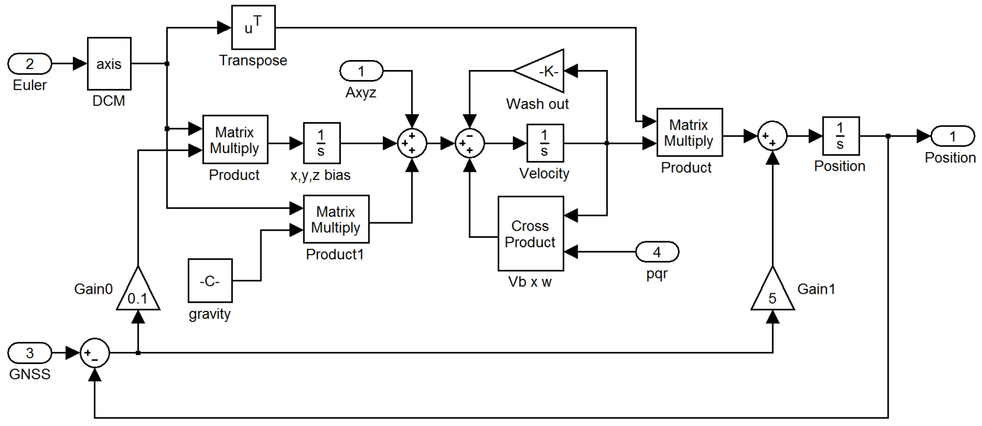

Figure 6.6: Constrained INSGNS Filter

6.5 GNSS Augmented Air Data Navigation

Another navigation solution that is attractive to micro UAV is the use of air data to provide a type of dead reckoning navigation. Dead reckoning navigation based on air data augmented with GNSS information is attractive as it provides a reliable navigation solution robust to temporary loss of GNSS data. The reliance on air data as the primary navigation source rather than acceleration also removes an integration step from the calculation meaning the solution suffers less from drift if GNSS is lost.

A simple Air Data augmented Global Navigation System (ADGNS) filter for air data navigation is shown in Fig. 6.7.

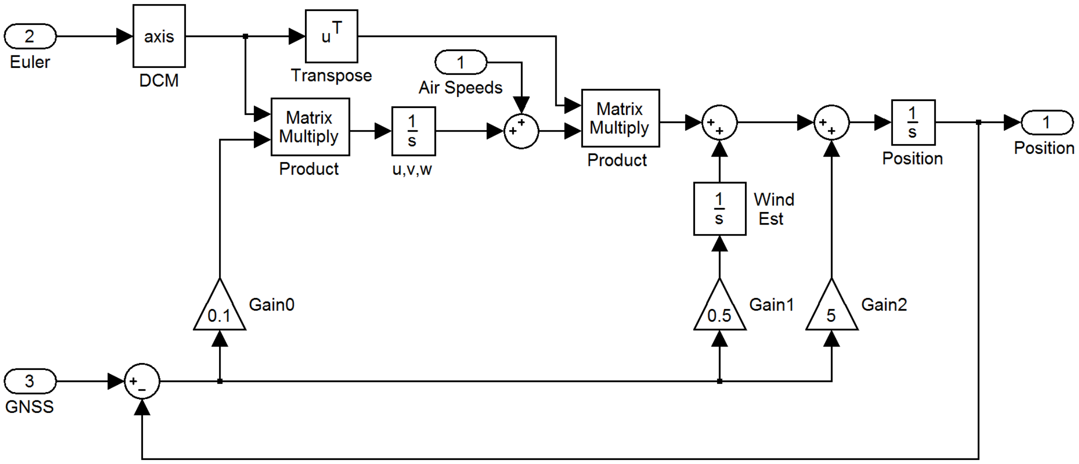

Figure 6.7: ADAGNS Filter Structure

The filter consists of three terms, local integral (K0), global integral (K1) and global proportionality (K2). The global proportionality provides convergence between the air data and GNSS navigation solutions when GNSS data is available. When GNSS data is not present or is of questionable value K2 can be dynamically altered depending on the confidence on data. It is not necessary to alter the height term in K2 as height is calculated locally from pressure altitude data. The global integral term (K1) seeks to compensate for the presence of wind. As a result of this K1 is smaller than K2 maintaining the stability of the system. K1 can be chosen depending on the confidence in the initial conditions and the variability of the wind. If large height changes are expected then the integral must contain a height compensation function to take into account the veering, backing and intensity changes of the wind with height. Alternatively K1 can be tuned to include this uncertainty in wind. Finally, the local integral term (K0) seeks to compensate for the presence of air speed calibration error. For this term to have the desired effect it must have a longer time base than the global integration term. This means that K0 must be significantly smaller than K1.

6.6 Simulation

Due to time constraints the three filters presented here have not been formally analysed to confirm stability. The three filter architectures, described in Sections 6.3, 6.4 and 6.5, will now be subject to extensive simulation to show their expected behaviours. To enable an effective comparison the gains of the filters are tuned to give the best performance (lowest standard deviation) while GNSS data is present.

6.6.1 Set-up

Along with computational burden one of the key points of interest to UAV is the GNSS denied performance of the navigation filters. To test the GNSS denied performance of the filters the Bow Tie flight pattern from Chapter 4 is employed again. The Bow Tie flight pattern is shown in Fig. 6.8. In this test, aircraft complete as many laps of the bow tie as required.

The bow tie pattern is a good flight pattern to use because it encompasses a balanced flight path, inducing straight and level, and turning in both directions; therefore including a good variety of accelerated and un-accelerated flight phases. Included in the simulation is a 15 knot wind at 90 degrees anticlockwise from north (Westerly). A westerly wind is chosen as it is the most common wind direction at the test site. The Bow Tie flight pattern used for this test does not include a height change. This simplifies real world test presented in Chapter 8. The lack of height changes also simplifies simulation (as there is no variation in wind with height modelled) and filter performance comparison, although detracts from realism.

To compare the GNSS denied performance of the filters the GNSS data was frozen after 400 seconds. This is to reflect the way that the real GNSS module

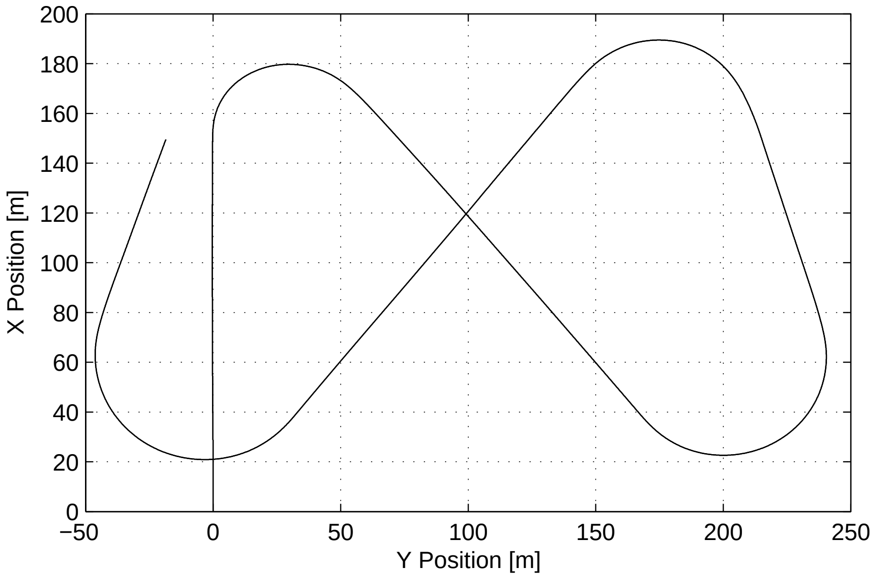

Figure 6.8: Idealised Simulated Flight Test Pattern

used in testing fails. The aircraft was then commanded to continue lapping the bow tie flight pattern. The test was stopped when the navigation error exceeded 100m. 100m is felt to be a representative distance, as if a micro UAV was more than 100m away from its target position, then an operator may not be able to see the aircraft. This would usually mean that the aircraft would be permanently lost.

6.6.2 Results

Fig. 6.9 shows that all three navigation methods perform adequately or within the accepted accuracy of the GNSS module while provided with GNSS data.

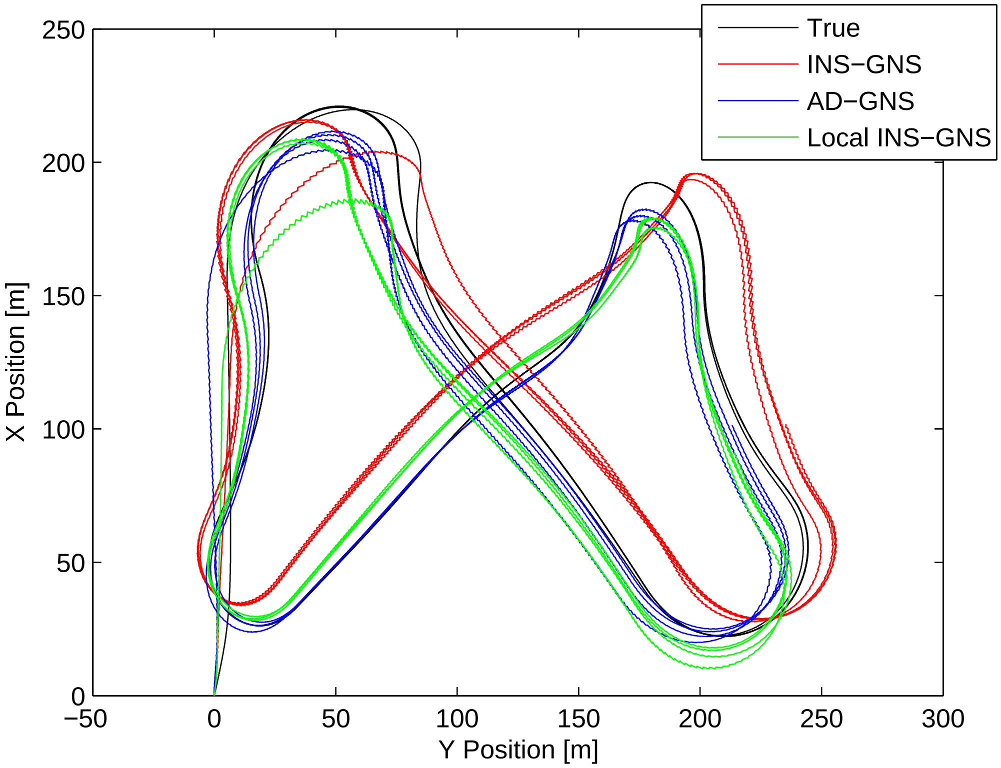

Figure 6.9: Comparison of Bowtie Flight Paths

However once GNSS data is denied the three filters have quite different performance as shown in Fig. 6.10. The purely inertial navigation approach quickly diverges. This is to be expected as any small errors in acceleration will be integrated to form non-trivial errors in velocity. These non-trivial errors in velocity will be once again integrated to give an infinite error in position with time. The constrained inertial navigation approach has the same basic error behaviour. However two of the axes have their error constrained, this means that position error build-up will be slowed providing an improved solution. The pressure-based method on the other hand only utilises one integration step meaning that the error divergence is linear with time. This provides a more stable and reliable solution than inertial measurement based approaches. However this pressure augmented approach is sensitive to wind and relies on a good estimation of wind to provide an acceptable position estimate.

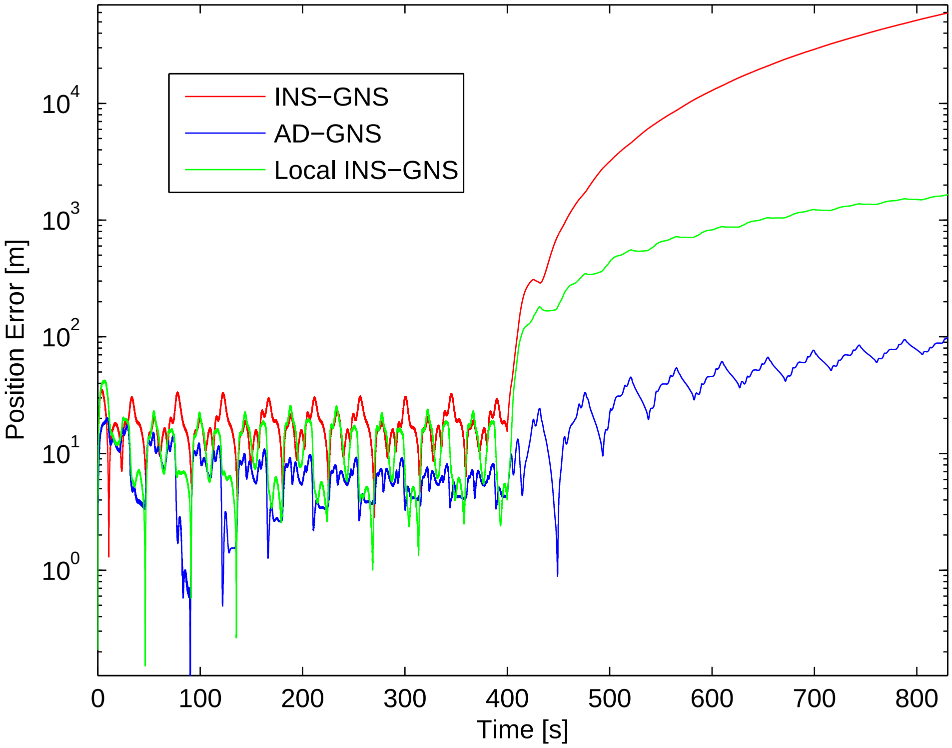

Figure 6.10: Comparison of Simulated Position Error

Of more importance is the fact that Fig. 6.10 shows that the air data based navigation solution takes more than 430 seconds for the position error to build to 100m. This is contrasted with the inertially based navigation solution takes less than 70 seconds to reach the 100m error that was deemed unacceptable. In the 430 seconds that the air data derived solution took to reach 100m error the inertially based solution reached nearly 60km error. The constrained inertial solution was better with an error of a little more than 1.6km in the 430 seconds that the air data solution took to reach 100m error.

It has been demonstrated that the air data augmented solution to the navigation problem is equivalent if not better than the inertially augmented solution with the presence of GNSS data. Once GNSS data is denied the air data augmented solution provides a superior position estimate.

6.7 Conclusion

This chapter has detailed three navigation filters that are suitable for application on micro to small UAV with limited possessing power and sensor performance. The first two filters followed a conventional approach using inertial measurements while the second used a air pressure data to derive a position estimation. Both approaches rely on GNSS for a reference position and stable solutions. The simulation results show that both solutions provide adequate navigation performance with the presence of GNSS data. If GNSS data is denied the air data derived solution provides the most reliable means of navigation. With the quality of air data sensors used for the simulation the air data derived navigation solution provides adequate position information for more than 5 minutes.

Although GNSS denial has been investigated in this chapter, the filters are intended for use in a navigation system to improve the robustness of the navigation system in aggressive turns, and even aerobatics, where the satellite lock may be lost for a few seconds at a time.

The ADGNS described in this chapter will be subject to further investigation and real world validation in Chapter 8.

Chapter 7

Avionics Hardware Development

7.1 Introduction

This chapter details the hardware development along with some preliminary details of the real life practical flight testing carried out. Simulations have been exhaustively used in Chapters 4, 5 and 6 to verify the algorithms but this often is not sufficient for the widespread adoption of an approach. This chapter seeks to document and explain the development of the hardware necessary to effectively test the theory developed in Chapters 4, 5 and 6 in the real world.

To implement new techniques the system architecture must be open, allowing rapid development and deployment. There is no such open source MEMS autopilot available, as a result it is necessary to combine a diverse range of robotics, aerospace and automotive technologies to provide this functionality. A detailed discussion of the development of such a sensor platform is given. The hardware developed and used for this thesis was developed from first principals to be a modular research tool.

This chapter is broken down into the following sections:

- Introduction and motivation
- Sensor developments
- Processor developments
- Servo control modules
- Communication set-up

- Aircraft

Following the discussion of the various modules capabilities a summary of the performance and functionality is given.

7.2 Motivation

After the initial studies into autonomous soaring had been completed it was decided to implement the soaring algorithms developed in reality. To that end a Micropilot MP2028 autopilot was purchased. Unfortunately initial studies proved that this autopilot was incapable of tracking the trajectories desired.

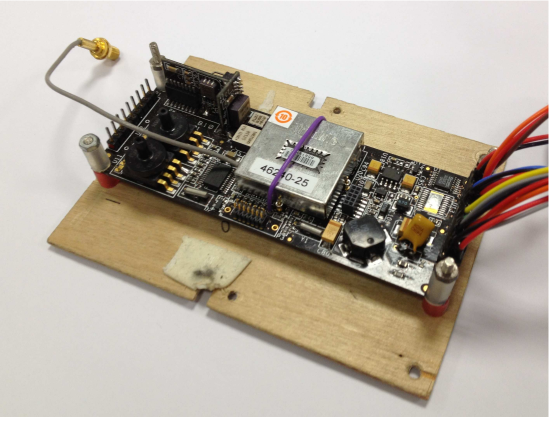

Figure 7.1: Micropilot MP2028 Autopilot

This lack of capability from commercial autopilots demonstrated a development need. It was therefore decided to concentrate efforts on developing algorithms that would enable autopilots to efficiently and accurately track more varied dynamic trajectories. This has been a common theme over the last couple of years as many universities have chosen to develop their own open source autopilots as they have encountered similar problems. Notable institutions that continue to develop their own hardware and software include; North Carolina State University [22] and NASA [6].

Loughborough Universities Centre for Autonomous Systems (LUCAS) currently operates a large VICON flight test facility. This VICON test facility is based upon a number of infra-red cameras providing position and attitude information to a conventional desktop computer. This off-board computing enables the use of powerful desktop processors and development software such as MATLAB/Simulink. This off-board computing architecture was the inspiration for the first-generation of sensors investigated.

7.3 Sensor Evolution

7.3.1 Initial Sensor Ethos

As explained in Chapter 2, three orthogonal gyroscopes are all that is needed to provide a rudimentary estimate of attitude. However gyroscopes drift progressively over time. This means that gyroscopes need external references for initial condition and to constrain drift. To constrain drift accelerometers and magnetometers are customarily used. All of these sensors can be readily purchased on existing breakout boards, that can be connected to data acquisition systems.

To support this off-board architecture it was decided to purchase a remote data acquisition system. One of the most attractive data acquisition systems at the time was produced by Tronix. Their Dacio 300 data acquisition system already supported 8 analogue and 16 digital sensors over a wireless serial connection. The Tronix Dacio 300 Data acquisition system is shown in Fig. 7.2.

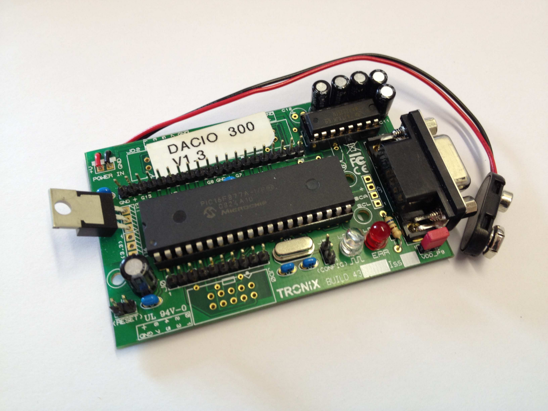

Figure 7.2: Tronix Dacio 300 Data Acquisition System

Through extensive tests it was discovered that the massive amounts of data required severely limited the maximum achievable data rate, although the connection was quite stable.

This Dacio 300 data acquisition system was used for initial testing. However the Dacio 300 data acquisition system used a form of SSC32 ASCII-based interrogation to provide data to the user. This interrogation method although versatile inevitably causes a large data overhead. This rendered the effective data rate to be approximately 30Hz. 30Hz was still considered an acceptable data rate but the data rate was not deterministic. This lack of determinism combined with the poor serial port handling capabilities of MATLAB meant that the data could not be time-integrated reliably. As the same data was being requested for each sample a minor software alteration was desired. However, unsurprisingly, Tronix did not want to release the information necessary to facilitate this change. Loughborough University had the facilities to manufacture the required equipment. To that end an initial data acquisition board was manufactured with the same processor and largely similar peripherals. This enabled a complete reprogramming of the data acquisition system, customised to the project requirements. This data acquisition system is shown in Fig. 7.3.

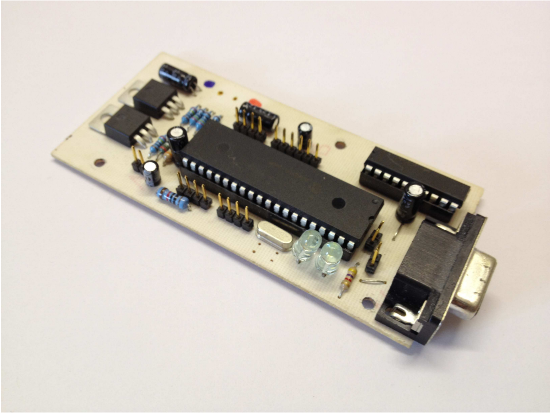

Figure 7.3: Loughborough University Data Acquisition System

With the unmitigated success of this data acquisition system it was a logical progression to redesign the system with integral sensors.

Fig. 7.4 shows one of the first combined sensor suite to be used.

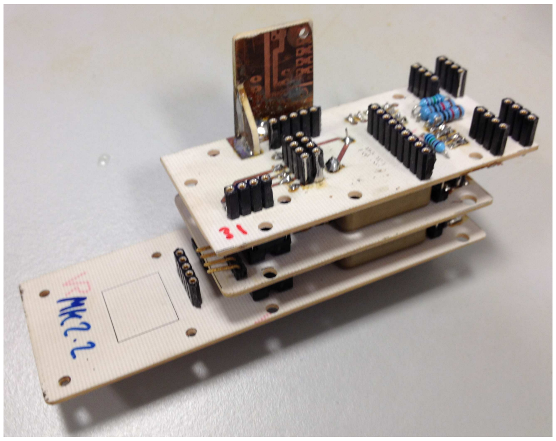

Figure 7.4: Initial Sensor Breakout

The sensor suite shown in Fig. 7.4 does have a small amount of on-board processing although this processing power was merely used to encrypt and send the data from sensors to a remote computer. This sensor suite, although basic, enabled many experiments to be carried out to assess the performance flaws associated with conventional MEMS sensor behaviour, and ultimately proved the inspiration for the approaches advocated. Chapter 4 documents the extensive theoretical work and simulation which were carried out to investigate the feasibility of using air data to augment the conventional three sensors; gyroscopes, accelerometers, and magnetometers.

7.3.2 Jetstream Flight Test Hardware

In order to validate the algorithms a flight test was conducted using the Cranfield University National Flying Laboratory Centre's Jetstream 31 aircraft whilst conducting a dynamic mode demonstration flight. This allowed the algorithms to be validated against a high accuracy sensor suite.

The sensor suite was secured to the National Flying Laboratory Centre's Jetstream 31 aircraft whilst conducting a dynamic mode demonstration flight. The suite was located next to the aircraft's IMU which was used to provide reference data for an effective comparison. During the flight test itself, no data processing was attempted. The data from the aircraft's IMU and the raw data from the sensor suite were stored for post-processing on the ground after the flight.

The aircraft's on-board sensors were used to provide the pressure information for the tests carried out as it was impractical to use custom sensors. The use of the aircraft's sensors is justifiable as the data quality is comparable to the quality obtainable by a UAV's on-board sensors.

For certification reasons nothing could be directly connected to the aircraft's systems nor could anything be radiated; this means that wireless communication could not be used. For physical reasons the new sensor suite could not be connected to a laptop via cables so integral data logging was necessary.

A Gumstix Overo Fire, shown in Fig. 7.12, [4] was chosen as an On-board Processor Unit (OPU) due to its small footprint and lightweight nature in addition to its implementation of an open source Linux kernel. The sensors were connected to the OPU via a high speed I2C bus which enabled bidirectional communication to the full range of sensors. Software can be written directly to the OPU in C++ and compiled in situ or developed remotely and uploaded. The OPU includes a micro SD card slot which provides a means of deterministic high speed data storage. In addition to providing onboard processing for the AHRS, the OPU includes Wireless Local Area Network (WLAN) and Bluetooth capabilities which enable short range real-time remote communication.

The suite was electrically isolated from the other aircraft systems to prevent interference. For this reason batteries were used to power the suite. Typical power consumption was measured at around 2 Watts, this was with WLAN and Bluetooth disabled. Raw sensor data was recorded by the OPU to an 8GB micro SD card to enable post processing. No processing was conducted during the test. The compass was not calibrated for location on the test as there was insufficient time.

Figure 7.5: Jetstream Flight Test Hardware

Figure 7.6: Jetstream Flight Test Aircraft

The sensor hardware used during the flight test is listed below and shown in Fig. 7.5.

- Gyroscopes: Three orthogonal Analogue Devices ADXRS610 [9] were used in combination with three Texas Instruments 16-bit ADS1115 ADCs.
- Accelerometers: One, three-axis Analogue Devices ADXL330 accelerometer in conjunction with the 10-bit high speed ADC on a PIC18LF458. This ADC is digitally interlaced to 16-bit resolution.
- Magnetometer: A Honeywell HMC6343 three-axis magnetometer

7.4 Sensor Development

Although the sensor packages used for initial testing and for the Jetstream flight test experiment were adequate, the sensor suite continued to develop. There were a few drivers behind this development. The first sensor suite was low in computational power (5MIPS) and had a crude sensor set up. The Jetstream flight test sensor suite had a much better sensor package and an extremely powerful ARM9 Gumstix core running a full Linux operating system. The complexities of coding in a full PC style operating system while controlling low-level hardware proved extremely complex. This complexity coupled with the physical sensitivity of the tiny processor proved impractical.

Fig. 7.7 shows the next generation of inertial measurement unit produced. This generation shared the same sensor layout as the sensor suite used for the Jetstream flight test but with a significantly updated processor and had a smaller footprint.

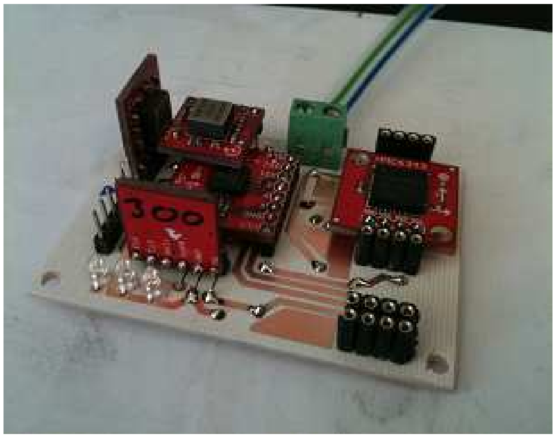

Figure 7.7: Low Cost MEMS Sensors Used for AHRS

This sensor suite was used to provide attitude data to enable a T-Rex 450 to hover unaided. The flight control for the helicopter was conducted off-board on a desktop PC in conjunction with the VICON tracking facility used for position.

Although hovering was demonstrated on a number of occasions data communication with the PC proved troublesome and less than reliable. This demonstrated that outdoor flight using off-board processing was feasible but not practical. It was therefore decided to revise the sensors suite to enable the inclusion of an OPU.

The inclusion of an OPU in addition to the possessing power available on-board the sensor board itself made on-board AHRS calculations possible. Further revisions also followed a more modular model. This meant that processors could be changed and further sensors added as necessary without remaking existing delicate sensors boards. To enable this modular model to be better executed a slightly different on-board data communication method was adopted.

This modular system architecture is more computationally intensive than a single processor set-up as many of the low level tasks such as timing loops, more data transfers required, etc, are repeated on each processor. However this system architecture does mean that new developments can be carried out and tested separately from other elements.

Early sensor boards such as those shown in Fig. 7.5 and Fig. 7.7 utilised an Inter-Integrated Circuit (I^2C) bus. This is a versatile and widely used digital bus but means that a central supply and logic voltage is needed. This is a problem for two reasons. Firstly, not all sensors use the same voltage for their supply and logic levels, posing big regulation problems. Secondly, with the foreseeable expansion of the sensor suite to include more sensors and more importantly more processing power, power regulation at higher wattages becomes a design challenge. Central power control makes the system more susceptible to serious damage when a module is connected wrongly. When these factors were coupled it meant that distributed power management was a more attractive option.

To help facilitate the hardware interface a common power rail was added to the I^2C bus to form a common power input/output bus. This common power and data bus meant that a single ribbon cable could be sent around the aircraft with equipment able to be clipped onto this common rail as required using the standard IDE type connector. This 6 wire bus will be referred to as the common I/O bus from here on.

With the aid of this new system architecture a host of developments were made. New pressure sensors, gyroscopes, accelerometers, magnetometers, processors, GNSS, and servos control boards were developed. These modules will now be discussed in more detail in the following sections.

7.4.1 Inertial Measurement Unit

The next generation inertial measurement unit board used the same sensors as shown in Fig. 7.7 but with the inclusion of the more generic common I/O bus.

This inertial measurement units is shown in Fig. 7.8.

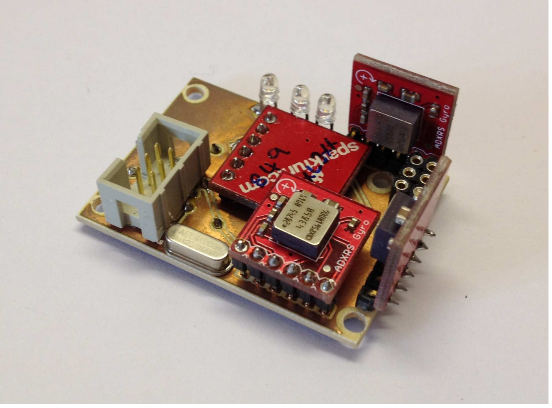

Figure 7.8: Modular MEMS IMU on a Common I/O bus

During the development of the hardware numerous sensor combinations were assessed. This assessment process looked at trade-offs between cost, functionality, accuracy and data quality. For example of particular importance was the choice of gyroscopes. The original gyroscopes used were InvenSense IDG-300 [1]. Although these have a wide measurement range and provide good quality data they lack a stable bias. This makes them unsuitable for dead reckoning applications. The gyroscopes were changed for Analogue Devices ADXRS610 [9], as shown in Fig. 7.8. This sacrifices measurement range in favour of bias stability. The Analogue Devices gyroscopes also had the added advantage of being temperature compensated. Later on in the project, 2010, InvenSense released the IMU-3X00. These gyroscopes had the benefit of a wide measurement range and a stable bias. The IMU-3X00 are less expensive and easier to interface to but were not available on a breakout board. This meant that the circuitry had to be developed from scratch using reflow soldering techniques.

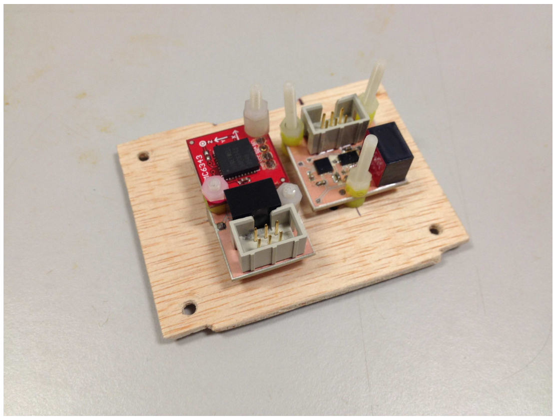

Figure 7.9: New Modular MEMS IMU Sensors on a Common I/O bus

The performance of the final IMU is summarised in the Table 7.1 and Table 7.2

Table 7.1: ADXL345 Accelerometer Performance

Typical X/Y/Z Bias	40/40/80 [mg]
Maximum X/Y/Z Bias	150/150/250 [mg]
Horizontal Error due to Bias in 60s	900 [m]
Typical Alignment Error	1.6 [deg]
Full Scale Range	16 [g]
Scale Error	10 [%]
Noise RMS at 100Hz Data Rate	34 [mg]

Table 7.2: IMU-3200 Gyroscope Performance

Typical Bias	40 [deg/s]
Gyroscope Angle Random Drift	60 [deg/$\sqrt{hr}$]
Scale Range Used	1000 [deg/s]
Scale Error	6 [%]
Angle Error in 360 degrees	22 [deg]
Alignment Error	1 [deg]
Noise RMS at 100Hz Data Rate	0.38 [deg/s]

The performance data shown in Table 7.1 and Table 7.2 are from the data sheets and are impressive but do not tell the whole story. The performance data shown in Table 7.1 and Table 7.2 is for idealised conditions and does not take into account the fact that the sensors are mounted in an avionics bay that is fixed directly to the chassis of the aircraft. This means that significant vibration from the motor, propeller, actuators, aerodynamic turbulence and undercarriage is passed onto the sensors with little damping. However, tumble calibration was used to make sure the gyroscope and accelerometer scale factors were well within 5% and the sensors were biased before each flight, therefore scaling errors and accelerometer bias were not considered in the simulation. The presence of larger noise powers with smaller biases, on the real flight test data, mean that significantly larger noise powers were used in conjunction with smaller biases for the simulation environment, as summarised in Table 7.3.

Table 7.3: Gyroscope and Accelerometer Noise Modelled

Gyroscope	
Bias	10 [deg/s]
Gimble Lock	1000 [deg/s]
Noise RMS	350 [mg]
Accelerometer	
Acceleration Saturation	155 [m/s/s]
Noise RMS	18 [deg/s]

7.4.2 Air Data Module

The structure that provided the best quality sensor data is to collect the data via a series of analogue to digital converters on a Programmable Integrated Circuit (PIC). The PIC samples the sensors at approximately 4KHz and applies a low pass filter on the data ready to be passed to the higher level processor at a lower sample rate of 100Hz. This approach is used to obtain fast and smooth air data in the form of airspeed and pressure altitude from small inexpensive sensors as shown in Fig. 7.10.

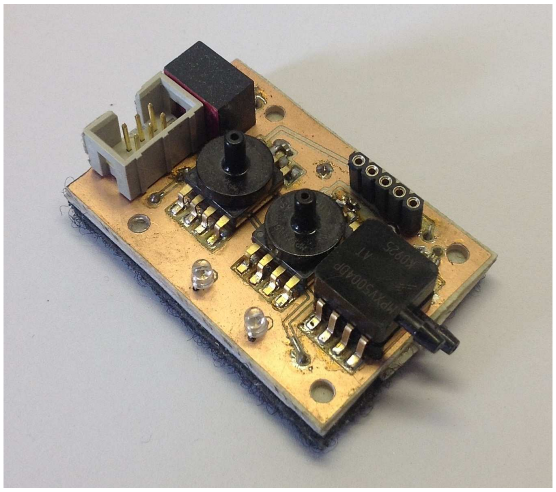

Figure 7.10: Modular Pressure Sensors on a Common I/O bus

These pressure sensors were then carefully calibrated against GNSS data. Despite being carefully calibrate the sensors consistently displayed biases, despite the air data tracking the true value correctly. Off-sets in altitude were dealt with by using pressure height (usually referred to as QFE by pilots) rather than altitude. Off-sets in pressure velocity are less straight forward to deal with as the calculation involves a velocity squared, V^2, term. This meant that it was possible to have a bias of up to 2m/s on pressure velocity, although typically around 0.4m/s. Performance figures for the Analogue Devices MPXV5004G series sensors are available but the presence of high speed analogue to digital converters and filtering skews the results so Table 7.4 shows the combined accuracy.

This air data module, with its class-A power regulation, well-designed analogue filters and massive digital over-sampling providing smooth and accurate data with negligible latency. The RMS noise powers and biases shown in Table 7.4 are used to model noise and biases in the simulation environment.

7.4.3 Magnetometer Module

The Honeywell HMC6343 was chosen as the magnetometer for this project as it offers better accuracy than most digital compasses while offering an integrated I^{2}C bus. The Honeywell HMC6343 is shown in Fig. 7.9 on a breakout board that provides power and conversion to the common I/O bus. Table 7.5 summarises the magnetometer performance as configured on the custom hardware, as such

Table 7.4: Air Data Sensor Performance

Air Speed	
Resolution	0.01 [m/s]
Measurement Range	0-75 [m/s]
Typical Bias	0.5 [m/s]
Maximum Bias Error	2 [m/s]
Noise RMS at 100Hz Data Rate	0.1 [m/s]

Pressure Height	
Resolution Used	0.1 [m]
Resolution Available	0.01 [m]
Measurement Range Used	±300 [m]
Typical Bias	0.2 [m]
Maximum Bias Error	0.8 [m]
Noise RMS at 100Hz Data Rate	0.2 [m]

the figures differ slightly from the component data sheet.

Table 7.5: HMC6343 Magnetometer Performance

Feild Range	2 [gauss]
Resolution	7 [milli-gauss]
Measurement Rate	10 [Hz]
Signal to Noise Ratio	70
Heading Resolution	0.1 [deg]
Heading Accuracy RMS	5 [deg]
Heading repeatability ($\sigma 1$) RMS	±0.3 [deg]
Heading Hysteresis ($\sigma 1$) RMS	±0.3 [deg]

To overcome the problem that the magnetometers need to be tilt compensated, and the fact that the HMC6343 is designed for accelerated conditions, the tilt compensation is done on the main processor using roll and pitch information from the AHRS. Non-linearity and biases are evidently present in the magnetometer data but the unit is calibrated in location for soft and hard iron effects so these are ignored. A noise power of 5 deg/s RMS is added to the simulated data as the module performed poorly with the extra noise present while the aircraft is flying.

7.4.4 GNSS Module

The Locosys LS20031 satellite receiver [39] used for this module was one of the fastest modules available on the market when the GNSS module was first designed. The GNSS module has changed little from its first design in early 2009 although the parsing processor used to interface the GNSS module's National Marine Electronics Association (NMEA) communication protocol to the common I/O bus has been updated several times. The performance of the GNSS module is shown in Table 7.6. The satellite receiver is capable of using Satellite-Based Augmentation Systems (SBAS) including the Wide Area Augmentation System (WAAS) , the European Geostationary Navigation Overlay Service (EGNOS) and the Multi-functional Satellite Augmentation System (MSAS).

Table 7.6: LS20031 GNSS Module Performance

2D RMS Accuracy	3 [m]
2D RMS Accuracy with SBAS	2.5 [m]
Measurement Rate	10 [Hz]
Number of channels	32
Frequency Used [MHz]	L1 1575.42, C/A code
Hot Start Acquisition Time	2 [s]

There was no error modelled on the GNSS data in simulation. This is because the module has filters on it that mean the error is difficult to mimic and the GNSS is only used as a reference in the simulations, meaning there is no need to model the error. GNSS latency is modelled as a delay of 0.1s which is the refresh rate of the module.

7.5 Processor Evolution

The evolution of processing power is one of the major drivers behind the evolution of the centreboard used. The original Tronix Dacio 300 data acquisition board is based around a 5 MIPS (Million instructions per second) microchip PIC16F877A. The PIC16F877A is a versatile 8-bit processor but lacks serious computing power. As newer processors were released they were adopted. Microchip processors were used as the University already possessed programming licenses. ARM Processors are a direct competitor to microchip processors. ARM processors tend to be cheaper and more powerful but are less well equipped and more operationally sensitive. As can be seen from Fig. 7.11 a number of processors were used. Eventually the dsPIC family of processors was settled upon. The dsPIC family of microchip processors are the most powerful, competent processors that the University license supports. The dsPIC family of processors are 16-bit processes that operate at 40 MIPS. This represents an extremely large performance improvement of between 10x and 30x depending upon the amount of floating point numerical manipulation carried out.

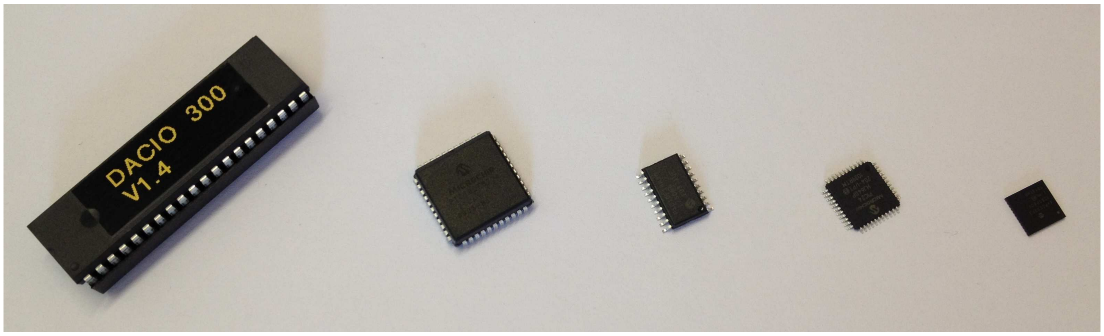

Figure 7.11: Evolution of Processors

Gumstix processor sticks were also investigated. These processors are capable of operating a full Linux operating system. These processors are extremely powerful and can be used to good effect. However their expensive and delicate nature means that under normal lab operating conditions their practical operation is beyond the budget of this project. The Gumstix central processing unit is shown in Fig. 7.12.

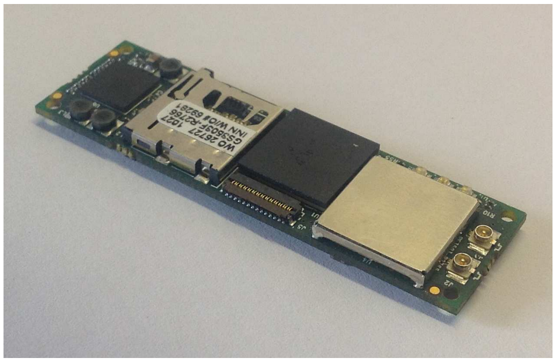

Figure 7.12: Gumstix Processor

With the Gumstix processor difficult to program and even more temperamental to operate a family of OPU were developed. As mentioned the latest OPU uses a dsPIC33FJ128GPX04 series processor. This processing board has the following capabilities:

- Two master I^2C buses to allow a wide variety of sensors to be plugged in
- A slave I^2C bus to allow interface with a higher level processor like Gumstix if desired
- A UART socket to allow communication with the ground or with a higher level processor like Gumstix if desired
- A full chip programming header

Although there are no addressing clashes for the sensors, the ribbon cables used are not twisted pairs, this means that only a limited length of cable can be used and therefore limits the number of sensors on a bus. It is for this reason that a second master I^2C bus was found helpful. The OPU is shown in Fig. 7.13.

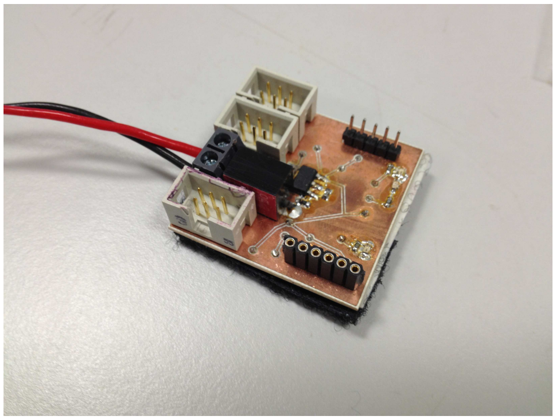

Figure 7.13: On-board Processing Unit

This OPU unit made it possible to code the algorithms developed on-board. The processors used are summarised in Table 7.7.

Table 7.7: Processor Performance

Processor	Bit Count	CPU Speed	ROM	RAM	MIPS
PIC16F877A	8	20 Mhz	14.3 Kb	0.3 Kb	5
PIC18F14k50	16	48 Mhz	16 Kb	0.7 Kb	10
PIC18F458	16	40 Mhz	32 Kb	1.5 Kb	10
dsPIC33FJ128GP204	16	73 Mhz	128 Kb	16 Kb	40
OMAP 3530 ARM7	32	720 Mhz	512 MB	512 MB	1400

The transfer of the algorithms from MATLAB/Simulink into C was time consuming. The algorithms were developed in the MATLAB/Simulink environment. Once the algorithms were deemed ready they were re-coded in embedded MATLAB, using a structure layout. The MATLAB structure format is similar to the CCS (hardware version of C) software used for the processors. Once this code was checked it was transferred to CCS, where bracket types and declarations were changed to enable compilation.

7.6 Servo Control Modules

Other ancillary circuit boards were also produced to enable ground tests. A robot controller board was produced to control a Lynxmotion Rover as shown in Fig. 7.14. This enabled GNSS tracking ground tests.

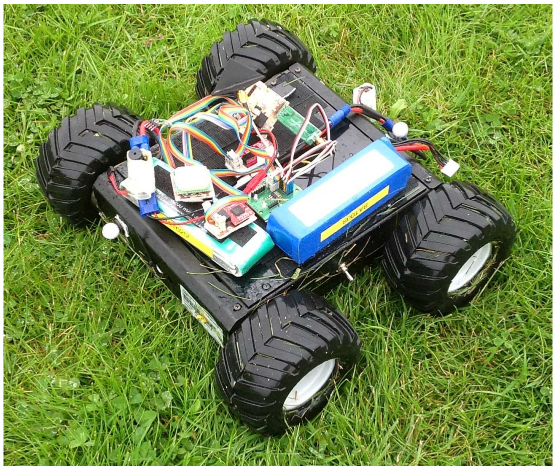

Figure 7.14: Lynxmotion Rover with Avionics Fitted

The controller board used is shown in Fig. 7.15. This board was designed by the author and subsequently commercial produced as it was extensively used by project students and more were needed than could be practicably made by hand. This servo controller board proved very versatile having a powerful processor with 4 general purpose input/output rails, I^2C and a serial header, along with a PGC/PGD [43] full chip programming header.

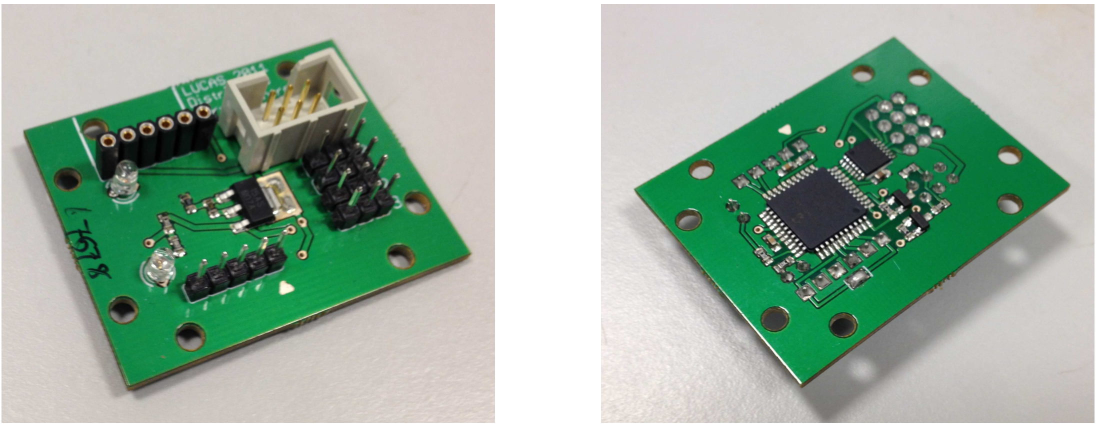

Figure 7.15: Rover Servo Control Board

The servo controller board shown in Fig. 7.15 could only support a maximum of 4 servo channels, aircraft require a board capable of supporting more servos. To that end the board shown in Fig. 7.16 was developed. The aircraft servo control has 8 servo inputs and 8 servo outputs to enable full fail-safe control of aircraft.

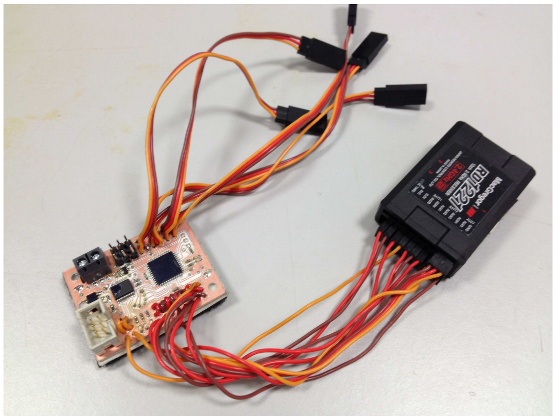

Figure 7.16: Final Version of the Fail-Safe Control Module

This fail-safe was designed to be able to make critical decisions as to the health of the on-board equipment. The fail-safe module was able to interrogate the receiver to determine the status of the communication link with the pilot on the ground. The fail-safe module was also able to interrogate the central processing unit to ascertain the functionality of the on-board flight control system. Given this information the fail-safe module then decided how to allocate control of the aircraft. This system enabled the pilot on the ground to remain in full control of the aircraft's systems, operating overrides etc. If however the aircraft lost contact with the ground the on-board systems would recognise this and perform a set procedure as chosen by the pilot on start-up. Typically this was to attempt to fly back over the take-off area at a safe altitude (normally 100 m high). This system prevented the aircraft being needlessly lost, as the normal fail-safe mode adopted by the receiver would be to perform a controlled crash.

7.7 Communication Set-up

7.7.1 Hardware

The Tronix Dacio 300 was supplied with high power Bluetooth modules. This was slightly surprising as Bluetooth is normally regarded as a short range method for serial communication. Initial investigations quickly proved Bluetooth to be a formidable means of communication. The modules supplied were capable of over 100m range. The modules were fitted with better aerials which boosted range to over 500m. Because of the nature of the Bluetooth command protocol few packets are lost, although the data connection is not as fast as Wi-Fi.

Although the Tronix Bluetooth module is one of the fastest on the market it is quite big and bulky for an aircraft to carry. It was for this reason the Tronix modules were replaced by Sparkfun BlueSmirf modules, as shown in Fig. 7.18.

ZigBee radio modules were also experimented with. ZigBee radio modules offer a rebroadcasting feature allowing a number of modules to communicate with each other. This offers the capability of multiple UAVs communicating with a ground station or cooperating with one another. The ZigBee radio modules although communicating with each other at a high data rate are throttled to 115200 baud on output by design. This is half the combined data rate of the Bluetooth modules which can operate at 230400 baud. The ZigBee radio modules

Figure 7.17: Tronix Bluetooth Module

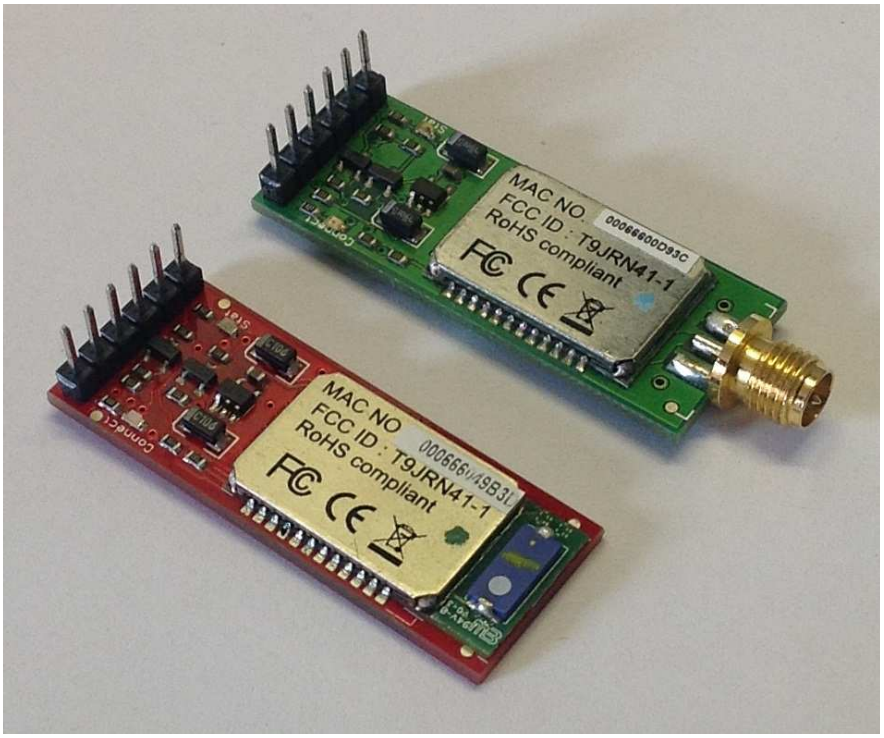

Figure 7.18: Sparkfun Bluetooth Modules

are shown in Fig. 7.19.

The obvious solution to this throttled data rate is to use Wi-Fi. Roving Networks provides a range of Wi-Fi based Wi-fly modules capable of providing data rates up to 1 Mbps. A Wi-fly module is shown in Fig. 7.20.

An alternative to Roving Networks Wi-fly modules are Carambola modules. Carambola modules offer the possibility to data log on the module simultaneous to transmission. Carambola modules are shown in Fig. 7.21 in base station and aircraft configuration.

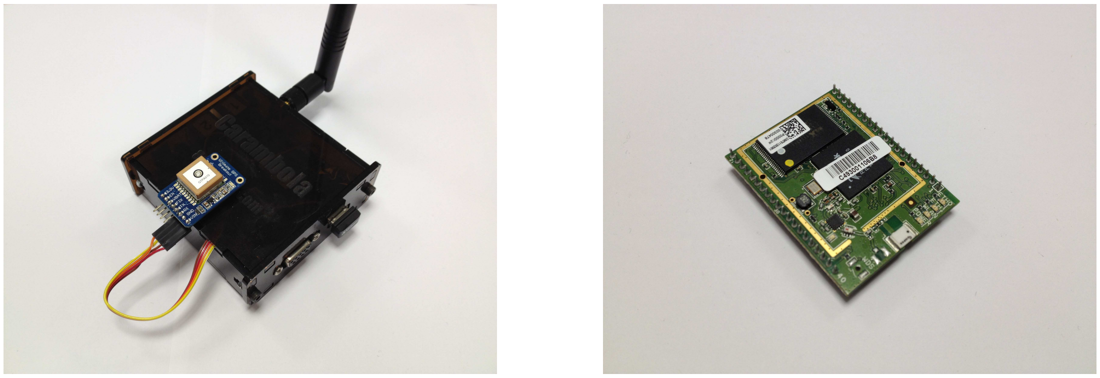

Figure 7.21: Carambola Radio Modules

As it stands for point to point communication Bluetooth is still the preferred method as it is both fast and provides a more stable means of communication than the alternatives.

7.7.2 Communications Protocol

Along with trying a range of different communication hardware a number of different communication protocols were also investigated. A formal communication protocol, whether custom or commercial, was needed because two-way communication was occasionally essential. A good example of this needing to communicate with the aircraft is the setting of target way-points. Changing the aircraft's current target way-point may originate from the need to repeat a section of test or the desire to bring the aircraft home (closer to the pilot to facilitate an easier landing). This subsection briefly describes the communication protocols tested and gives a justification of the final protocol used.

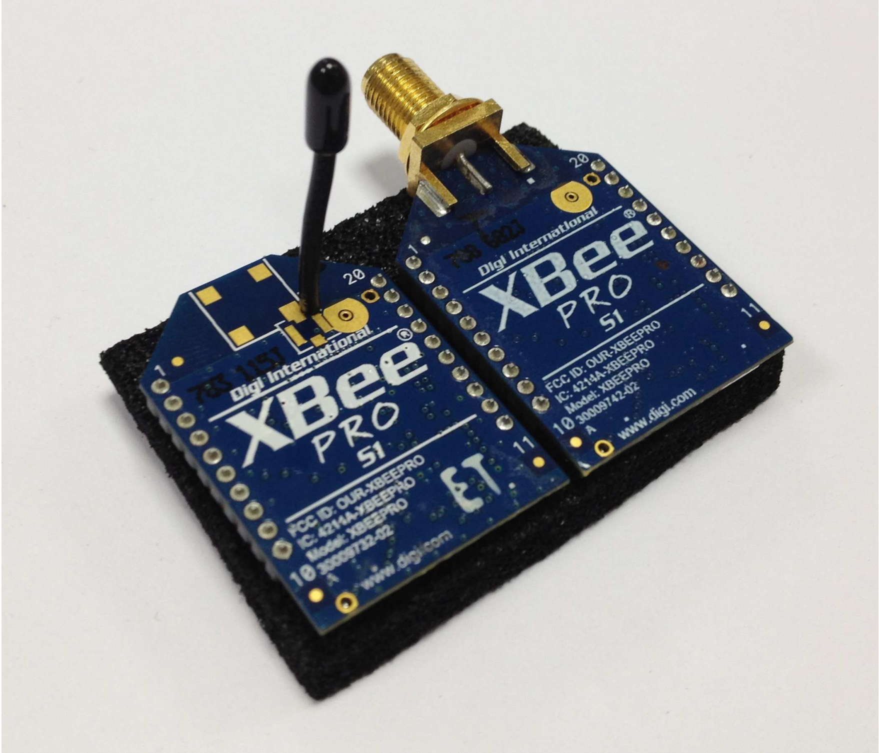

Figure 7.19: ZigBee Radio Modules

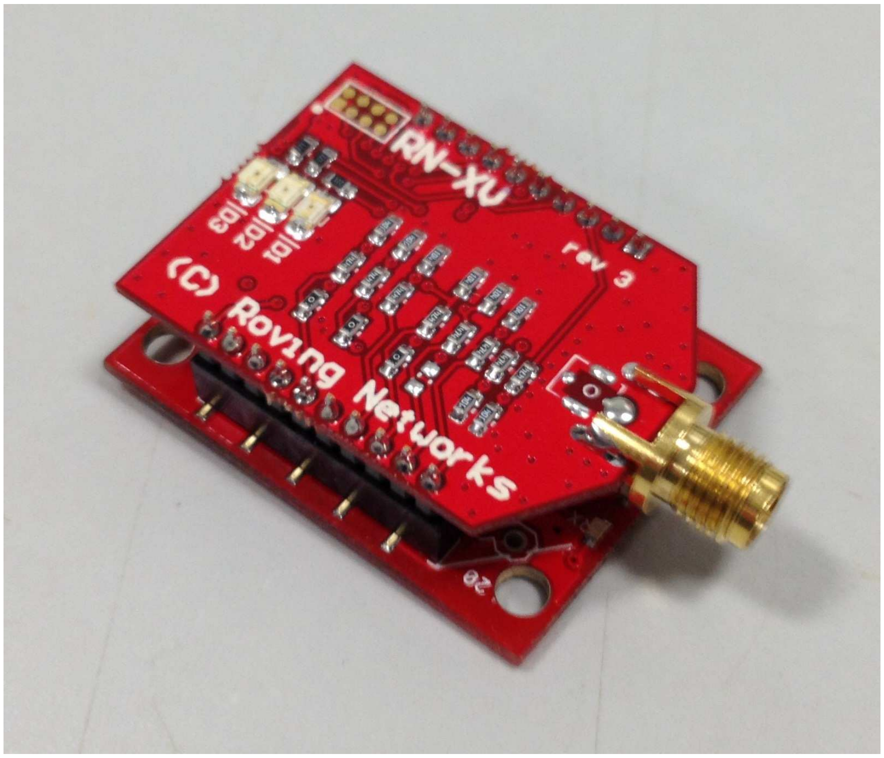

Figure 7.20: Wi-fly Radio Modules

The original Dacio 300 data acquisition board came with a custom data communication protocol developed by Tronix. This communication protocol was similar to the Lynximotion communication protocol used on their SSC 32 servo controller. The SSC 32 communication protocol is a simple ASCII-based communication protocol designed for high school students. ASCII-based communication protocols only use half of the available characters and can support sum checks. As a result the SSC 32 communication protocol is reliable and easy-to-use resulting in it being widely adopted. The key drawback to the Lynximotion ASCII-based system is that it is a request based protocol; where the user has to request each piece of data required in succession. This need to request the data repeatedly slows the protocol, although means that protocol is extremely reliable. Using this Protocol the data rate was limited to around 10 Hz. This data communication protocol which we were locked into while using Tronix hardware was one of the key contributing factors to moving on to custom hardware.

Using in-house custom hardware it was possible to develop a custom data communication protocol or implement existing communication protocols. The MAVLink protocol is an existing open source communication protocol that is designed for an application to micro air vehicles.

This MAVLink communication protocol is a cut-down version of communication protocols used by larger UAVs. This communication protocol is well-established, reliable, with a good redundancy, and data integrity checks. Sets of information are sent in relatively small packet groups meaning that even on poor communication hardware limited amounts of data is lost. However the MAVLink protocol is based on protocols for larger aircraft this means that the protocol is intended for a relatively slow refresh rate. Despite the MAVLink protocol being successfully used by other projects at Loughborough University it proved impossible to modify the MAVLink protocol to operate fast enough to get all of the desired data back from the test aircraft at sufficiently high refresh rates. This was unfortunate as the MAVLink protocol is arguably the best of the ones tried.

As the MAVLink protocol proved too slow, a custom protocol based on the Tronix/Lynximotion protocols was developed. The protocol developed, unlike the MAVLink protocol, was again ASCII-based. This ASCII-based approach enabled extremely simple communication between the aircraft and ground with the user able to simply type commands into hyper-terminal software. Key alterations between the Tronix/Lynximotion protocols and the one developed was the removal of the need to request data. The communication protocol provided the set of data requested repeatedly until the dataset requested was altered. This persistent feedback of the data until requested for different data meant that the entire dataset (accelerometers, gyroscopes, magnetometer, IAS, VSI, pressure altitude, GNSS, ADGNS, and Time) could be obtained at over 100 Hz. The simplicity of this communication protocol also facilitated user control of the aircraft for way-point or task selection.

7.8 Aircraft Used for Practical Testing

Fig. 7.22 shows the selection of UAVs used for the testing of the algorithms presented in this thesis. From Left to right in Fig. 7.22 the aircraft are a Seagull EP-Pioneer, X-Models XCalibur and Phase3 Squall HP.

Figure 7.22: Aircraft Used During Testing and Development

The XCalibur is a high performance motor glider originally developed for racing. The XCalibur is the basis for the performance predictions in Chapter 3. The EP-Pioneer was used for the validation of the attitude heading reference and navigation systems to be presented in Chapter 8. The EP-Pioneer was chosen in preference to the XCalibur as it has long durable landing gear while the XCalibur has a simple skid. The EP-Pioneer also has an easier to access avionics bay.

7.9 Conclusion

A powerful modular open architecture sensor suite and on-board processing unit that allows straight forward implementation of new algorithms has been introduced. The performance of the sensors has been given along with how the sensors were modelled in the simulation environment. A brief introduction to the processors and the communication set-up used gives an overview of the autopilot's capabilities. This sensor suit will be used in Chapter 8 to verify the algorithms developed and tested in the simulation environment in Chapters 4, 5 and 6.

Chapter 8

Practical Testing

8.1 Introduction

In order for new techniques to be adopted it is vital that the techniques advocated are thoroughly tested in realistic real-world scenarios. This chapter presents the practical flight tests carried out to validate the theoretical and simulation results from Chapters 4, 5 and 6. To implement new techniques an open system architecture is needed. Just such an open architecture system was developed and detailed in Chapter 7. With the hardware and algorithms in place the validation is dealt with in the following sections:

- Validation of the air data augmented reference data
- Validation of the air data augmented attitude heading reference system
- Validation of air data augmented navigation

A summary of each aspect is provided at the end of the respective section. The implications of all of the aspects are highlighted in the conclusion.

8.2 Validation of the Attitude Heading Reference System

In order to validate the AHRS it is necessary to deal with the two aspects of, attitude reference and filtering separately. Good reference attitude data is a prerequisite to any form of filtering of the AHRS and therefore is dealt with first.

Once the reference data is validated then the AHRS filtering techniques will be validated.

8.2.1 Reference Data for the Attitude Heading Reference System

In order to validate the algorithms for correcting the reference data for the AHRS it is essential to have a high accuracy external reference that can be used as a comparison. The reference data used for this part of the validation was supplied by the sensors on the National Flying Laboratory Centre's Jetstream 31 aircraft. This aircraft has a high accuracy IMU which is used for the comparison. For the validation of the algorithms to be representative of the UAV application an extra set of lower quality sensors was placed next to the aircraft's IMU. The sensors used for this test are detailed in Chapter 7.

The data for this comparison was collected as part of a dynamic mode demonstration flight. During the flight test itself, no data processing was attempted. The data from the aircraft's IMU and the raw data from the sensor suite were stored for post-processing on the ground after the flight. The aircraft's on-board sensors were used to provide the pressure information for the tests carried out as it was impractical to use custom sensors. The use of the aircraft's sensors is justifiable as the data quality is comparable to the quality obtainable by a UAV's on-board sensors.

The test condition is the taxi out, take-off and climb to altitude. This prolonged test is representative of the first phase of a typical mission. The test contains three areas of interest; the turn at the end of the runway to runway heading, the take-off roll and climb to altitude. For completeness the air data augmented technique advocated in Chapter 4 will be compared with a tilt sensing technique that does not take into account the global accelerations of the aircraft. The aircraft's on-board ring laser IMU is used as a reference for the comparison.

The 180 degree turn onto take-off heading starts at around 40 seconds into the test data presented in Fig. 8.1 and Fig. 8.2. It can be seen that the unbalanced turn of the aircraft is estimated with acceptable accuracy by both techniques. This is because the aircraft is travelling slowly and there is limited centripetal acceleration.

The second flight phase of interest is the take-off roll. The take-off roll starts

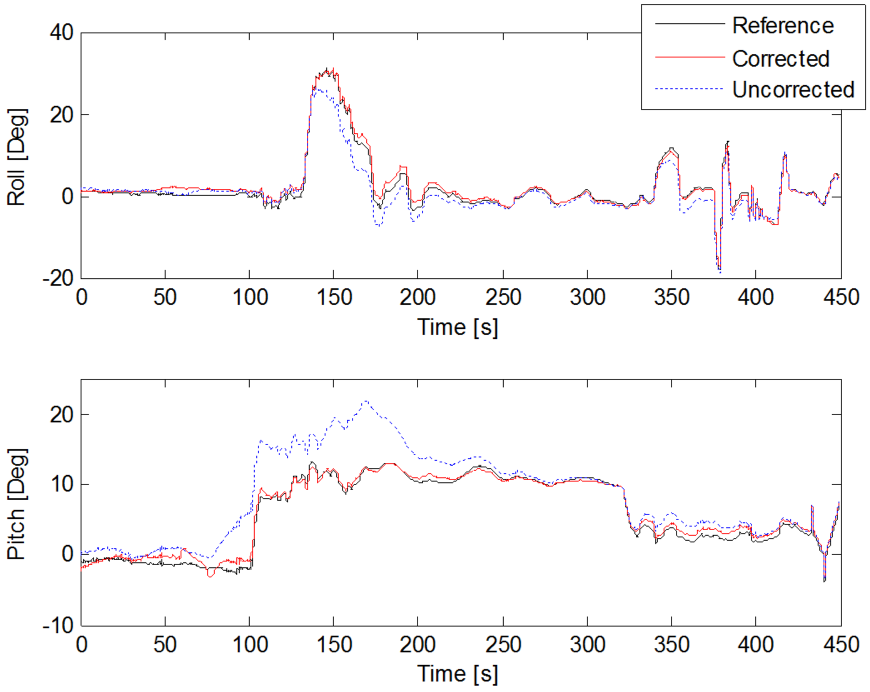

Figure 8.1: A Comparison of Estimated Attitudes Provided by the Air Data and Non-Air Data augmented Reference Algorithms

at approximately 75 seconds into the data presented in Fig. 8.1 and Fig. 8.2. This is of key interest as it is a critical flight phase, with the aircraft likely to be heavy, travelling fast and in close proximity to hard objects. As the aircraft accelerates the perceived gravity vector on the aircraft is thrown rearward. The result of this is that an estimate that does not take this acceleration into account perceives a change in the aircraft's pitch angle. The normal way of preventing this spurious data from having a devastating effect on the estimation is to measure the vector magnitude of accelerations of the aircraft; if the aircraft is not within a finite tolerance of the expected gravitational accelerations the data is merely ignored. It can be seen in Fig. 8.1 that the pitch estimations converge as the aircraft stabilizes in un-accelerated flight.

The third area of interest is the climb to altitude, and of particular interest is the coordinated turn off the runway heading. The turn starts at around 130 seconds into the test data presented in Fig. 8.1 and Fig. 8.2. In a balanced turn the acceleration of the aircraft is perpendicular to the wings of the aircraft. This means that the roll angle measured by the on-board sensors will always tend to zero. Again this is not necessarily a problem as the accelerated flight condition can be noted and the filtering stopped. This lack of a roll estimation would pose a problem for an aircraft that is expected to perform circling flight for prolonged periods; as the aircraft would be fully reliant on the gyroscopes for a roll estimation. The result of not ignoring the spurious data is shown in Fig. 8.1 and Fig. 8.2; the roll angle estimation tends to zero prematurely. This means the aircraft is vulnerable to the spiral mode.

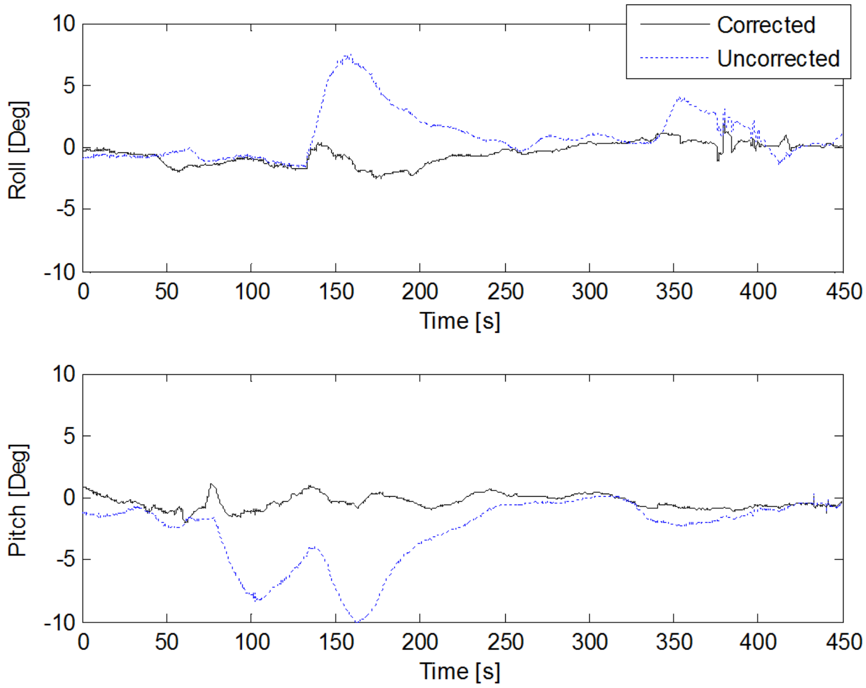

Figure 8.2: A Comparison of Errors in the Estimated Attitudes provided by an Air Data and Non-Air Data augmented Reference Algorithms

It has been demonstrated that by using air data to correct for global accelerations of the fixed wing aircraft in question, that a significant improvement in the estimation of the attitude of the aircraft can be had. The verification presented showed that the low cost MEMS sensors are capable of errors of less than 4 degrees, with a standard deviation of less than 2 degrees, when compared with the inertial measurement unit on-board the National Flying Laboratory Centre's Jetstream 31 aircraft. This error in the estimation was larger than expected and may originate from misalignment of the MEMS sensors with respect to the aircraft's IMU. The elimination of the need to stop or alter the filtering process during accelerated flight conditions means that the aircraft's flight control system is not as susceptible to incipient spiral mode failure. This opens up the use of MEMS sensors to UAVs that require accurate estimations of pose in order to perform accurate dynamic manoeuvres for prolonged periods.

8.2.2 Complete Attitude Heading Reference Flight Test

8.2.2.1 Set-up

The set-up for the practical testing of the algorithms developed is as similar to the simulation set-up as is possible. However, inevitably, the simulation set-up does not fully encapsulate all of the uncertainties. The aircraft used for the practical testing was an EP Pioneer as shown in Fig. 8.3.

Figure 8.3: Seagull EP Pioneer

The actual trajectory of the flight tests carried out is shown in Fig. 8.4. The test flight trajectory differs from the simulation flight trajectory in two ways. Firstly, the autopilot although capable of an automatic take-off has not yet

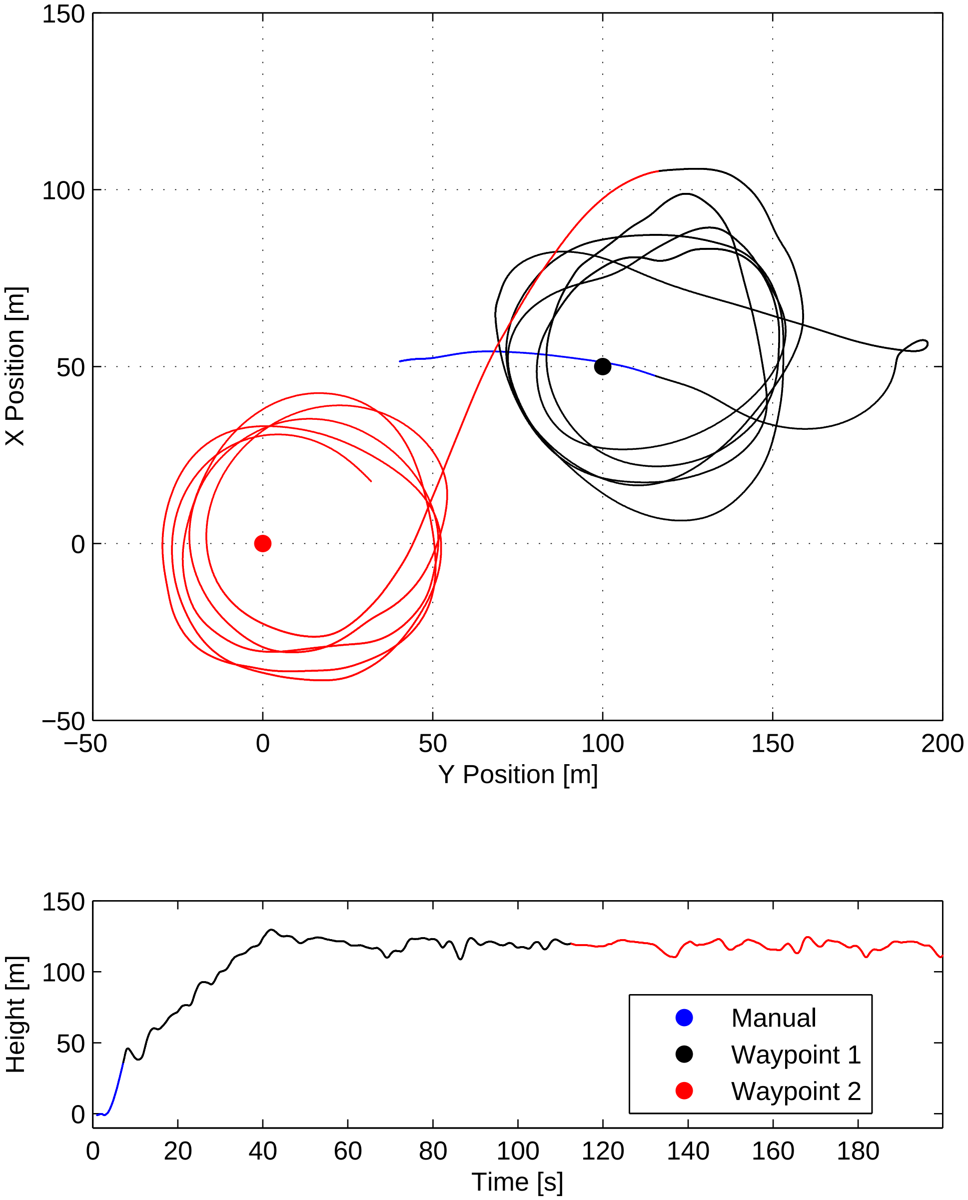

Figure 8.4: Actual Practical Flight Test Position

successfully demonstrated one. It was therefore felt that for the safety of the equipment involved the autopilot would be given command of the aircraft at the earliest appropriate point after take-off. Command was given to the autopilot approximately 7 seconds after take-off and at an altitude of approximately 40m. Secondly, the aircraft was allowed to orbit the first way-point for approximately 60 seconds before being tasked with the second way-point. This delay in selecting the second way-point was necessitated by the fact that the aircraft was flying in extremely strong wind conditions (8m/s WWS gusting 12m/s). The strong wind conditions meant that the flight control algorithm, that is given no prior information about wind conditions, took approximately 40 seconds to stabilise. This results in the aircraft already being at the desired altitude by the time the first orbit was completed. To facilitate an effective comparison between the simulation and practical results the aircraft was commanded to continue to orbit the first way-point for a further 60 seconds before moving on to the second way-point. It can be graphically seen from Fig. 8.4 how the wind compensation algorithm stabilised with time; the second way-point is more accurately circled. Ideally the test would be repeated in calmer conditions.

Another key difference between the simulation environment and reality is the lack of a truth model for the practical experiment. It was decided that the use of highly specialised laser ring gyroscopes was outside the remit of this project, instead the EKF solution will be used as the truth model for the practical experiments. Although the EKF solution is clearly not perfect, the objective of the filters derived is to provide the performance of a Kalman filter with low computational burden. As a target is to mimic the EKF it is therefore appropriate to use this data as the truth model.

8.2.2.2 Results

As with the simulation set-up, control was handed to the autopilot with a high initial pitch angle, approximately 1 radian. As in the simulation, the autopilot was commanded to circle at a high bank angle (approximately 1 radian) so the high initial pitch angle was unsustainable with the power output of the aircraft. The autopilot therefore lowered the pitch angle to a more sustainable value to continue the climb. This demonstrates the accuracy of the simulation model but, as in the simulation results, lowers the non-linearity in pitch and therefore reduces the difficulty for the filter. Fig. 8.5 shows the pitch angle estimation for the selection of filters investigated. Again the reader is not supposed to ascertain the relative accuracies of the filter from this plot rather to gain an overview of the aircraft attitudes.

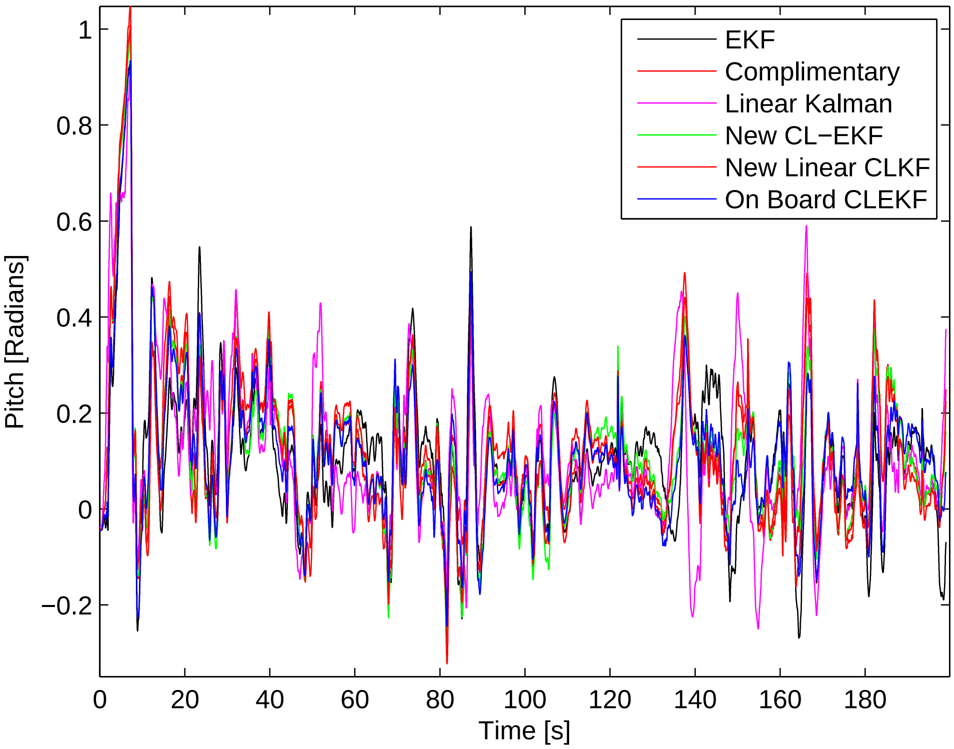

Figure 8.5: Pitch Angle for AHRS Flight Test

As alluded to in the previous paragraph and simulation results the aircraft was tasked with tightly orbiting a way-point. In nil wind conditions this would result in the aircraft executing a continuous high banked turn as shown in the simulation results. However with the presence of wind for the aircraft to maintain its orbit the bank angle must be varied. Fig. 8.6 shows that the autopilot had to vary the bank angle between its full allowable range of +/-1.3 radians to maintain station. This adds considerable difficulty to the task of filtering the AHRS data. Fig. 8.6 clearly shows the change in orbit location and direction at 120 seconds.

If the EKF attitude data is used as the reference truth model it is possible to compare the relative accuracies of the filters. Fig. 8.7 shows the pitch error variance of the filters. The linear Kalman filter performs the worst of all the filters shown. The likely reason for the Kalman filter performing worse than the simu-

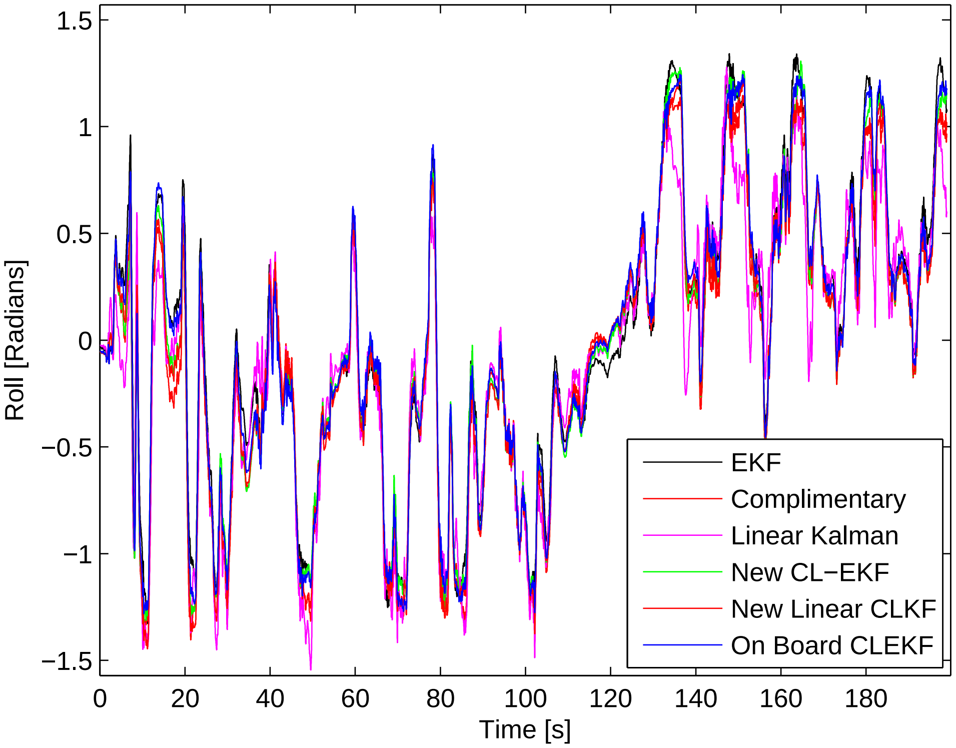

Figure 8.6: Roll Angle for AHRS Flight Test

lation runs would otherwise suggest could be attributed to the more challenging filtering conditions provided by the less stable attitude of the real aircraft. The complimentary filter performs as expected being the next most accurate with the linear closed loop Kalman filter providing similar but slightly better performance. The new closed loop extended Kalman filter provides the closest estimate to the extended Kalman filter. Of specific note is the on-board implementation of the closed loop extended Kalman filter. This filter is identical to the post processed closed loop extended Kalman filter with the only difference being that it was implemented on-board the aircraft. This on-board implementation of the CLEKF is even closer to the EKF solution. There are two reasons for this. Firstly the on-board CLEKF had access to more accurate gyroscope information as the gyroscope readings could only be relayed to the ground to three decimal places. Secondly as the calculation was done on-board the effect of data loss in the communication protocol is completely eliminated. The fact that the estimation of the on-board implementation of the CLEKF is closer to the extended Kalman filter supports the justification of using the EKF as the truth model.

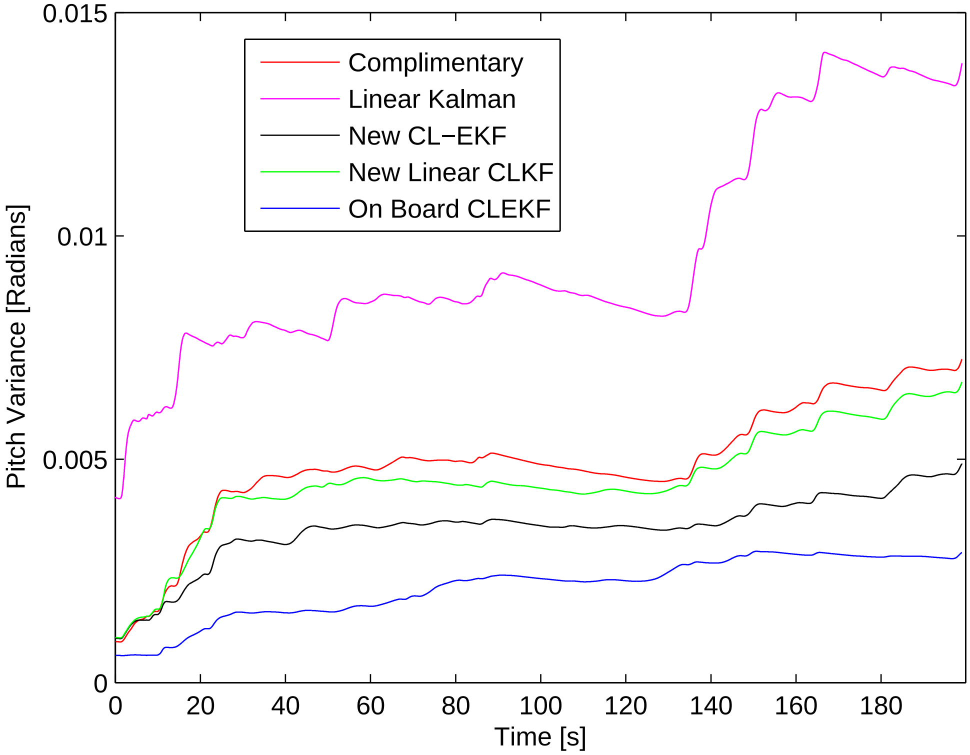

Figure 8.7: Pitch Variance for AHRS Flight Test

Fig. 8.8 shows the roll error variance of the filters. Fig. 8.8 demonstrates much the same behaviour patterns as Fig. 8.7 but with a further exaggeration between the relative accuracy of the filters. This clearer spread in relative accuracies is due to the increased non-linearity of the filtering problem in roll, as the aircraft spends approximately 50% of the time at roll angles beyond 45 degrees. As in Fig. 8.7, Fig. 8.8 shows that the new CLEKF filter provides the closest solution to the EKF. However one key difference is the greater spread in the relative variances of the complimentary and linear CLKF filters.

Flight test results from the attitude heading reference study show the proposed filter fulfils the desired specification for a filter with significantly better performance than complimentary filters while retaining their computational elegance of a complimentary filter. Tables 8.1 and 8.2 summarise the results presented.

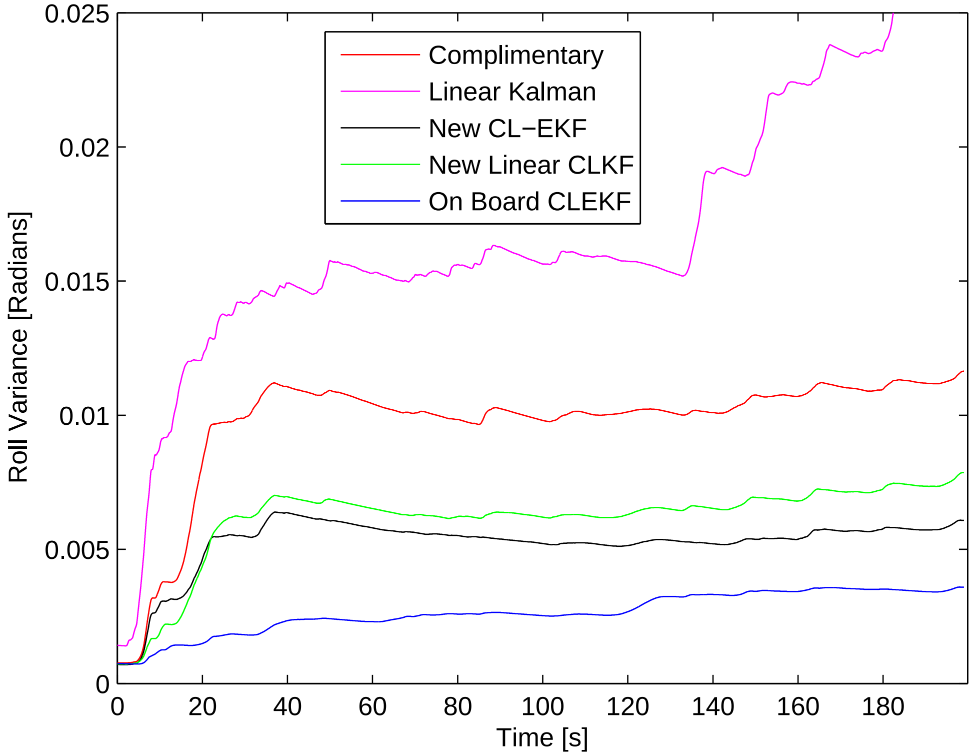

Figure 8.8: Roll Variance for AHRS Flight Test

Table 8.1: Comparison of Pitch Angle Estimations

Methodology	Variance	Standard Deviation [rad]
Linear Kalman	0.01386	0.1177
Complimentary	0.007241	0.0851
New Linear Kalman Filter	0.006727	0.0820
New Non-linear Kalman Filter	0.004902	0.0700
New Non-linear Kalman on-board	0.002913	0.0540

Table 8.2: Comparison of Roll Angle Estimations

Methodology	Variance	Standard Deviation [rad]
Linear Kalman	0.02607	0.1615
Complimentary	0.01164	0.1079
New Linear Kalman Filter	0.00786	0.0887
New Non-linear Kalman Filter	0.006076	0.0779
New Non-linear Kalman on-board	0.003591	0.0599

8.3 Air Data Augmentation of Global Navigation Systems

Another significant area of interest is navigation performance, particularly navigation performance with poor or denied access to GNSS. Following from the developments presented so far in this report it is possible to extrapolate a similar structure to utilise air data to form a navigation solution. Three navigation solutions that provide a limited redundancy against loss of GNSS will now be presented and discussed with the aid of simulated and real test data.

8.3.1 Practical Testing of Air Data Augmented Global Navigation

8.3.1.1 Set-up

To retain equivalency to the simulation results this same bow tie flight pattern is utilised for the practical testing. However, as in the attitude heading reference system verification testing carried out, wind plays a part.

8.3.1.2 Results

Fig. 8.9 shows that all three methods are capable of providing stable augmented navigation solutions while in the presence of GNSS data. This is a confirmation of the estimated simulation results.

Fig. 8.10 shows the relative position error of each filtration method. One key difference between the simulation and the practical results is the fact that the

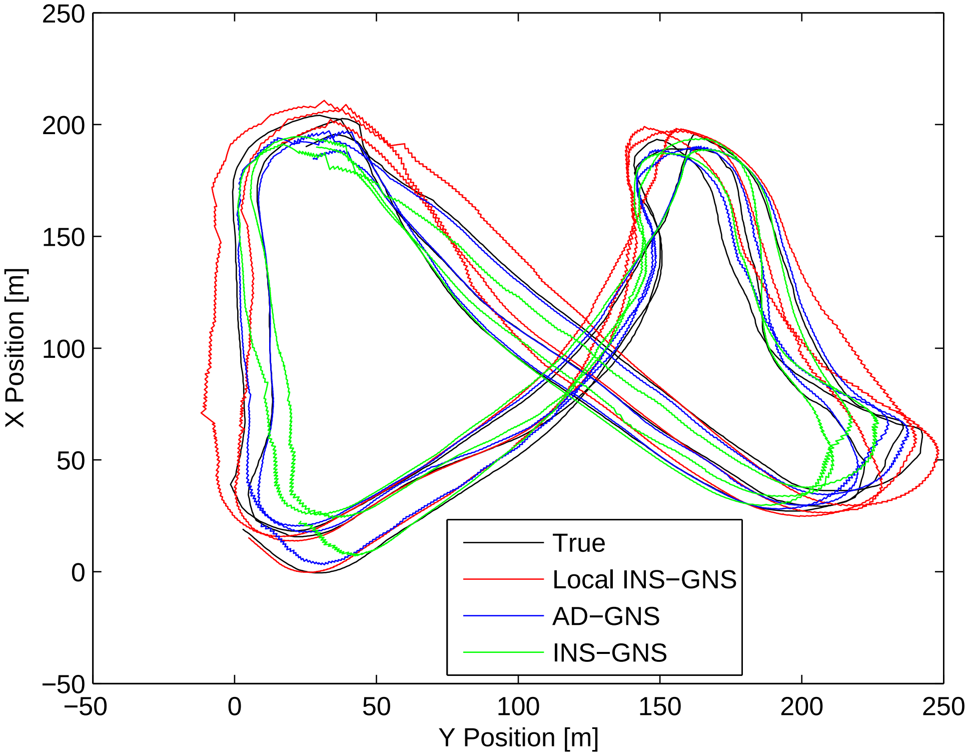

Figure 8.9: Actual Bow Tie Flight Pattern Achieved

pressure based and constrained inertial navigation solutions display remarkably similar error characteristics, where in the simulation results there was a clear separation. This is mainly due to the fact that the strong wind conditions in the test meant that the wind estimation was not of sufficient fidelity. The consequence of this poor wind estimation is a higher rate of drift than predicted by simulation. The lower estimation errors of the inertially based solutions also indicates that the noise modelled on the accelerometers in the simulations is slightly over estimated. This is consistent with the ethos of this project as there is a strong desire to be rigorous in the testing carried out by not using overly flattering scenarios at any point.

The three methods of augmenting GNSS have been investigated, inertial navigation, constrained inertial navigation and air data augmented. All three methods provided adequate estimates of position while GNSS data was available, providing estimates within the expected error of the GNSS module. Once the GNSS data is no longer available the air data augmented solution presented provided

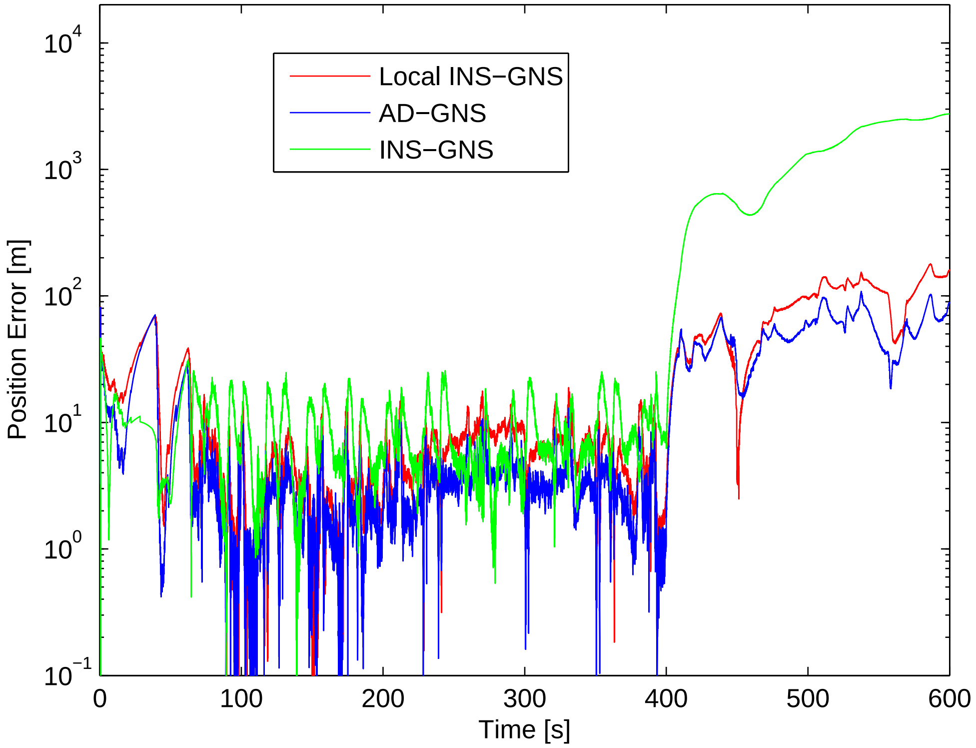

Figure 8.10: Comparison of Position Error with GNSS Failure at 400 Seconds

the most accurate solution in both simulation and real life tests despite the wind estimation not having sufficient time to fully converge to the true value.

8.4 Conclusion

This chapter has seen the verification of the methodologies used by real-world testing.

Firstly, the air data augmentation technique advocated in Chapter 4 was validated against Cranfield University National Flying Laboratory Centre's Jetstream 31 aircraft's highly accurate laser inertial measurement unit. Results show the air data augmented approach was capable of estimating the attitude of the aircraft to within 4 degrees maximum error and with a standard deviation of less than 2 degrees (0.03 rad). This correlation between the reference data and the aircraft's IMU means that the air data augmented approach can be reasonably relied upon to provide reference data for advanced filtering techniques. The adoption of this air data augmented reference eliminates the need to stop or alter the filtering process during accelerated flight conditions, meaning that the aircraft's flight control system is not as susceptible to incipient spiral mode failure. This opens up the use of MEMS sensors to UAVs that require accurate estimations of attitude in order to perform accurate dynamic manoeuvres for prolonged periods.

Secondly, the advanced closed loop extended Kalman attitude filter derived in Chapter 5 was validated, against existing filtering techniques, using realistic conditions on a real UAV. Climbing and circling flight was used to provide challenging filtering conditions for the filters. The new CLEKF has been shown to track the performance of a EKF with an error 2.7 times less than that of a complimentary filter with equivalent computational burden.

Thirdly, the air data augmentation technique presented in Chapter 6, for making the global position estimation more robust, has been compared to the same range of more traditional inertially augmented GNSS filters, as presented in Chapter 6. Results show that despite the air data augmentation technique being poorly tuned and the accelerometers performing better than had been modelled, the air data augmentation technique still outperformed the inertially augmented GNSS filters.

The practical tests presented in this chapter correlate extremely closely with expectations based on the simulation results presented in Chapters 4, 5 and 6.

Chapter 9

Conclusions

9.1 Summary

This thesis presents the research work conducted in facilitating efficient extraction of atmospheric energy from naturally occurring air currents caused by shallow layer cumulus convection. A broad range of disciplines were employed to enable this research to be conducted, including mathematical analysis, hardware development, software development, avionic hardware manufacture, software/hardware integration and flight test operation, to achieve the following objectives:

- to improve the parametric models used to accurately reflect structures of the shallow layer cumulus convection, otherwise known as thermals, in the UK, aiding understanding and performance projections.
- to design and demonstrate a range of methods to utilise atmospheric convection for extending the range and endurance of modern UAVs
- to derive and practically test a new closed loop implementation of the EKF for the AHRS, with a fraction of the computational burden while guaranteeing stability.
- to design and practically validate the inclusion of air data into the navigation system and thereby improve the robustness of the global navigation system and facilitating highly aggressive manoeuvres to be executed safely.

The research contributions of this thesis to the development of UAV performance lies in two distinct but intimately related areas: the design of flight control systems and strategies, and the development of highly accurate navigation algorithms of autonomous soaring UAVs. These contributions are summarised as follows:

Firstly, to enable accurate modelling of soaring flight, existing parametric thermal models were modified to specifically reflect the climate of the UK. This parametric thermal model was combined with other atmospheric prediction models to arrive at the first parametric atmospheric map to capture the time dependent nature of thermals, this included the growth, rise, drift, and death of the convective structure in the 3 dimensional map.

Secondly, a detailed non-linear aircraft dynamics model has been developed in MATLAB/Simulink and used to investigate the use of thermals to extend the range and endurance of modern UAVs. The application of the speed-to-fly theory to UAVs was discussed in conjunction with both maximising energy conservation and controlling target arrival time. Simulations showed that massive energy savings can be provided by the use of convection while offering the ability to precisely control arrival times over large distances. The application of soaring techniques to persistence over a target was investigated under similar conditions. While being tasked with persistence the XCalibur motor glider, modelled in the simulations, never used its main motor.

Thirdly, one of the key prerequisites to efficiently extracting atmospheric energy is efficient trajectory tracking. To facilitate real aircraft to accurately track trajectories, a new AHRS was developed which more closely integrates the air pressure data into the attitude solution. This air data augmentation technique was combined with a new closed loop implementation of the EKF to provide substantially superior attitude estimation than provided by a complimentary filter with an equivalent computational demand. This closed loop extended Kalman filter can be tuned off-line enabling analytical proof of stability to be provided, making it ideal for safety critical applications with low computational power. This new AHRS was subject to extensive real world flight tests demonstrating even better performance than was shown in the simulation environment.

Finally, attention was given to the navigation system. An air data augmented global navigation system was developed following a similar structure to that of the AHRS. This air data augmented navigation system was tested with the presence of GNSS data and without. The air data augmented navigation system was tested in both simulation and in reality demonstrating the ability to effectively provide a safeguard against GNSS denial or satellite tracking failure for a few minutes. This ability was verified while using a relativity aggressive flight pattern, demonstrating a potential application to UAVs that are required to perform aerobatics or operate in built up areas.

None of the testing carried out would have been possible without the custom avionics hardware developed specifically for this project. The development of the hardware was time consuming and complex but resulted in a modular system with more than five times the central processing power of the commercial autopilots available. One of the key benefits of using custom hardware was the ability to close-couple sensors, that would not normally have had a relationship, with new and unusual techniques.

9.2 Discussion and Future Research Directions

This thesis has presented several developments that represent large steps towards making everyday UAVs more robust, accurate, and energy efficient, however not all of the assertions have been rigorously proven.

The 3 dimensional time dependent atmospheric environment, used for the investigation of the potential benefits of allowing UAVs to employ soaring techniques, has been built by combining existing parametric atmospheric models with information from specialist publications relating to soaring. This model although closely following the information available has yet to be verified. Verification of this atmospheric model would require a large number of flights to be performed in order to record data and establish a statistical correlation with the predictions made by the model. Flights would be required as current meteorological measurements are only taken down to a resolution of 2km. This is insufficient to verify the thermal models. Accurate atmospheric models are of interest to a large number of people and will continue to be a valid area of research. One reason why validation flights were not attempted is the fact that UK air law changed, towards the end of this project, to restrict UAVs to less than 400ft above ground level. This had a major impact on the direction of this project and also means that other techniques like gust soaring are of more interest than previously. Gust soaring extracts energy from atmospheric turbulence caused by trees and other objects. Gust soaring although only offering a fraction of the energy of static soaring is an intriguing area for future research. The soaring techniques presented provided a massive energy saving over the use of the main motor but it was noted that 100% savings were not possible due to the power consumption of the on-board systems. It is noted that the control surface actuation is a major power draw and future work may wish to look at minimising control surface movement, whilst still providing the required trajectory tracking.

The air data augmented approach to attitude estimation has been validated by practical testing. Rigorous analytical proof of stability and practical validation of the attitude heading reference system has been provided. The air data augmented navigation algorithm, intended to aid the robustness of the global position estimation, has been tested thoroughly in real life but has not yet been analytically proven stable in all situations. This proof of stability although not needed for all applications is clearly desirable and is a viable area for further work.

The robust and accurate techniques for attitude and position estimation, although developed for soaring, have application to all tasks demanding ultra high precision or the precise execution of sustained aggressive manoeuvres. A common manoeuvre that would particularly benefit from the extra position and attitude accuracy is UAV auto-land. The techniques advocated would mitigate the landing accuracy penalty that a cramped abbreviated landing pattern would normally have with its incessant turning. The availability of smaller landing patterns makes smaller working areas achievable.

In summary, the proposed attitude heading reference and navigation algorithms described in this thesis have advanced the capabilities and robustness of UAVs by enabling more aggressive trajectories to be tracked accurately and reliably and thus facilitate the exploitation of advanced techniques like soaring to extend the range and endurance of UAVs. It is hoped that this will contribute to the future development of UAVs and encourage future work in related areas.

Appendix A

Kalman Filters

The Kalman filter is named after Rudolph E. Kalman, who in 1960 and 1961 published his now renowned papers with a statistically optimal recursive solution to the discrete-data linear filtering problem [32]. The Kalman filter is a form of Linear Quadratic Estimation (LQE) provided by a computationally efficient set of recursive equations. Despite the elegance of the filter it is only relativity recently, from the 1990s, that computers have been powerful enough to widely utilise Kalman filters. With the advancement in computing power the Kalman filter has proliferated applications requiring statistically optimal state estimators. Applications other than guidance, navigation that use Kalman filters include signal processing, computer graphics and economics.

A.1 The Linear Kalman Filter

The LKF is a set of mathematical equations that utilises state space formulation to provide a relatively computationally efficient recursive method for, statistically optimally, estimating of the state vector $x \in \Re^n$ of a discrete-time controlled process by minimising the mean of the squared errors. The process is assumed to be governed by a linear stochastic difference equation of the form of Equation (A.1).

$$x_k = Ax_{k-1} + Bu_k + w_{k-1} \tag{A.1}$$

This system is assumed to be driven by the state transition matrix, A, and disturbed by Gaussian noise w_k. The measurement vector $z \in \Re^n$ is assumed to be related to the state via the measurement matrix, H, in the form given in Equation (A.2), this is also assumed to have Gaussian noise present v_k.

$$z_k = Hx_k + v_k \tag{A.2}$$

Although most noise is not truly 'Gaussian', central limit theorem is used to assume Gaussian noise [49]. Similarly there is an assumption of equal power density at all frequencies or 'White' noise. As a recursive algorithm the LKF consists of two distinct steps, time update and measurement update, or prediction and correction. [58].

A.2 The Extended Kalman Filter

The EKF is a non-linear version of the Kalman filter which linearises about the current estimate of the mean and covariance of the system, via a form of Taylor series, so that a form of the linear Kalman filter equations can be applied. The EKF is widely regarded as a standard filter for non-linear state estimation in attitude and navigation systems; although other Kalman filter types like Unscented are applied.

The process is assumed to be governed by a non-linear stochastic difference function of the form of Equation (A.3).

$$x_k = f(x_{k-1}, u_k, w_{k-1}) \tag{A.3}$$

where u_k is a forcing function and w_{k-1} is the process noise. Similarly the non-linear measurement function is in the form given by Equation (A.4), where $z \in \Re^n$, v_k is the measurement noise.

$$z_k = h(x_k, v_k) \tag{A.4}$$

The linearisation of this non-linear process has two widely accepted problems:

1. Linearisation can lead to highly unstable filter behaviour if the local linearity assumption is violated
2. The derivation of the Jacobean matrices are non-trivial in most applications and can lead to significant difficulties in practical implementation

A.3 The Unscented Kalman Filter

The UKF [30] is an extension of the EKF to deal with the fact that if the process and measurement model are strongly non-linear the EKF can perform poorly. The UKF belongs to a family of sigma point Kalman filters that use a form of a deterministic sampling technique known as the unscented transform to project the mean and covariance non-linearly. The UKF method makes use of the same system model and measurement model as the EKF. To project the mean and covariance a set of sigma (sample) points distributed about the mean are projected using non-linear functions, these new sigma points are used to generate the new estimate of mean and covariance. These non-linear functions effectively preserve the Gaussian distribution assumption. This method has two useful attributes, strongly non-linear behaviour can be captured, and the Jacobian matrix no longer needs to be calculated.

Appendix B

Publications

1. Jonathan Clarke and Wen-Hua Chen, “Trajectory Generation for Autonomous Soaring UAS”, *Proceedings of the 17th International Journal of Automation and Computing* (IJAC), Vol. 9, No. 3 pp. 248-256, 2012. ISSN: 1476-8186.
2. Cunjia Liu, Jonathan Clarke, Wen-Hua Chen, and John Andrews, “Rapid prototyping flight test environment for autonomous unmanned aerial vehicles”, *International Journal of Modelling, Identification and Control*, Vol. 12, No. 3, pp. 200-209, 2011, DOI: 10.1504/IJMIC.2011.039699.
3. Owen McAree, Jonathan Clarke, Wen-Hua Chen, “Development of an Autonomous control system for a small fixed pitch helicopter”, *Advanced Computer Control (ICACC), Proceedings of 2nd International Conference on Advanced Computer Control*, Vol. 3, pp. 13-17, 27-29 March 2010, Shenyang, China. ISBN:978-1-424-5845-5, DOI: 10.1109/ICACC.2010.5486728.
4. Jonathan Clarke, Owen McAree, and Wen-Hua Chen, “Development of an Open Architecture Attitude Heading Reference System using Micro-Electro-Mechanical Sensors”, *Proceedings of Workshop on Human Adaptive Mechatronics* (HAM), Loughborough, 2010.
5. Cunjia Liu, Jonathan Clarke, Wen-Hua Chen, and John Andrews. “Modelling and identification of a miniature helicopter”, *Proceedings of Workshop on Human Adaptive Mechatronics* (HAM), Loughborough, 2010.

References

[1] IDG-300 integrated dual-axis gyro. Technical report, InvenSense, DOC-00075-01, 2222006, 2006. 143

[2] *Instrument Flying Handbook*. Federal Aviation Administration, ISBN 1-5602-7706-8, 2007,2008. 25

[3] Blue Bear home page. `http://www.bluebear.co.uk/`, Jun 2008. 71, 120

[4] Gumstix home page. `http://www.gunstix.com/`, March 2010. 139

[5] I. H. Abbott and A. E. Von Doenhoff. *The Theory of Wing Sections*. Dover, ISBN 0-486-60586-8, 1949, 1959. 76

[6] M. J. Allen. Autonomous soaring for improved endurance of a small uninhabited air vehicle. In *43rd AIAA Aerospace Sciences Meeting and Exhibit*, page 998. NASA Dryden Flight Research Center, Edwards, California,, 10-13 Jan, AIAA-2005-1025 2005. ix, 9, 11, 12, 13, 14, 15, 16, 22, 59, 71, 135

[7] M. J. Allen. Updraft model for development of autonomous soaring uninhabited air vehicles. In *44rd AIAA Aerospace Sciences Meeting and Exhibit*, 9-12 Jan, AIAA 2006-1510 2006. 14, 22, 43, 44, 45

[8] M. J. Allen and V. Lin. Guidance and control of an autonomous soaring vehicle with flight test results. In *45rd AIAA Aerospace Sciences Meeting and Exhibit*, page 351. NASA Dryden Flight Research Center, Edwards, CA, 10-13 Jan, AIAA-2007-867 2007. 9, 36, 59, 60

[9] AnalogDevices. *ADXRS610*. D06520-0-4/07(0), 2007. 25, 140, 143

[10] R. H. Barnard and D. R. Philpott. *Aircraft Flight*. Pearson, ISBN 0-13-120043-7, 3rd edition, 1989, 1995, 2004. 76

[11] D. B. Beard and R. W. Kingston. Real-time attitude and position estimation for small UAVs using low-cost sensors. In *AIAA 3rd Unmanned Unlimited Technical Conference Online Proceedings Conference Proceeding*, AIAA-2004-6488, 2004. 26, 30, 71, 73, 74, 75, 83

[12] S. Bonnabel, P. Martin, and P. Rouchon. A non-linear symmetry-preserving observer for velocity-aided inertial navigation. In *American Control Conference*, page 5, Jun 2006. 76

[13] M. Boslough. *Autonomous Dynamic Soaring Platform for Distributed Mobile sensor arrays.* Sandia National Laboratories Report, SAND2002-1896, 2002. 21

[14] T. Bradbury. *Meteorology and Flight, A Pilot's Guide to Weather, third edition.* A & C Black Ltd, 2000. 13, 16, 43, 45

[15] J. Castellanos, S. Lesecq, N. Marchand, and J. Delamare. A low-cost air data attitude heading reference system for the tourism airplane applications. In *Sensors, IEEE*, page 4, Nov 2005. 76

[16] A. Chakrabarty and J. W. Langelaany. Flight path planning for UAV atmospheric energy harvesting using heuristic search. In *AIAA Guidance, Navigation, and Control Conference*, AIAA 2010-8033, Aug 2010, AIAA 2010-8033. 11

[17] A. Cocconi. AC Propulsion's solar electric powered SoLong UAV. Technical report, AC Propulsion Inc, Nov 2006. 21

[18] J. H. Cochrane. Maccready theory with uncertain lift and limited altitude. Technical report, University of Chicago Internal Report, May 1999. x, 54, 55

[19] I. D. Cowling, S. Willcox, Y. Patel, P. Smith, and M.Roberts. Increasing persistence of UAVs and MAVs through thermal soaring. *The Aeronautical Journal*, 113(1145), 2009. 23

[20] J. Delafield. *Gliding Competitively.* A & C Black, ISBN 0-7136-2224-5, 1982. 13, 15, 19, 43, 46, 47

[21] T. Do, S. K. Park, and Y. S. Suh. Attitude estimation using accelerometers with constrained external acceleration. In *Control Automation and Systems (ICCAS), 2010 International Conference on*, pages 2427–2430, Oct 2010. 76

[22] D. J. Edwards. Implementation details and flight test results of an autonomous soaring controller. Technical report, North Carolina State University, 2008. 9, 13, 22, 36, 43, 52, 53, 59, 60, 71, 135

[23] M. Euston, P. Coote, R. Mahony, J. Kim, and T. Hamel. A complementary filter for attitude estimation of a fixed-wing UAV. In *Intelligent Robots and Systems, 2008. IROS 2008. IEEE/RSJ International Conference on*, pages 340 –345, sept. 2008. 91, 120

[24] D. Gebre-Egziabher, G. Elkaim, J. Powell, and B. Parkinson. A gyro-free quaternion-based attitude determination system suitable for implementation using low cost sensors. *Position Location and Navigation Symposium, IEEE*, (pp. 185-192), 2000. 30

[25] J. Gedeon. Dynamic analysis of dolphin style thermal cross country flight. Proceedings of the XIV OSTIVCongress, Organisation Scientifique et Technique Internationale du Vol ‘a Voile, 1974. ix, 13, 14, 43

[26] Honeywell. *HG9900 Navigation-Grade Inertial Measurement Unit (IMU)*. N61-0491-000-001:Layout 1, March 2009. 25

[27] H. Hong, J. G. Lee, C. G. Park, and H. S. Han. A leveling algorithm for an underwater vehicle using extended Kalman filter. In *Position Location and Navigation Symposium, IEEE 1998*, pages 280 –285, apr 1998. 25, 30

[28] R. Irvinea, F. Innesa, A. Brownb, S. Vosperb, G. Rooneyb, B. Devenishb, M. Hookc, and E. Sparksc. Autonomous soaring project phase 2. In *2nd SEAS DTC Technical Conference - Edinburgh*, 2007. 23

[29] F. Irving. *The Paths of Soaring Flight*. Imperial College Press, ISBN 1-886094-055-2, 1999, 2006. ix, 11, 12, 13, 43, 53

[30] S. Julier and J. K. Uhlmann. A new extension of the Kalman filter to nonlinear systems. In *International Symposium Aerospace Defense Sensing, Simulation and Controls, Orlando*, 1997. 30, 181

[31] D. Jung and P. Tsiotras. Inertial attitude and position reference system development for a small uav. *AIAA 07-2763*, 2007. 126

[32] R. E. Kalman. A new approach to linear filtering and prediction problems. *Transaction of the ASME - Journal of Basic Engineering*, pages 35–45, 1960. 30, 179

[33] J. A. Kyle. Optimal soaring by a small autonomous glider. Technical report, Oregon State University, 2006. 53

[34] J. W. Langelaan. Long distance/duration trajectory optimization for small UAVs. In *Guidance, Navigation and Control Conference, Aug 16-19 2007. Hilton Head, South Carolina*, 2007. 23

[35] N. Lawrance and S. Sukkarieh. A guidance and control strategy for dynamic soaring with a gliding UAV. In *Robotics and Automation, 2009. ICRA '09. IEEE International Conference*, pages 3632 –3637, may 2009. 21

[36] D. Lee, S. Longo, and E. C. Kerrigan. Predictive control for soaring of unpowered autonomous UAVs. In *4th IFAC Nonlinear Model Predictive Control Conference*, Aug 23-27, 2012. 23

[37] H. T. Lee, I. M. Kroo, and C. K. Patel. Extracting energy from atmospheric turbulence. Technical report, 2008. 23

[38] D. H. Lenschow and P. L. Stephens. The role of thermals in the convective boundary layer. *Boundary-Layer Meteorology*, 19:509–532, 1980. 10.1007/BF00122351. ix, 11, 15, 17, 18, 45

[39] Locosys Technology Inc. *LS20030-3 Data Sheet*, 1.0 edition, Oct 2007. 148

[40] P. B. MacCready-Jr. Optimum airspeed selector. *Soaring*, Jan-Feb, page 10 1958. 8, 10, 13, 36, 43, 53

[41] P. S. Maybeck. *Stochastic models, estimation, and control*, volume 141 of *Mathematics in Science and Engineering*. Academic Press, 1979 , ISBN 0-12-411042-8. 30

[42] N. Metni, J. Pflimlin, T. Hamel, and P. Soueres. Attitude and gyro bias estimation for a VTOL UAV. *Control Engineering Practice*, 14, 2006. 25

[43] Microchip. *dsPIC33FJ32GP302/304, dsPIC33FJ64GPX02/X04, and dsPIC33FJ128GPX02/X04 Data Sheet*. Microchip, ds70292b edition, 2008. 121, 152

[44] MicroPilot. Micropilot home page. `http://www.MicroPilot.com/`, March 2010. 71, 120

[45] M. Nagy, T. Vicsek, and Z. Akos. Comparing bird and human soaring strategies. *Procedings of National Academy of Science USA*, 105:4139–4143, 2008. 8

[46] C. K. Patel and I. Kroo. Control law design for improving UAV performance using wind turbulence. In *44th AIAA Aerospace Sciences Meeting and Exhibit*, Jan 2006. 21

[47] D. Piggott. *Gliding, A Handbook on Soaring Flight*. A & C Black, 2002, 1997, 1990, 1986, 1976, 1971, 1967, 1958. 13, 15, 23, 43, 59

[48] H. Reichmann. *Cross-Country Soaring*. Soaring Association of America, Inc, ISBN 1-883813-01-8, 1975, 1993. x, 8, 23, 55, 56

[49] J. Rice. *Mathematical Statistics and Data Analysis*. Duxbury Press, second edition, 1995, ISBN 0-534-20934-3. 180

[50] R. E. Sheldehl and P. C. Kilmes. Aerodynamic characteristics of seven symmetrical airfoil sections through 180-degree angle of attack for use in aerodynamic analysis of vertical axis wind turbines. Technical report, Sandia National Laboratories, 1981. x, 38, 39, 40

[51] L. Sherry, C. Brown, B. Motazed, and D. Vos. Performance of automotive-grade mems sensors in low cost ahrs for general aviation. In *Digital Avionics Systems Conference, 2003. DASC '03. The 22nd*, volume 2, pages 12.C.2 – 12.1–5 vol.2, Oct 2003. 76

[52] G. Siouris. *Aerospace Avionics Systems: A Modern Synthesis*. Academic Press, 1993. ix, 33, 34, 120

[53] G. L. Smith, S. F. Schmidt, and L. A. McGee. Application of statistical filter theory to the optimal estimation of position and velocity on board a circumlunar vehicle. *National Aeronautics and Space Administration*, 1962. 30

[54] R. F. Stengel. *Flight Dynamics*. Princeton, ISBN 0-691-11407-2. 37, 38, 50, 75, 76

[55] Y. S. Suh. Attitude estimation using low-cost accelerometer and gyroscope. In *Proceedings of the 7th Korea-Russia International Symposium*, 2003. 24, 72, 73

[56] C. E. Wallington. *Meteorology for Glider Pilots, Third International Edition*. John Murray Publishers, Ltd, 1989. ix, 11, 13, 15, 19, 43, 46, 53

[57] A. Welch. *Pilots' Weather*. William Clowes and Sons, Ltd, ISBN 0-7195-2661-2, 1979, 1973. ix, 11, 15, 20, 47

[58] G. Welch and G. Bishop. An introduction to the Kalman filter. Technical report, Department of Computer Science University of North Carolina, 2006. 30, 180

[59] J. Wharington. Autonomous control of soaring aircraft by reinforcement learning. Technical report, Royal Melbourne Institute of Technology, 1998. ix, 9, 12, 13, 21, 43, 59, 60, 61

[60] J. Wharington. Heuristic control of dynamic soaring. In *Control Conference, 2004. 5th Asian*, volume 2, pages 714 – 722, July 2004. 21

[61] J. Wharington and I. Herszberg. Control of a high endurance unmanned air vehicle. *ICAS-98-3,7,1, AIAA A98-31555, 21st ICAS Congress*, September 13-18, 1998. 8, 21

[62] T. S. Yoo, S. K. Hong, H. M. Yoon, and S. Park. Gain-scheduled complementary filter design for a mems based attitude and heading reference system. *Sensors*, 11:3816 – 3830, 2011. 24, 25, 30, 71, 72, 73, 90, 91

[63] P. Zhang, J. Gu, E. E. Milios, and P. Huynh. Navigation with IMU/GPS/digital compass with unscented Kalman filter. In *Proceedings of the IEEE International Conference on Mechatronics & Automation*, July 2005. 25

[64] Y. J. Zhao. Optimal patterns of glider dynamic soaring. *Optimal Control Applications and Methods*, 25(2):67–89, 2004. 18, 21, 52